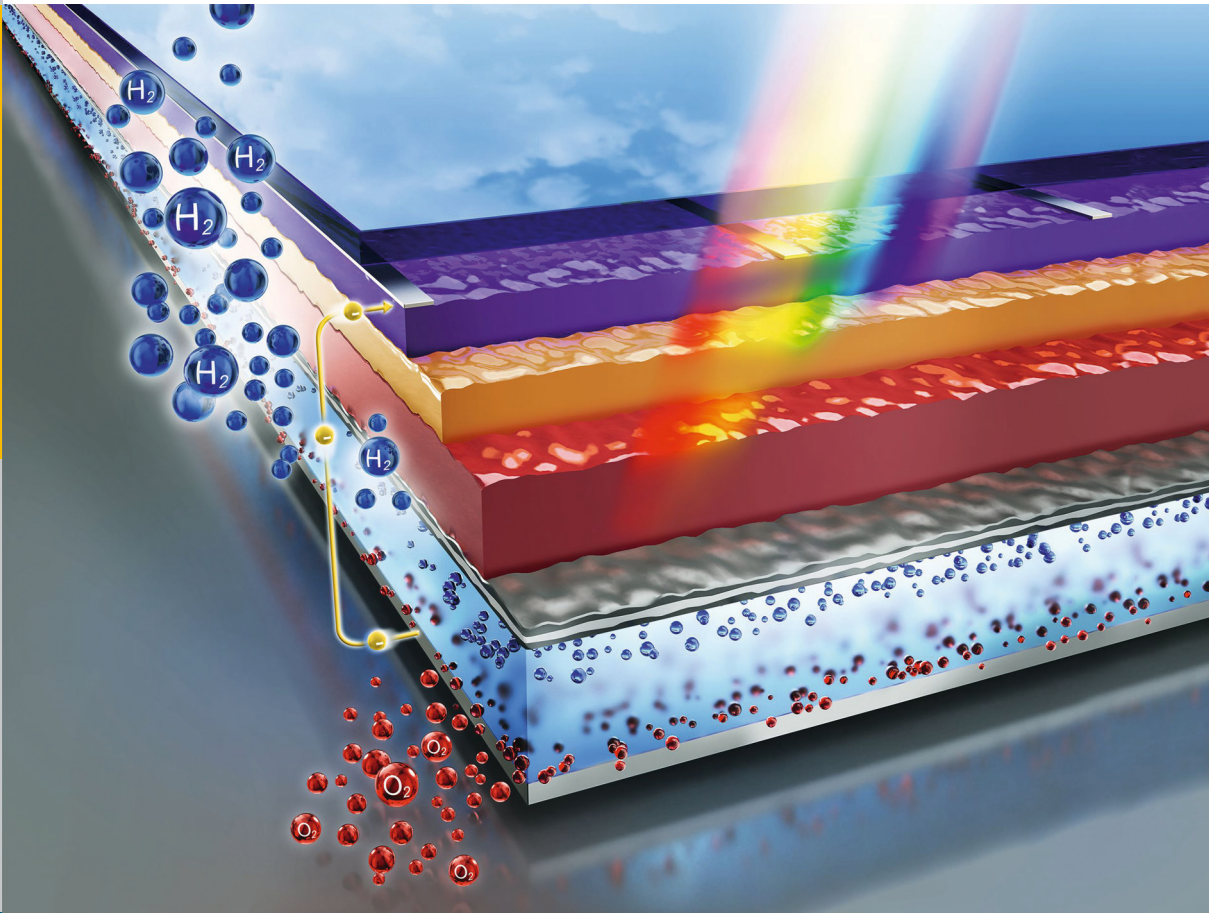


# Light induced water splitting using multijunction thin film silicon solar cells

Félix Urbain



Energie & Umwelt /  
Energy & Environment  
Band/ Volume 323  
ISBN 978-3-95806-148-4

# **Light induced water splitting using multijunction thin film silicon solar cells**

Von der Fakultät für Elektrotechnik und Informationstechnik  
der Rheinisch-Westfälischen Technischen Hochschule Aachen  
zur Erlangung des akademischen Grades eines  
Doktors der Ingenieurwissenschaften genehmigte Dissertation

vorgelegt von

Félix Urbain, M.Sc. M.Sc. MBE

aus Luxemburg

**Berichter:**

Universitätsprofessor Dr. Uwe Rau

Rheinisch-Westfälische Technische Hochschule Aachen / Forschungszentrum Jülich

Universitätsprofessor Dr. Wolfram Jaegermann

Technische Universität Darmstadt

Tag der mündlichen Prüfung: 30. Mai 2016

Diese Dissertation ist auf den Internetseiten der Hochschulbibliothek online verfügbar.



Forschungszentrum Jülich GmbH  
Institute of Energy and Climate Research  
IEK-5 Photovoltaics

# Light induced water splitting using multijunction thin film silicon solar cells

Félix Urbain

Schriften des Forschungszentrums Jülich  
Reihe Energie & Umwelt / Energy & Environment

Band / Volume 323

---

ISSN 1866-1793

ISBN 978-3-95806-148-4



Bibliographic information published by the Deutsche Nationalbibliothek.  
The Deutsche Nationalbibliothek lists this publication in the Deutsche  
Nationalbibliografie; detailed bibliographic data are available in the  
Internet at <http://dnb.d-nb.de>.

Publisher and  
Distributor: Forschungszentrum Jülich GmbH  
Zentralbibliothek  
52425 Jülich  
Tel: +49 2461 61-5368  
Fax: +49 2461 61-6103  
Email: [zb-publikation@fz-juelich.de](mailto:zb-publikation@fz-juelich.de)  
[www.fz-juelich.de/zb](http://www.fz-juelich.de/zb)

Cover Design: Grafische Medien, Forschungszentrum Jülich GmbH

Printer: Grafische Medien, Forschungszentrum Jülich GmbH

Copyright: Forschungszentrum Jülich 2016

Schriften des Forschungszentrums Jülich  
Reihe Energie & Umwelt / Energy & Environment, Band / Volume 323

D 82 (Diss. RWTH Aachen University, 2016)

ISSN 1866-1793  
ISBN 978-3-95806-148-4

The complete volume is freely available on the Internet on the Jülicher Open Access Server (JuSER)  
at [www.fz-juelich.de/zb/openaccess](http://www.fz-juelich.de/zb/openaccess).



This is an Open Access publication distributed under the terms of the [Creative Commons Attribution License 4.0](https://creativecommons.org/licenses/by/4.0/),  
which permits unrestricted use, distribution, and reproduction in any medium, provided the original work is properly cited.

To my parents.

*Mengen Elteren.*



# Abstract

It has been widely recognised that fossil fuel reserves are not sufficient to cover the energy demand of our societies in the future, even if the energy utilisation would stagnate on today's level. The extent of the problem is also associated with the emission of the greenhouse gas  $\text{CO}_2$  upon combustion of fossil fuels that can lead to unpredictable climate changes on earth. Nature's own processes of fuel generation based on biomass utilisation are considered to be not efficient enough to replenish the used resources on a short time scale. To relieve this predicament, a transition from fossil fuels to renewable energy sources is therefore imperative and unavoidable. Renewable and carbon-free energy from wind and solar radiation are the only means which can fully replace fossil fuels and are able to cover an increasing energy demand in the future. But up to now, these fluctuating energy resources lack an appropriate and efficient storage technology.

Light induced water splitting, a process that mimics natural photosynthesis, provides a viable example of an ecofriendly energy concept as it converts solar energy into a storable and clean chemical fuel with a high gravimetric energy density, namely hydrogen. To be competitive with fossil fuels or hydrogen production by other means, this process must however become highly efficient and low-cost. In this regard, the utilisation of semiconductor based devices for the photoelectrochemical generation of hydrogen from water and sunlight is a promising and elegant means to store renewable energy and has been attracting considerable interest among research groups worldwide. To split water efficiently into its components hydrogen and oxygen the semiconductor photoelectrode has to meet several requirements:

- A high quantum efficiency to utilise the solar spectrum efficiently for the generation of charge carriers,
- The generation of a photovoltage at the working point of approx. 1.6 V to sustain the hydrogen and oxygen evolution reactions and to account for additional losses (overpotentials),
- Electrochemical stability in a harsh and corrosive environment, and
- Fast kinetics of the charge transfer at the solid/liquid junction to inhibit unintended side reactions (catalysis).

For this purpose, particularly designed multijunction solar cells on the basis of hydrogenated amorphous (a-Si:H) and microcrystalline silicon ( $\mu$ c-Si:H) were developed and characterised in this work. The chosen approach deviates from previous studies on thin film silicon solar cells and focused more on the development of efficient high voltage devices, suitable for water splitting applications. Therefore, a development route has been described to achieve high photovoltages with emphasis on the optimal fabrication parameter regimes for the intrinsic absorber layers. Firstly, the adjustment of the opto-electronic and structural properties of the intrinsic a-Si:H and  $\mu$ c-Si:H silicon absorber layers and their implementation in single junction solar cells were investigated. Secondly, the single junction solar cells were implemented in multijunction solar cells, which were optimised in terms of photovoltage and photocurrent by varying the process parameters and thickness of the intrinsic absorber layers. The photocurrents of the individual sub cells were additionally adjusted by integrating microcrystalline silicon oxide as intermediate reflecting layers. It was found that the electronic properties of the individual series-connected sub cells can be adjusted to systematically tune the photovoltage between 1.5 V and 2.8 V with photovoltaic conversion efficiencies over 11.5 % for tandem and over 13.0 % for triple and quadruple junction cells. This allows for an efficient and bias-free water splitting process. Furthermore, the effects of prolonged illumination and temperature variation on the photovoltaic parameters of the multijunction solar cells were investigated.

For the application of the developed high voltage multijunction solar cells as photocathodes in photovoltaic-electrochemical cell (PV-EC) devices for water splitting, special attention needed to be devoted to the solar cell/electrolyte interface. Therefore, the chemical and electronic surface structure of the solar cells was manipulated by protective coatings and catalysts in order to minimise corrosion damage and overpotential losses, respectively. By this means, not only the material and fabrication costs were reduced but also the overall solar-to-hydrogen efficiency of the integrated photoelectrochemical devices was significantly increased. A record efficiency of 9.5 % was achieved, which outperforms all other thin film silicon based devices, as the former record was 7.8 %.

Modeling the integrated PV-EC system in terms of a series connection of a solar cell and an electrolysis cell showed excellent agreement with the experimental results. It was shown that the model can be used to analyse the relevant losses in the system and allows for a prediction of the efficiency limits for thin film silicon based water splitting devices based on the solar cell performance.

# Zusammenfassung

Es ist allgemein anerkannt, dass die Reserven der fossilen Brennstoffe nicht ausreichen um die Energienachfrage heutiger Gesellschaften auch in Zukunft abdecken zu können. Nicht einmal im Falle einer Stagnation des Energieverbrauchs auf heutigem Stand. Das Ausmaß des Problems ist ebenfalls mit der Emission des CO<sub>2</sub> Treibhausgases verbunden, welches bei der Verbrennung fossiler Brennstoffe entsteht und zu unvorhersehbaren Klimaveränderungen auf der Erde führen kann. Die natureigenen Prozesse zur Brennstoffgewinnung basierend auf Biomassennutzung werden ebenfalls als nicht effizient genug angesehen um die verbrauchten Ressourcen kurzfristig aufzufüllen. Um diesem Dilemma zu entgehen, ist ein Übergang von fossilen Brennstoffen zu erneuerbaren Energiequellen deshalb unabdingbar. Erneuerbare Energien ohne Kohlenstoff aus Wind und Sonnenlicht sind potenziell in der Lage mit fossilen Brennstoffen zu konkurrieren oder sie künftig sogar vollständig zu ersetzen um so eine nachhaltige Energieversorgung zu garantieren. Jedoch fehlt es diesen fluktuierenden Energiequellen noch an geeigneten und effizienten Speichertechnologien.

Eine Möglichkeit besteht darin, den Solarstrom nach dem Prinzip der künstlichen Photosynthese direkt zur Spaltung von Wasser einzusetzen. Bei diesem umweltschonenden Energiekonzept wird die Sonnenenergie in Wasserstoff umgewandelt, ein gut speicherbarer und chemisch reiner Energieträger mit einer hohen gravimetrischen Energiedichte. Für den wirtschaftlichen Betrieb müssen die Kosten und der Wirkungsgrad der solaren Wasserstofferzeugung jedoch noch weiter verbessert werden. In diesem Zusammenhang stellt die Verwendung von Halbleiterbauelementen zur direkten Nutzung von Sonnenlicht zur photoelektrochemischen Generation von Wasserstoff aus Wasser einen vielversprechenden und eleganten Weg dar. Um Wasser effizient photoelektrochemisch in seine Bestandteile Wasserstoff und Sauerstoff zu spalten, muss dabei die Halbleiter-Photoelektrode vielfältige Voraussetzungen erfüllen:

- Erzeugung einer Spannung am Arbeitspunkt von ca. 1,6 V um die Wasserstoff- und die Sauerstoffentwicklungsreaktionen zu treiben und zusätzliche Verluste, sogenannte Überspannungen, zu kompensieren,
- hohe Quantenausbeute für die effiziente Nutzung des Sonnenspektrums zur Generation von Ladungsträgern,
- elektrochemische Stabilität unter stark korrosiven Bedingungen und

- schnelle Kinetik des Ladungstransfers an der fest/flüssig-Grenzfläche um ungewollte Neben- und Rekombinationsreaktionen zu verhindern (Katalyse).

Zu diesem Zweck werden in dieser Arbeit speziell ausgelegte Mehrfachstapelzellen auf der Basis von amorphen und mikrokristallinen Silizium-Absorbern hergestellt und untersucht. Der hierfür gewählte Ansatz weicht dabei von vorangegangenen Untersuchungen an Dünnschicht-Silizium Solarzellen ab und orientiert sich stärker an der Entwicklung von speziell für die Wasserspaltung geeigneten Bauelemente mit hoher Ausgangsspannung. Es werden daher die Prozessschritte beschrieben welche für die Entwicklung hoher Photospannungen notwendig sind. Ein besonderes Augenmerk wird dabei auf die Herstellungsparameter der intrinsischen Absorberschichten gelegt. Als erstes steht das Anpassen der opto-elektronischen und strukturellen Eigenschaften der intrinsischen amorphen und mikrokristallinen Absorberschichten mit anschließender Implementierung in Einfachsolarzellen im Vordergrund. Der zweite Schritt besteht darin die entwickelten Einfachzellen in Mehrfachstapelzellen zu integrieren. Die Photospannung und die Stromdichte der Stapelsolarzellen werden dabei durch das Anpassen der Prozessparameter und der intrinsischen Absorberschichtdicke optimiert. Eine Anpassung der Stromdichten in den verschiedenen Einzelzellen wird außerdem durch das Einfügen von reflektierenden mikrokristallinen Siliziumoxid Zwischenschichten gewährleistet. Durch den mehrschichtigen seriellen Aufbau der Solarzellen können hohe Ausgangsspannungen zwischen 1,5 V und 2,8 V erreicht werden mit photovoltaischen Wirkungsgraden von über 11,5 Prozent für Tandem- und von über 13,0 Prozent für Dreifach- und Vierfachzellen. Diese Kennwerte ermöglichen eine effizient betriebene Photoelektrolyse. Darüberhinaus, wird ebenfalls auf den Einfluss von langanhaltender Belichtung und von Temperaturschwankungen auf die photovoltaischen Parameter der Solarzellen eingegangen.

Für die Anwendung der entwickelten Mehrfachstapelzellen als Photokathoden in photoelektrochemischen Bauelementen zur Wasserspaltung spielt die Solarzelle/Elektrolyt Grenzfläche eine entscheidende Rolle. Zur Minimierung von Verlusten und korrosiven Nebenreaktionen werden die chemische und elektronische Oberflächenstruktur in geeigneter Weise durch Schutzschichten und Katalysatoren modifiziert. Hierdurch können nicht nur die Material- und Herstellungskosten reduziert werden, sondern auch der Wirkungsgrad integrierter photoelektrochemischer Bauelemente deutlich gesteigert werden. Im Rahmen dieser Arbeit wurde ein Rekord-Gesamtwirkungsgrad von 9,5 Prozent erreicht, ein Wert der die Effizienz entsprechender Bauelemente auf Silizium-Basis deutlich übersteigt. Der bisherige Rekordwert lag bei 7,8 Prozent.

Die Modellierung des integrierten photoelektrochemischen Baulementes wird anhand eines Ersatzschaltbildes bestehend aus der Serienverschaltung einer Solarzelle mit einer Elektrolyse-Zelle realisiert. Die modellierten Werte weisen eine sehr gute Übereinstimmung mit den experimentell gemessenen Werten auf und ermöglichen so die Verluste des Gesamtsystems genau zu analysieren. Des Weiteren erlaubt das vorgestellte Modell Vorhersagen über die mit der Silizium-Dünnschichttechnologie maximal zu erreichenden Wirkungsgrade anzustellen.





# Contents

<b>1</b>	<b>Introduction</b>	<b>1</b>
<b>2</b>	<b>Principles of photoelectrochemical solar energy conversion</b>	<b>7</b>
2.1	Basic concepts of photovoltaics . . . . .	7
2.1.1	Light absorption in semiconductors . . . . .	7
2.1.2	Electrons in semiconductors . . . . .	9
2.1.3	Semiconductor junctions . . . . .	11
2.1.4	Operation principle of thin film <i>pin</i> solar cells . . . . .	12
2.2	Basic concepts of electrochemistry . . . . .	17
2.2.1	Charge transport in electrolytes . . . . .	17
2.2.2	Fermi level and standard potential of redox systems . . . . .	17
2.2.3	Electrochemical reaction kinetics . . . . .	20
2.3	Basic concepts of photoelectrochemical water splitting . . . . .	23
2.3.1	Principles of solar water splitting . . . . .	23
2.3.2	Metal/electrolyte interface . . . . .	23
2.3.3	Semiconductor/electrolyte interface . . . . .	25
2.3.4	Buried junction devices . . . . .	29
<b>3</b>	<b>Fundamentals and experimental details of thin film silicon solar cells</b>	<b>33</b>
3.1	Fundamentals of thin film silicon absorber materials . . . . .	33
3.1.1	Hydrogenated amorphous silicon a-Si:H . . . . .	33
3.1.2	Hydrogenated microcrystalline silicon $\mu\text{c-Si:H}$ . . . . .	37
3.2	Techniques and methods for the preparation of thin film silicon solar cells . . . . .	39
3.2.1	Plasma enhanced chemical vapor deposition . . . . .	40
3.2.2	Solar cell preparation . . . . .	44
3.3	Characterisation of thin film silicon absorber layers . . . . .	45
3.4	Characterisation of solar cells . . . . .	47
3.4.1	Photovoltaic parameters . . . . .	47
3.4.2	Quantum efficiency . . . . .	49
<b>4</b>	<b>Characterisation and modeling of photovoltaic-electrochemical devices</b>	<b>53</b>
4.1	Overview on photovoltaic-electrochemical devices . . . . .	53
4.2	Photoelectrochemical measurements . . . . .	55
4.2.1	Measurement setup . . . . .	55

4.2.2	Electrochemical methods . . . . .	56
4.3	Device modeling . . . . .	60
4.3.1	Series circuit model . . . . .	61
4.3.2	Input parameters . . . . .	62
4.4	Solar-to-Hydrogen efficiency calculation . . . . .	67
<b>5</b>	<b>High voltage multijunction thin film silicon solar cells</b>	<b>71</b>
5.1	Experimental details . . . . .	71
5.2	a-Si:H absorber layer properties and a-Si:H single junction solar cells	72
5.2.1	Intrinsic a-Si:H absorber layers . . . . .	73
5.2.2	a-Si:H single junction solar cells . . . . .	74
5.3	$\mu$ c-Si:H absorber layer properties and $\mu$ c-Si:H single junction solar cells	77
5.3.1	Intrinsic $\mu$ c-Si:H absorber layers . . . . .	78
5.3.2	$\mu$ c-Si:H single junction solar cells . . . . .	78
5.4	Tandem junction solar cells . . . . .	87
5.4.1	a-Si:H/ $\mu$ c-Si:H tandem junction solar cells . . . . .	87
5.4.2	a-Si:H/a-Si:H tandem junction solar cells . . . . .	91
5.5	Triple and quadruple junction solar cells . . . . .	93
5.5.1	a-Si:H/ $\mu$ c-Si:H/ $\mu$ c-Si:H . . . . .	94
5.5.2	a-Si:H/a-Si:H/ $\mu$ c-Si:H . . . . .	96
5.5.3	a-Si:H/a-Si:H/ $\mu$ c-Si:H/ $\mu$ c-Si:H . . . . .	98
5.6	Light induced degradation . . . . .	100
5.7	Temperature-dependent photovoltaic performance . . . . .	104
5.8	Summary and conclusions . . . . .	106
<b>6</b>	<b>Thin film silicon based photovoltaic-electrochemical devices</b>	<b>113</b>
6.1	Photocathode/electrolyte contact . . . . .	113
6.1.1	Catalytic and optical properties of single metal layer contacts	114
6.1.2	Metal stacks as photocathode contact . . . . .	116
6.2	Multijunction based PV-EC devices . . . . .	121
6.2.1	Influence of the catalyst . . . . .	123
6.2.2	Influence of the electrolyte . . . . .	124
6.2.3	Influence of light induced degradation . . . . .	127
6.3	Device analysis by modeling . . . . .	129
6.3.1	Modeling of the current-voltage characteristics . . . . .	130
6.3.2	Temperature-dependent photoelectrochemical performance . .	136
6.4	Summary and conclusions . . . . .	142
<b>7</b>	<b>Conclusion and future prospects</b>	<b>147</b>

---

<b>Bibliography</b>	<b>153</b>
<b>Appendix</b>	<b>I</b>
<b>Glossary</b>	<b>VII</b>
<b>List of Publications</b>	<b>XIII</b>
<b>Curriculum vitae</b>	<b>XIX</b>
<b>Acknowledgments</b>	<b>XXI</b>
<b>List of Figures</b>	<b>XL</b>
<b>List of Tables</b>	<b>XLIV</b>



# 1 Introduction

The increasing energy demand is one of our society's major future challenges [1]. Since the industrial revolution in the 18<sup>th</sup> century, the world population has seen a rapid increase and there is no end in sight: scientific studies prognosticate that the world's population is odds-on to increase from today's 7.3 billion people to 9.7 billion in 2050 and 11.2 billion at the century's end [2]. The concomitant global energy demand is projected to reach 30 TW by 2050 and 46 TW by 2100 [3].

The early energy challenge has led to the development of the modern industrial society, which has been governed by the conversion of chemical energy stored in carbon-based fossil fuels into heat, work and carbon dioxide (CO<sub>2</sub>). Today, 80 % of our energy needs are met by fossil fuels, *i.e.* oil, coal, and natural gas, whose chemical energy has been locked up over millennia by plant photosynthesis. However, these finite natural resources are being depleted at an ever increasing rate, with associated rises of greenhouse gases, particularly atmospheric CO<sub>2</sub>, which is considered to be the main cause of the climate change. Stabilising and eventually lowering global rates of CO<sub>2</sub> emission poses a grave challenge and requires to overturn the current carbon-rich energy infrastructure and draw increasingly on cost-effective, environmentally benign and efficient energy concepts [4, 5].

Against this backdrop, it becomes vital to exploit renewable and sustainable energy sources, in particular solar energy. The sun directs annually considerably more solar energy towards the Earth's surface than the world's annual energy consumption [6]. Hence, solar energy has the potential to cover all our energy needs and will therefore certainly make a substantial contribution to the world's energy landscape in the coming decades. Unfortunately, the availability of the sunlight is highly variable, as it is subjected to a day/night cycle, to the presence of clouds, to geographical location, etc. This intermittency of the solar energy necessitates the implementation of energy storage solutions, preferably on a large scale. An attractive possibility is the storage of solar energy in the form of a chemical fuel. Compared to mechanical-based storage systems, capacitors or batteries, chemical fuels have a 2-3 orders of magnitude higher energy density and thus, provide the most effective way of storing energy [1]. This is because the energy is stored in the smallest possible configuration: chemical bonds [7]. Examples of chemical fuels are hydrogen, methane, methanol, gasoline, diesel, coal and wood. Most of these fuels require a source of carbon in their synthesis routes. For this, CO<sub>2</sub> would be a prominent candidate,

also in view of the environmental concerns already mentioned. However, capturing CO<sub>2</sub> without using fossil fuels is a highly challenging and costly task [7]. In spite of that, direct photoelectrochemical conversion of CO<sub>2</sub> into a fuel appears to be even more tricky, as the electrochemical half-reactions for the conversion of CO<sub>2</sub> to, *e.g.*, methanol [8] or methane [9] involve complex six- and eight-electron transfer steps, respectively.

The synthesis of hydrogen, on the contrary, offers several important advantages. It does not require a carbon source and can be conducted *via* a water splitting reaction, in which water is being used as a convenient and abundant fuel source. The splitting of water molecules into their atomic components hydrogen and oxygen requires 237 kJ/mol, *i.e.* 1.23 eV of energy per electron, which can be very well provided by most of the photons within the sunlight spectrum (wavelengths  $\leq 1008$  nm). Moreover, hydrogen has the highest mass energy density among all the chemical fuels and can be readily used to generate power either via combustion or in a fuel cell [10,11]. Alternatively, it can be refined further to liquid hydrocarbons. In addition to that, only two electrons are involved in the reduction half-reaction to form H<sub>2</sub>. The photoreduction of water is therefore considerably easier as the photoreduction of CO<sub>2</sub>.

To be competitive with fossil fuels or hydrogen production by other means [12], the water splitting process must, however, become highly efficient and low-cost. In this context, integrated semiconductor based photoelectrochemical systems emerged as adequate candidates and have been attracting considerable interest among research groups worldwide [13]. These systems offer an adequate pathway because they can be operated at standard temperature and pressure regimes and because the systems can be built as compact devices, which require fewer additional components (frames, wires, etc.) compared to decoupled photovoltaic-plus-electrolyser systems.

Photoelectrochemical water splitting was first reported by Fujishima and Honda in 1972 using TiO<sub>2</sub> as light absorbing semiconductor [14]. Since then, a variety of semiconducting materials and device configurations have been examined for their usability as water splitting photoelectrodes [15]. Yet, practical water splitting remains challenging due to the stringent requirements that photoelectrodes have to fulfil, in particular with respect to high output voltages and current densities, and long-term electrochemical stability [16].

Regardless of the chosen semiconductor material for light induced water splitting, integrated photoelectrochemical device structures generally constitute of a photovoltaic (PV) cell connected electrically with catalysts of an electrolysis cell.

Based on this assumption, it becomes possible to assess the maximum efficiency for the solar-to-hydrogen energy conversion in a PV-electrochemical device. To do so, the seminal derivation by Shockley and Queisser that establishes the maximum conversion efficiency limit (detailed balance limit) for a single semiconductor junction PV cell [17] must be linked with the reaction kinetics for catalysts used in electrochemical (EC) cells [18–21]. The electrochemical reaction kinetics were computed assuming Butler-Volmer kinetics [22]. Fig. 1.1 displays the accordingly calculated<sup>1</sup> efficiency  $\eta$  for a PV-EC system plotted versus the open-circuit voltage  $V_{OC}$  of the single absorber PV cell for varying individual PV and catalysis performance.

For  $V_{OC}$  values below 1.23 V of the PV cell, the water splitting reactions cannot be driven and thus,  $\eta_{STH}$  equals 0 % (see Fig. 1.1). For photovoltages above 1.23 V, hydrogen can theoretically be generated by the PV-EC system and the shape of the resulting  $\eta_{STH}$  efficiency curves (red, blue, and black curves in Fig. 1.1) describes the balance between two different sources of limitations. The right side of the curves represents the photocurrent limits based on insufficient light absorption by high photovoltage, *i.e.* wide band gap semiconductors. Hence, this side of the PV-EC curves follows the trend of the  $\eta_{PV}$  curve showing the Shockley-Queisser limit of the PV part (yellow curve in Fig. 1.1). The left side of the modeled  $\eta_{STH}$  curves displays the limits due to imperfect catalyst kinetics, which make for inefficient use of the absorbed photons. It becomes obvious that an improved PV cell performance (indicated by the green arrow in Fig. 1.1) can compensate for less efficient catalyst materials (indicated by the black arrow in Fig. 1.1) and *vice versa*. For the ideal case of zero losses in the PV-EC system (red solid curve in Fig. 1.1), the water splitting reaction requires 1.23 V and an efficiency of 30.5 % can be achieved. In reality, however, the photoelectrolysis of water requires photovoltages over 1.6 V to run autonomously, taking into account imperfect catalyst kinetics [21, 24]. As apparent from Fig. 1.1, higher required photovoltages ( $V_{OC}$ ) limit the overall solar-to-hydrogen efficiency in single wide band gap PV cells. A viable solution to this lies in the application of multijunction solar cells, which provide higher photovoltages, offer an improved utilisation of the solar spectrum, and reduced thermalisation losses in comparison to single junction devices [25, 26].

---

<sup>1</sup>The calculation was based on the variation of the Butler-Volmer parameters (transfer coefficient  $\alpha$  and exchange current density  $j_0$ , see Section 2.2.3) and on the variation of the parameters of the Shockley-Queisser (SQ) theory (short-circuit current density  $J_{SC}$  and saturation current density  $J_0$  relative to the maximum available short-circuit current density  $J_{SC,SQ}$  and saturation current density  $J_{0,SQ}$  in the SQ-limit, respectively) [17, 23]. The calculation assumes equal areas available for the light absorption and for the water splitting reactions.



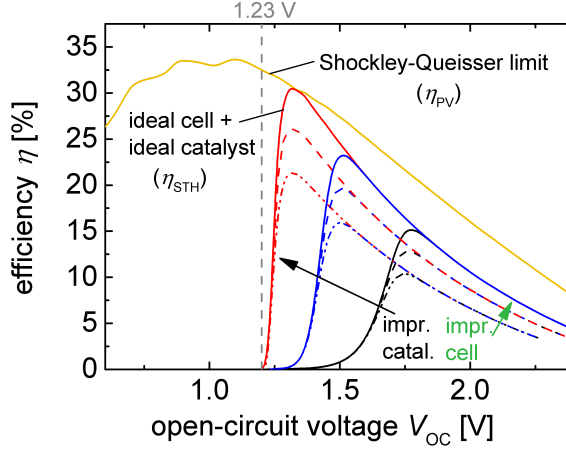


**Fig. 1.1** Solar-to-hydrogen efficiency  $\eta_{\text{STH}}$  as a function of the open-circuit voltage  $V_{\text{OC}}$  of a single absorber photovoltaic (PV) cell for varying performance of the PV cell and electrochemical catalyst. The yellow solid curve shows the Shockley-Queisser (SQ) limit for a single band gap PV cell efficiency  $\eta_{\text{PV}}$ . The thermodynamically required voltage for the operation of a photoelectrochemical device for water splitting is 1.23 V. The black arrow indicates an improved electrochemical catalytic activity and the green arrow indicates an improved PV cell performance. For the black, blue, and red curves the transfer coefficient  $\alpha$  was varied from 0.15 to 0.25 to 1 and the exchange current density  $j_0$  was varied from  $10^{-8}$  to  $10^{-6}$  to  $0.1 \times 10^3 \text{ mA/cm}^2$ . For the dotted, dashed, and solid curves,  $J_{\text{SC}}$  was varied from 0.9 to 0.95 to  $1 \times J_{\text{SC,SQ}}$  and  $J_0$  was varied from 100 to 20 to  $1 \times J_{0,\text{SQ}}$ . A theoretical maximum efficiency of 30.5 % can be found at the crossing point of the red solid curve with the SQ-limit. For this ideal case of zero losses, the theoretical operation point of the PV-EC device (1.23 V) coincides with the maximum power point of the ideal PV cell in the SQ-limit.

So far, the highest efficiencies for integrated solar water splitting systems (up to 18.3 %) have been reported for multijunction III-V semiconductor structures [27–29]. The widespread use, in particular of III-V semiconductors, is however still hampered by stability issues and cost limitations. In this regard, the silicon based thin film technology presents a promising pathway to sustainable solar hydrogen production, as it stands out due to its versatility, earth abundance, and low cost production [30, 31]. Photoelectrodes made of thin film silicon have recently

---

established their position as prominent devices under research for water splitting applications and are the central theme of this work.

In the scientific literature, numerous studies have successfully demonstrated unbiased solar water splitting using silicon based PV-EC devices [32]. In order to maximise the solar-to-hydrogen efficiency of these devices, the challenge, however, lies in the identification and understanding of the fundamental efficiency-limiting processes. In this regard, the present work focuses on the development, application, and modeling of new types of multijunction solar cells, specifically tailored to match the electrochemical requirements for water splitting.

This work consists of the following: First, in **Chapter 2**, the basic principles necessary to comprehend the photoelectrochemical conversion of solar energy into both electrical energy and chemical energy will be discussed. **Chapter 3** covers the methods and techniques used for the deposition and characterisation of thin film silicon solar cells. The PV-EC device is presented in detail in **Chapter 4**, with respect to the characterisation methods and to the modeling of the device. Additionally, a review of the relevant research on water splitting devices is provided to offer a basis for the understanding of the various experiments that are discussed later on. The results on the development of high voltage single and multijunction solar cells made of amorphous and microcrystalline silicon are elaborated in **Chapter 5**. Furthermore, the effects of prolonged illumination and temperature variation on the photovoltaic parameters of the multijunction solar cells were investigated. In **Chapter 6** the results on the application and modeling of the developed high voltage solar cells as photocathodes in PV-EC cell devices for water splitting are presented. Finally, **Chapter 7** provides a short summary and discusses the future prospects of this work.



## 2 Principles of photoelectrochemical solar energy conversion

*This chapter describes the principles necessary to comprehend the photoelectrochemical conversion of solar energy into both electrical energy and chemical energy. As the scientific language and concepts used in electrochemical literature differ from those used in solid-state physics in some aspects, the basic concepts of photovoltaics and electrochemistry shall be firstly discussed. This includes a short introduction in the solid-state semiconductor physics and a description of the relevant electrochemical principles. Secondly, the topic of photoelectrochemical water splitting, which combines the foregoing elaborated photovoltaic and electrochemical aspects, will be elucidated. Following a brief description of the thermodynamic requirements for the electrolysis of water, in particular the metal/electrolyte and semiconductor/electrolyte interfaces will be contrasted with each other. To close up, the buried junction device concept for light induced water splitting will be described and compared to the semiconductor/electrolyte junction device concept.*

### 2.1 Basic concepts of photovoltaics

#### 2.1.1 Light absorption in semiconductors

The absorption of photons takes place through the excitation of electrons into states of higher energy [33]. If a continuous range of excitation energy states is available in the absorbing material, photons of any arbitrary energy  $h\nu$  can be absorbed, with  $h$  the Planck's constant and  $\nu$  the frequency of the electromagnetic wave. This situation would be equivalent to an ideal black body. In fact, metals represent the closest approximation to black bodies, as they possess a continuous, uninterrupted range of excitation energies. Only the reflection of major parts of the incident light prevents them from being considered as ideal black bodies.

In semiconductors the situation looks different, as the range of excitation energies is interrupted by an energy band gap of width  $E_g$ , as schematically depicted in Fig. 2.1.

The energy gap separates the nearly fully occupied energy range of the valence band

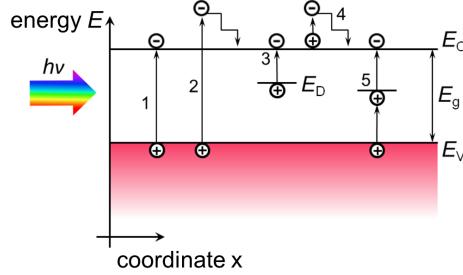


**Fig. 2.1** Schematic illustration of optical transitions in a semiconductor (at 300 K) upon light excitation. Electrons are excited from the valence band into the conduction band by the absorption of a photon with the energy  $h\nu$ , while leaving a vacancy or a hole in the valence band. The energy  $E_g$  defines the width of the band gap of a semiconductor (details can be found in the text).

(valence band edge  $E_V$ ) from the nearly unoccupied energy range of the conduction band (conduction band edge  $E_C$ ). For a direct band-to-band excitation of an electron from the valence band to the conduction band by the absorption of a photon, the photon must have an energy at least as high as the energy gap  $E_g = h\nu$  (transition 1 in Fig. 2.1). Electrons excited into higher energy levels of the conduction band (transition 2 in Fig. 2.1) are thermalised to the lower edge of the conduction band  $E_C$  within about  $10^{-12}$  to  $10^{-13}$  seconds [24]. For direct band-to-band transitions in direct semiconductors, the momentum conservation law for electron excitation by photon absorption is relaxed and the relation between the absorption coefficient  $\alpha_{\text{abs}}$  and the photon energy  $E_{\text{ph}}$  can be written as  $\alpha_{\text{abs}} \sim \sqrt{E_{\text{ph}} - E_g}$  [34]. Please note that this relation is valid only for light with photon energy larger than the band gap of the semiconductor and that it ignores all other sources of absorption other than the band-to-band absorption. For indirect semiconductors, the momentum of electrons does not remain constant and band-to-band transitions can only occur indirectly *via* an additional phonon in the semiconductor lattice. In this case, the relation between  $\alpha_{\text{abs}}$  and  $E_{\text{ph}}$  is given by  $\alpha_{\text{abs}} \sim (E_{\text{ph}} - E_g)^2$  [34].

In general, photons with smaller energies than  $E_g$  cannot excite an electron, and thus, cannot be absorbed, but may be transmitted or reflected by the semiconductor. However, if impurities are incorporated in the lattice, *e.g.* by doping, various other low energy electronic transitions become feasible. For instance, an excitation of an electron to or from a donor impurity level  $E_D$  within the band gap into the conduction band is

possible (transition 3 and 5, respectively in Fig. 2.1). Since the impurity concentration in the lattice (also related to the overlap of the wavefunctions) is relatively small, the corresponding absorption coefficient will be smaller by many orders of magnitude than that for a band-to-band transition. Within the conduction band electrons may also be excited to higher energy levels, where they start losing their energy by stepwise generation of phonons until they reach the lower edge of the conduction band  $E_C$  again (transition 4 in Fig. 2.1). Such intraband transitions require lower photon energies and predominantly occur in highly doped semiconductors [24]. In crystalline silicon (c-Si), for instance, the electrons can stay up to  $10^{-3}$  seconds in average in the conduction band before they recombine, which is a comparatively long time that allows the processes for the conversion of electron energy into electrical energy to take place *via* charge transport to an outer electrical circuit [33]. Recombination may be accompanied by the emission of a photon (radiative process) or the recombination may occur in a radiationless way by transferring the excess energy to a trap state within the band gap (Shockley-Read-Hall process). The excess energy through recombination may also be transferred to another free electron in the conduction band (Auger process).

### 2.1.2 Electrons in semiconductors

Electrons in semiconductors can be interpreted as low-density particle ensembles and their occupancy in the conduction band can be approximated by the Boltzmann function [34]:

$$n_e \approx N_C \exp \left[ -\frac{E_C - E_F}{kT} \right] \quad , \quad (2.1)$$

where  $N_C$  is the density of energy states within a few  $kT$  above the conduction band edge. As seen in the foregoing section, the excitation of an electron from the valence band to the conduction band leaves a positively charged hole in its place in the valence band. Note that there is a chemical analogy with the dissociation of a liquid such as water into  $\text{H}_3\text{O}^+$  and  $\text{OH}^-$ . In semiconductors equal numbers of oppositely charged species are produced upon excitation in order to preserve charge neutrality. In this case, the position of the Fermi level  $E_F$  lies approximately in the middle of the energy gap, as shown in Fig. 2.2(a)). Analogous to metals, the Fermi energy of a semiconductor is the electrochemical potential for electrons  $\tilde{\mu}_e$ , *i.e.* the thermodynamic work required to add one electron to the material [35] (see Section 2.2).

Intrinsic semiconductors exhibit a rather low conductivity, since the intrinsic

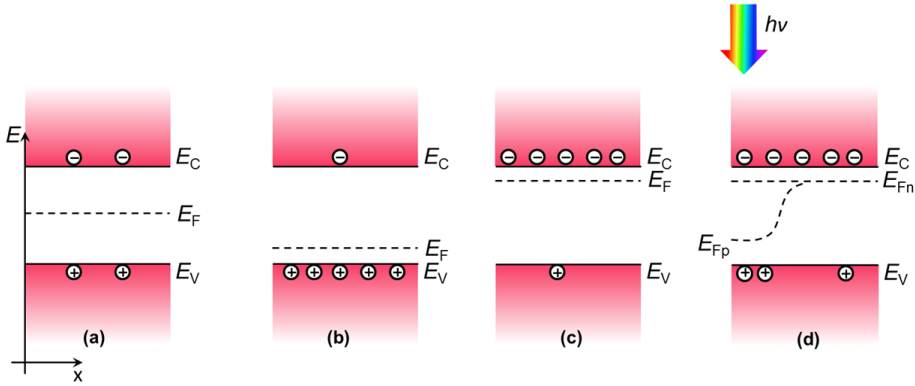


**Fig. 2.2** Relative position of the Fermi level  $E_F$  for an intrinsic semiconductor (a), for a  $p$ -type semiconductor (b), and for an  $n$ -type semiconductor (c). The splitting of the quasi-Fermi levels  $E_{Fn}$  for electrons and  $E_{Fp}$  for holes upon excitation by light, for instance, is shown in the illustration (d).

carrier concentrations under ambient conditions are very low. The latter can be increased by orders of magnitude by doping, *i.e.* by adding altermvalent impurities in the intrinsic material. If a semiconductor is doped with donor ( $n$ -type doping) or acceptor ( $p$ -type doping) atoms, the Fermi level shifts towards the conduction or valence band edge, respectively, in order to preserve charge neutrality (see Fig. 2.2(b) and (c), respectively). Depending on the distance of the donor and acceptor levels with respect to the corresponding bands, electrons are thermally excited into the conduction band and holes into the valence band [24].

The foregoing discussion strictly refers to semiconductors in equilibrium, where the Fermi level, *i.e.* the electrochemical potential is constant throughout the semiconductor. If the equilibrium is disturbed upon light excitation for instance, the electron and hole densities are increased to above their equilibrium value. Consequently, the electron and hole densities cannot be determined by the same Fermi level and it becomes necessary to define quasi-Fermi levels  $E_{Fn}$  and  $E_{Fp}$  for electrons and holes, respectively. In doped semiconductors, the quasi-Fermi level of the majority charge carriers stays (nearly) constant upon illumination, whereas the quasi-Fermi level of the minority charge carriers varies with the distance from the excitation area (see Fig. 2.2(d)). The quasi-Fermi levels play an important role, not only for semiconductor/semiconductor junctions (see following Section 2.1.3), but also for processes at the semiconductor/electrolyte interface, because the relative position of the

quasi-Fermi level with respect to that in a liquid solution yields the thermodynamic force which drives an electrochemical reaction [24] (see Section 2.3).

### 2.1.3 Semiconductor junctions

When two differently doped semiconductor materials are brought into contact, a charge transfer flow across the interface occurs on account of the difference in concentration of charge carriers in the two materials. For  $pn$  junctions, electrons from the  $n$ -type side start to diffuse into the  $p$ -type side and holes in the  $p$ -type side start to diffuse across into the  $n$ -type side. The diffusion current is proportional to the charge concentration gradient between both materials. This process leaves ionised donor or acceptor atoms as immobile impurities behind, creating a region near the interface, which is depleted of mobile carriers. This region is called depletion region. The accumulation of electric charges of opposite polarities near the interface gives rise to an electric field, which in turn causes a drift of carriers in the direction opposite to the diffusion. The diffusion of carriers continues until the drift current balances the diffusion current, thereby reaching thermal equilibrium as indicated by a constant Fermi energy. This situation is shown in Fig. 2.3 for homo- and hetero- $pn$  junctions, and for a  $pin$  junction.

In homo- $pn$  junctions (Fig. 2.3(a)) two semiconductor materials with the same band gap energy are brought into contact or one semiconductor is doped in different regions with different elements. A heterojunction always consists of two different materials with different band gaps. Due to the change in the band gap energies, a discontinuity exists in the conduction and valence band edges at the junction. This affects the effective fields for the two carrier types in different ways. Usually, one type of carrier is assisted by the field change, while the other is opposed. In Fig. 2.3(b) for instance, the field that drives electrons to the  $n$  side is increased, while the field driving holes towards the  $p$  side is decreased. In contrast to  $pn$  junctions,  $pin$  junctions have an undoped layer between the highly or even degenerately-doped  $p$  and  $n$  regions. These layers can be designed with slightly higher band gap energies than the intermediate  $i$ -layer in order to enhance the transparency for the incident light (see Fig. 2.3(c)). This extends the electric field over a wider region and elongates the depletion region. This type of junction is preferable in materials with short minority carrier diffusion lengths and will be discussed in more detail in the following section.



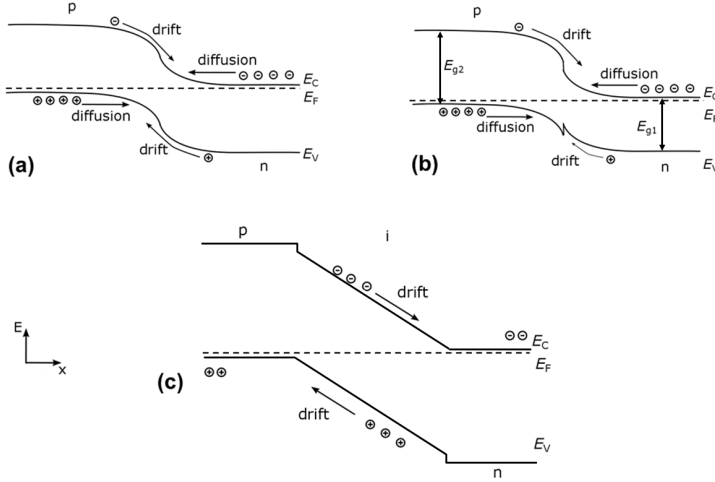


**Fig. 2.3** Energy band diagrams of a homo- $pn$  junction (a), of a hetero- $pn$  junction (b), and of a  $pin$  junction (c) in equilibrium condition (details can be found in the text).

## 2.1.4 Operation principle of thin film $pin$ solar cells

### Single junction solar cells

In doped thin films of hydrogenated amorphous (a-Si:H) or microcrystalline silicon ( $\mu\text{c-Si:H}$ ), the defect density is high compared to crystalline Si, causing reduced charge carrier lifetimes. Hence, the  $pn$  junction structure used in c-Si solar cells cannot be applied in thin film silicon solar cells. The transport of photogenerated charge carriers therefore must be realised by a drift process, which is achieved by inserting an intrinsic layer ( $i$ -layer) between the  $p$ -type and  $n$ -type regions, as schematically depicted in Fig. 2.4. The embedded intrinsic layer works as absorber layer and expands the space charge region of the  $pin$  solar cell [36,37]. The thickness of the  $i$ -layer directly influences the light absorption of the solar cell and in the particular case of a-Si:H absorber layers, the effect of light induced degradation, which increases with the layer thickness [38,39] (see Section 3.1.1).

As shown in Fig. 2.4(b), upon illumination the electric field generated by the  $p$ - and  $n$ -layers leads to the separation of the photogenerated electron-hole pairs. Following the electric field, holes are driven to the  $p$ -side, and electrons to the  $n$ -side

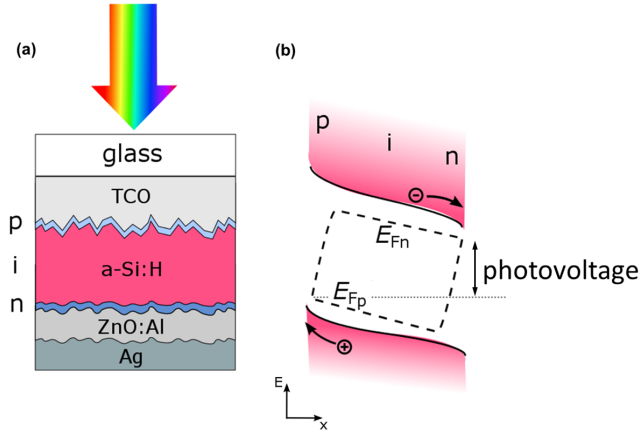


**Fig. 2.4** (a) Structure of a *pin* a-Si:H solar cell in superstrate configuration. The incident light enters the solar cell through a transparent conductive oxide (TCO) coated glass substrate. The rear side of the solar cell is composed of a ZnO:Al/Ag back contact. (b) Band diagram of a *pin* solar cell under illuminated conditions. The *p*- and *n*-layer produce an electric field that leads to the separation and the transportation of photogenerated charge carriers to the electrodes. Electrons move to the *n*-side and holes are transported to the *p*-side of the solar cell. The splitting of the quasi-Fermi levels  $E_{Fn}$  and  $E_{Fp}$  defines the photovoltage of the solar cell.

of the solar cell. Consequently, the separation of charge carriers builds up a voltage between both doped layers. This voltage is called photovoltage and it is defined by the splitting of the quasi-Fermi levels  $E_{Fn}$  and  $E_{Fp}$  [33] (see Fig. 2.4(b)). In open-circuit conditions the photovoltage is called open-circuit voltage  $V_{OC}$ . A photocurrent can be picked up if the *p*- and *n*-layers are connected through electrodes by an external circuit. The thickness of the doped layers is a critical parameter, as it strongly influences the photocurrent and the photovoltage of the solar cell: with thinner *p*-layers ( $\sim 10$  nm) more light enters the intrinsic absorber layers of a *pin* solar cell, and thus the photocurrent of the device increases. Thicker doped layers ( $\sim 30$  nm) on the other hand enhance the internal electric field within the *pin* structure, which leads to an increase in the photovoltage. Note that the band diagram in Fig. 2.4(b) is just a simplified picture of an ideal solar cell, as depicted in Fig. 2.4(a). In reality, additional effects occur, such as electronic defects at the *p*-/*i*- and *n*-/*i*-interfaces and in the *i*-layer, respectively, leading to an attenuation of the electric field due to interface recombination, and thus, to lower photovoltages [40, 41].

In Fig. 2.4(a) it is illustrated that the incident light enters the solar cell through a transparent conductive oxide (TCO) coated glass substrate. According to the deposition sequence of the  $p$ -,  $i$ - and  $n$ -layers, thin film silicon cells can be classified as  $pin$  or  $nip$  cells. Details on the structure and fabrication of  $nip$  cells can be found in Ref. [42]. The solar cells presented in this work were deposited in a  $pin$  and in a stacked  $pin$  sequence, respectively. In  $pin$  solar cells, also called superstrate cells, a transparent substrate serves as the window of the solar cell, and the  $p$ -layer is the first layer deposited on the substrate followed by the  $i$ - and  $n$ -layer deposition. In general, it is necessary to illuminate the solar cell through the  $p$ -layer, because in the thin film silicon material, particularly in a-Si:H, the hole mobility is significantly lower compared to the electron mobility (typically two order of magnitude lower [43]). By doing so, most of the incoming sunlight is absorbed in the  $i$ -layer region close to the  $p$ -layer, which features a shorter distance for the low mobility holes to travel to the  $p$ -layer contact.

To increase the light absorption in the  $i$ -layer, without increasing the  $i$ -layer thickness, the front and back electrodes are textured, as visualised in Fig. 2.4(a). In this case, the light path in the solar cell is prolonged by light scattering at the surface of the TCO front electrode and of the back contact, which consists of a stacked aluminium doped zinc oxide/silver (ZnO:Al/Ag) reflector. Further details on the fabrication process of  $pin$  solar cells can be found in Section 3.2.

### Multijunction solar cells

Multijunction solar cells are composed of several  $pin$  single junction sub cells stacked upon one another and monolithically connected in series. For a single junction solar cell, the light absorption occurs only in a certain wavelength range and thus, a certain part of the solar spectrum cannot be used, *i.e.* photons with energies less than the band gap of the absorber material do not contribute to charge carrier generation and the photon energies exceeding the band gap cause thermalisation. For a better use of the solar spectrum, a-Si:H and  $\mu c$ -Si:H multijunction absorber layers, with different band gaps were arranged in tandem, triple, and quadruple junction configurations in this work. Such stacked configurations allow to guide the photons into the absorber layer where the band gap matches the photon energy, which reduces thermalisation losses. Fig. 2.5 schematically shows the multijunction solar cell configurations investigated in this work. The absorber layer sequence in the multijunction cells is chosen in a way that the incident light first reaches materials with the higher band gaps. Accordingly, a-Si:H, which has a higher band gap energy

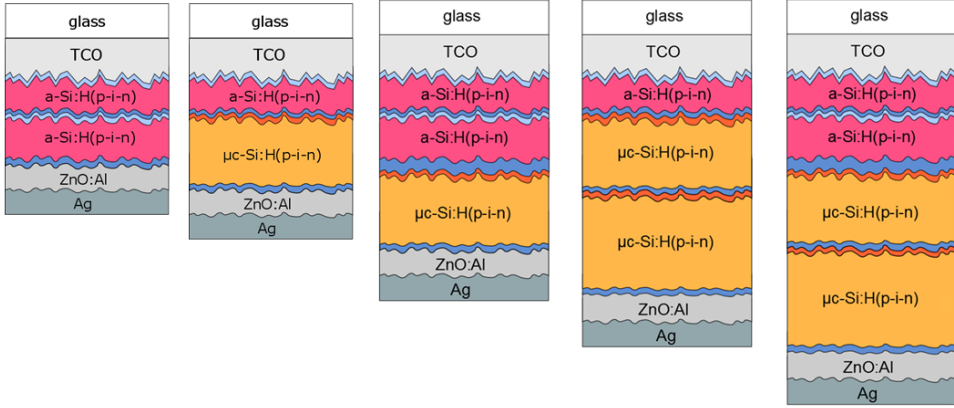


**Fig. 2.5** Schematic drawing of the a-Si:H/a-Si:H and a-Si:H/ $\mu$ c-Si:H tandem, the a-Si:H/a-Si:H/ $\mu$ c-Si:H and a-Si:H/ $\mu$ c-Si:H/ $\mu$ c-Si:H triple and the a-Si:H/a-Si:H/ $\mu$ c-Si:H/ $\mu$ c-Si:H quadruple junction solar cell structures in *pin* configuration investigated in this work.

than  $\mu$ c-Si:H, is always used as top cell material where high energetic light in the wavelength region between 400 – 600 nm is absorbed. The transmitted infrared light is led to the middle and/or bottom  $\mu$ c-Si:H absorber layers, as schematically illustrated in Fig. 2.6(a). Similar to the single junction cells, a ZnO:Al/Ag layer stack reflects light that is not absorbed during the first pass through the multijunction cell back into the sub cells so that the effective light path in the absorber materials is enhanced. A number of studies demonstrate that an increase in the number of sub cells in a multijunction device results in higher theoretical limits for the electrical conversion efficiency [26, 44, 45].

The electrical series connection of the sub cells is achieved by a recombination junction, as exemplarily shown for an a-Si:H/a-Si:H/ $\mu$ c-Si:H *pinpinpin* structure in Fig. 2.6(b). In the a-Si:H top cell, holes are transported to the front TCO contact, whereas electrons move to the *n*-layer, adjacent to the *p*-layer of the second a-Si:H middle cell. For the a-Si:H middle and the  $\mu$ c-Si:H bottom cell the situation is the same. At these *n*-/*p*-interfaces, the electrons need to recombine with holes transported from the middle cell and bottom cell, respectively, in order to ensure a continuity in the current transport. To increase the density of states available for the recombination, a sufficiently high defect density at the *n*-/*p*-interface, *i.e.* highly doped *n*- and *p*-layers are required to maintain a high recombination rate [46, 47].

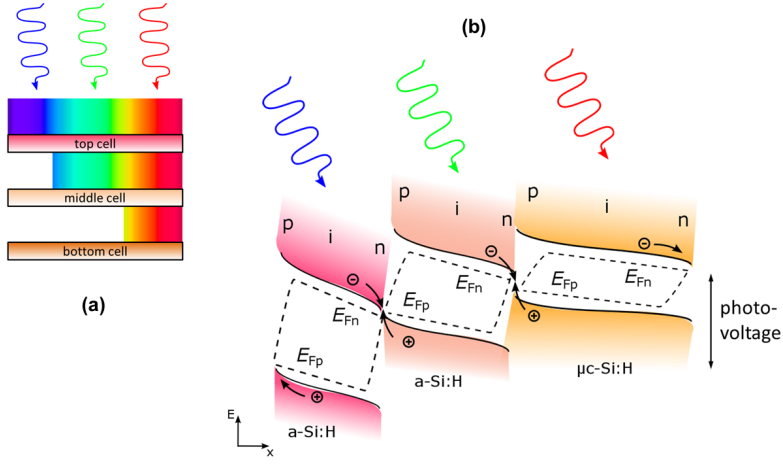


**Fig. 2.6** (a) Illustration of the spectral distribution in a multijunction solar cell structure, for the example of a triple junction cell. (b) Band diagram of a *pin* multijunction solar cell under illuminated conditions (as an example a triple junction solar cell is shown). Holes and electrons from the *a*-Si:H top and middle cell, and the  $\mu$ c-Si:H bottom cell, respectively, have to recombine at the *n*-/*p*-interfaces to ensure a continuous current. The interfaces are called recombination junctions. The sum of the splitting of the quasi-Fermi levels  $E_{Fn}$  and  $E_{Fp}$  of the top, middle and bottom cell defines the photovoltage of the multijunction cell.

Assuming that no losses occur at the recombination junction, the photovoltage can be defined as the sum of the individual sub cell photovoltages, defined by the splitting of the quasi-Fermi levels  $E_{Fn}$  and  $E_{Fp}$ , as shown in Fig. 2.6(b). Since the sub cells are connected in series, the total current through the multijunction cell is limited by the sub cell that delivers the lowest current. Ideally, the photocurrent density generated by the solar cell is equally distributed among all sub cells, so-called "current-matched". This would avoid an electric field along the recombination junction by an incomplete recombination, and thus, provide the highest possible photocurrent [48,49]. Alternatively, the so-called "power matching" of the photocurrents can be applied to optimise the maximum performance output of the solar cell instead of the current matching [50].

## 2.2 Basic concepts of electrochemistry

### 2.2.1 Charge transport in electrolytes

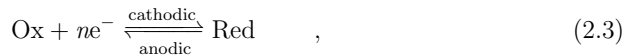
In contrast to solid-state materials such as metals and semiconductors, the current in liquid electrolytes is carried by ions [24]. Positively and negatively charged ions are formed by the dissociation of salts in a polar solvent, for instance  $\text{H}_2\text{SO}_4$  or  $\text{KOH}$  in water. Whereas in a semiconductor usually one type of charge carriers (majority carriers) dominates due to doping, in the electrolyte both types of carriers are always present in equal concentrations. In analogy to the solid-state electronic conductivity, the conductivity in a liquid solution is given by

$$\sigma = F (z_1 \mu_+ + z_2 \mu_-) C \quad . \quad (2.2)$$

In Eq. 2.2  $z_1$  and  $z_2$  are the charges of the ions,  $\mu_+$  and  $\mu_-$  are the mobilities of the positively and negatively charged ions (given in  $\text{cm}^2/\text{Vs}$ ), respectively,  $C$  is the concentration of the ions (given in  $\text{mol}/\text{cm}^3$ ), and  $F$  is the Faraday constant. Experiments show that the mobility of most ions is around  $10^{-4} \text{ cm}^2/\text{Vs}$ , which is about 5-6 orders of magnitude smaller than the mobility of electrons and holes in a crystalline semiconductor. Low ion concentrations can limit the device efficiency due to a high resistive losses. The influence of the ion concentration of the device performance will be discussed in Section 4.3. Please note that pure water does not contain enough ions to allow for a reasonable conductivity and therefore cannot be used for an electrolysis process.

### 2.2.2 Fermi level and standard potential of redox systems

Redox systems are characterised by molecules or ions in a solution which can be reduced and oxidised by a pure electron transfer. The corresponding reaction is given by



in which Red is the reduced and Ox the oxidised species (*e.g.* Red:  $\text{H}_2$ , Ox:  $2\text{H}^+$ ) [24] and  $n$  is the number of charge carriers. In analogy to the Fermi energy, introduced in the foregoing photovoltaic descriptions, the electrochemical potential  $\tilde{\mu}_i$  is defined as the work required to add a charged particle of species  $i$  to a redox system under constant pressure  $p$  and temperature  $T$ . It can be expressed as the partial derivative

of the Gibbs free energy  $G$  of the phase under consideration with respect to the number  $N$  of charged particles of species  $i$ , by

$$\tilde{\mu}_i = \left( \frac{\partial G}{\partial N_i} \right)_{p,T} = \mu_i + n_i e \phi \quad . \quad (2.4)$$

The term  $n_i e \phi$  indicates the work needed to transfer one mole of  $n$ -valent ions from a remote position into an electrolyte solution with a potential  $\phi$ , with  $n_i$  being the charge number of species  $i$  and  $e$  the elementary charge. If there are no charged particles, the electrochemical potential equals the chemical potential  $\mu_i$ .

All chemical and electrochemical potentials are usually given in units of joule per mole (J/mol), whereas Fermi energies are usually given in units of electron volts (eV). The electrochemical potential of a single electron in a redox electrolyte is given by the Nernst expression [51]

$$E_{\text{redox}} = \tilde{\mu}_e = E_{\text{redox}}^0 + \frac{RT}{nF} \ln \frac{c_{\text{Ox}}}{c_{\text{Red}}} \quad . \quad (2.5)$$

In Eq. 2.5,  $c_{\text{Ox}}$  and  $c_{\text{Red}}$  are the concentrations (roughly activities) of the oxidised and reduced species, respectively, in the redox system [51] and  $R$  is the universal gas constant. The standard electrode potential  $E_{\text{redox}}^0$  [52] of an electrochemical reaction is commonly referred to the standard hydrogen electrode (SHE), *i.e.* to the redox potential of the  $\text{H}_2/\text{H}^+$  couple, which is defined as 0 V versus SHE [53]. This arbitrary chosen reference potential is in contrast with the electron energy in vacuum, which is adopted as absolute standard reference in other branches of the chemistry and physics community. It is estimated that the SHE lies at -4.5 eV with respect to the vacuum level [54, 55]. This enables to relate the standard electrochemical potential  $E_{\text{redox}}^0$  (as defined with reference to SHE) to the Fermi level  $E_{\text{F,redox}}$  in the electrolyte (expressed versus the vacuum reference), by

$$E_{\text{F,redox}} = -(4.5 \text{ eV} + eE_{\text{redox}}^0) \quad . \quad (2.6)$$

At equilibrium, the Fermi level in the solid-state band structure and the electrochemical potential of a redox couple can be brought onto a common energy scale, which facilitates the quantitative description of photoelectrochemical concepts. Fig. 2.7 shows the Fermi energy scale using the vacuum level as a reference and the electrochemical scale using the standard hydrogen electrode as a reference. However, in spite of the common terminology, the particles in a solution do not behave like free electrons in a semiconductor which obey Fermi-Dirac statistics [57].

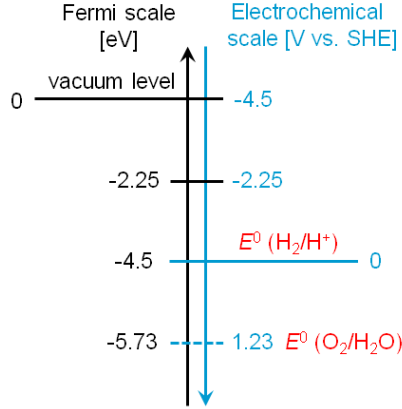


**Fig. 2.7** Comparison of the Fermi energy scale using the vacuum level as a reference and the electrochemical scale using the standard hydrogen electrode (SHE) potential as a reference. The electrochemical potential of the oxygen evolution reaction ( $\text{O}_2/\text{H}_2\text{O}$ ) was calculated for  $p\text{H}$  0. The standard electrode potentials of various redox couples under standard conditions ( $T = 298.15$  K;  $p = 1$  bar;  $c_{\text{Ox}} = c_{\text{Red}} = 1$ ) have been compiled in tables in literature (*e.g.* [56]).

The electrode potential can also be referred to the reversible hydrogen electrode (RHE) [58]. Unlike the SHE, the measured potential of the RHE does not change with the  $p\text{H}$  [59]. The potential of the RHE can be approximated by

$$E_{\text{RHE}} = E_{\text{redox}}^0 + \frac{2.303RT}{nF} \log \frac{c_{\text{Ox}}}{c_{\text{Red}}} \quad . \quad (2.7)$$

The factor 2.303 results from the conversion from a natural logarithm to the common logarithm (compare with Eq. 2.5), which is more often used in electrochemistry. For the  $\text{H}_2/\text{H}^+$  redox couple,  $c_{\text{Red}} = 1$ , while  $c_{\text{Ox}}$  is not unity, but corresponds to that of the electrolyte solution. Thus, for  $T = 298.15$  K, Eq. 2.7 can be written as

$$E_{\text{RHE}} = E_{\text{redox}}^0 + 0.059 \log c_{\text{Ox}} = E_{\text{redox}}^0 + 0.059 \text{ pH} \quad , \quad (2.8)$$

with  $p\text{H}$  being defined as common logarithm of the reciprocal of the hydrogen ion activity in a solution [60].



### 2.2.3 Electrochemical reaction kinetics

The foregoing discussion strictly refers to redox systems under equilibrium, where the occurring cathodic and anodic processes have the same reaction rate. In an electrochemical cell the equilibrium can be disturbed by applying an overpotential to the system or by adding reactants, which will increase either the cathodic or the anodic reaction rate and lead to a net current flow. The resulting current/potential interdependency is governed by the charge transfer reaction process at the electrode/electrolyte interface, whose finite velocity unavoidably limits electrochemical reactions of the form  $\text{Ox} + ne^- \xrightleftharpoons[\text{anodic}]{\text{cathodic}} \text{Red}$ . The charge transfer requires a certain activation energy  $\Delta G^*$ , as illustrated in the reaction coordinate diagram in Fig. 2.8.

In the free-energy profile,  $\Delta G^*$  is the barrier height of an initial reactant to an intermediate state within the so-called Helmholtz double layer, which will be discussed in Section 2.3.2. Intermediate states near the metal or semiconductor electrode surface may occur if an adsorbed molecule participates in the reaction, or if energy states within the energy gap at a semiconductor surface are involved, or if just more than one electron is involved in the reaction [24]. Fig. 2.8 illustrates the effect of an applied overvoltage to the redox system. As exemplarily shown, the barrier height for the anodic reaction  $\Delta G_{+}^*$  is decreased with respect to the equilibrium condition ( $\Delta G_{\text{eq}+}^*$ ) by varying the electrode potential *via* an external voltage, *i.e.* an overpotential  $\eta_{\text{ct}}$ . The activation energy for the cathodic reaction  $\Delta G_{-}^*$ , on the contrary, is increased with respect to the equilibrium condition ( $\Delta G_{\text{eq}-}^*$ ). The overpotential necessary to drive the charge transfer is the difference between the electrochemical potential and the electrode potential for the equilibrium case under standard conditions [24] and can be written as [58]

$$\eta_{\text{ct}} = (E_{\text{redox}} - E_{\text{redox}}^0) \quad . \quad (2.9)$$

In fact,  $\eta_{\text{ct}}$  is a specific property of the electrode material. Fig. 2.8 furthermore illustrates the effect of a variation of the concentration ratio  $c_{\text{Ox}}/c_{\text{Red}}$  by adding reactants in the solution, which leads to a similar effect as that caused by an application of an external voltage. For instance, an increase of  $c_{\text{Ox}}$  speeds up the cathodic reaction rate, which leads to a smaller barrier height for the cathodic reaction in the equilibrium and in the polarisation condition compared to the barrier heights for the anodic reaction, as shown in Fig. 2.8.

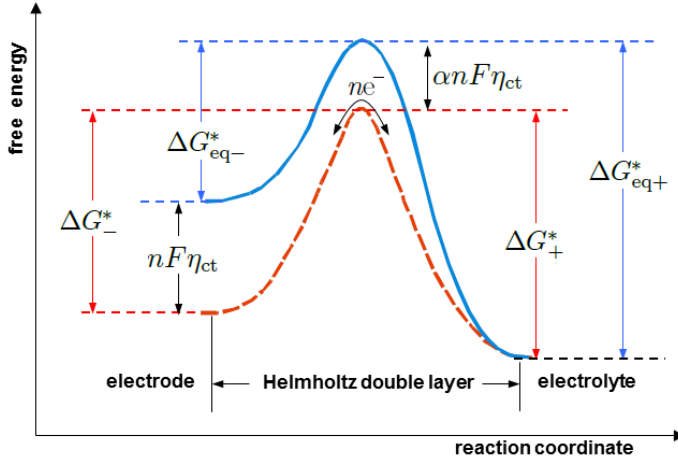


**Fig. 2.8** Free-energy versus reaction coordinate diagram for a redox system under equilibrium (blue curve) and under polarisation (red curve) for  $c_{\text{Ox}} > c_{\text{Red}}$ .  $\Delta G_{\text{eq-}}^*$  and  $\Delta G_{\text{eq+}}^*$  denote the activation energies for the cathodic and anodic reactions, respectively under equilibrium.  $\Delta G_{-}^*$  and  $\Delta G_{+}^*$  denote the activation energies for the cathodic and anodic reactions, respectively, for applied bias conditions.  $\alpha$  is the transfer coefficient and  $\eta_{ct}$  is the overpotential. The figure is adapted from Ref. [61].

As apparent from Fig. 2.8, the linear relation between the overpotential and the activation energies can be given by

$$\Delta G_{+}^* = \Delta G_{\text{eq+}}^* - \alpha n F \eta_{ct} \quad , \quad (2.10)$$

$$\Delta G_{-}^* = \Delta G_{\text{eq-}}^* + (1 - \alpha) n F \eta_{ct} \quad . \quad (2.11)$$

The transfer coefficient  $\alpha$  defines to what extent the activation energies are varied upon application of an external voltage and usually lies between 0.3 and 0.7. Any variation in the activation energies results in a net current flow. The overall current-voltage dependence of an electrochemical reaction can be obtained by the superposition of the cathodic and anodic reaction kinetics and is described by the Butler-Volmer expression [22]

$$j = j_0 \left[ \exp \left\{ \frac{\alpha n F}{RT} \eta_{ct} \right\} - \exp \left\{ - \frac{(1 - \alpha) n F}{RT} \eta_{ct} \right\} \right] \quad . \quad (2.12)$$

In Eq. 2.12 the exchange current density  $j_0$  is a measure for the velocity of the charge transfer under equilibrium condition and thus, a measure for the catalytic activity of an electrode. It is influenced by the activation energy and by the concentration of the reactants.

For sufficiently large overpotentials  $|\eta_{\text{ct}}| \gg RT/nF$  (which is in the range of interest for this work), one of the exponential terms of Eq. 2.12 can be neglected compared to the other (cathodic or anodic term, depending on the sign of  $\eta_{\text{ct}}$ ) and the Butler-Volmer equation can be approximated with a reasonable accuracy by

$$j = j_0 \exp\left(\frac{\alpha n F}{RT} \eta_{\text{ct}}\right) \quad . \quad (2.13)$$

By taking the logarithm of Eq. 2.13, the Tafel equation is obtained

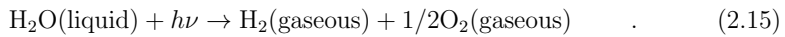
$$\eta_{\text{ct}} = b \log \frac{j}{j_0} \quad . \quad (2.14)$$

The Tafel behavior describes the overpotential required to overcome the activation barrier, *i.e.* to force the current to flow for a specific reaction. The Tafel slope  $b = RT/(\alpha n F)$  describes the change in potential per decade of current (mV/dec). In fact, the Tafel slope contains information regarding the mechanism of a reaction and can be utilised to identify the rate determining step of the overall reaction [58, 62]. In this work, the Tafel slope  $b$  and the exchange current density  $j_0$  were employed as parameters to model the current density-voltage behavior of hydrogen and oxygen evolution catalysts *via* Eq. 2.14 (see Section 4.3 and 6.3). Both parameters can either be evaluated experimentally or found in the literature for various electrode or catalyst materials.

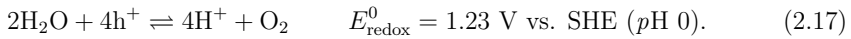
## 2.3 Basic concepts of photoelectrochemical water splitting

### 2.3.1 Principles of solar water splitting

The splitting of one mole of water into gaseous  $\text{H}_2$  and  $\text{O}_2$  by the action of sunlight produces one mole of hydrogen gas and a half-mole of oxygen gas in their normal diatomic forms [63]



The appropriate hydrogen evolution reaction (HER) and oxygen evolution reaction (OER) with the corresponding redox potentials are given by



The reduction half-reaction is a two-electron transfer reaction, while four charge carriers are involved in the oxidation of water to form oxygen [7]. At standard temperature (298 K) and concentrations (1 mol/L, 1 bar), the free-energy change of the reaction  $\Delta G^0$  is 237.2 kJ/mol (thermodynamically uphill reaction), which corresponds to 2.46 eV per molecule  $\text{H}_2\text{O}$ . Since two electrons are involved in the water splitting reaction, the energy needed per electron is 1.23 eV. Combining the overpotential losses associated with both reactions (2.16) and (2.17), a realistic minimum required potential is 1.6 V for the water decomposition.

### 2.3.2 Metal/electrolyte interface

By immersing a semiconductor or a metal electrode in a redox electrolyte, a dynamic equilibrium ensues, which manifests itself by a flow of charge from one phase to the other in order to equilibrate the disparate electrochemical potentials (analogous to the semiconductor *pn* junction, described in Section 2.1.3) [51]. This leads to a potential difference across the electrode/electrolyte interface, and thus, an electrical field is generated. The field will contribute to the redistribution of mobile ions and water dipole molecules in the region near the electrode. The process of redistribution

at the metal/electrolyte interface builds up a double layer, which at the solution side consists of several layers, as presented in Fig. 2.9.

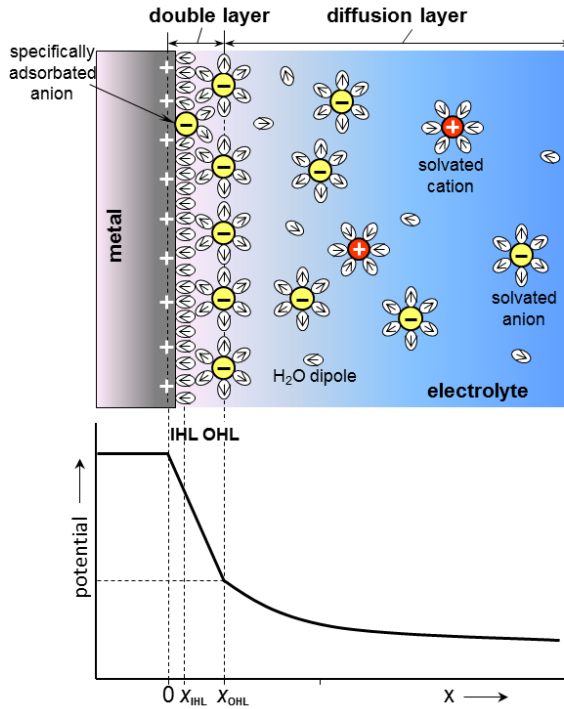


**Fig. 2.9** Schematic illustration of the metal/electrolyte interface according to the Helmholtz model. The model consists of a double layer (inner and outer Helmholtz layer, IHL and OHL, respectively) and of a diffusion layer (adjacent to the double layer) and the electrolyte solution (adjacent to the diffusion layer, not shown here), which contains solvated cations and anions, respectively, and water dipoles. The potential drop across the metal/electrolyte interface is shown below the illustration. The figure is adapted from Ref. [61].

The first, so-called inner Helmholtz layer (IHL) is only a few angstroms thick and is formed by solvent molecules and specifically adsorbed ions. The adjacent layer is called outer Helmholtz layer (OHL) and is formed by a positive or negative layer of solvated ions, depending on the charge on the electrode. According to the Helmholtz

model, the potential over the metal/electrolyte interface is considered to change linearly from the metal surface to the edge of the OHL, as displayed in the lower part of Fig. 2.9. Since the interaction between the electrode and the solvated ions involves only long-range forces, a concentration profile of the solvated ions extends from the OHL into the bulk of the electrolyte exists. This layer is called diffusion layer and is characterised by a three-dimensional distribution of mobile solvated ions. The electrical field in this region is assumed to decrease exponentially with the distance from the electrode. Since the high electronic conductivity of a metal cannot support an electric field in it, almost all the potential drop at the interface occurs within the double layer and the diffusion layer in the electrolyte phase. This aspect is a major point of distinction from the corresponding semiconductor/electrolyte interface, which will be discussed in the following section.

### 2.3.3 Semiconductor/electrolyte interface

Similar to the metal/electrolyte interface, the equilibration of the disparate electrochemical potentials, as shown in Fig. 2.10(a), gives rise to a flow of charge between the two phases [64]. In the electrolyte, the density of states of solvated ions as a function of energy can be approximately described by a Gaussian distribution function [24, 65]. It is proportional to the concentration of reduced and oxidised species and usually higher compared to the density of states in a semiconductor. The concentration of ions in the reduced state can be considered as a density of electronically occupied energy states in the electrolyte. The concentration of oxidised ions is therefore the density of electronically unoccupied states in the electrolyte [66].

The associated band bending after the contact is shown in Fig. 2.10(b) for an *n*-type and in Fig. 2.10(c) for a *p*-type semiconductor interface. After the contact, the net result of equilibration is that  $E_F = E_{F,\text{redox}}$  [51] (see Section 2.2.2). In the case of the *n*-type semiconductor interface, the charge needed for equilibration was provided by the donor atoms. Similar to the semiconductor/semiconductor junction, discussed in Section 2.1.3, a depletion region is built-up near the interface, which contains positive charges from the ionised donors and results in a positive bending at the interface (Fermi level moves 'down'). The higher density of states in the electrolyte dictates that the Fermi level in the semiconductor moves farther than the corresponding level  $E_{F,\text{redox}}$ .

Therefore, as illustrated in Fig. 2.11, the equilibration process, in contrast to the metal case, leads to a potential drop not only in the electrolyte, but also within

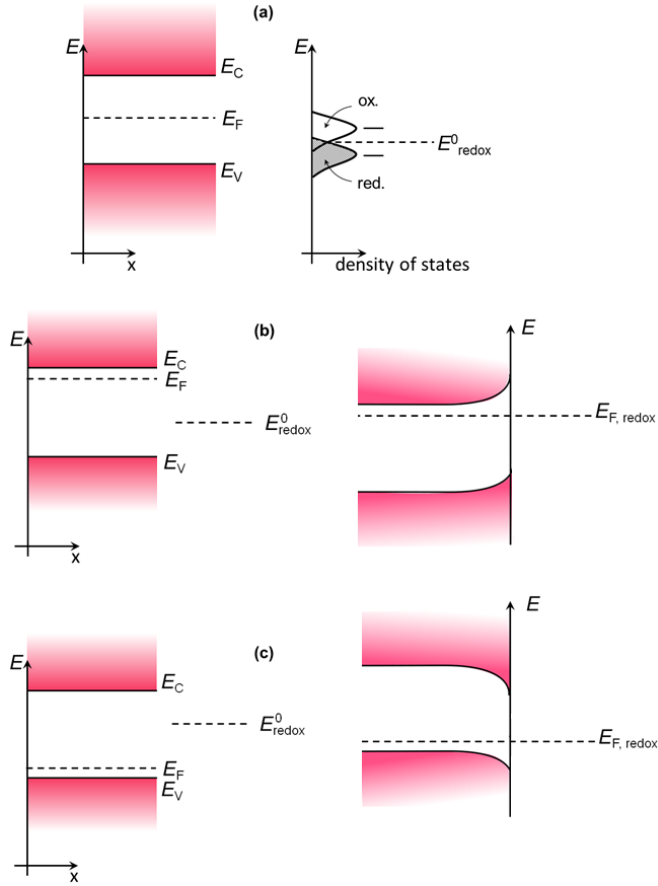


**Fig. 2.10** (a) Schematic illustration of the energy levels in a semiconductor (left-hand side) and in a redox electrolyte (right hand side) shown on a common vacuum reference scale. (b) The semiconductor/electrolyte interface before and after equilibration (*i.e.* contact of the two phases) shown for an *n*-type semiconductor. (c) Same as in (b), but for a *p*-type semiconductor.

the semiconductor. In fact, the interfacial potential drop across the semiconductor/electrolyte junction is partitioned as potential drop in the semiconductor  $V_{\text{SC}}$ , in the Helmholtz layer  $V_{\text{H}}$ , and in the diffusion layer  $V_{\text{D}}$  of the electrolyte. This leads to the most simple equivalent series circuit model comprising three capacitors  $C_{\text{SC}}$ ,  $C_{\text{H}}$ , and  $C_{\text{D}}$ , as depicted in the lower part of Fig. 2.11 [24, 51].

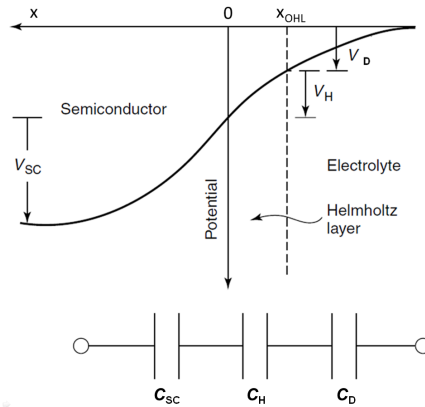


**Fig. 2.11** Schematic illustration of the potential drop at the semiconductor/electrolyte interface. A simplified equivalent circuit for the interface at equilibrium, including the three capacitors  $C_{SC}$ ,  $C_H$ , and  $C_D$ , is shown in the lower part of the figure. The figure is adapted from Ref. [51].

Semiconductor based photocathodes and photoanodes, also called photocatalysts, are widely used and under examination in the literature. Examples for investigated photocatalysts are III-V semiconductors (*e.g.* GaP [67, 68] or GaInP<sub>2</sub> [69]), crystalline Si [31, 70, 71], group VI-dichalcogenides [72–75], CdS coated CuGaSe<sub>2</sub> [76], nanostructured WO<sub>3</sub>/BiVO<sub>4</sub> [77], and hematite ( $\alpha$ -Fe<sub>2</sub>O<sub>3</sub>) [78]. Practical water splitting, however, remains challenging due to the stringent requirements that photocatalysts have to fulfil, with respect to their band gap energy and electrochemical properties [79]:

- appropriate band edge positions of the semiconductor for overall water splitting,
- suitable solar visible-light absorption, *i.e.* band gap energy lower than 3 eV,
- stability against corrosion in aqueous environments and in the photocatalytic reaction.

From a thermodynamic point of view, solar water splitting requires that the conduction band edge of the photocatalyst is located at a more cathodic (negative) potential than the proton reduction potential ( $H_2/H^+$ , see electrochemical scale in Fig. 2.7). Furthermore, to facilitate water oxidation, the valence band edge of the photocatalyst must exceed the oxidation potential of water ( $O_2/H_2O$ ), *i.e.* + 1.23 V vs. SHE at pH 0. Therefore, a theoretical semiconductor band gap energy of 1.23 eV is required



to drive the overall water splitting reaction [79] without external bias. In fact, however, it is not sufficient that the energy band edges comprise the  $\text{H}_2/\text{H}^+$  and  $\text{O}_2/\text{H}_2\text{O}$  potentials. Rather, the electron and hole quasi-Fermi levels of the semiconductor must straddle the electrochemical potential levels with sufficient extra separation to allow for band bending, overpotentials, and interfacial recombination [80]. Therefore, the required band gap for single absorber photocatalysts considerably increases to values of  $> 2.0$  eV [81]. In Fig. 2.12 the band positions of various exemplarily chosen photocatalyst materials with respect to the water reduction and oxidation potentials are shown [79].

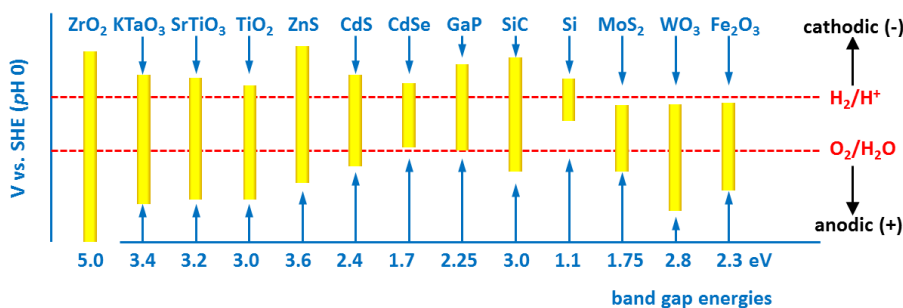


**Fig. 2.12** Schematic illustration of the band structures of various photocatalyst materials, including the band gap energies and the positions of the band edges relative to the water reduction and oxidation potentials (V vs. SHE, pH 0) [79]. Cathodic (negative) and anodic (positive) potential directions are indicated on the right side of the illustration.

For  $\text{TiO}_2$ ,  $\text{CdS}$ , and  $\text{SiC}$  from Fig. 2.12 the band gap energies are lower than (or equal to) 3 eV and the band edge positions 'straddle' the redox levels. Hence, these semiconductors fulfil two of the above mentioned requirements for overall water splitting. Metal chalcogenides, such as  $\text{CdS}$  or  $\text{CdSe}$ , are however not stable in the water oxidation reaction because the  $\text{S}^{2-}$  or  $\text{Se}^{2-}$  anions are more susceptible to oxidation than water, which leads to the oxidation [82] and degradation [83] of these photocatalysts. Although  $\text{MoS}_2$ ,  $\text{WO}_3$ , and  $\text{Fe}_2\text{O}_3$  function as photocatalysts for  $\text{O}_2$  evolution with adequate band gap energies ( $\leq 3$  eV), their conduction band edge is located at a more anodic (positive) potential than the potential for water reduction. As a result, these photocatalysts cannot reduce  $\text{H}^+$  to  $\text{H}_2$ . *Vice versa*,  $\text{GaP}$  and bare  $\text{Si}$  cannot oxidise water to  $\text{O}_2$  as their valence band edges do not exceed the oxidation potential of water.

This shows that a large number of semiconductor electrodes are not suitable for water splitting due to their intrinsic electronic properties. The few semiconductor materials, which thermodynamically allow water splitting, exhibit significantly higher overpotentials compared to metal electrodes. This is mainly caused by slower charge carrier transfer kinetics [84, 85] and by the larger potential drop at semiconductor/electrolyte interfaces [7].

Devices utilising semiconductor/electrolyte junctions, are referred to as photoelectrochemical (PEC) or photoelectrosynthetic cells [86]. Commonly, the performance of these devices is enhanced by the incorporation of a catalyst at the semiconductor/electrolyte interface to improve the interfacial charge transfer kinetics [87].

### 2.3.4 Buried junction devices

The elaborated thermodynamic and stability issues in semiconductor photoelectrodes being in direct contact to the electrolyte can be avoided by 'burying' the semiconductor junction in an integrated photovoltaic-electrochemical (PV-EC) device. Metal layers present prominent candidates to bury the semiconductor PV structure, as they can protect the semiconductor surface from the electrolyte and act as a catalyst. Fig. 2.13 schematically depicts an integrated buried junction device based on a triple junction thin film silicon solar cell with a ZnO:Al/Ag rear contact and a metal HER catalyst layer (as investigated in this work). Additionally, the appropriate band diagram illustration is depicted in Fig. 2.13.

The integrated device is composed of four main components: the multijunction solar cell (here an a-Si:H/a-Si:H/ $\mu$ c-Si:H solar cell) to provide sufficient photovoltage and photocurrent for the water splitting reactions, a catalyst layer to enhance the HER, which is deposited on the rear contact of the solar cell at the photocathode/electrolyte interface, the electrolyte, which should provide high ionic conductivity, and an anode, which is usually coated with a metal oxide catalyst layer to enhance the OER. The solar cell together with the attached HER catalyst compose the photocathode of the PV-EC device. The PV-EC device configuration presented in Fig. 2.13 can be illuminated through the glass substrate of the integrated solar cell, which offers the advantage that the incident light directly enters the photocathode through the TCO coated glass substrate without being attenuated by a surrounding medium (*e.g.* light scattering or shadowing by the electrolyte, by a co-catalyst or by evolving gas bubbles). A major role in this configuration is governed by the metallic contact at the photocathode/electrolyte interface, which has to fulfil multiple

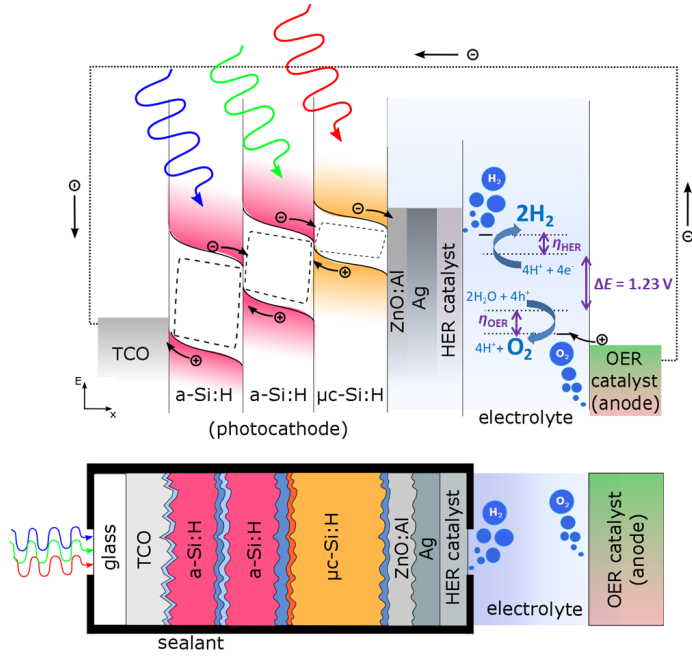


**Fig. 2.13** Band diagram illustration and schematic structure of a buried junction device, with its components: the multijunction photocathode (as example a-Si:H/a-Si:H/μc-Si:H) under non-biased illumination condition, a hydrogen evolution reaction (HER) catalyst layer at the photocathode/electrolyte interface, the electrolyte, and the anode with the oxygen evolution reaction (OER) catalyst. The energy levels for the HER and OER and the respective reactions are indicated in the illustration. Hydrogen evolution occurs at the rear side of the photocathode and oxygen occurs at the anode side.  $\Delta E = 1.23$  V is the thermodynamic potential required for water electrolysis at 25 °C.  $\eta_{\text{HER}}$  and  $\eta_{\text{OER}}$  indicate the overpotentials for the HER and OER, respectively. The different colors of the silicon absorber layers indicate different band gaps.

requirements, such as: optical reflection of incident light back into the photocathode, protection of the photocathode from the electrolyte and undesired chemical reactions, and promotion of the catalytic reaction and a good electrical contact between the PV structure and the electrolyte. The investigation of the photocathode/electrolyte contact will be discussed in Section 6.1. Under operation of the PV-EC device the electrons are injected from the rear side (HER catalyst layer) of the photocathode into the electrolyte for the HER (see Fig. 2.13) and thus the holes are transferred

from the TCO front contact of the photocathode to the anode for the OER.

In fact, this configuration can be interpreted as a series connection of a photovoltaic cell and an electrolysis cell, in which the electrolysis cell is biased by the photovoltage generated in the semiconductor junction upon illumination. In relation to this, the configuration offers the advantage that the photovoltage and the photocurrent generated by the semiconductor structure are available for the electrolysis independent of the energy band positions at the solid/liquid interface. The water splitting reactions are governed only by the metal/electrolyte junction, where the overpotential of the respective metal catalyst plays the major role. Hence, in contrast to the semiconductor/electrolyte junction PEC cells, the semiconductor or the solar cell structure and the catalysts can therefore be developed individually. By this means, the photovoltaic and the electrochemical parts of the device, such as the catalysts for the  $\text{H}_2$  evolution reaction (HER) and the  $\text{O}_2$  evolution reaction (OER), respectively, can be adapted and combined in a flexible way. A more detailed description of photovoltaic-biased electrochemical devices, including the characterisation techniques, and the device modeling is presented in Chapter 4.



## 3 Fundamentals and experimental details of thin film silicon solar cells

*This chapter is concerned with the techniques and methods used to prepare silicon thin films and solar cells. Prior to the description of the experimental details, the fundamental aspects of thin film silicon as photoactive absorber material and the operation principle of thin film silicon solar cells will be discussed. Next, the influence of the most important deposition parameters during the plasma enhanced chemical vapor deposition, which was used for the preparation of the thin films, is explained. Finally, the methods are described with which the material properties and the solar cell performance were evaluated throughout this manuscript.*

### 3.1 Fundamentals of thin film silicon absorber materials

The scope of the present section is to describe the properties of hydrogenated amorphous and microcrystalline silicon, which were used as photoactive absorber materials for the photoelectrochemical energy conversion in this study. The descriptions provide the background necessary to comprehend the evaluation of the experimental data in the following chapters. For a more thorough and detailed insight into the topics, the reader is referred to standard textbooks such as Refs. [30,43,88,89].

#### 3.1.1 Hydrogenated amorphous silicon a-Si:H

##### Structure

In contrast to its crystalline analogous, amorphous silicon is defined by the absence of long-range order in the atomic positions. Although the Si-atoms are tetrahedrally bonded and usually fourfold coordinated, like in the crystalline form, bonding lengths and angles of amorphous silicon vary from the well-ordered crystalline lattice structure which causes structural defects. Prominent defect configurations are weak/heavily strained bonds and three- or fivefold coordinated Si atoms, leading to dangling

bonds within the network. These open bonds considerably deteriorate the electrical properties of the silicon material. To enable the application in optoelectronic devices, hydrogen is incorporated into the material (a-Si:H) to partially passivate the dangling bonds [43]. The incorporation of hydrogen reduces the defect density of the a-Si:H material from above  $10^{19} \text{ cm}^{-3}$  (without passivation) [43] to around  $10^{15} - 10^{16} \text{ cm}^{-3}$  without changing the amorphous structure [90].

The electronic structure of a-Si:H is described by the density of states  $N(E)$ , as it is shown in Fig. 3.1. From the  $N(E)$  plot, basically three types of states can be

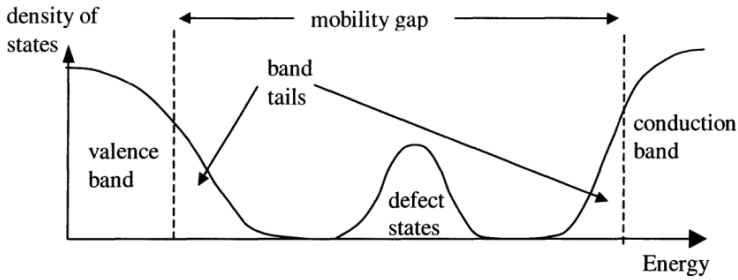


**Fig. 3.1** Electronic structure of hydrogenated amorphous silicon (a-Si:H) described by a density of states  $N(E)$ , taken from Ref. [91]. Three types of states can be identified: extended band-like states (valence and conduction band), localised band-like states (band tails), and localised defect states in the energy gap.

identified: (i) Extended band-like states, which similar to crystalline silicon (c-Si) allow overlapping of electronic wavefunctions and thus, form the conduction and valence band of the semiconductor. (ii) Localised band-like states which do not overlap and result from more distorted bonds are called band-tails. In these states charge carriers move with reduced mobility and can be activated into the conduction band when activated upon temperature increase (above the room temperature). To differentiate from the classical band gap, a mobility gap is defined in a-Si:H. As indicated in Fig. 3.1, the mobility gap separates the valence and conduction band mobility edges and is approximately the optical gap energy of the semiconductor [91]. Since the edge from extended to localised states is not abrupt, the value of the optical gap depends on the definition and evaluation (see the method of Photothermal deflection spectroscopy in Section 3.3), respectively, and values between 1.6 [92] and 1.9 eV [93] are typically found. (iii) Localised defect states distributed in the energy

gap which result from highly distorted and non-saturated bonds (dangling bonds). These states act as recombination centers for charge carriers and deteriorate the transport of excess charge carriers [94].

### Growth mechanism

The predominant features of the a-Si:H material are defined during the growth process. Thus, it is anticipated that the electronic properties vary with the deposition process parameters and consequently a detailed understanding of the growth mechanism is essential for the optimisation of the electronic properties.

During the plasma enhanced chemical vapor deposition (see Section 3.2.1) the process gas mixture dissociates upon impact of accelerated electrons. This process produces precursors, predominantly  $\text{SiH}_3$  in usual deposition conditions [43], which have one unsaturated bond at the Si-atom. When these molecule fragments reach and diffuse over a hydrogen-terminated substrate surface, they may abstract one H-atom from a Si-atom under formation of  $\text{SiH}_4$ , which does not contribute to the film growth, leaving a dangling bond on the Si-atom. To this open bond a second  $\text{SiH}_3$  may diffuse and attach to the silicon atom: the film grows [95], as schematically shown in Fig. 3.2. Higher deposition temperatures enhance the surface diffusivity and the abstraction and desorption of hydrogen, respectively, which leads to less hydrogen in the a-Si:H network.

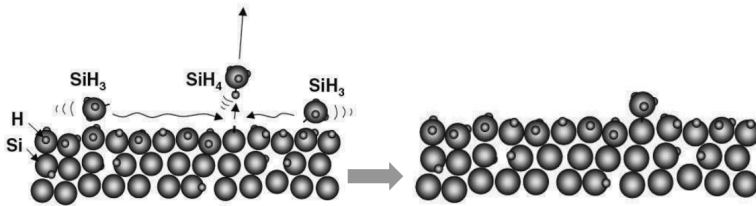


**Fig. 3.2** Schematic drawing of the growth mechanism of amorphous silicon.  $\text{SiH}_3$  molecule fragments diffuse over a hydrogen terminated surface and can abstract a hydrogen atom from a Si-atom, leaving a dangling bond.  $\text{SiH}_4$  is formed which does not contribute to the film growth. A second  $\text{SiH}_3$  may diffuse to the left dangling bond and attach to the substrate [96].



### Optical properties

Due to the long-range disorder in the a-Si:H network, the momentum conservation law for electron excitation by photon absorption is relaxed. This makes a-Si:H behave like a material with a direct band gap. Hence, no additional phonon is required for the optical transition [97], which can occur *via* a direct 'two-body' collision (photon, electron). An indirect 'three-body' collision (photon, electron, phonon) occurs less frequently and consequently, the absorption coefficient for indirect semiconductors, *e.g.* crystalline silicon, is lower compared to direct semiconductors, where layers of several hundred nanometers are sufficient to absorb most of the sunlight. By changing the deposition conditions, *e.g.* hydrogen dilution or deposition temperature, the optical gap values can be varied over 100 meV [85,98]. Alloying with carbon leads to a widening of the optical gap over 2.0 eV [99] whereas the incorporation of germanium reduces the optical gap [99].

### Light induced degradation

Thin film silicon material, especially a-Si:H can suffer from the light induced degradation (LID), which mainly causes additional metastable electronic defects in the optical gap, acting as recombination centres and thus, reducing the photovoltaic performance of a-Si:H based devices. As a consequence the efficiency of a-Si:H solar cells can decrease when exposed to light over significant periods of time. This effect, known as Staebler-Wronski effect, has been intensively investigated [43,100]. The effect can be reversed by annealing at temperatures above 150 °C [100]. Although a detailed microscopic model of the Staebler-Wronski-effect is still under discussion, it is however known that the deterioration of the device performance can be reduced by using thinner a-Si:H absorber layers in single [101] and in stacked cells [39]. It is expected that the built-in field distribution is less affected in thinner a-Si:H layers upon light exposure.

### 3.1.2 Hydrogenated microcrystalline silicon $\mu\text{c-Si:H}$

#### Structure and growth

Hydrogenated microcrystalline silicon is a phase mixture of crystals embedded in amorphous tissue. Fig. 3.3 shows a schematic model that illustrates the microstructure of hydrogenated microcrystalline silicon ( $\mu\text{c-Si:H}$ ) deposited by plasma enhanced chemical vapor deposition [102, 103].

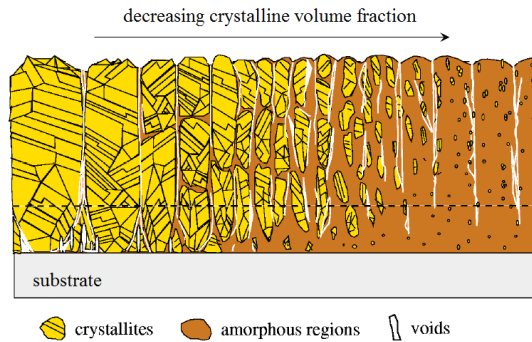


**Fig. 3.3** A schematic model which illustrates the microstructure of hydrogenated microcrystalline silicon ( $\mu\text{c-Si:H}$ ) deposited by plasma enhanced chemical vapor deposition on a glass substrate. From the left side to the right hand side the film structure changes from highly microcrystalline silicon to almost amorphous silicon, *i.e.* the crystalline volume fraction decreases. This illustration is taken from Ref. [102].

As illustrated, from the left to the right side, the film structure change from highly crystalline  $\mu\text{c-Si:H}$ , characterised by columnar crystalline grains (approximately 100 nm high) to predominantly amorphous silicon regions. The properties of the prepared films depend on various deposition parameters [103]. One important parameter, which is investigated in this work, is the silane concentration  $SC$ . It is defined as the ratio of the silane gas flow and the total gas flow, *i.e.* as

$$SC = \frac{\text{SiH}_4[\text{sccm}]}{\text{SiH}_4[\text{sccm}] + \text{H}_2[\text{sccm}]} \quad (3.1)$$

The variation of  $SC$  induces a transition between the amorphous and microcrystalline growth regime [103]. The related amount of crystalline volume fraction (or crys-

tallinity) is a crucial factor for the application in solar cells. The crystallinity, which is the portion of crystalline phase in relation to the total volume, significantly affects the solar cell parameters and is usually determined by Raman spectroscopy (see Section 3.3). A decrease of the  $SC$  leads to highly microcrystalline silicon [104, 105], characterised by an increase of the crystalline volume fraction (see Fig. 3.3). In highly crystalline  $\mu c$ -Si:H material columnar grains with diameters up to 200 nm can be observed. Note that such big columns do not correspond to single crystallites, but they consist of a large number of coherent domains ( $\sim 10$  nm, see Fig. 3.3), separated by structural defects, *e.g.* stacking fault and twin boundaries [105, 106]. The grains between the columns are passivated by the surrounding amorphous tissues, preventing the post-deposition atmosphere in-diffusion [107, 108].

### Optical properties

Fig. 3.4 shows the absorption spectra, *i.e.* the absorption coefficient  $\alpha_{\text{abs}}$  as a function of the photon energy  $E_{\text{ph}}$  for a-Si:H [109],  $\mu c$ -Si:H [110], and c-Si material [111]. The absorption spectra of  $\mu c$ -Si:H and c-Si overlap in a wide energy range and both materials show a similar indirect optical band gap energy of 1.1 eV [36, 112].

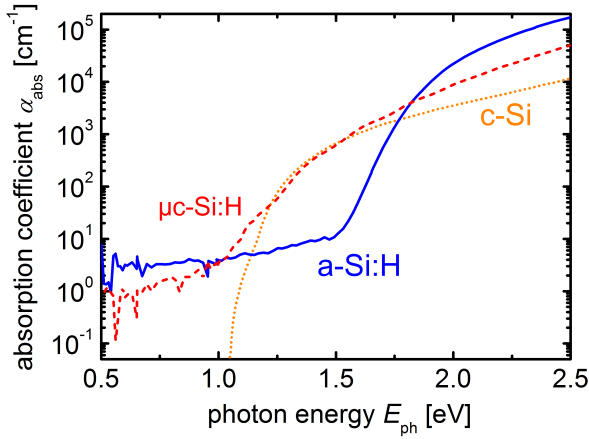


**Fig. 3.4** Absorption coefficient  $\alpha_{\text{abs}}$  as a function of the photon energy  $E_{\text{ph}}$  of a-Si:H (blue solid curve),  $\mu c$ -Si:H (red dashed curve), and c-Si (orange dotted curve).

Above photon energies of 1.85 eV  $\mu\text{c-Si:H}$  exhibits a lower absorption coefficient than a-Si:H. Consequently,  $\mu\text{c-Si:H}$  absorbs more light in the infrared region, whereas a-Si:H is used to absorb light in the high energy region. Stacking a-Si:H and  $\mu\text{c-Si:H}$  in multijunction configurations therefore leads to a better use of the solar spectrum. In these configurations the a-Si:H absorber layers are typically deposited at thicknesses between 80 and 400 nm and the  $\mu\text{c-Si:H}$  absorber layers have thicknesses usually above 1  $\mu\text{m}$ . The absorption below photon energies of 1.0 eV in the a-Si:H and  $\mu\text{c-Si:H}$  materials is related to defect levels in the sub-gap region. The absorption spectra of the nearly defect-free c-Si material, on the other hand, exhibits no significant absorption below 1.0 eV and follows the  $\alpha_{\text{abs}} \sim (E_{\text{ph}} - E_g)^2$  relation (see Section 2.1.1).

### Light induced degradation

In contrast to a-Si:H based solar cells,  $\mu\text{c-Si:H}$  solar cells with highly crystalline absorber layers are significantly more stable against light induced degradation [113, 114]. However, the highest solar cell efficiencies are typically achieved near the transition of the amorphous growth regime [103, 115]. Consequently, in such  $\mu\text{c-Si:H}$  solar cells stronger light induced performance degradation was observed [116–118]. The impact of LID on the performance of thin film silicon solar cells will be discussed in Section 5.6.

## 3.2 Techniques and methods for the preparation of thin film silicon solar cells

This section describes the techniques and processes for the preparation of thin films and the solar cells. Among the methods to deposit amorphous and microcrystalline silicon, such as reactive sputtering, Photo-CVD, Electron Cyclotron Resonance (ECR) microwave deposition, Pulsed Laser Deposition (PLD) or Hot-Wire Chemical Vapour Deposition [119], the Plasma Enhanced Chemical Vapour Deposition (PECVD) yields the best device quality a-Si:H and  $\mu\text{c-Si:H}$  layers and is used in industrial scale volume. All silicon layers and solar cells in this work have been deposited by PECVD at various frequencies. In the following the PECVD system operation and structure will be described exemplarily by means of the system that was used for this work. Further details on the PECVD process can be found in the Refs. [36, 119–121].

### 3.2.1 Plasma enhanced chemical vapor deposition

The growth mechanisms of a-Si:H and  $\mu$ c-Si:H are described in the Sections 3.1.1 and in 3.1.2. In the PECVD process, the decomposition of the gases occurs in a glow discharge process excited by an electrical field in vacuum at a pressure of, typically, 1 mbar [122].

#### Deposition system

The PECVD process was performed in a six-chamber PECVD system (manufactured by the MRG Inc., Denver) shown in Fig. 3.5. Substrates of a maximum size of  $10 \times 10 \text{ cm}^2$  can be loaded (*via* the load lock) into the system and transferred (in the transfer locks) between six deposition process chambers, as illustrated in Fig. 3.6.

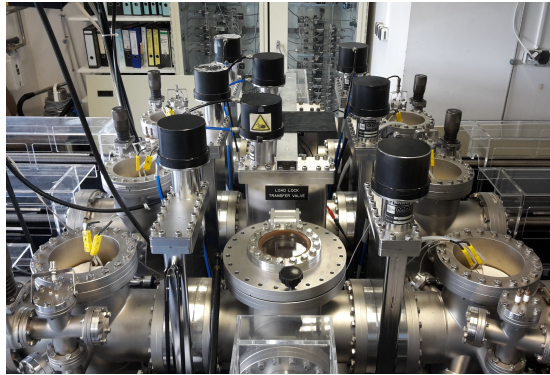


**Fig. 3.5** Photograph of the PECVD system used to process the thin film silicon layers and solar cells. The system consists of six chambers used for different doped and undoped deposition processes.

Each process chamber was only used for the deposition of a particular type of thin film layer, thus, *p*-, *i*-, and *n*-layers are deposited in different chambers. This avoids cross contaminations and residual doping effects and thus, enhances the quality of the layers and the performance of the solar cells. Furthermore, the reliability and the reproducibility of the processes are increased. All the chambers are separated from each other by transfer valves. The substrates are fixed into metal carriers and are transferred by an automated transfer system of rails and transfer arms. Fig. 3.7

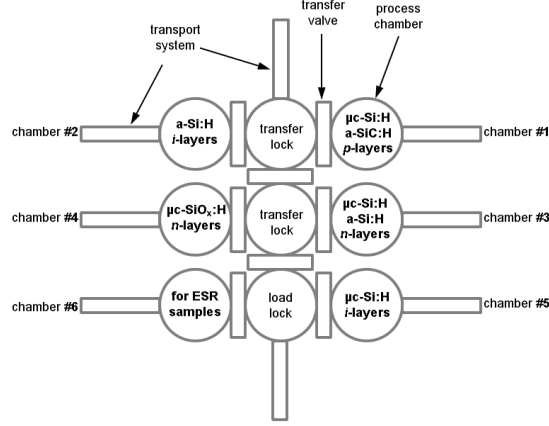


**Fig. 3.6** Schematic outline of the six-Chamber PECVD deposition system used in this work for the deposition of the silicon thin films and shown in Fig. 3.5. Each chamber is only used for a certain type of process. The respective  $p$ -,  $i$ -, and  $n$ -layer processes are indicated. The chambers are connected *via* evacuated transfer locks and load locks to transfer the substrate, using the transport system. This system allows to move the substrate between the process chambers without breaking the vacuum. The transfer valves separate the chambers from each other. The chamber designated for electron spin resonance (ESR) sample preparation was not used in this work.

shows a schematic drawing of a deposition chamber. Further details on the design and operation principle of the 6-chamber system components can be found in the Refs. [116,123].

In the process chamber the substrate is fixed in face down configuration and grounded by the rails. The substrate temperature  $T_s$  was solely controlled by adjusting the heater temperature, which is attached only a few millimeters above the substrate and thus, indirectly heats the substrate due to radiation. In order to correlate  $T_s$  to the heater temperature, calibration measurements have been conducted by means of a pyrometer [98]. In this work  $T_s$  was varied between 70 °C and 250 °C and it was found that a waiting time of 30 minutes in the respective chamber is necessary to heat up or cool down the substrate to the required temperature.

The electrode plate is powered by an RF-generator (or an VHF-generator) and is placed below the substrate, which acts as counter electrode. Both electrodes are separated by a fixed electrode distance. The power produced by the RF-generator is

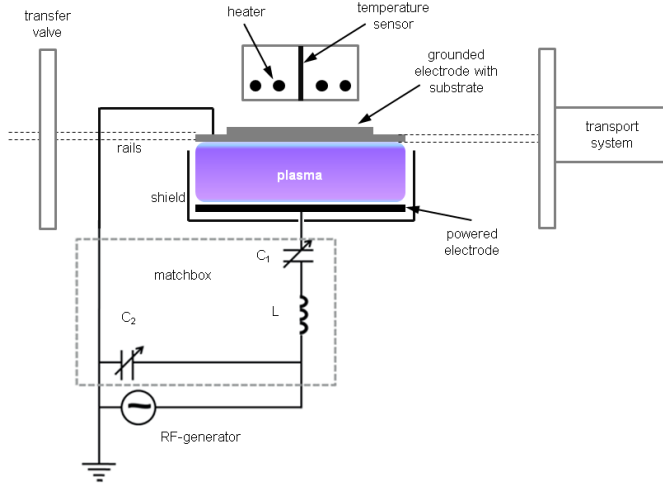


**Fig. 3.7** Principle design of the process chambers in the 6-chamber system for the preparation of silicon thin films. Except from the electrode distance, all the process chambers have the same construction. Capacitive plasma excitation between the powered and grounded electrode is provided by an RF-field. The picture is not drawn to scale.

capacitively coupled to the electrode *via* a matchbox, which consists of an inductive coil ( $L$ ) and two variable capacitors ( $C_1$ ,  $C_2$ ). Their capacities are manually adjusted such that the impedance of the matchbox matches the impedance of the plasma and the deposition system components. Also the RF power from the generators needs to be adjusted manually, whereas the transport system, the valves, and the deposition parameters, such as gas flows, heater temperature, deposition pressure, are controlled by a computer based system.

### Deposition parameters

In the present work, an alternating electrical field at radio frequency ( $RF = 13.56$  MHz) or very high frequency ( $VHF = 94.7$  MHz) was used. For the deposition of the intrinsic absorber layers, silane ( $SiH_4$ ) and hydrogen ( $H_2$ ) were used as process gases. To dope the *p*-type material, gas containing boron (trimethylboron; TMB) or, for *n*-type doping, gas containing phosphorus (phosphine;  $PH_3$ ) was used. Alloying of the doped layers was achieved by adding additional process gases. For instance,

to widen the optical gap and enhancing the transparency of the first *p*-type layer in a *pin* cell structure, carbon was incorporated by adding methane ( $\text{CH}_4$ ) to the  $\text{SiH}_4$ ,  $\text{H}_2$ , TMB gas mixture. *n*-type microcrystalline silicon oxide ( $\mu\text{c-SiO}_x\text{:H}$ ) layers, which serve as intermediate reflectors or back contact layer [124,125], were deposited by adding carbon dioxide ( $\text{CO}_2$ ) to the  $\text{SiH}_4$ ,  $\text{H}_2$ ,  $\text{PH}_3$  gas mixture. The deposition parameters used for the preparation of the intrinsic and doped silicon thin film layers are summarised in Table 3.1. For the dopant source, 2 %  $\text{PH}_3$  in  $\text{SiH}_4$  or 1 % trimethylboron  $\text{B}(\text{CH}_3)_3$  (TMB) diluted in helium (He) was used. In Table 3.1, the dopant gas flows refer to the  $\text{PH}_3$  flow and TMB flow as net flow of dopant gas only (excluding the dilution gas) [122].  $\text{SiH}_4$  and  $\text{H}_2$  have a purity of 99.9999 % (6.0). Other gases, *e.g.*  $\text{CH}_4$ ,  $\text{CO}_2$ , and  $\text{PH}_3$  have a purity of 5.5, 4.6, and 5.0, respectively.

**Table 3.1** Deposition parameters of the individual thin film silicon layers used in the present work unless otherwise stated.

Layer	Plasma power density [mW/cm <sup>2</sup> ]	Plasma excitation frequency [MHz]	Electrode distance [mm]	Deposition pressure [mbar]	$\text{SiH}_4$ flow [sccm]	$\text{H}_2$ flow [sccm]	$\text{CH}_4$ flow [sccm]	He flow [sccm]	$\text{CO}_2$ flow [sccm]	Dopant gas flow [sccm]
<b>p-type</b>										
a-SiC:H	18	13.56	20	1.05	12	110	10	11.8	-	0.12
$\mu\text{c-Si:H}$	60<	94.7	20	0.4	1.5	200	-	2	-	0.02
<b>n-type</b>										
a-Si:H	18	13.56	20	0.67	84	-	-	-	-	1.2
$\mu\text{c-Si:H}$	150	13.56	20	4	1	200	-	-	-	0.02
$\mu\text{c-SiO}_x\text{:H}$	150	13.56	20	4	1	200	-	-	0.75	0.02
$\mu\text{c-SiO}_x\text{:H}$ (IR)	150	13.56	20	4	1	501	-	-	2	0.08
<b>intrinsic</b>										
a-Si:H	15	13.56	12	4	10, 4	90, 96	-	-	-	-
$\mu\text{c-Si:H}$	120	94.7	12	1.5	4.0 - 6.0	98	-	-	-	-



### 3.2.2 Solar cell preparation

So far, the deposition process of silicon thin films was described. Now, the steps for the fabrications of solar cells will be given. First, the substrate on which the silicon thin films are deposited has to be chosen. In this work, glass substrates were used for the investigation of single layers. The solar cells were deposited onto two types of substrates, each coated with a different kind of transparent conductive oxide:

- "Corning" glass: 1.1 mm thick Corning type Eagle glass substrates coated with a thin  $\text{SiO}_2$  layer for the deposition of single silicon layers for material investigation. The substrates were cleaned by DeContam and in an ultrasonic bath for about two hours to ensure a residue-free surface. Subsequently, they were rinsed with deionised water and dried by a spin dryer. Subsequently, 10 nm of  $\text{SiO}_2$  was deposited by electron beam evaporation, to prevent peeling-off of the silicon layers.
- "Asahi (VU)":  $\text{SnO}_2:\text{F}$  with a pyramidal structure coated on 3.2 mm thick white glass, which is glass with a low iron content (Asahi type "VU"). This type of substrate was used for a-Si:H single junction for a-Si:H/a-Si:H tandem junction and for a-Si:H/a-Si:H/ $\mu\text{c-Si:H}$  triple junction solar cells.
- ZnO:Al: sputtered and subsequently HCl etched ZnO:Al on 1.1 mm thick glass from Corning type Eagle [126, 127]. This type of substrate was used for  $\mu\text{c-Si:H}$  single junction, for a-Si:H/ $\mu\text{c-Si:H}$  tandem junction, for a-Si:H/ $\mu\text{c-Si:H}$ / $\mu\text{c-Si:H}$  triple junction and for quadruple solar cells.

After the deposition of the silicon layers, a ZnO:Al/Ag reflecting rear contact was deposited [128]. The ZnO layer is aluminium doped and sputtered from a ceramic target with 1 wt.%  $\text{Al}_2\text{O}_3$  with a thickness of 70 nm over the whole  $10 \times 10 \text{ cm}^2$  substrate area. The Ag pads and grids were deposited by thermal evaporation through a shadow mask defining the individual active cell areas of  $1 \text{ cm}^2$ . The thickness of the Ag layers was varied between 300 nm and 700 nm in this work. Uncovered ZnO:Al was etched off by using a 0.25 % HCl-solution. The sample preparation was finished by an annealing step at  $160^\circ \text{C}$  for about 30 minutes at ambient atmosphere. For some selected solar cells, an antireflection foil from the Solarexcel company (now a part of DSM Advanced Surfaces) is used on the light incident side of the solar cell glass substrate to reduce optical losses [129].

### 3.3 Characterisation of thin film silicon absorber layers

This section addresses the measurement techniques used to investigate the structural, optical and electronic properties of single a-Si:H and  $\mu$ c-Si:H absorber layers.

#### Film thickness

The thickness of the deposited films was measured by means of a DEKTAK 3030 profilometer. After the deposition, two adjacent stripes were ablated by means of a laser [130]. The wavelength of the laser was chosen in a way that only the silicon film is removed, so that the substrate remains unchanged. The fine tip of the profilometer moves over the sample surface and the engraved stripes and the instrument simultaneously displays the height profile. The difference between surface and bottom of the cavity gives the silicon thickness. The deposition rate was then acquired by dividing the measured thickness by the deposition time.

#### Raman spectroscopy

The crystalline volume fraction of the  $\mu$ c-Si:H absorber layers was probed using Raman spectroscopy. The method is based on the inelastic scattering of photons with molecules or atoms in the lattice. Monochromatic light from a laser is focused onto the sample and a certain fraction of this light interacts inelastically with the lattice, *i.e.* photons are partly emitted or absorbed. The spectrum of inelastically scattered photons contains information about the material and structure specific lattice oscillation energy. Ref. [131] is recommended for further readings. The ratio of integrated intensities attributed to crystalline and amorphous regions,

$$I_c^{\text{RS}} = \frac{I_c}{I_c + I_a} \quad , \quad (3.2)$$

was used as semi-quantitative value of the crystalline volume fraction [105]. A detailed description on the determination of the crystalline silicon volume ratio from Raman measurements can be found in Ref. [132]. Samples were characterised either by a laser beam ( $\lambda = 532$  nm) directed on the as-produced sample, or, for selected samples, the Raman intensity ratio depth profile of the structure of the intrinsic absorber layer along the growth axis was determined by a gradient etching method

( $\lambda = 488 \text{ nm}$ ) [133, 134]. Here, Raman scattering measurements were carried out on slantwise etched craters through the solar cell structure.

### Infrared spectroscopy

Infrared (IR) spectroscopy was used to evaluate the hydrogen content  $c_H$  in the intrinsic a-Si:H absorber layers. The technique enables to detect IR active bonding configurations and molecules in a material. Incident light causes oscillations of the chemical bonds or molecules and is absorbed at a characteristic wavelength due to excitation of electric dipoles in the material. The oscillation frequencies of the induced molecular vibrations give information on the bonding structure and its close environments, as they are proportional to the bonding and the dielectric constant. An IR transmission spectrum was measured between  $400$  and  $2400 \text{ cm}^{-1}$  using a Nicolet 5700 Fourier transform infrared (FTIR) spectrometer. This spectrum was normalised to the spectrum of the crystalline silicon wafer substrate, which is mostly transparent for infrared radiation. The Fourier transformation and translation into absorption was done by the OMNIC software on the measuring computer. To avoid absorption by other compounds, the measurement chamber was purged with nitrogen during the recording of the spectrum for the sample and the silicon wafer reference. A more detailed description of the evaluation of the hydrogen content is given in Ref. [98].

### Photothermal deflection spectroscopy

Photothermal deflection spectroscopy (PDS) was performed to measure the spectral optical absorption of the intrinsic a-Si:H layers. From these spectra the gap energy  $E_{04}$  with a PDS absorption coefficient of  $10^4 \text{ cm}^{-1}$  was extracted, which served as an estimate for the optical gap of silicon layers in this work. The measurement setup consists of a cavity filled with an optically transparent carbon tetrachloride  $\text{CCl}_4$  fluid surrounding the sample. The  $\text{CCl}_4$  fluid has a strong temperature-dependent refractive index [135]. Upon illumination with a monochromatic light in the wavelength range between  $310 \text{ nm}$  (halogen lamp) and  $2600 \text{ nm}$  (high pressure xenon lamp) the absorption of light induces a heating of the a-Si:H layer, as no charge carriers are extracted. Consequently, a refractive index profile is present near the surface of the sample, which depends on the amount of the monochromatic light that is absorbed. The difference in the refractive index is detected by the deflection of a passing laser beam. The deflection can then be translated into the absorption

coefficient  $\alpha_{\text{abs}}$ . The measurement error is assumed to be below 10 %. A typical setup and more detailed evaluation procedure for the calculation of  $\alpha_{\text{abs}}$  by means of PDS can be found elsewhere [136, 137].

### Optical photometry

The spectral reflectance of the solar cells were obtained from measurements using a calibrated spectrometer (Perkin Elmer LAMBDA 950) with a spectral band width of 250 nm to 2500 nm. In this work the wavelength range between 300 nm to 1200 nm was investigated. For the reflectance measurement, the sample is positioned on the opposite side of the optical entrance. To include scattered light, an integrated sphere with highly reflective and diffuse coating is installed. More details on the employed set-up and the measurement technique can be found in Ref. [138].

## 3.4 Characterisation of solar cells

In this section the characterisation methods to acquire the relevant photovoltaic parameters are described. In this work, the solar cell performance was evaluated by means of illuminated current density-voltage measurements and by spectrally resolved quantum efficiency measurements.

### 3.4.1 Photovoltaic parameters

The parameters used to evaluate the photovoltaic performance of a solar cell are the conversion efficiency  $\eta_{\text{PV}}$ , the open-circuit voltage  $V_{\text{OC}}$  ( $j = 0 \text{ mA/cm}^2$ ), the short-circuit current density  $J_{\text{SC}}$  ( $V = 0 \text{ V}$ ), the fill factor  $FF$ , all of which can be derived from the illuminated current density-voltage ( $j$ - $V$ ) characteristics, as depicted in Fig. 3.8.

The  $j$ - $V$  characteristic of a solar cell, as exemplarily shown in Fig. 3.8, can be approximated by the superposition of the  $j$ - $V$  curves of a diode in the dark and the generated photocurrent density  $j_{\text{photo}}$  [139]. The photogeneration of charge carriers results in a shift of the  $j$ - $V$  curve into the fourth quadrant and the photocurrent

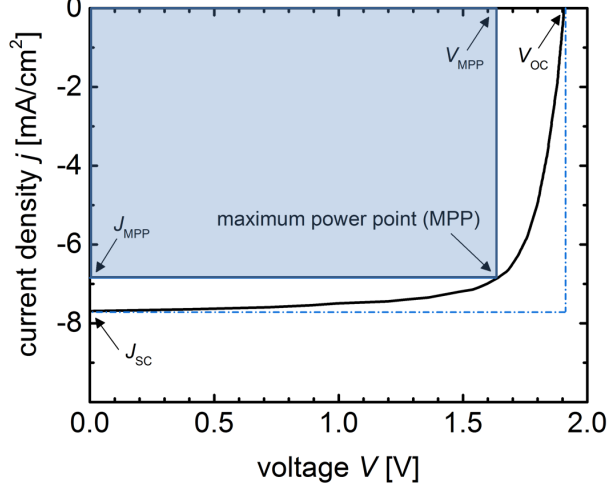


**Fig. 3.8** Illuminated current density-voltage ( $j$ - $V$ ) characteristic of a solar cell (black curve), indicating the maximum power point (MPP),  $J_{SC}$ ,  $V_{OC}$ ,  $V_{MPP}$ ,  $J_{MPP}$ , and the derivation of  $FF$ .

density  $j_{\text{photo}}$  adds to the dark current of an ideal diode  $j_{\text{diode}}$  so that the diode equation changes to

$$j = j_0 \left( e^{\frac{qV_{\text{diode}}}{kT}} - 1 \right) - j_{\text{photo}} \quad , \quad (3.3)$$

where  $j_0$  is the dark saturation current,  $V_{\text{diode}}$  the voltage of the diode,  $T$  the temperature,  $k$  as the Boltzmann factor, and  $q$  the elementary charge. At any point of the  $j$ - $V$  curve in the fourth quadrant the power density  $P$  delivered by the solar cell is defined by the product of  $j$  and  $V$ . The maximum power point MPP is the point where  $P$  of the solar cell reaches its maximum, with the corresponding current density  $J_{MPP}$  and voltage  $V_{MPP}$ . The fill factor  $FF$  is defined as the ratio of the blue rectangle with the dashed border in Fig. 3.8, *i.e.* as the quotient of  $(J_{MPP} \cdot V_{MPP}) / (J_{SC} \cdot V_{OC})$ . The most important parameter to characterise a solar cell is the solar energy conversion efficiency  $\eta$ , which is defined as the ratio between the maximum power provided by the solar cell and the power of the incident light,

and can be calculated *via*

$$\eta_{PV} = \frac{J_{MPP} \cdot V_{MPP}}{P_i} = \frac{J_{SC} \cdot V_{OC} \cdot FF}{P_i} \quad , \quad (3.4)$$

with  $P_i$  as the total integrated power input density (AM 1.5G, 100 mW/cm<sup>2</sup>). The slopes of the  $j$ - $V$  characteristic under illumination at  $j = 0$  and  $V = 0$  are a measure for the shunt ( $R_{sh}$ ) and parallel resistance ( $R_p$ ) of the solar cell, respectively.

The  $j$ - $V$  characteristics of solar cells are measured in this work by means of a class A double source Air-Mass (AM)1.5 solar simulator (WACOM-WXS-140S-Super) at standard test conditions (AM1.5G, 100 mW/cm<sup>2</sup>, 25 °C). The solar cells were mounted on a copper block, which was connected to an electrical heating and water cooling system to ensure a good temperature control ( $\pm 1$  °C). The  $j$ - $V$  measurements were carried out by a computer-controlled voltage source with the possibility to measure the current response (SMU 238, Keithley).

### 3.4.2 Quantum efficiency

The spectrally resolved quantum efficiency ( $QE$ ) describes the percentage of electron-hole pairs created upon the absorption of a photon in the solar cell that contribute to the extracted photocurrent. Thus, the technique provides detailed insights into the optical absorption and carrier extraction in solar cells. The quantum efficiency is defined as

$$QE(\lambda) = \frac{j_{ph}(\lambda)}{e \cdot \Phi(\lambda)} \quad . \quad (3.5)$$

Eq. 3.5 describes the  $QE$  as the ratio between the photocurrent density  $j_{ph}$  (as a measure for the number of collected charge carriers) and the number of photons that impinge the solar cell perpendicularly, given by  $e \cdot \Phi(\lambda)$ , with  $e$  as the elementary charge and  $\Phi(\lambda)$  as the quantum flux per time and unit area for a certain wavelength  $\lambda$ . In this work, only the external quantum efficiency was considered, for which the total incident light is taken into account. The internal quantum efficiency, on the contrary, would take into account only the incoupled light, excluding the reflected part.

For the determination of the (external) quantum efficiency, the spectral response  $S(\lambda)$  is measured by means of the Differential Spectral Response (DSR) method. A detailed description of the experimental DSR setup used in this work is given in Ref. [140]. The spectral response is defined as the ratio of the generated photocurrent

density  $j_{\text{ph}}(\lambda)$  to the irradiance  $E_{\text{ph}}(\lambda)$  which reaches the solar cell. Using a reference photodiode with a known spectral response  $S(\lambda)$ , the photocurrent density  $j_{\text{ph}}(\lambda)$  of the solar cell can be derived. The quantum efficiency is then calculated by  $QE(\lambda) = S(\lambda)hc/e\lambda$ .

In this work, the  $QE$  measurements of the multijunction solar cells were conducted using a monochromator in a wavelength range between 300 nm to 1100 nm. Individual sub cell  $QEs$  of the tandem, triple, and quadruple cells were separately determined using LEDs and a spectrally filtered bias light from a tungsten lamp. Bias light intensities of approximately 1 mW/cm<sup>2</sup> were used to saturate the respective sub cells, while the intensity of the probing light was around 1000 times lower. The individual sub cell photocurrent densities  $J_{\text{QE}}$  are calculated from the integration of the  $QE$  over the corresponding wavelength range:

$$J_{\text{QE}} = e \int_{\lambda_{\text{start}}}^{\lambda_{\text{end}}} QE(\lambda) \Phi(\lambda) d\lambda \quad . \quad (3.6)$$

The wavelengths used in this work for the saturation of the multijunction sub cells are presented in Table 3.2.

**Table 3.2** Overview of the used light wavelengths for the saturation of the individual sub cells in tandem, triple and quadruple junction solar cells for the  $QE$  evaluation.

Cell type	Top cell	Middle cell 1	Middle cell2	Bottom cell
a-Si:H/ $\mu$ c-Si:H	695 nm	-	-	450 nm
a-Si:H/a-Si:H	695 nm	-	-	450 nm
a-Si:H/ $\mu$ c-Si:H/ $\mu$ c-Si:H	695 nm	765 nm and 470 nm	-	525 nm
a-Si:H/a-Si:H/ $\mu$ c-Si:H	590 nm	780 nm and 400 nm	-	525 nm
a-Si:H/a-Si:H/ $\mu$ c-Si:H/ $\mu$ c-Si:H	590 nm	780 nm and 400 nm	525 nm and 830 nm	625 nm

---

As an example, for the a-Si:H/ $\mu$ c-Si:H/ $\mu$ c-Si:H triple cell, light with 695 nm wavelength was used for the saturation of the middle and bottom cell assuring that the top cell, which photocurrent is intended to be measured, limits the current of the whole device. For the measurement of the bottom cell, light of 525 nm wavelength was used to saturate the top and the middle cell. In the case of the middle cell *QE* measurement, the top cell was saturated with a 470 nm light and the bottom cell was saturated with 765 nm light.





## 4 Characterisation and modeling of photovoltaic-electrochemical devices

*A considerable number of device configurations for light induced water splitting has been proposed in literature over the last several years. Recently, special attention has been devoted to integrated photovoltaic-electrochemical devices based on thin film silicon solar cells. Even though III-V semiconductor based devices still provide the highest efficiencies in terms of bias-free water splitting, thin film silicon based PV-EC devices offer important advantages in terms of low-cost production, earth-abundance and, as will be shown in this work, adaptability of the photovoltaic parameters to the specific requirements of photoelectrochemical systems. Therefore, Section 4.1 of this chapter is concerned with the characteristics of PV-EC devices based on thin film silicon, also in comparison to other types of water splitting devices. The working principle of the herein developed PV-EC devices was highlighted in Section 2.3.4, including the specific function description of its main device components: the solar cell, the HER and OER catalyst, respectively, and the electrolyte. In Section 4.2 of this chapter, the experimental setup and the measurement techniques used to characterise the complete PV-EC device are described. Section 4.3 deals with the modeling of the PV-EC device characteristics, which is presented by means of a series circuit model approach. Coupled therewith, the current density-voltage characteristics of a solar cell and a PV-EC device are compared. The last part of this chapter gives a short overview on the solar-to-hydrogen efficiency calculation methods.*

### 4.1 Overview on photovoltaic-electrochemical devices

Photoelectrolysis of water by semiconductor based devices represents a prominent route that raised increasing interest among research groups worldwide [12, 141]. Among state-of-the-art solar fuel generators, integrated PV-EC devices, also called PV-biased electrosynthetic cells [86], based on multijunction III-V semiconductor

structures provide the highest solar-to-hydrogen (STH) efficiencies up to 18.3 % [27–29]. The widespread use of III-V semiconductors for water splitting applications is however still hampered by stability issues and cost limitations.

Although not as efficient, thin film silicon based PV-EC devices, which have been explored over the last 20 years, have established their position as emergent platform for the development of integrated water splitting devices and the study of various reactor designs [87, 142–144]. This has been possible, in particular, thanks to the ability to provide high photovoltages in multijunction structures. Furthermore, the thin film silicon device concept allows to fabricate monolithic cells that can be integrated in a compact water splitting device. Other studies, in contrast, use module connections of several solar cells, *e.g.* copper indium gallium selenide (CIGS) [145], crystalline silicon [146], or perovskite solar cells [147] to provide the sufficient voltage to run the HER and OER, respectively, without an external bias.

Even though the achieved STH efficiencies in module based water splitting devices are remarkable [32], the multijunction thin film silicon concept offers several advantages compared to series connected solar cells: usually the series connection requires an additional processing step (laser scribing or solar tabbing wire connection) compared to the monolithic multijunction solar cell fabrication process, which becomes particularly relevant in industrial applications. Additionally, series connected cells cannot be adjusted precisely with respect to the specifically demanded photovoltage of the complete system, which varies with the overpotentials of the employed catalysts for the HER and OER. Considering that the photocurrent at the respective required voltage determines the STH efficiency (see Section 4.4), the photovoltage/photocurrent tradeoff has prevented higher STH efficiencies so far. In crystalline silicon solar cells, for instance, the photovoltage can be adjusted only in large steps of approx. 600 mV by connecting several cells in series. However, in such a case, the increase in voltage is accompanied by a significant decrease in photocurrent and device efficiency (if the active solar cell area remains unchanged). The same, however, also applies to multijunction solar cells made merely of amorphous silicon alloys (a-Si:H and a-Si:Ge:H), which have been applied for unbiased solar water splitting by Delahoy *et al.* [148] and Khaselev *et al.* [28], for instance. Therefore, it is crucial to develop solar cells with the ability to tune the photovoltage not only in large but also in small steps in order to fulfill the particular requirements of various PV-EC systems. At the same time a change in the photovoltage should ideally not impair the device efficiency.

This task can be performed by monolithic multijunction solar cells made of thin

films of amorphous (a-Si:H) and microcrystalline ( $\mu$ c-Si:H) silicon. Combinations of a-Si:H and  $\mu$ c-Si:H allow for a more precise adjustment of the PV parameters and suffer less from stability issues under prolonged illumination (Staebler-Wronski effect) compared to their all-amorphous counterparts, as will be presented in Chapter 5.

## 4.2 Photoelectrochemical measurements

### 4.2.1 Measurement setup

The setup of the photoelectrochemical measurement cell is shown in Fig. 4.1 and consists of a polytetrafluoroethylene (PTFE) cell body and three electrodes:

- a working electrode (photocathode),
- a counter electrode (anode), and
- a Ag|AgCl reference electrode in 3 M potassium chloride (KCl) [0.268 V vs. standard hydrogen electrode (SHE)].

The potential of the working electrode was controlled by a Gamry Reference 600 (C3, Haar, Germany) potentiostat/galvanostat. Impedance spectra can be measured in the frequency range between 10  $\mu$ Hz and 1 MHz with a minimum voltage and current resolution of 1  $\mu$ V and 20 aA, respectively. The accuracy of the measured potential and current are  $\pm 0.3$  % of the selected ranges. Electrolytes were prepared from ultrapure deionised water (18 M $\Omega$ , Millipore, Schwalbach, Germany) and analytical grade chemicals. For the determination of *pH* values and conductivities of the electrolyte solutions an inoLab Level 3 measuring system (WTW GmbH and Co. KG, Weilheim, Germany) was used. The accuracy is specified to be below  $\pm 0.5$  %.

In the measurement setup, shown in Fig. 4.1, the photocathode is fixed by a bolt-on metal plate, which has an optical aperture of 0.5 cm<sup>2</sup> for the illumination of the photocathode. The aperture was chosen to be compatible with the standard solar cell geometry at IEK-5. The photocathode/electrolyte contact area was defined by an O-ring sealing aperture and was also 0.5 cm<sup>2</sup>. For the OER catalyst, a RuO<sub>2</sub> coated titanium sheet was employed as anode (15 g/m<sup>2</sup> RuO<sub>2</sub>, 3 cm<sup>2</sup> active area, supplied by Metakem). Photocathode and anode were separated by a distance of 2 cm. The reservoir of the measurement cell has a volume of approx. 30 ml for the electrolyte. No stirring of the electrolyte was involved during the photoelectrochemical measurements as it requires an additional energy input and would have to be factored in the STH

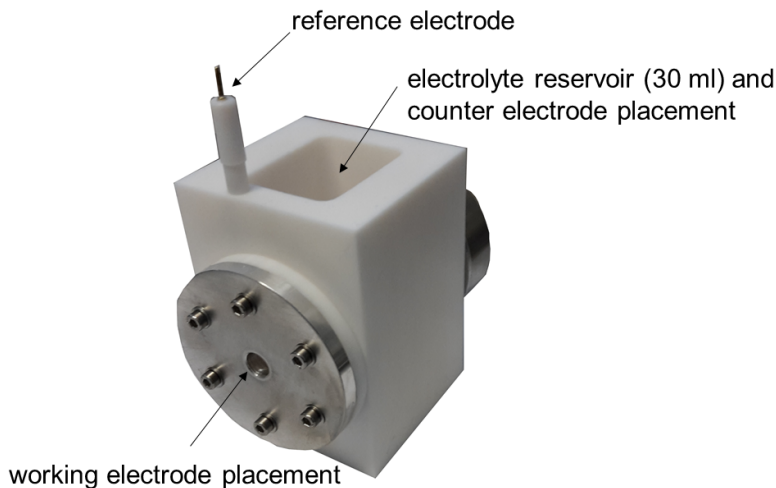


**Fig. 4.1** Photograph of the PV-EC cell used in this work to characterise the PV-EC devices. The setup consists of a Teflon cell body and three electrodes: a working electrode (multijunction photocathode), a counter electrode and a Ag|AgCl reference electrode in 3 M potassium chloride (CH instruments, Inc., Austin, TX, USA). The photocathode is fixed in between the cell body and a metal plate, to which it is electrically contacted. The metal plate is connected with the potentiostat and has an  $0.5 \text{ cm}^2$  optical aperture for illumination of the photocathode.

efficiency calculation. White light photocurrent measurements were performed under simulated AM 1.5 solar illumination ( $100 \text{ mW/cm}^2$ ) using an Oriel LCS-100 solar simulator (model 94011A). Electrical contact between the TCO coated glass substrate, *i.e.* the front contact of the solar cell and the metal plate, was made by a silver paste. The metal plate was then connected to the potentiostat.

## 4.2.2 Electrochemical methods

The electrochemical measurement methods which were conducted in this work are briefly discussed in the following. A more detailed insight in the most common electrochemical methods is given in Ref. [58].

### Potentiostatic measurement

During the potentiostatic measurements a constant potential or voltage is imposed on the working electrode for a specific time period and the current density is measured over time. In this work, potentiostatic measurements were used to evaluate the stability of the photoelectrochemical devices.

### Linear sweep voltammetry

The potential can be varied in different ways. It depends on the analytical method, whether potential steps or linear sweeps are applied. In this work the linear sweep technique will be preferred. This technique consists on applying an external potential to the WE, which is linearly scanned with a particular scan rate  $\nu$  (in mV/s), and measuring the resulting current density. The resulting  $j$ - $V$  characteristics are called voltammograms.

### Three-electrode vs. two-electrode measurement

In this work both, the three-electrode and the two-electrode configuration were applied to examine the performance of the photoelectrochemical devices. Therefore, it is important to elucidate the differences between both measurements and to comprehend the information that each measurement provides. With the PV-EC setup, shown in Fig. 4.1, three- and two-electrode measurements can be conducted.

In the three-electrode configuration, schematically depicted in Fig. 4.2(a), the potential of the working electrode (WE), *i.e.* the photocathode, is referred to an Ag|AgCl reference electrode (RE) and therefore the potential of the WE is measured with respect to that of this specific RE, which has a fixed constant potential ("potential  $E$  [V vs. Ag|AgCl]"). For standardisation the potential is also usually referred to that of the RHE ("potential  $E$  [V vs. RHE]", see Eq. 2.8 in Section 2.2.2). To obtain a current density-voltage curve of the photocathode, the potential versus the RE is scanned and the current monitored as a function of this potential scan. In order to maintain a constant potential, no current should flow through the RE. The performance of the counter electrode (CE) is usually not of importance. Its role is to sustain the balance of charge carriers (electrons) for the HER reaction at the WE. Three-electrode measurements therefore only show the WE performance and ignore any polarisation that might occur at the CE [149]. The

distance between the WE and the RE is kept as small as possible to minimise the ohmic potential drop between them. Furthermore, WE and CE should be aligned plane-parallel to avoid inhomogeneous current distribution, and the CE should be of sufficient size such that it is not limiting the total current.

The two-electrode configuration, shown in Fig. 4.2(b), consists only of two electrodes, namely the WE and the CE, while the RE is not needed. Hence, the potential/voltage of the WE (photocathode) is measured with respect to the CE (anode, *e.g.* RuO<sub>2</sub>). To clarify that the measurements is conducted with two electrodes, the voltage can be labeled as "PV-EC voltage  $V$  vs. RuO<sub>2</sub> [V]", for instance. In contrast to the three-electrode measurement, the CE potential is not constant, but a function of the current density (overpotential) and the local  $pH$  and concentration of dissolved O<sub>2</sub> gas. This technique therefore allows to evaluate the performance of the complete PV-EC device and is equivalent to the photovoltaic  $j$ - $V$  measurement described in Section 3.4.1.

In Fig. 4.2(c) and (d) the differences in the  $j$ - $V$  characteristics measured in a three- and in a two-electrode configuration for an a-Si:H/a-Si:H and an a-Si:H/ $\mu$ c-Si:H tandem junction based photocathode become apparent. Apart from the nomenclature differences ("potential" in a three-electrode and "voltage" in a two-electrode setup), distinct changes in the onset potentials for cathodic current  $E_{\text{onset}}$  appear, which was taken as the value at a photocurrent density of  $-0.5 \text{ mA/cm}^2$  in this work (see Fig. 4.2(c) and (d)). In the three-electrode setup the measured potential of the photocathode (WE) is independent of the potential losses at the CE, and thus, this technique allows to evaluate the performance of the photocathode without being distracted by the anode. In contrast, the two-electrode measurement monitors the  $j$ - $V$  behavior of the complete PV-EC device and accounts for the losses at both PV-EC electrodes. Consequently,  $E_{\text{onset}}$  is shifted in positive bias direction (anodic direction) in the two-electrode measurement (see Fig. 4.2(c)) compared to the three-electrode measurement (see Fig. 4.2(d)). Nevertheless, from the two-electrode measurement a STH efficiency of the complete PV-EC device can be estimated based on the current density at 0 V applied bias (operation photocurrent density  $j_{\text{op}}$ ) multiplied by the value of 1.23 [7] (see right ordinate in Fig. 4.2(d)). The STH efficiency calculation will be discussed in more detail in Section 4.4. The three-electrode measurement does not provide a device efficiency, but rather a photocathode efficiency.

From Fig. 4.2(c) and (d) it can be seen that the saturation photocurrent densities of the curves remained nearly the same in the three- and in the two-electrode measurement. This is because the illumination was the same in both configurations.

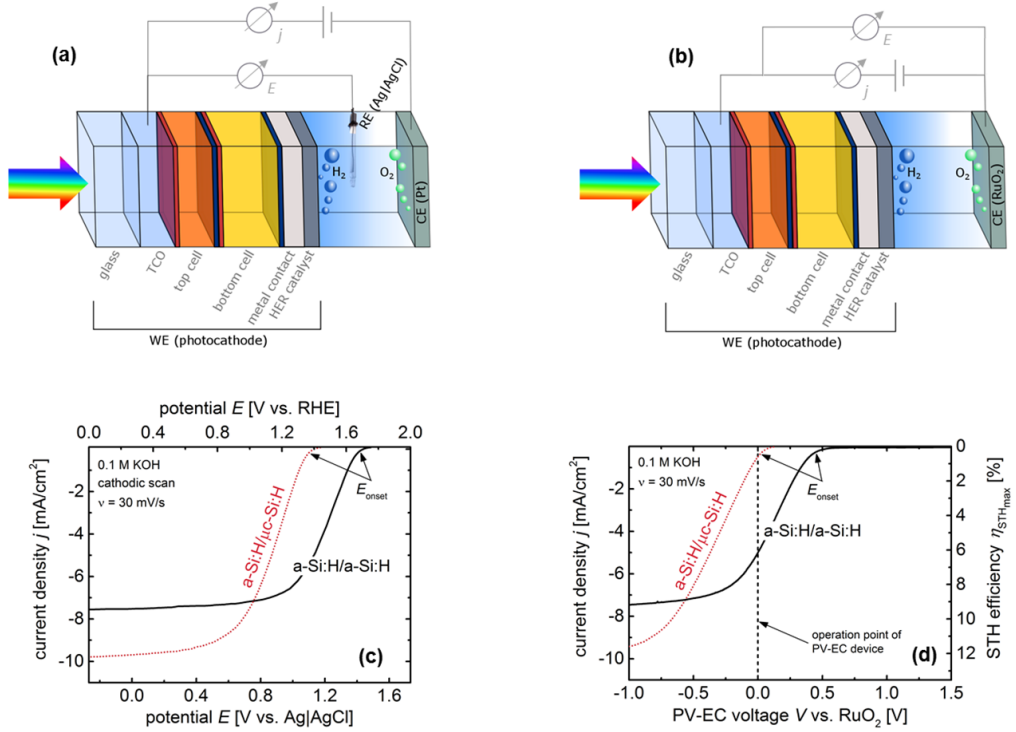


**Fig. 4.2** Schematic drawing of a tandem junction based photocathode in a three-electrode **(a)** and in a two-electrode setup **(b)**, respectively. In the three-electrode setup the reference electrode (RE) is positioned close to the working electrode (WE, photocathode). In the two-electrode setup only the WE and the CE are employed as electrodes. The corresponding voltammograms for the three-electrode setup **(c)** and for the two-electrode setup **(d)** are placed below the corresponding schematic drawing. In the three-electrode measurement the WE potential is measured with respect to the Ag|AgCl RE or with respect to the RHE (see Section 2.2.2). In the two-electrode setup the PV-EC device voltage is measured with respect to the CE (*e.g.* RuO<sub>2</sub>). The right ordinate in **(d)** depicts the achievable STH efficiency as a function of the photocurrent density at 0 V applied bias (operation point of PV-EC device). The onset potential for cathodic current  $E_{\text{onset}}$ , the scan rate, and the used electrolyte solution are indicated in **(c)** and **(d)**, respectively.



The "fill factor"<sup>1</sup> of the curves measured in the three-electrode configuration, however, are better than for the curves measured in the two-electrode configuration. This can be explained by the fact that the distance between the WE and the RE was kept as small as possible (less than 0.5 cm), whereas the distance between the WE and the CE in the two-electrode configuration was higher and is at approx. 2 cm (conditioned by the device geometry). In fact, the electrolyte imposes an additional series resistance for the PV-EC system, and thus, smaller electrolyte distances promote improved "fill factors" of the devices. The effects of the electrolyte resistance and other factors on the performance of PV-EC devices were investigated in more detail by means of a series circuit model in Section 4.3.

### Electrochemical impedance spectroscopy

In this work, electrochemical impedance spectroscopy (EIS) measurements were carried out to determine the electrolyte resistance. The EIS experiments were performed in a three-electrode setup by applying an AC amplitude of 10 mV in a frequency range between 10 kHz and 0.1 Hz superimposed over a DC potential of interest.

## 4.3 Device modeling

In the PV-EC device, as presented in Section 2.3.4, the main components, namely the solar cell, the catalyst for the HER, the electrolyte, and the catalyst for the OER are electrically arranged in series. Thus, the current density-voltage characteristics of the PV-EC device can be modelled by merging the current density-voltage characteristics of the catalyst material with the PV characteristics of the solar cell. Similar photoelectrochemical device modeling approaches have been shown elsewhere [150–152]. The advantage of the semi-empirical approach presented here is the flexibility to use experimental and literature based modeled data in concert for the device modeling [153, 154].

---

<sup>1</sup>For the PV-EC devices, the fill factor value is usually not calculated like in the PV measurements and does not directly enter the STH efficiency calculation (see Section 4.4). The term "fill factor" is rather used to describe the shape of the PV-EC  $j$ - $V$  curves, which can significantly affect the  $j_{op}$ , and thus, the STH efficiency.

### 4.3.1 Series circuit model

The model underlying series connection of the PV-EC device components is shown in the equivalent circuit in Fig. 4.3. In the PV-EC device the photocurrent density  $j_{\text{photo}}$  is generated by the solar cell (photovoltaic cell). The parallel and the shunt resistances of the photovoltaic cell are denoted by  $R_p$  and by  $R_s$ , respectively. The electrochemical load of the PV-EC system is represented by the series connected electrolysis cell, including the current-dependent overpotentials for the HER and OER catalysts,  $\eta_{\text{HER}}(j)$  and  $\eta_{\text{OER}}(j)$  respectively, and the electrolyte ohmic drop  $jR$ .

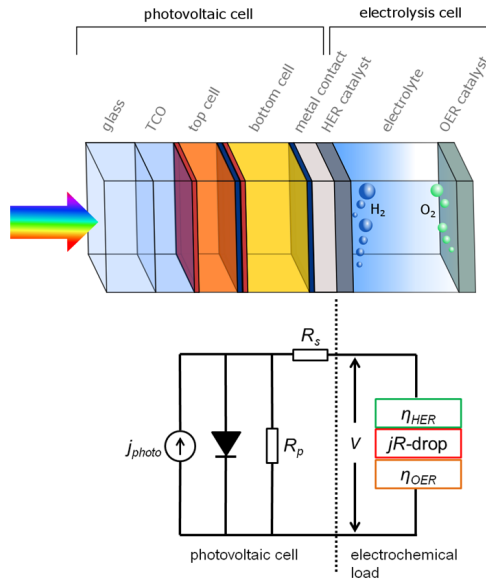


**Fig. 4.3** Schematic drawing of a tandem junction based PV-EC device with its photovoltaic and electrochemical components. Below, the equivalent circuit used to model the PV-EC device is depicted. The photovoltaic cell is connected in series with the electrolysis cell, which represents the electrochemical load of this device, including the current-dependent overpotentials for the HER and OER,  $\eta_{\text{HER}}(j)$  and  $\eta_{\text{OER}}(j)$  respectively, and the electrolyte ohmic drop  $jR$ . The photocurrent density  $j_{\text{photo}}$  is generated by the photovoltaic cell. The parallel and the shunt resistances of the photovoltaic cell are denoted by  $R_p$  and by  $R_s$ , respectively.

Mathematically the series-connected photovoltaic-electrochemical coupling can be written as:

$$V_{\text{PV-EC}}(j) = V_{\text{PV}}(j) - \Delta E - \eta_{\text{OER}}(-j) + \eta_{\text{HER}}(j) + jR \quad , \quad (4.1)$$

where  $V_{\text{PV}}(j)$  is the current density-voltage measurement of the solar cell and  $\Delta E = 1.23 \text{ eV}$  is the thermodynamic potential difference required in order to split  $\text{H}_2\text{O}$  into  $\text{H}_2$  and  $\text{O}_2$  at  $25^\circ\text{C}$ .  $\eta_{\text{OER}}(j)$  denotes the current-dependent overpotential at the anode and  $\eta_{\text{HER}}(j)$  denotes the current-dependent overpotential of the cathode. In order to take the different sign of the anodic current for the anode into account, the corresponding three-electrode measurement has to be mirrored at the potential axis, *i.e.* subtracted in Eq. 4.1.

### 4.3.2 Input parameters

The input parameters of the series circuit model are basically the current density-voltage data of the PV-EC device components. In this work, the  $j$ - $V$  data of the solar cell  $V_{\text{PV}}(j)$  are experimentally determined by illuminated  $j$ - $V$  measurements (see Section 3.4.1). The electrolyte resistance  $R$  was measured by means of impedance spectroscopy. The  $j$ - $V$  data of the HER and OER catalysts can either be measured experimentally, or modeled by the Tafel equation relationship (see Eq. 2.14 in Section 2.2) using literature data for the Tafel slope  $b$  and the exchange current density  $j_0$ . The corresponding literature data of various catalyst materials are listed in Table 6.3 in Section 6.4. Fig. 4.4 shows the current density-voltage measurements of the four PV-EC circuit components.

As example, an a-Si:H/a-Si:H tandem junction cell (see cell 130/130 in Table 5.3) was chosen as solar cell and the catalysts for the HER and the OER were Ni and  $\text{RuO}_2$  coated electrodes, respectively, whose  $j$ - $V$  characteristics were modeled by using literature data. A  $0.1 \text{ M KOH}$  solution was taken as electrolyte, with a resistance of  $50 \Omega$ . The hereout modeled current density-voltage characteristic  $V_{\text{PV-EC}}(j)$  of the PV-EV device, based on Eq. 4.1, is also plotted in Fig. 4.4.<sup>2</sup>

The illustration allows to draw the comparison between PV and PV-EC characteristics. As apparent from Fig. 4.4, the  $V_{\text{PV}}(j)$  and  $V_{\text{PV-EC}}(j)$  curves differ, in particular the open-circuit voltages and the "fill factors". As already briefly discussed,

---

<sup>2</sup>Note that the model can also be used to calculate the voltammogramm of a three-electrode measurement. In this case, only the  $\eta_{\text{OER}}(j)$  and the  $\Delta E$  term have to be removed from Eq. 4.1.

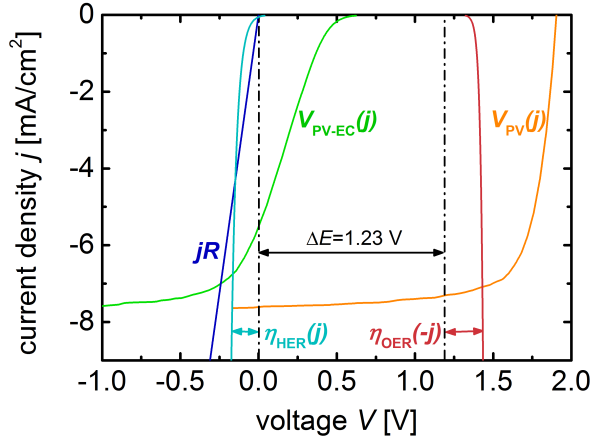


**Fig. 4.4** Current density-voltage characteristics of the main four circuit components of the PV-EC device:  $j$ - $V$  measurement of the solar cell ( $V_{PV}(j)$ , orange curve), modeled voltammogram of the  $\text{RuO}_2$  anode in a 0.1 M  $\text{H}_2\text{SO}_4$  solution with the associated  $\eta_{\text{OER}}(-j)$  (red curve), modeled voltammogram of the Ni HER catalyst layer in a 0.1 M KOH solution with the associated  $\eta_{\text{OER}}(j)$  (light blue curve), and the resistance of the 0.1 M KOH electrolyte ( $jR$ , dark blue line). The voltammogram of the PV-EC device ( $V_{PV-EC}(j)$ , green curve) was computed *via* on Eq. 4.1.

the reduced "fill factors" are caused by the electrolyte resistance. The flattening of the  $V_{PV-EC}(j)$  curve at open-circuit condition results from the Butler-Volmer electrode kinetics (see Section 2.2.3). At  $V = V_{\text{OC}}$  the flatband potential  $V_{\text{fb}}$  is reached. Here, charge carriers from the photocathode (electrons) have no available reduction states in the electrolyte, *i.e.* they cannot reduce  $\text{H}^+$  ions and thus, no current can flow. Only by applying a large positive voltage  $V \gg V_{\text{fb}}$  the photoelectrode can inject charge carriers (holes) into the oxidation states of the electrolyte. The photocathode would then become an anode and exhibit a positive anodic current.

### Electrolyte resistance

In the following, the effects of the electrolyte resistance on the  $V_{PV-EC}(j)$  voltammograms will be elucidated by means of the series circuit model. The photovoltaic cell, the HER, and the OER catalyst are kept constant for this investigation. An

a-Si:H/a-Si:H solar cell was chosen as photovoltaic cell, Pt was employed as HER catalyst and for the OER catalyst  $\text{RuO}_2$  was taken. In Fig. 4.5(a) the modeled PV-EC voltammograms for an increasing electrolyte resistances  $R$  are shown.

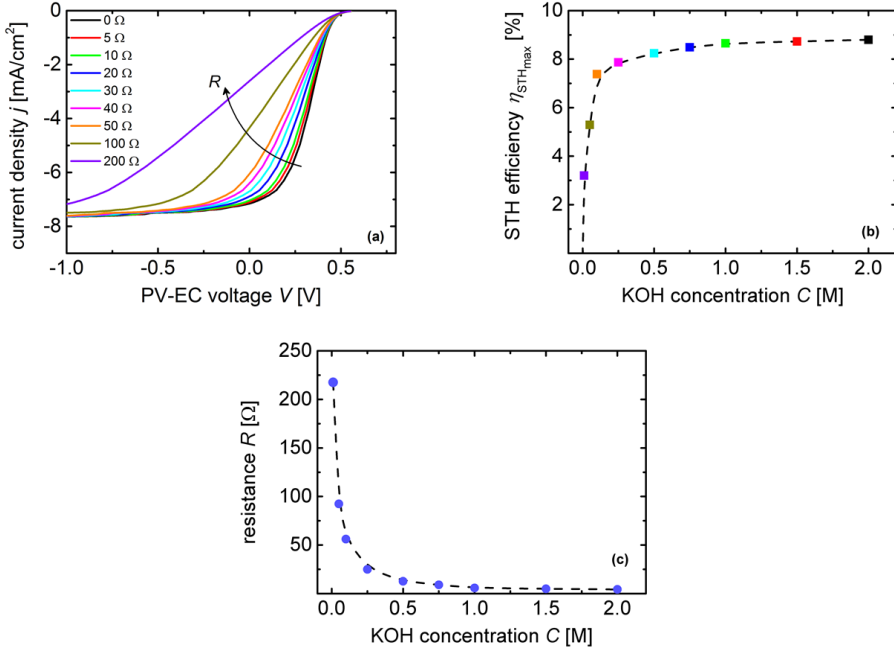


**Fig. 4.5** (a) Modeled current density-voltage curves of the PV-EC device for increasing electrolyte resistances  $R$ . The PV-EC device is composed of an a-Si:H/a-Si:H solar cell, a Pt HER and a  $\text{RuO}_2$  OER catalyst. The respective  $b$  and  $j_0$  values are kept constant and can be found in Table 6.3. The electrolyte resistance is increased from 0  $\Omega$  to 200  $\Omega$ . The  $j$ - $V$  curves were computed *via* on Eq. 4.1. (b) The solar-to-hydrogen efficiency calculated from the operation photocurrent density  $j_{\text{op}}$  of the PV-EC device from (a) as a function of the KOH electrolyte concentration  $C$ . (c) Corresponding measured resistances  $R$  of KOH electrolyte solutions for different concentrations  $C$ . The dotted lines in (b) and (c) serve as a guide to the eye.

As apparent from Fig. 4.5(a), neither the saturation photocurrent density nor the onset potential for cathodic current was significantly affected by the electrolyte resistance. However, the "fill factor" of the  $j$ - $V$  curves decreased drastically, in particular for the high resistance regime ( $R > 50$   $\Omega$ ) due to the increased ohmic

losses in the electrolyte ( $jR$ -drop). Thereby, the operation photocurrent density  $j_{\text{op}}$  (at 0 V) decreased considerably from 6.1 mA/cm<sup>2</sup> for 50  $\Omega$  to 2.6 mA/cm<sup>2</sup> for 200  $\Omega$ . For electrolyte resistances between 50 to 0  $\Omega$ , however, the effect on  $j_{\text{op}}$  and thus, on the STH efficiency of the PV-EC device was less pronounced (approx. 1 mA/cm<sup>2</sup> and 0.8 % absolute, respectively). This is also apparent from Fig. 4.5(b), which plots the STH efficiency calculated *via* Eq. 4.4 versus the KOH electrolyte concentration  $C^3$ . The corresponding measured resistances of KOH electrolyte solutions as a function of the electrolyte concentration can be found in Fig. 4.5(c). From Fig. 4.5(b) it becomes evident that for the given set-up the STH efficiency did not increase significantly for concentrations higher than 1 M. Therefore, it is reasonable to use a maximum electrolyte concentration of 1 M. Higher concentrations induce more severe chemical stability issues, as will be further discussed in Chapter 6.

### Catalyst activity

For the investigation of the effect of the catalyst activity, only the properties ( $j_0$  and  $b$ ) of the HER catalyst were varied in the model, while the catalytic activity of the OER remained unchanged. First the  $j_0$  was varied, while  $b$  was kept constant at 30 mV/dec. Fig. 4.6(a) shows the effect on the HER catalyst performance alone and Fig. 4.6(b) shows the impact on the PV-EC device performance. As electrolyte resistance 50  $\Omega$  were assumed. It can be observed that the onset potential for cathodic current for the catalyst (see Fig. 4.6(a)) and for the PV-EC device (see Fig. 4.6(b)) decrease with decreasing exchange current density. The "fill factor" of the curves is not affected. Consequently, the performance of the PV-EC device decreases as well.

The second step then was to vary the Tafel slope  $b$ , while keeping  $j_0$  at a constant value of 1 mA/cm<sup>2</sup>. Fig. 4.7(a) and (b) display the effect on the HER catalyst alone and on the PV-EC device voltammograms, respectively.

---

<sup>3</sup>Please note that the black square at  $C = 2$  M in Fig. 4.5(b) does not correspond to 0  $\Omega$ , but rather to a resistance of approx. 3  $\Omega$  (experimentally measured, see Fig. 4.5(c)).

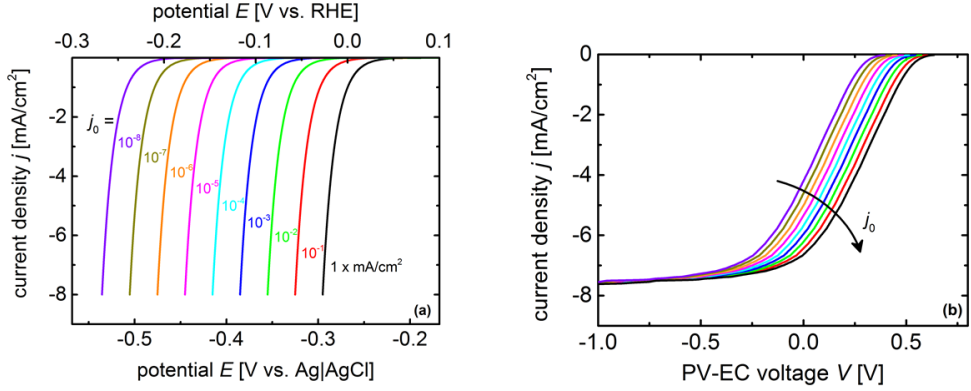


**Fig. 4.6** Modeled current density-voltage curves of the HER catalyst (a) and of the PV-EC device (b) for a decreasing exchange current density  $j_0$  via Eq. 4.1. The respective  $b$  value was kept constant at 30 mV/dec. The PV-EC device is composed of an a-Si:H/a-Si:H solar cell and a RuO<sub>2</sub> OER catalyst. An electrolyte resistance of 50  $\Omega$  was assumed.

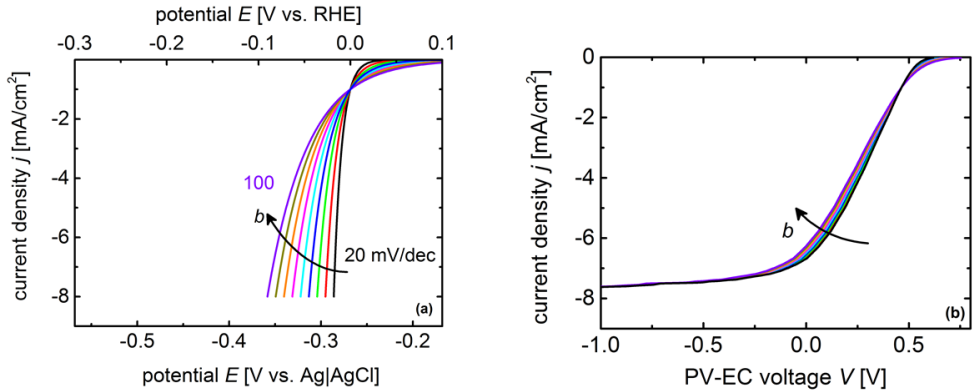


**Fig. 4.7** Modeled current density-voltage curves of the HER catalyst (a) and of the PV-EC device (b) for a decreasing Tafel slope  $b$  via Eq. 4.1. The respective  $j_0$  value was kept constant at 1 mA/cm<sup>2</sup>. The PV-EC device is composed of an a-Si:H/a-Si:H solar cell and a RuO<sub>2</sub> OER catalyst. An electrolyte resistance of 50  $\Omega$  was assumed.

In contrast to the  $j_0$  value, a change in the  $b$  value does not significantly affect the onset potential for cathodic current (at  $-0.5 \text{ mA/cm}^2$ ), but the "fill factor" decreases upon a decrease of  $b$  (see Fig. 4.7(a)). However, as can be deduced from the  $V_{\text{PV-EC}}(j)$  curves in Fig. 4.7(b), the effect on the PV-EC device performance is rather weak, compared to the impact of  $j_0$  (see Fig. 4.6(b)).

The results show, that with the presented series circuit model, the photocurrent density-voltage characteristics of the photovoltaic cell can be used in concert with the current density-voltage characteristics of the electrochemical components to predict the current density-voltage behavior of the complete PV-EC device. This decoupled approach therefore allows to predict the overall PV-EC device efficiency, and furthermore to evaluate how variations of the specific component characteristics, *e.g.* the electrolyte resistance and the catalytic activity, affect the  $j$ - $V$  characteristic of the complete PV-EC device. The validation of the model, based on real case studies, will be presented in Section 6.3.

## 4.4 Solar-to-Hydrogen efficiency calculation

The solar-to-hydrogen efficiency is a key metric that facilitates comparison of the performance between various solar fuel production systems. However, some of the claimed efficiencies are evaluated either under non-standard conditions (*e.g.* more than one sun illumination) or in three-electrode setups. It is important to note that three-electrode measurements only provide photoelectrode efficiencies and not device efficiencies. Hence, real STH efficiencies need to be measured in two-electrode setups. But also for studies dealing with two-electrode measurements, the STH efficiencies reported in the literature are difficult to compare, because calibrated and certified efficiency measurements under defined standard conditions are still not ensured for water splitting devices. Recently attempts to standardise measurement methods, definitions and reporting protocols are initiated [155, 156]. Nevertheless, the most accurate method to calculate the STH efficiency is to define it in terms of the free energy stored in the hydrogen [157] as

$$\eta_{\text{STH}} = \frac{\text{mol H}_2 \text{ m}^{-2}\text{s}^{-1} \times 237 \text{ kJ mol}^{-1}}{\text{total integrated power input density (W m}^{-2}\text{)}} \quad , \quad (4.2)$$

where  $237 \text{ kJ mol}^{-1}$  denotes the Gibbs free energy and the input power is the incident light intensity (AM 1.5,  $100 \text{ mW/cm}^2$ ). To apply this methodology it is necessary



to include  $\text{H}_2$  and  $\text{O}_2$  gas collection data. This would ensure that only  $\text{H}_2$  and  $\text{O}_2$  molecules are involved in the measurements, *i.e.* that a closed reaction cycle is measured. However, the used measurement set-up in this work does not allow for a quantitative evaluation of the gas amounts. An upgrade of the set-up regarding gas separation and collection was beyond the scope of this work, but is currently under construction.

Alternatively, the STH efficiency can be expressed as a function of the generated photocurrent density  $j_{\text{op}}$  at 0 V applied bias. In fact, this methodology also requires to accurately control the gas generation in order to confirm stoichiometric gas evolution ( $\text{H}_2$  and  $\text{O}_2$ ) in the absence of any sacrificial electron donors or acceptors [157]. If sacrificial agents are used, it would be invalid to use the term "STH efficiency" or speak of solar "water splitting". For instance, the corresponding thermodynamic potentials for hydrogen decomposition *via* electrolysis for hydriodic acid (HI) or hydrobromic acid (HBr) are lower than 1.23 V [158], namely 1.07 V and 0.54 V for HBr and HI splitting, respectively. Organic molecules such as methanol oxidise even easier ( $\text{CH}_3\text{OH}/\text{CO}_2$ ,  $\Delta E = 0.05$  V) [159].

Nevertheless, during operation of the PV-EC device the generated photocurrent density  $j_{\text{op}}$  can be used to calculate the STH efficiency  $\eta_{\text{STH}}$  of the PV-EC device [160] *via*

$$\eta_{\text{STH}} = \frac{\Delta E \times |j_{\text{op}}| \times \eta_{\text{F}}}{\text{total integrated power input density}} \quad (4.3)$$

$j_{\text{op}}$  is the operating photocurrent density when no bias is applied, and the input power is the incident light intensity (AM 1.5, 100 mW/cm<sup>2</sup>).  $\eta_{\text{F}}$  is the faradaic efficiency for hydrogen evolution and is a very crucial parameter in Eq.4.3.  $\eta_{\text{F}}$  indicates the ration of the measured photocurrent to the molar  $\text{H}_2$  generation rate. Hence, a 100 % faradaic efficiency would mean that the measured photocurrent directly corresponds to the molecular hydrogen generation *via* proton reduction.

Assumptions of 100 % faradaic efficiency are widely used in the field of photo-electrochemical water splitting [87, 161, 162]. Even though this assumption is not always valid, it provides a consistent method for the comparison of the performance between various solar fuel production systems. Laboratories, however, should be advised to use methods for direct identification and quantification of  $\text{H}_2$  and  $\text{O}_2$  to establish faradaic efficiencies [157]. Considering this, an estimated STH efficiency  $\eta_{\text{STH}_{\text{max}}}$  under the assumption of unity faradaic efficiency can be defined as

$$\eta_{\text{STH}_{\text{max}}} = \frac{\Delta E \times |j_{\text{op}}|}{\text{total integrated power input density}} \quad (4.4)$$

$\eta_{\text{STH}_{\text{max}}}$  gives an upper bound efficiency and the subscript "max" shall point out the 'strong' assumption of a 100 % faradaic efficiency throughout this work.

Nevertheless, in order to validate this assumption, the faradaic efficiency was estimated by means of a volumetric technique in this work<sup>4</sup>. To maintain the simplicity of the demonstration device setup and avoid making separate compartments for the OER and HER, respectively, the experiment was conducted in a gas tight photoelectrochemical cell (type Zahner). The evolved gas volume was measured using an inverted burette to collect the gases during photoelectrochemical water splitting at a current density of 7 mA/cm<sup>2</sup> in 0.1 M KOH. As a photocathode, an a-Si:H/a-Si:H/ $\mu$ c-Si:H triple junction solar cell with a ZnO/Ag/Pt rear contact was used. Prior to the measurement, the aqueous solution, which was used as a barrier, was saturated with oxygen by bubbling molecular oxygen through the solution. No membrane was integrated between the anode and the cathode. Thus, recombination of hydrogen and oxygen or reduction of oxygen on the photocathode could be an issue in particular under prolonged operation. The theoretically expected total gas volume was calculated by combining Faraday's law of electrolysis with the ideal gas law

$$V_{\text{theo}} = \frac{R T}{F p z} Q \quad . \quad (4.5)$$

Here,  $R$  is the ideal gas constant,  $T$  is the absolute temperature,  $F$  is Faraday's constant,  $p$  is the pressure,  $z = 4/3$  is the number of electrons involved<sup>5</sup>, and  $Q$  is the charge (integrated photo current). The measurement error was estimated to be  $\Delta V_{\text{theo}} = \pm 0.2$  ml. The generated gas volume by the a-Si:H/a-Si:H/ $\mu$ c-Si:H photocathode over the operation time is shown in Fig. 4.8(a).

The faradaic efficiency  $\eta_F$  of the water splitting process is plotted in Fig. 4.8(b) and was computed as the ratio between measured and theoretically expected total gas volume as

$$\eta_F = \frac{V_{\text{meas}}}{V_{\text{theo}}} \quad . \quad (4.6)$$

According to first order propagation of error, the uncertainty of the faradaic efficiency was

$$\Delta \eta_F = \frac{\Delta V_{\text{meas}}}{V_{\text{theo}}} \quad . \quad (4.7)$$

<sup>4</sup>The method description and efficiency calculations presented in this section were published in F. Urbain *et al.*, Energy Environ. Sci. **9** (2016), 145-154 [144] (Supplementary information).

<sup>5</sup>For the water splitting reaction four electrons are transferred while three units of gas are generated, giving a  $z$  value of 1.33 if the volume refers to the total gas flow.

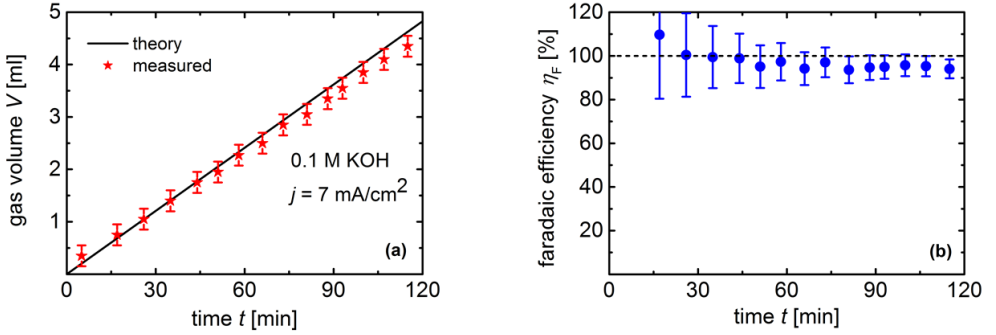


**Fig. 4.8** (a) Generated volume of gas produced by an a-Si:H/a-Si:H/ $\mu$ c-Si:H triple junction based photocathode under AM 1.5 solar illumination for two hours of operation at  $7 \text{ mA/cm}^2$  in 0.1 M KOH. The black line shows the theoretical gas volume for 100 % faradaic efficiency and the red stars are the measured data. The measurement error was estimated to be  $\Delta V_{\text{theo}} = \pm 0.2 \text{ ml}$ . (b) Evaluated faradaic efficiency over time calculated from the measured gas volume.

Even though the volumetric measurement data confirms that the assumption of 100 % faradaic efficiency is valid for the PV-EC system, the presented STH efficiencies in this work shall still be considered as maximum STH efficiency  $\eta_{\text{STH,max}}$ . A key control experiment on the hydrogen generation needs to be performed to prove a 2/1  $\text{H}_2/\text{O}_2$  ratio *via* gas chromatography, for instance. This would ensure that only  $\text{H}_2$  and  $\text{O}_2$  molecules are involved in the measurements, *i.e.* that really a closed reaction cycle is measured.

## 5 High voltage multijunction thin film silicon solar cells

*This chapter reports on the results of the development of high voltage single and multijunction solar cells made of amorphous and microcrystalline silicon for the application as photocathodes in integrated PV-EC devices. Solar cells made of amorphous and microcrystalline silicon have been extensively developed in the past, with major focus on high conversion efficiencies [163]. The approach presented here, however, focuses on the development of high  $V_{OC}$  devices, suitable for water splitting applications. Therefore, a development route is described to achieve high voltage devices with emphasis on the optimal fabrication parameter regimes for the intrinsic absorber layers. To start with, the results on the development of suitable opto-electronic and structural properties of the intrinsic amorphous and microcrystalline silicon absorber layers and their implementation in single junction solar cells are presented (see Sections 5.2 and 5.3). It is shown that the material properties of the individual sub cell absorber layers can be systematically adjusted such that the photovoltages of multijunction devices cover a wide range of photovoltages from 1.4 V up to 2.8 V with photovoltaic efficiencies up to 13.6 % (see Sections 5.4 and 5.5). Furthermore, the effects of prolonged illumination and temperature variation on the photovoltaic parameters of the multijunction solar cells are investigated (see Sections 5.6 and 5.7). The different cell types are evaluated in regard to their potential for water splitting at the end of this chapter in Section 5.8.*

### 5.1 Experimental details

All thin film silicon layers were deposited by a plasma enhanced chemical vapor deposition technique in a multi chamber system (for further details see Section 3.2.1). The deposition parameters, including the gas mixtures used for the deposition of doped a-Si:H,  $\mu$ c-Si:H and  $\mu$ c-SiO<sub>x</sub>:H layers can be found in 3.2. For the intrinsic absorber layers, a mixture of silane (SiH<sub>4</sub>) and hydrogen (H<sub>2</sub>) gases was used. The *p*- and *n*-type layers were all deposited at a substrate temperature of 180 °C and had a

thickness of 15-30 nm. For the deposition of the intrinsic a-Si:H layers,  $T_s$  was varied between 70 °C and 250 °C. In the single junction solar cells the a-Si:H absorber layers had a thickness of 400 nm. The respective thicknesses for the a-Si:H and  $\mu$ c-Si:H layers used in multijunction configurations are indicated in the respective sections. For all intrinsic  $\mu$ c-Si:H layers a substrate temperature of 180 °C was applied and the material properties were investigated as a function of the silane concentration. The thicknesses of the investigated  $\mu$ c-Si:H absorber layers were varied between 450 nm and 1300 nm. The sample names of the deposited solar cell in this study along with the deposition and photovoltaic parameters can be found in Table A1–Table A6.

If not stated otherwise, the solar cells were characterised by current–voltage ( $J$ – $V$ ) measurements at standard test conditions (100 mW/cm<sup>2</sup>, 25 °C) using a double source (Class A) AM 1.5 sun simulator described in Section 3.4.1. Light induced degradation was performed under open-circuit conditions at 55 °C under simulated sun spectrum (1000 W/m<sup>2</sup>) during 1000 h. Furthermore, spectral response measurements quantum efficiency of the single and multijunction solar cells were conducted using a monochromator in a wavelength range between 300 nm to 1100 nm. The corresponding wavelengths used for the saturation of the individual sub cells of multijunction solar cells are presented in Section 3.4.2 in Table 3.2.

## 5.2 a-Si:H absorber layer properties and a-Si:H single junction solar cells

The experiments that led to the results presented in this section were carried out in the framework of the diploma thesis of Ms Karen Wilken at the Forschungszentrum Jülich [98]. The diploma thesis focused on the development of low-temperature fabricated amorphous silicon material with high optical gaps for the application in single and tandem junction solar cells with high open-circuit voltages. The present Ph.D. thesis expands on the findings shown in [98] and employs the low-temperature fabricated a-Si:H layers for the development of high voltage multijunction solar cells. In this section, the key results necessary to comprehend the further investigations of this work will be highlighted. For more details on the fabrication and characterisation of low-temperature a-Si:H layers, the reader is referred to the corresponding diploma thesis [98].

The open-circuit voltage of a properly designed a-Si:H solar cell mainly depends on the optical gap energy of the absorber layer [85, 164]. Thus, attempts for the

variation in the optical gap energy of intrinsic a-Si:H absorber layers were made.<sup>1</sup> The a-Si:H material optimisation was mainly performed as a function of the substrate temperature  $T_s$  and the silane concentration  $SC$ .

### 5.2.1 Intrinsic a-Si:H absorber layers

The optical gap of a-Si:H correlates with the hydrogen content of the material [92]. Therefore, FTIR measurements were conducted to estimate the amount of hydrogen in intrinsic a-Si:H layers. Fig. 5.1 shows the hydrogen content  $c_H$  as a function of the substrate temperature for a-Si:H layers deposited with different silane concentrations. The general trend indicates that a decrease in  $T_s$  resulted in an increase of  $c_H$ . This behavior can be attributed to the increased desorption of hydrogen at higher substrate temperatures. As the deposition temperature increases, the desorption of hydrogen atoms is energetically favored. Thus, less hydrogen is incorporated into the layer [165]. No clear dependency of  $c_H$  on the silane concentration in the chosen range was visible in the FTIR data. The hydrogen content in all samples investigated was between 10.6 % and 16.8 %.

For the determination of the optical gap energy of the a-Si:H material, absorption spectra for different  $T_s$  and  $SC$  were measured and subsequently evaluated, with respect to  $E_{04}$  as an estimation of the optical gap. The evaluated  $E_{04}$  values for all samples are shown in Fig. 5.2. In the considered temperature range, the optical gap energy  $E_{04}$  decreased by approximately 80 meV with increasing  $T_s$  for a given  $SC$ . Additionally, a slight dependency of the  $E_{04}$  data on the  $SC$  data could be extracted. For a constant  $T_s$ , an average difference of approximately 30 meV between  $SC$  of 4 % and 10 % was observed. Considering all a-Si:H absorber layers, the optical gap was varied by 120 meV from 1.86 eV to 1.98 eV.

The results presented in Fig. 5.1 and Fig. 5.2 suggest that the the hydrogen content is directly linked to the optical gap in a-Si:H material. In fact, it is commonly observed that the optical gap energy of a-Si:H increases with increasing fraction of bound hydrogen in the a-Si:H material [43]. A possible explanation suggested that the hydrogen could be involved in the breaking of weak Si-Si bonds that are responsible for the states in the top of the valence band. Consequently, by increasing  $c_H$ , stronger Si-H bonds emerge, which leads to states deep in the valence band. As a result, the valence band edge shifts down. The conduction band remains

---

<sup>1</sup>The results presented in this section were also published in F. Urbain, K. Wilken *et al.*, Int. J. Photoenergy **2014** (2014), 249317 [85].

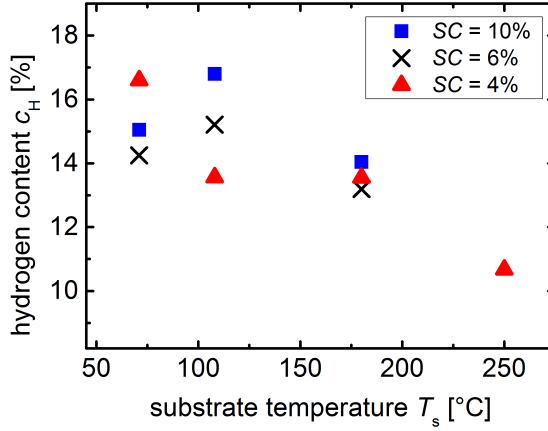


**Fig. 5.1** Hydrogen content  $c_H$  as a function of the substrate temperature  $T_s$  during the deposition of intrinsic a-Si:H layers, with different silane concentrations  $SC$ . The thickness of the layers was 400 nm. The data is taken from Refs. [85,98] (By courtesy of K. Wilken, Forschungszentrum Jülich).

unaffected and thus, the optical gap energy increases [43,92]. Other microscopic models involve a discussion of the effects of nanosized void configurations on the hydrogen incorporation in a-Si:H material [166,167].

For low-temperature deposited a-Si:H layers, it is well accepted that the a-Si:H material suffers an increase of the defect density, which leads to a deterioration of the solar cell performance [90,168]. As shown in Ref. [98], the adjustment of  $SC$ , however, allows to maintain a material with a reasonable electronic quality (low defect density) even at a very low deposition temperature. These results demonstrated that the electronic quality of the a-Si:H material deposited at low substrate temperatures around 70 °C could be improved, in terms of defect absorption density, by using lower silane concentrations during the deposition.

### 5.2.2 a-Si:H single junction solar cells

The investigated intrinsic a-Si:H absorber layers with different optical gap energies were subsequently applied in single junction solar cells in a *pin* configuration. The

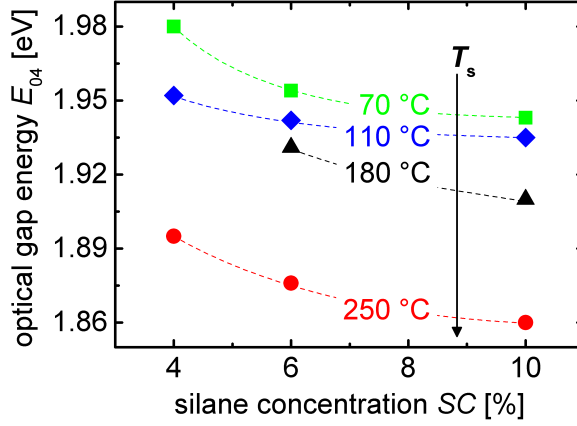


**Fig. 5.2** Optical gap energy  $E_{04}$  as a function of the silane concentration  $SC$  for intrinsic a-Si:H layers deposited at different substrate temperatures  $T_s$ . The dotted lines are to guide the eye. The data is taken from Refs. [85,98] (By courtesy of K. Wilken, Forschungszentrum Jülich).

solar cells were prepared with intrinsic a-Si:H layers at silane concentrations of 4 % and 10 %, in order to consider the entire range of  $E_{04}$  absorber layer energies (from 1.86 eV to 1.98 eV) for the relevant temperatures, shown in Fig. 5.2. The performance of the a-Si:H solar cells as a function of  $T_s$  is displayed in Fig. 5.3.

By reducing  $T_s$  from 250 °C down to 110 °C, the open-circuit voltage  $V_{OC}$  increased with decreasing  $T_s$  and was varied from 802 mV up to a value of 946 mV, achieved in the case of an absorber layer with a silane concentration of 4 % and a substrate temperature of 130 °C (see Fig. 5.3(b)). In this temperature range (110 °C – 250 °C), the fill factor  $FF$  was only slightly affected, and varied between 68.5 % and 73.8 % for an  $SC$  of 10 % and between 70.2 % and 74.2 % for an  $SC$  of 4 % (see Fig. 5.3(c)). The best efficiency  $\eta_{PV}$  of 10.3 % was obtained with an intrinsic a-Si:H layer with an  $SC$  of 10 %, deposited at 180 °C (see Fig. 5.3(a)).



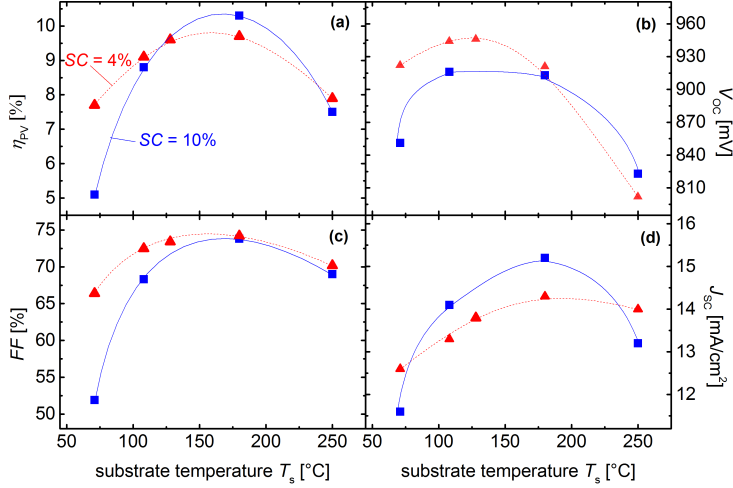


**Fig. 5.3** Photovoltaic parameters of single junction solar cells (efficiency  $\eta_{PV}$  (a), open-circuit voltage  $V_{OC}$  (b), fill factor  $FF$  (c), short-circuit current density  $J_{SC}$  (d)) as a function of the substrate temperature  $T_s$  of the intrinsic a-Si:H layer, with 10 % (blue squares) and 4 % (red triangles) silane concentration  $SC$ , respectively. The intrinsic a-Si:H layers had a thickness of approx. 400 nm. The lines are to guide the eye. The data is taken from Refs. [85, 98] (By courtesy of K. Wilken, Forschungszentrum Jülich).

For even lower  $T_s$  of 70 °C, the entire performance parameters tend to deteriorate considerably, as compared with the solar cells deposited at  $T_s$  of 110 °C or above. In the 70 °C temperature region, an increased defect absorption density [98] and a higher optical gap  $E_{04}$  (see Fig. 5.2) significantly impaired the electronic material quality. Nevertheless, as already mentioned in the preceding section, through the use of a lower  $SC$  during the low-temperature deposition, a significant improvement of the optoelectronic properties of a-Si:H material was achieved [98]. When  $SC$  was reduced down to 4 %, a significant improvement in  $V_{OC}$  and  $FF$  was observed in the case of solar cells deposited at temperatures below 180 °C. For  $T_s = 70$  °C and  $SC = 4$  %, all the parameters were enhanced, compared to the 70 °C cell with  $SC = 10$  %, and  $\eta_{PV}$  yielded 7.7 % (see Fig. 5.3(a)). This underlines that a combination of low deposition temperature and reduced  $SC$  of the absorber layer was necessary to obtain

high voltage solar cells with an appropriate efficiency level.

Fig. 5.3(d) presents the  $J_{\text{SC}}$  data of the solar cell series as a function of  $T_s$ . From 70 °C to 180 °C,  $J_{\text{SC}}$  increased with increasing  $T_s$  and, except for  $T_s$  of 70 °C, the solar cells with  $SC = 10\%$  promoted higher  $J_{\text{SC}}$  compared to the cells with a SC of 4 %. This can be explained by the wider  $E_{04}$  gap of a-Si:H layers with  $SC = 4\%$ , in comparison to layers with  $SC = 10\%$  (see Fig. 5.2). However, for  $T_s$  of 250 °C,  $J_{\text{SC}}$  decreased for both  $SC$ .

In Ref. [98], it was demonstrated by means of quantum efficiency measurements of the solar cells from Fig. 5.3 that the decrease in  $J_{\text{SC}}$  for  $T_s$  of 250 °C was caused by the drop in photocurrent in the short wavelength region. It was suggested that boron diffusion from the  $p$ -type layer (deposited at 180 °C) into the intrinsic a-Si:H layer (deposited at 250 °C) caused a deterioration of the  $p$ -/ $i$ -interface. This deterioration led to a reduction of the short wavelength  $QE$  and hence,  $J_{\text{SC}}$  decreased.

### 5.3 $\mu\text{c-Si:H}$ absorber layer properties and $\mu\text{c-Si:H}$ single junction solar cells

The open-circuit voltage  $V_{\text{OC}}$  in  $\mu\text{c-Si:H}$  solar cells strongly correlates with crystallinity and with the thickness of the absorber material [103, 169, 170]. Apart from that,  $V_{\text{OC}}$  is also influenced by the intrinsic-type interface properties. Therefore, the optimisation of the  $\mu\text{c-Si:H}$  solar cells was conducted by the following routes:<sup>2</sup>

- variation of the intrinsic  $\mu\text{c-Si:H}$  absorber layer thickness,
- control of the  $\text{SiH}_4$  flow during deposition of the intrinsic  $\mu\text{c-Si:H}$  absorber layer, aiming to maintain a low crystallinity growth across the entire  $i$ -layer, and
- incorporation of an intrinsic amorphous buffer layer at the  $n$ -/ $i$ -interface of the  $\mu\text{c-Si:H}$  solar cell.

---

<sup>2</sup>The results presented in this section were published in F. Urbain *et al.*, J. Mater. Res. **29** (2014), 2605-2614 [40].

### 5.3.1 Intrinsic $\mu\text{c-Si:H}$ absorber layers

First, intrinsic  $\mu\text{c-Si:H}$  absorber layers were investigated with respect to the crystallinity  $I_{\text{C}}^{\text{RS}}$  of the layers, which was mainly controllable through the silane concentration ratio  $SC$  during the growth, as shown in Fig. 5.4. Raman spectroscopy measurements were conducted to estimate the crystalline volume fraction in the samples. As apparent from Fig. 5.4,  $I_{\text{C}}^{\text{RS}}$  strongly decreased with an increasing  $SC$  of the intrinsic  $\mu\text{c-Si:H}$  absorber layer.

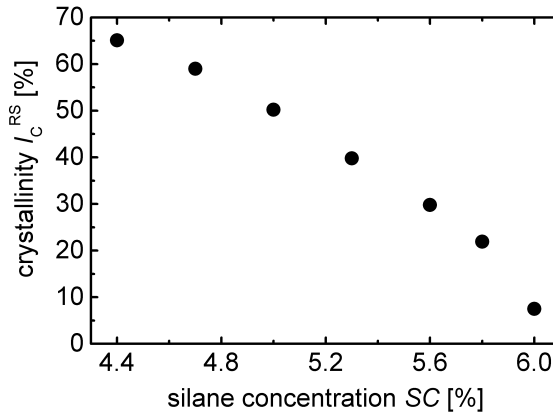


**Fig. 5.4** Crystallinity  $I_{\text{C}}^{\text{RS}}$  as a function of the silane concentration  $SC$  of the intrinsic  $\mu\text{c-Si:H}$  absorber layer. All investigated layers had a thickness of 800 nm.

### 5.3.2 $\mu\text{c-Si:H}$ single junction solar cells

#### Thickness variation of the $\mu\text{c-Si:H}$ absorber layer

The performance of the  $\mu\text{c-Si:H}$  solar cells, with respect to  $V_{\text{OC}}$ , as a function of the evaluated crystallinity of the absorber layers is presented in Fig. 5.5. The absorber layer thicknesses of the investigated solar cells were 1300, 650, and 450 nm.

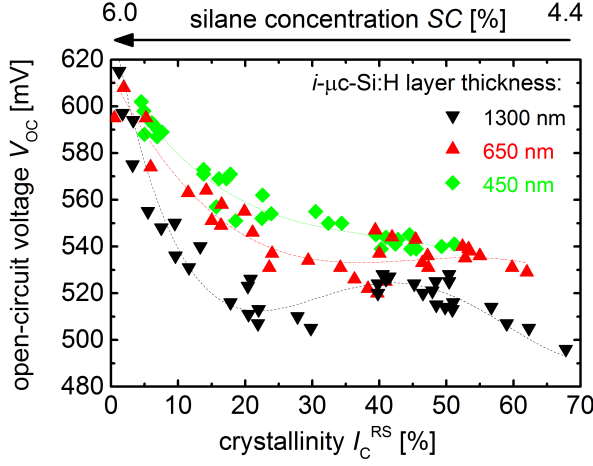


**Fig. 5.5** Open-circuit voltage  $V_{OC}$  of  $\mu\text{c-Si:H}$  single junction solar cells as a function of the crystallinity  $I_C^{RS}$  of the intrinsic  $\mu\text{c-Si:H}$  absorber layers (arrow on the upper abscissa illustrates the corresponding trend for the silane concentration  $SC$ ). Absorber layer thicknesses of 1300 nm (black triangles), 650 nm (red triangles), and 450 nm (green diamonds) were investigated. The dashed lines serve as a guide to the eye.

It is well accepted that a decrease in  $I_C^{RS}$ , *i.e.* an increase in  $SC$ , leads to an increase in  $V_{OC}$  because the material increasingly becomes amorphous [103, 171]. For the 1300 nm thick  $\mu\text{c-Si:H}$  absorber layers, the data shows that from  $I_C^{RS}$  of 15 % to 70 % there was only a weak effect on  $V_{OC}$ . In this region, the data points suggest a curvature and the open-circuit voltage varied between 490 mV and 530 mV with a  $V_{OC}$  maximum at a crystallinity of 50 % - 40 %. A strong increase in  $V_{OC}$  from 530 mV to 620 mV was visible only for  $I_C^{RS}$  values below 15 %. A similar trend of the  $V_{OC}$  data as a function of the  $SC$  data for thick  $\mu\text{c-Si:H}$  absorber layers above 1.5  $\mu\text{m}$  was already reported in [103, 169]. By reducing the thickness of the  $\mu\text{c-Si:H}$  absorber layers to 650 nm and 450 nm, respectively, the general trend in Fig. 5.5 indicates that  $V_{OC}$  increased for a given crystallinity with decreasing thickness. The open-circuit voltage of  $\mu\text{c-Si:H}$  solar cells is assumed to be limited by the bulk recombination in the absorber layer [171–173]. Therefore, a decrease of the thickness of this layer may lead to an increase in  $V_{OC}$  due to the reduced volume. Overall, this was confirmed by the results of this work, which indicate that thinner absorber layers tend to enable higher  $V_{OC}$  values, especially in the moderate crystallinity range. As an example,

for  $I_C^{RS}$  of around 30 %,  $V_{OC}$  increased by around 60 mV (from 500 mV to 560 mV) when the absorber layer was reduced from 1300 nm to 450 nm.

### SiH<sub>4</sub> profiling

This part focuses on the growth control of the  $\mu$ c-Si:H absorber layer by means of adjustment of the SiH<sub>4</sub> gas flow during the deposition, aiming to obtain a moderate crystallinity (around 50 %) of the absorber layer across the entire *i*-layer. This adapted deposition process will be denoted as "SC profiling" hereafter. Preceding studies show that profiling could lead to flattening of the crystallinity profile and to an improved device performance [174,175]. Fig. 5.6(a) depicts the Raman intensity ratio depth profile of the structure of the  $\mu$ c-Si:H solar cell along the growth axis, including *n*- and *p*-type layers and the intrinsic 1300 nm thick absorber layer.

First, a  $\mu$ c-Si:H solar cell deposited with a standard deposition process (*SC* of 4.4 % and 5 %, black dots in Fig. 5.6(a)) was investigated. The corresponding *SC* profile (change of *SC* during deposition time) is shown in Fig. 5.6(b) (black dotted line). The corresponding Raman depth profile data, presented in Fig. 5.6(a), reveals that the crystallinity of the solar cell was varied between 42 % and 70 % over the cell thickness. To a cell thickness of 1000 nm,  $I_C^{RS}$  consistently increased from 42 % to 70 % and decreased again down to around 50 % from 1000 nm to 1300 nm. A reduction in the crystallinity with an increasing  $\mu$ c-Si:H layer thickness was previously observed [105]. The steep decrease in  $I_C^{RS}$  between 1300 nm and 1350 nm could be attributed to the contribution of the amorphous *n*-layer. In order to achieve a homogeneous crystallinity across the absorber layer, *SC* was stepwise adjusted during the growth of the intrinsic absorber layer, as shown in Fig. 5.6(b) (red solid line). The resulting Raman crystallinity depth profile is presented in Fig. 5.6(a) (red squares). The data shows that the *SC* profiling could effectively lead to a more even distribution (flattening) of the crystallinity over the entire cell thickness at a moderate  $I_C^{RS}$ . It is also evident in Fig. 5.6(a) that the approach to maintain a homogenous crystallinity could be applied in the case of any absorber layer thickness. Overall, with this adapted deposition process the efficiency of the solar cell was enhanced from 7.2 % to 7.8 %, along with a gain in  $V_{OC}$  of up to 20 mV. The detailed *j*-*V* characteristics are shown in Fig. 5.6(c), where both solar cells were made with an Ag back contact.

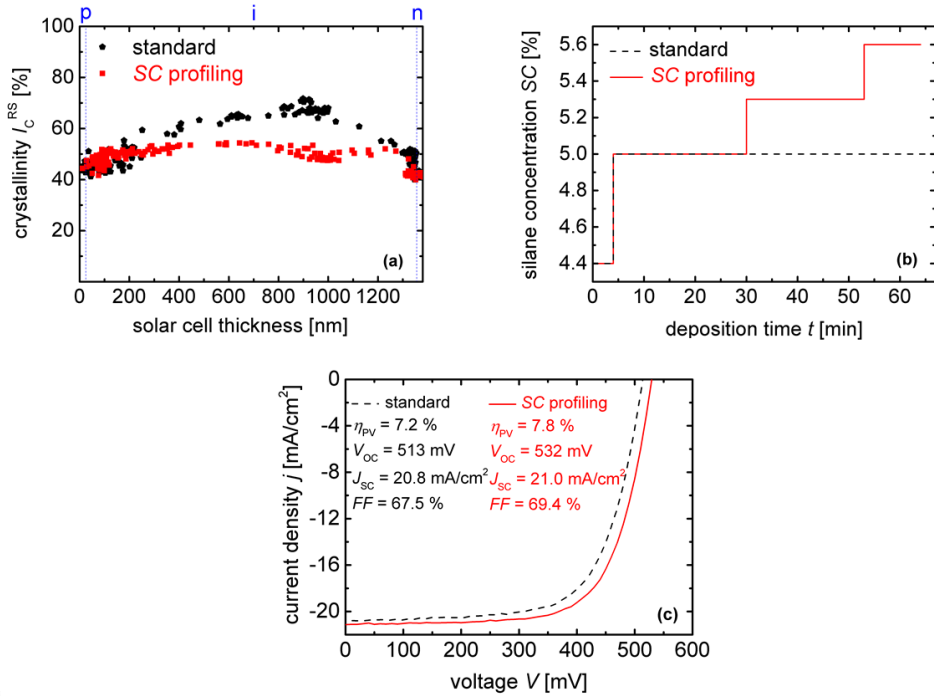


**Fig. 5.6** (a) Raman crystallinity depth profile of the  $\mu\text{c-Si:H}$  *pin* solar cell structure without profiling of the silane concentration  $SC$  (standard, black dots) and with profiling of the silane concentration  $SC$  ( $SC$  profiling, red squares) during the deposition of the 1300 nm thick intrinsic absorber layer, respectively. *n*- and *p*-type layers and the intrinsic 1300 nm thick absorber layer are indicated by the blue dashed lines. (b) Silane concentration  $SC$  profile of a standard (dotted black line) and adapted (red line) deposition process of an intrinsic  $\mu\text{c-Si:H}$  absorber layer. (c) Current density-voltage  $j$ - $V$  measurements of  $\mu\text{c-Si:H}$  solar cells (1300 nm thick absorber layers) deposited with a standard deposition process (dotted black curve) and a  $\mu\text{c-Si:H}$  solar cell deposited with a stepwise adapted  $SC$  profile of the intrinsic absorber layer (red curve). Both solar cells have a Ag back reflecting contact.

### Buffer layer incorporation

This section addresses the effects of an intrinsic amorphous buffer layer at the *n*-/*i*-interface on the performance of the  $\mu\text{c-Si:H}$  solar cell, as schematically shown in

Fig. 5.7(a). Similar approaches led to an increase in  $V_{OC}$  and efficiency [174, 176].

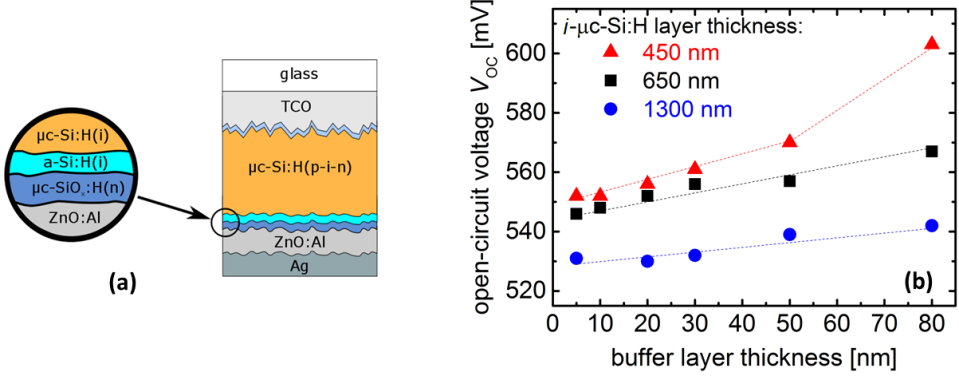


**Fig. 5.7** (a) Schematic drawing of the  $\mu\text{c-Si:H}$  solar cell with the incorporated  $n-i$  buffer layer. (b) Open-circuit voltage  $V_{OC}$  of  $\mu\text{c-Si:H}$  solar cells as a function of  $n-i$  buffer layer thickness (5, 10, 20, 30, 50, 80 nm) for different intrinsic  $\mu\text{c-Si:H}$  absorber layer thicknesses (blue circles: 1300 nm, black squares: 650 nm, red triangles: 450 nm). All absorber layers were deposited at  $SC = 5\%$ . The maximum error in the  $V_{OC}$  determination is below 5 mV.

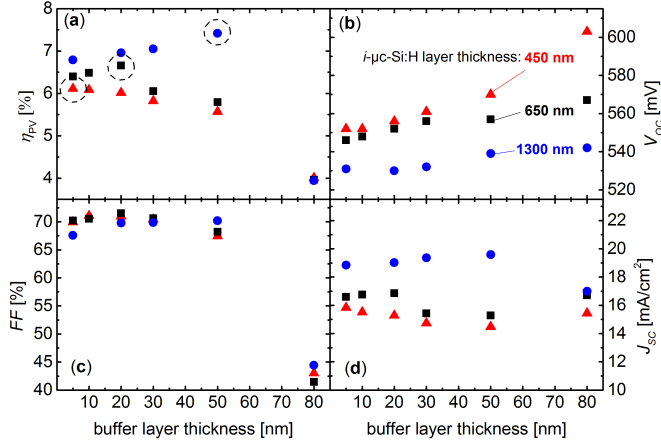
However, these studies have dealt with microcrystalline buffer layers at the  $p/i$ -interface, *i.e.* at the front side of the  $pin$  solar cell. The implementation of an intrinsic amorphous buffer layer after the  $p$ -layer at the  $p/i$ -interface would however hinder the crystalline growth of the subsequent intrinsic  $\mu\text{c-Si:H}$  absorber layer, which is why this concept was not applied in this work. Here, an amorphous buffer layer is deposited after the deposition of the intrinsic  $\mu\text{c-Si:H}$  absorber layer between the  $i$ - and the  $n$ -layer.  $n-i$  buffer layers<sup>3</sup> of different thicknesses were incorporated in solar cells with different absorber layer thicknesses. It is assumed that the buffer layer at the  $n/i$ -interface acts as a defect passivation layer and reduces interface recombination. Similar effects have been reported for silicon heterojunction solar cells [177, 178].

Fig. 5.7(b) shows the  $V_{OC}$  data as a function of the buffer layer thickness (5, 10, 20, 30, 50, 80 nm) for different  $\mu\text{c-Si:H}$  absorber layer thicknesses (1300 nm, 650 nm, 450 nm). The buffer layer thickness was estimated based on calculated deposition rate of the buffer layer, giving an error in thickness determination within  $\pm 10\%$ . The

<sup>3</sup>Deposited at 180 °C at  $SC$  of 10 %

silane concentration of 5 % and corresponding crystalline volume fraction were kept constant for all investigated  $\mu\text{c-Si:H}$  solar cells. It is apparent that  $V_{\text{OC}}$  increased with an increasing buffer layer thickness. Moreover, the effect of the buffer layer on the solar cell performance seems to increase with decreasing cell thickness, because the increase in  $V_{\text{OC}}$  was more pronounced for thinner cells. In this regard, it is known that the properties of the solar cell become more interface-sensitive when the cell thickness is reduced [41, 172, 176]. The 1300 nm thick solar cells exhibited a maximum  $V_{\text{OC}}$  of 540 mV. The 650 nm thick cells exhibited up to 568 mV, and 450 nm thick cells even promoted 603 mV.

Fig. 5.8 shows the photovoltaic parameters as a function of the buffer layer thickness for different  $\mu\text{c-Si:H}$  absorber layer thicknesses. As shown in Fig. 5.8, for



**Fig. 5.8** Photovoltaic parameters of  $\mu\text{c-Si:H}$  solar cells (conversion efficiency  $\eta_{\text{PV}}$  (a), open-circuit voltage  $V_{\text{OC}}$  (b), fill factor  $FF$  (c), short-circuit current density  $J_{\text{SC}}$  (d)) as a function of the buffer layer thickness for different  $\mu\text{c-Si:H}$  absorber layer thicknesses: 1300 nm (blue circles), 650 nm (black squares), and 450 nm (red triangles). Dotted circles indicate the optimal buffer layer thickness for the corresponding  $i\text{-}\mu\text{c-Si:H}$  layer thickness, in terms of  $V_{\text{OC}}$  and conversion efficiency  $\eta_{\text{PV}}$ .

solar cells with 80 nm thick buffer layers the conversion efficiency strongly decreased. This is mainly due to the poor fill factors. The  $J_{\text{SC}}$  was barely affected by increasing



the buffer layer thickness. Overall, the optimal buffer layer thickness, in terms of  $V_{OC}$  and efficiency could experimentally be identified for each particular solar cell thickness (see dotted circles in Fig. 5.8). The 1300 nm thick solar cell showed the best performance with a buffer layer thickness of 50 nm, the optimal buffer layer thickness for the 650 nm thick cell was 20 nm and a 5 nm buffer layer thickness exhibited the best performance in the 450 nm thick cell.

Fig. 5.9 summarises all presented routes discussed above and shows the photovoltaic conversion efficiency  $\eta_{PV}$ , fill factor  $FF$ , and short-circuit current density  $J_{SC}$  plotted versus  $V_{OC}$  for six series of depositions labeled "1300 nm", "650 nm", "450 nm", "1300 nm +  $SC$  profiling + buffer layer (50 nm)", "650 nm + buffer layer (20 nm)", and "450 nm + buffer layer (5 nm)". The range of  $j$ - $V$  values in each series were obtained by varying  $I_C^{RS}$ , *i.e.*  $SC$  at which the intrinsic absorber layer was deposited (see Fig. 5.5). The measured  $j$ - $V$  data of the best cell in terms of a high  $\eta_{PV}$  and a high  $V_{OC}$  ("best-cell") are stated in Table 5.1.

For the 1300 nm series (see ■ data points in Fig. 5.9),  $SC$  was varied between 4.4 % and 6.0 %. This resulted in a broad  $V_{OC}$  range of 490 mV to 620 mV, which was in agreement with the results shown in Fig. 5.5. The maximum solar energy conversion efficiency was obtained for  $V_{OC}$  of 528 mV,  $SC = 5.0$  % (see Table 5.1). Here, a further increase in the crystallinity, *i.e.* a decrease of  $SC$  to 4.4 %, did not lead to an increase of  $J_{SC}$  (see Fig. 5.9(b)). Consequently,  $\eta_{PV}$  slightly decreased along with  $FF$  and  $V_{OC}$ . In the range of  $V_{OC}$  values between 500 mV to 530 mV,  $J_{SC}$  continuously decreased from around 21 mA/cm<sup>2</sup> down to around 10 mA/cm<sup>2</sup> with an increasing  $SC$  from 5.0 % to 5.6 %. By increasing  $SC$ , the  $\mu c$ -Si:H material became more amorphous and therefore the photocurrent density decreased. As the fill factor only varied within a small range (see ■ data points for 500-530 mV in Fig. 5.9(c)) the conversion efficiency and photocurrent density trends in this data region resembled and suggest a sort of 'branching'. This behavior may result from the fact that in the  $SC$  range from 5.0 % to 5.6 %, the  $\mu c$ -Si:H material is highly sensitive, with respect to its crystallinity. In this  $SC$  regime, slight changes in  $SC$  during the growth of the  $i$ -layer can cause significant effects on the structural layer properties, including variations of the crystallinity over the entire  $i$ -layer thickness. As a consequence, the photovoltaic parameters, in particular  $J_{SC}$  and  $FF$  may also vary over a wide range for very slight changes in  $SC$  (and  $V_{OC}$ ). Hence,  $\eta_{PV}$  will also be affected in a similar way.

As can be suggested from Fig. 5.9, the  $SC$  profiling for the  $\mu c$ -Si:H cells (see □ data points) could attenuate the sensitivity of the material to some extend. Here,

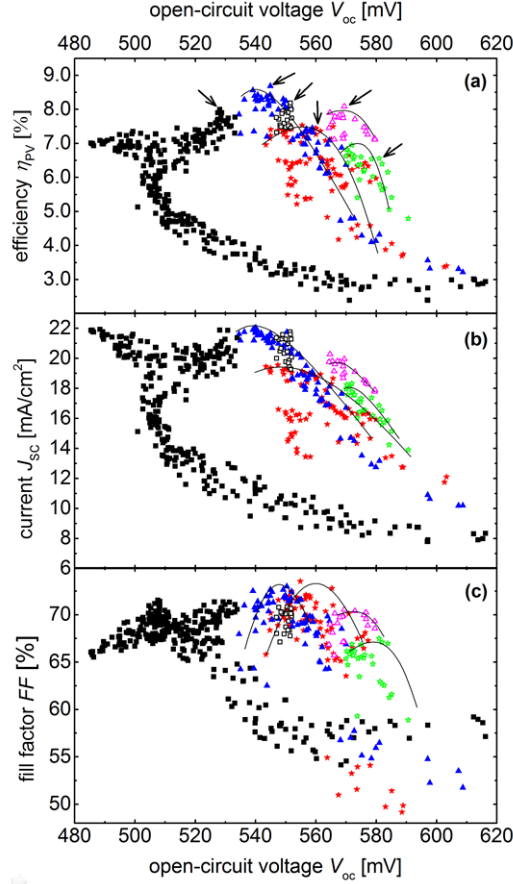


**Fig. 5.9** Solar cell parameters: (a) conversion efficiency  $\eta_{PV}$ , (b) short-circuit current density  $J_{SC}$ , and (c) fill factor  $FF$  vs. the open-circuit voltage  $V_{OC}$  in a 1300 nm (■), a 650 nm (▲), and a 450 nm thick  $\mu\text{c-Si:H}$  absorber layer series (★), in a 1300 nm thickness combined with the  $SC$  profiling and incorporated buffer layer (50 nm) series (□), in a 650 nm thickness combined with incorporated buffer layer (20 nm) series (△), and in a 450 nm thickness combined with incorporated buffer layer (5 nm) series (☆). The trends of the six series around the best-cell  $V_{OC}$  are indicated by solid lines as a guide to the eye. Table 5.1 summarises the best-cell parameters for the solar cells indicated by arrows in (a).

the results suggest that the  $\mu\text{c-Si:H}$  growth was stabilised and that the achieved moderate and constant crystallinity level (around 50 %) effectively increased the best-cell  $V_{\text{OC}}$  up to 551 mV along with an increased conversion efficiency from 8.0 % to 8.2 % (see Table 5.1). Please note that for this series also a buffer layer of 50 nm thickness was implemented.

In the 530 mV to 620 mV region for the standard 1300 nm series (see ■ data points),  $SC$  was varied between 5.6 % and 6.0 %, inducing a largely amorphous growth of the absorber layer, which was confirmed by the strong increase in  $V_{\text{OC}}$ . The  $J_{\text{SC}}$  data remained at low values between 10 mA/cm<sup>2</sup> to 8 mA/cm<sup>2</sup> and  $FF$  strongly decreased down to 55 %, indicating a reduction in the electronic quality of the material (see Fig. 5.9(b) and (c), respectively).

The 650 nm (see ▲ data points in Fig. 5.9) and 450 nm series (see ★ data points in Fig. 5.9) depict the photovoltaic parameters for decreased absorber layer thicknesses. Compared to the 1300 nm series, both series showed increased best-cell  $V_{\text{OC}}$  values of 545 mV for the 650 nm and 565 mV for the 450 nm series (see Table 5.1).  $J_{\text{SC}}$  and  $FF$  were less affected (see Fig. 5.9(b) and (c), respectively) relative to the 1300 nm series. Best-cell efficiencies of 8.6 % and 7.5 % were achieved for the 650 nm and the 450 nm series, respectively (see Table 5.1).

The 650 nm thin solar cells with an incorporated 20 nm buffer layer (see △ data points in Fig. 5.9) exhibited a best-cell  $V_{\text{OC}}$  of 570 mV with 8.1 % conversion efficiency (see Table 5.1).

The highest best-cell  $V_{\text{OC}}$  of 580 mV was promoted by the 450 nm thin solar cells with a 5 nm buffer layer incorporated (see ☆ data points in Fig. 5.9). However, the light absorption of this very thin cells was rather low, which is in agreement with a reduced  $J_{\text{SC}}$  of 17 mA/cm<sup>2</sup> and a conversion efficiency of 6.7 % (see Table 5.1).

Overall, the results indicate that the implementation of the concepts described above can lead to an increase of the open-circuit voltage in single junction  $\mu\text{c-Si:H}$  solar cells without a significant deterioration of the other  $j$ - $V$  characteristics. Compared to a chosen reference cell with 8.0 % efficiency and 528 mV as  $V_{\text{OC}}$ , the presented optimisation routes ( $SC$  profiling, thickness reduction, and buffer layer incorporation) increased  $\eta_{\text{PV}}$  and  $V_{\text{OC}}$  of the 1300 nm thick cells to 8.2 % and 551 mV, respectively, and for the 650 nm cells to 8.1 % and even 570 mV, respectively. The 450 nm thick cells with 6.7 % efficiency provided the highest  $V_{\text{OC}}$  of 580 mV. The results furthermore show that  $V_{\text{OC}}$  of  $\mu\text{c-Si:H}$  solar cells can be increased in small approx. 10 mV steps, which may be of interest for devices where the required

voltage values need to be precisely adjusted within a small range. As will be shown in Chapter 6, integrated water splitting systems represent an example of such devices.

**Table 5.1** Photovoltaic parameters of the best-cell  $\mu\text{c-Si:H}$  devices from Fig. 5.9. The deposition parameters of the fabricated solar cells regarding the thicknesses of the absorber layer, the application of a  $SC$  profiling, and the incorporation of buffer layers at various thicknesses are listed.

Symbol	$\eta_{\text{PV}}$ [%]	$V_{\text{OC}}$ [mV]	$FF$ [%]	$J_{\text{SC}}$ [mA/cm <sup>2</sup> ]	Absorber layer thickness [nm]	$SC$ profiling	Buffer layer thickness [nm]
■	8.0	528	71.3	22.0	1300	w/o	w/o
▲	8.6	545	72.6	21.6	650	w/o	w/o
★	7.5	565	72.8	18.2	450	w/o	w/o
□	8.2	551	70.7	21.8	1300	with	50
△	8.1	570	70.6	20.1	650	w/o	20
☆	6.7	580	67.7	17.0	450	w/o	5

## 5.4 Tandem junction solar cells

In order to achieve sufficiently high open-circuit voltages to drive the water splitting reactions without an additional external bias, the developed single junction solar cells need to be combined and employed in multijunction solar cells. In the best case, the photovoltages of the single junction solar cells nearly sum up in the tandem configuration. Therefore, this section focuses on the development of high photovoltage a-Si:H/ $\mu\text{c-Si:H}$  and a-Si:H/a-Si:H tandem junction solar cells based on the integration of the herein developed single junction solar cells.

### 5.4.1 a-Si:H/ $\mu\text{c-Si:H}$ tandem junction solar cells

The optimised high open-circuit voltage  $\mu\text{c-Si:H}$  solar cells from the "1300 nm +  $SC$  profiling + buffer layer (50 nm)", "650 nm + buffer layer (20 nm)", and "450 nm +

buffer layer (5 nm)” series were subsequently utilised as bottom cells in a-Si:H/ $\mu$ c-Si:H tandem junction solar cells<sup>4</sup>. As a reference bottom cell, the ”1300 nm” series was used. Various combinations of the top and bottom cells, along with corresponding absorber layer parameters and photovoltaic device parameters ( $\eta_{PV}$ ,  $V_{OC}$ ,  $FF$ ,  $J_{SC}$ ) are listed in Table 5.2. The a-Si:H top cell was deposited at 130 °C with  $SC = 4\%$  (see 5.2.2). The respective thicknesses are also listed in Table 5.2.

**Table 5.2** Photovoltaic parameters of a-Si:H/ $\mu$ c-Si:H tandem junction solar cells fabricated with different series of  $\mu$ c-Si:H bottom cells and a-Si:H top cells for different silane concentrations  $SC$  and thicknesses. The corresponding current density-voltage measurements are depicted in Fig. 5.10.

Tandem cell	$\mu$ c-Si:H bottom cell		a-Si:H top cell		$\eta_{PV}$ [%]	$V_{OC}$ [mV]	$FF$ [%]	$J_{SC}$ [mA/cm <sup>2</sup> ]	$V_{MPP}$ [mV]	$J_{MPP}$ [mA/cm <sup>2</sup> ]
	Series	$SC$ [%]	Thick- ness [nm]	$SC$ [%]						
A	1300 nm	5	400	4.0	10.9	1390	72.3	10.8	1115	9.6
B	1300 nm + $SC$ profiling + buffer layer (50 nm)	5	400	4.0	10.5	1474	65.6	10.9	1184	8.9
C	650 nm + buffer layer (20 nm)	5.3	250	4.0	11.0	1504	73.0	10.0	1255	8.7
D	450 nm + buffer layer (5 nm)	5.3	150	4.0	9.7	1515	76.2	8.4	1259	7.5

The maximum power point (MPP) voltage and photocurrent density values,  $V_{MPP}$  and  $J_{MPP}$ , respectively, are also included in Table 5.2 for all tandem cells. The corresponding  $j$ - $V$  characteristics are presented in Fig. 5.10. As can be deduced from the data in Table 5.2, the optimisation of the  $\mu$ c-Si:H bottom cell effectively led to an increase in  $V_{OC}$  and  $V_{MPP}$  compared to the reference 1300 nm series (cell A). For the cell B and the cell D, however, the  $FF$  and the  $J_{SC}$ , respectively, decreased, which led to a lower conversion efficiency in both cases compared to the reference cell A. The combination of the  $SC$  profiling concept and the buffer layer incorporation in the 1300 nm series (cell B) led to an increase in  $J_{SC}$  and  $V_{OC}$  of 0.1 mA/cm<sup>2</sup> and 80 mV, respectively. However, the fill factor of this tandem cell decreased to 65.6 %, resulting in 1184 mV for  $V_{MPP}$  and an overall conversion efficiency of 10.5 %. For the 650 nm series with the incorporated buffer layer (cell C) the efficiency was maintained at

<sup>4</sup>The results presented in this section were published in F. Urbain *et al.*, J. Mater. Res. **29** (2014), 2605-2614 [40].

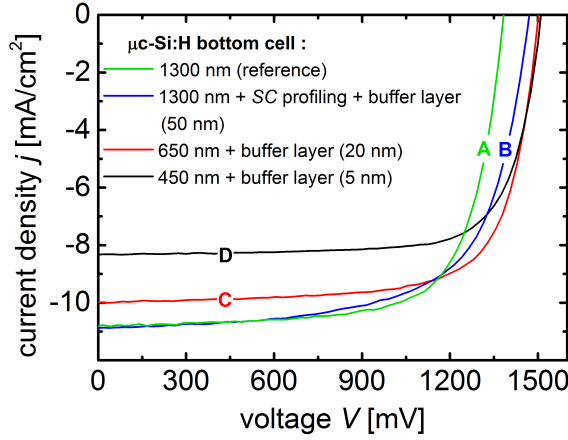


**Fig. 5.10** Current density-voltage  $j$ - $V$  measurements of a-Si:H/ $\mu$ c-Si:H tandem solar cells with different  $\mu$ c-Si:H bottom cells: "1300 nm" reference series (cell A, green curve), "1300 nm + SC profiling + buffer layer (50 nm) series" (cell B, blue curve), "650 nm + buffer layer (20 nm)" series (cell C, red curve), and "450 nm + buffer layer (5 nm)" series (cell D, black curve).

11.0 % along with a 100 mV increase in both,  $V_{OC}$  and  $V_{MPP}$ , compared to the cell A. The total thickness of this tandem cell was below 1  $\mu$ m. The tandem cell, with the 450 nm thin bottom cell with incorporate buffer layer (cell D) exhibited the highest  $V_{OC}$  and  $FF$  values. However, due to the decreased thickness of the sub cells (total tandem cell thickness was only 700 nm),  $J_{SC}$  and  $\eta_{PV}$  decreased.

In summary, this investigation proved the successful integration of single junction solar cells in tandem devices, because the voltages nearly added up (compare with the single junction cells presented in Section 5.2.2 and in Table 5.1). The tandem junction cell C exhibited the best high voltage/high current tradeoff and provided a high  $J_{MPP}$  of 8.7 mA/cm<sup>2</sup> along with the highest  $V_{MPP}$  of 1255 mV. Furthermore, this tandem cell had a total thickness below 1  $\mu$ m, accentuating its low-cost production and high stability against light induced degradation, as will be shown in Section 5.6.

The quantum efficiency measurements for the a-Si:H/ $\mu$ c-Si:H tandem solar cell series (same as in Table 5.2 and Fig. 5.10) are presented in Fig. 5.11. When the top and bottom cell thickness were decreased, the photocurrent densities of the top and bottom cell,  $J_{QE,top}$  and  $J_{QE,bot}$ , decreased while  $V_{OC}$  increased (see Table 5.2

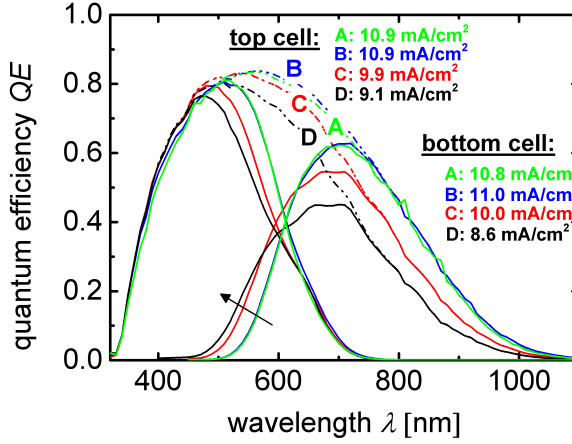


**Fig. 5.11** Quantum efficiency measurements of the four a-Si:H/ $\mu$ c-Si:H tandem junction solar cells from Table 5.2. Letter A denotes the "1300 nm" reference series (green curves), B the "1300 nm + SC profiling + buffer layer (50 nm) series" (blue curves), C the "650 nm + buffer layer (20 nm)" series (red curves), and D the "450 nm + buffer layer (5 nm)" series (black curves). The photocurrent densities of the top and bottom cell,  $J_{QE,top}$  and  $J_{QE,bot}$  are depicted in the figure. Arrow indicates the trend of increasing bottom cell QE in the wavelength range between 400 and 600 nm with decreasing  $\mu$ c-Si:H absorber layer thickness. Top and bottom cell photocurrent densities calculated from the QE curves are placed near the related measurements.

and Fig. 5.10). As the reduction of the top cell thickness is accompanied with a higher transparency, more light can enter the bottom cell. This was confirmed by the increase of the bottom cell QE in the wavelength range between 400 nm and 600 nm with a decreasing  $\mu$ c-Si:H absorber layer thickness (indicated by the arrow in Fig. 5.11). This might explain the relatively high photocurrent density of the tandem cell B of 10.0 mA/cm<sup>2</sup> with the 650 nm bottom cell compared to the tandem cell A with the 1300 nm bottom cell, *i.e.* with twice the thickness, which provided only a little higher photocurrent density of 10.8 mA/cm<sup>2</sup>.

### 5.4.2 a-Si:H/a-Si:H tandem junction solar cells

The foregoing a-Si:H/ $\mu$ c-Si:H tandem solar cells provided a maximum  $V_{OC}$  of 1.5 V. It will be shown in this work that 1.5 V is not sufficient in order to run the water electrolysis efficiently without an additional external bias. Nevertheless, the developed  $\mu$ c-Si:H cells were also used as sub cells in triple and quadruple junction cells, as will be shown in Section 5.5. The results on the application of the developed solar cells in PV-EC devices will be shown in Chapter 6. As an alternative to the a-Si:H/ $\mu$ c-Si:H tandems, the a-Si:H/a-Si:H cells, combining two high voltage single junction a-Si:H cells with low-temperature fabricated absorber layers (see Section 5.2), can be applied as high voltage tandem solar cells for water splitting.

Several tandem junction combinations of two a-Si:H single junction solar cells were realised<sup>5</sup>. The single junction solar cells for the top and the bottom cells were chosen based on the results presented in Section 5.2.2. The top and bottom cell combinations, along with the absorber layer parameters ( $SC$  and  $T_s$ ) and the photovoltaic device parameters are listed in Table 5.3. The a-Si:H bottom cell thickness was 400 nm and the top cell thickness was varied between 90 nm and 110 nm, respectively.

**Table 5.3** Photovoltaic parameters of a-Si:H/a-Si:H tandem junction solar cells fabricated with varying  $SC$  and  $T_s$  of top and bottom cell based on the results from Fig. 5.3.

Tandem cell	Top cell		Bottom cell		$\eta_{PV}$ [%]	$V_{OC}$ [mV]	$FF$ [%]	$J_{SC}$ [mA/cm <sup>2</sup> ]	$V_{MPP}$ [mV]	$J_{MPP}$ [mA/cm <sup>2</sup> ]
	$SC_{top}$ [%]	$T_{S,top}$ [°C]	$SC_{bot}$ [%]	$T_{S,bot}$ [°C]						
250/250	4	250	4	250	8.3	1602	71.8	7.2	1325	6.2
180/250	10	180	4	250	8.7	1700	68.5	7.4	1410	6.2
110/110	4	110	4	110	9.5	1870	77.5	6.6	1580	6.2
180/180	10	180	10	180	9.8	1796	78.8	7.0	1555	6.5
130/180	4	130	10	180	11.3	1806	74.2	8.4	1510	7.4
130/130	4	130	4	130	10.9	1913	74.0	7.7	1595	6.8

<sup>5</sup>The results presented in this section are based on the tandem cell development performed by K. Wilken [98] with additional optimisation of certain devices by the present author. The results were published in F. Urbain, K. Wilken *et al.*, Int. J. Photoenergy **2014** (2014), 249317 [85] and in F. Urbain, *et al.*, Chem. Phys. Lett. **638** (2015), 25-30 [179].



As presented in Section 5.2.2, the developed a-Si:H single junction cells provided a  $V_{OC}$  range between 800 mV and 950 mV (see Fig. 5.3). The data in Table 5.3 confirm that with the combination in tandem solar cells an even extended range of high open-circuit voltages was achieved, ranging from 1601 mV to 1913 mV. Similar to the results in the foregoing Section 5.4.1, the  $V_{OC}$  values of the tandem solar cells were in good agreement with the summed  $V_{OC}$  values of the respective individual sub cells (see Fig. 5.3), proving that the combination of single cells was successful. As already noted,  $J_{MPP}$  and  $V_{MPP}$  play an important role here and are presented in the last column of Table 5.3. The highest  $V_{MPP}$  and the highest  $V_{OC}$  of 1595 mV and 1913 mV, respectively, were achieved by the tandem cell combining two sub cells with an  $SC$  of 4 % and both top and bottom cell substrate temperatures  $T_{S,top}$  and  $T_{S,bot}$  of 130 °C (the tandem cell will be denoted as "a-Si:H/a-Si:H (130/130)" hereafter). For this tandem cell the bottom cell was 400 nm thick and the top cell had a thickness of 90 nm. The tandem cell consisting of a 4 %  $SC$  top cell (110 nm thick) with  $T_{S,top} = 130$  °C and a 10 %  $SC$  bottom cell (400 nm thick) with 180 °C for  $T_{S,bot}$ , exhibits the highest  $J_{SC}$  value of 8.4 mA/cm<sup>2</sup> and an  $\eta_{PV}$  of 11.3 % (the tandem cell will be denoted as "a-Si:H/a-Si:H (130/180)" hereafter).

The quantum efficiency measurements of the two best efficiency a-Si:H/a-Si:H tandem junction solar cells (cells 130/180 and 130/130 from Table 5.3) are presented in Fig. 5.12. As can be deduced from Fig. 5.12 both tandem solar cells were current-matched as in both cases the top and the bottom cell photocurrent densities are very similar.

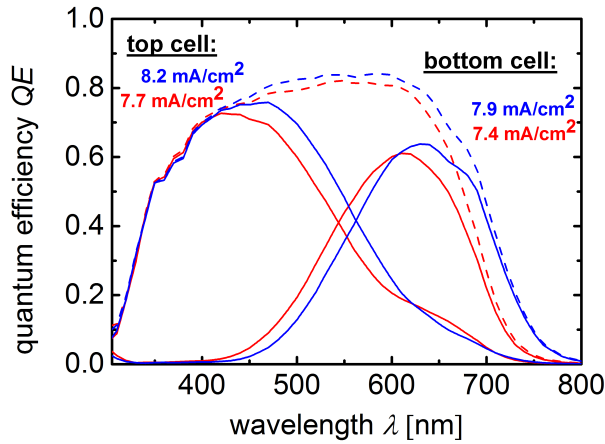


**Fig. 5.12** Quantum efficiency measurements of the 130/180 and of the 130/130 a-Si:H/a-Si:H tandem junction solar cells from Table 5.3, respectively. The photocurrent densities of the top and bottom cell,  $J_{QE,top}$  and  $J_{QE,bot}$  are calculated from the  $QE$  curves and placed near the related measurements.

## 5.5 Triple and quadruple junction solar cells

To extend the range of achievable photovoltages for the application in water splitting devices, triple and quadruple junction solar cells were developed<sup>6</sup>. Higher tunable photovoltages foster a higher flexibility in choosing different catalyst materials with different overpotential requirements in PV-EC configurations. Based on the results on a-Si:H and  $\mu$ c-Si:H absorber layers presented in Sections 5.2 and 5.3, respectively, this section exploits ways to improve the device efficiency in combination with high  $V_{OC}$  ranging from 2.0 V to 2.8 V. Due to requirements on the optical gap energy sequence, the top and bottom cell absorber layers were made of a-Si:H (high optical gap) and  $\mu$ c-Si:H, respectively, for all investigated multijunctions. For the middle cell absorber layers in triple junction solar cells either a-Si:H (lower optical gap) or  $\mu$ c-Si:H were applied, which leads to different voltage and current matching conditions and represents the two development paths discussed below.

<sup>6</sup>The results presented in this section were published in F. Urbain *et al.*, Energy Environ. Sci. **9** (2016), 145-154 [144] and in F. Urbain, *et al.*, Sol. Energy. Mat. Sol. Cells **145** (2016), 142-147 [39].

### 5.5.1 a-Si:H/ $\mu$ c-Si:H/ $\mu$ c-Si:H

The target for the a-Si:H/ $\mu$ c-Si:H/ $\mu$ c-Si:H triple junction solar cells was to achieve higher  $V_{OC}$  values than state-of-the-art a-Si:H/a-Si:H tandem junctions, *i.e.* above 1.9 V. For the top cell absorber layer a high optical gap a-Si:H material ( $1.95 \text{ eV} \pm 25 \text{ meV}$ ) was chosen to increase the light incoupling and the open-circuit voltage [85]. Furthermore,  $V_{OC}$  was increased by integrating nominally identical thin intrinsic a-Si:H buffer layers at the  $n$ -/ $i$ -interface of the  $\mu$ c-Si:H sub cells, in order to adjust the open-circuit voltage in a small range (see Section 5.3). To evaluate the different routes, three different types of a-Si:H/ $\mu$ c-Si:H/ $\mu$ c-Si:H cells were investigated (referred to as T1-T3):

- a reference cell without  $n$ - $i$  buffer layer (T1),
- the same cell as T1, but with 30 nm  $n$ - $i$  buffer layer for the bottom cell (T2),
- the same cell as T1 with a 30 nm  $n$ - $i$  buffer layer for the bottom and a 20 nm  $n$ - $i$  buffer layer for the middle cell (T3).

Table 5.4 summarises the performance of these triple junction cells, including layer preparation and PV parameters of the solar cells.

**Table 5.4** Overview of all relevant layer preparation and PV parameters ( $V_{OC}$ ,  $J_{SC}$ ,  $FF$ , and efficiency  $\eta_{PV}$ ) of a-Si:H/ $\mu$ c-Si:H/ $\mu$ c-Si:H devices.

Triple cell	$n$ - $i$ buffer layer	$\eta_{PV}$ [%]	$V_{OC}$ [mV]	$FF$ [%]	$J_{SC}$ [mA/cm <sup>2</sup> ]	$V_{MPP}$ [mV]	$J_{MPP}$ [mA/cm <sup>2</sup> ]
T1	w/o	11.1	1895	70.8	8.3	1602	6.8
T2	bottom	11.1	1958	68.1	8.3	1596	6.9
T3	bottom and middle	11.2	1976	67.6	8.4	1594	7.1

The sub cells had a thickness of 160 nm for the top, 1200 nm for the middle, and 1600 nm for the bottom cell. As presented in Table 5.4, the integration of intrinsic a-Si:H buffer layers at the  $\mu$ c-Si:H  $n$ -/ $i$ -interfaces led to an increase in  $V_{OC}$  by around 60 mV for one buffer layer (T2) and around 80 mV to 1976 mV for two buffer layers (T3), along with a slight decrease in  $FF$ . Although the voltage at the MPP was around 1.6 V for all cells, the photocurrent density at the MPP was increased by approx.  $0.3 \text{ mA/cm}^2$  from the cell T1 to T3. This result exemplarily demonstrated

that the open-circuit voltage can be increased very systematically within a small voltage range. However, in order to increase  $V_{\text{MPP}}$ , the fill factor of the tripe cells needs to be improved as well. Here, further investigations are required. As will be shown in Chapter 6, high adjustable photovoltages and photocurrents near the MPP of the solar cell are relevant in particular for water splitting applications, where the required PV performance strongly depends on the specific requirements of the chosen catalyst materials.

Fig. 5.13 depicts the quantum efficiency measurement of the triple junction cell T3. The  $QE$  data showed that all sub cells had very similar photocurrent densities of  $8.0 \text{ mA/cm}^2$ ,  $8.2 \text{ mA/cm}^2$ , and  $8.3 \text{ mA/cm}^2$  as presented in Fig. 5.13. These

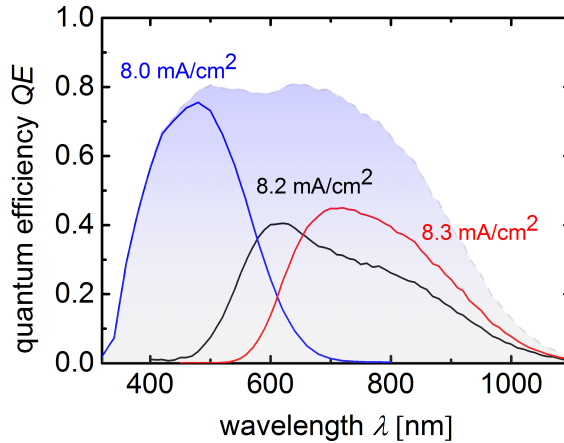


**Fig. 5.13** Quantum efficiency curves of a a-Si:H/ $\mu$ c-Si:H/ $\mu$ c-Si:H triple junction device corresponding to cell T3 from Table 5.4. Sub cell photocurrent densities calculated from the  $QE$  curves are placed near the related measurements and the total  $QE$  is displayed by the blue shaded area.

values were slightly lower than the  $J_{\text{SC}}$  value quoted in Table 5.4, where an anti-reflection foil was additionally used during  $j$ - $V$  measurements. From the total  $QE$  photocurrent density (shaded in blue) a slight dip between 500 nm and 650 nm was visible, which corresponds to reflection losses at the intermediate reflecting/absorber layer interface.

### 5.5.2 a-Si:H/a-Si:H/ $\mu$ c-Si:H

The aim of the a-Si:H/a-Si:H/ $\mu$ c-Si:H triple junction cells was the further expansion of the  $V_{OC}$  range beyond the values obtained with the a-Si:H/ $\mu$ c-Si:H/ $\mu$ c-Si:H cells to around 2.3 V. Additional emphasis was put on the matching of the photocurrent densities of the individual sub cells. Balanced and enhanced sub cell photocurrent densities were achieved by varying the sub cell thicknesses and by introducing a thicker  $n$ -type  $\mu$ c-SiO<sub>x</sub>:H intermediate reflecting (IR) layer after the a-Si:H middle cell [124, 125, 180]. The latter ensured that more short wavelength light was reflected back into the two (top and middle) a-Si:H sub cells. Similar to the a-Si:H/ $\mu$ c-Si:H/ $\mu$ c-Si:H, this triple cell type used the same wide optical gap a-Si:H top cell absorber layer ( $1.95 \text{ eV} \pm 25 \text{ meV}$ ). For the middle cell, an a-Si:H absorber layer with lower optical gap ( $1.91 \text{ eV} \pm 25 \text{ meV}$ ) was applied. Three different a-Si:H/a-Si:H/ $\mu$ c-Si:H devices were compared (referred to as T4-T6):

- a reference solar cell prepared without  $\mu$ c-SiO<sub>x</sub>:H IR layer (T4),
- a cell with a  $\mu$ c-SiO<sub>x</sub>:H IR layer (T5), and
- the same cell as T5, but with adapted sub cell thicknesses such that a balanced maximum photocurrent density level was provided by each sub cell (T6).

The experimental data of the triple junction cells, in terms of the  $QE$  measured photocurrent densities of each individual sub cell, the layer preparation (including layer thicknesses) and the PV parameters are presented in Table 5.5.

**Table 5.5** Overview of all relevant layer preparation and PV parameters ( $V_{OC}$ ,  $J_{SC}$ ,  $FF$ , and efficiency  $\eta_{PV}$ ) of a-Si:H/a-Si:H/ $\mu$ c-Si:H devices.

Triple cell	$\mu$ c-SiO <sub>x</sub> :H IR layer	$J_{QE,top}$ [mA/cm <sup>2</sup> ] ( $i$ -layer thickness) [nm]	$J_{QE,mid}$ [mA/cm <sup>2</sup> ] ( $i$ -layer thickness) [nm]	$J_{QE,bot}$ [mA/cm <sup>2</sup> ] ( $i$ -layer thickness) [nm]	$\eta_{PV}$ [%]	$V_{OC}$ [mV]	$FF$ [%]	$J_{SC}$ [mA/cm <sup>2</sup> ]	$V_{MPP}$ [mV]	$J_{MPP}$ [mA/cm <sup>2</sup> ]
T4	w/o	7.3 (80)	6.8 (400)	7.4 (1200)	12.8	2269	72.3	7.8	1859	6.9
T5	with	7.4 (80)	7.1 (400)	7.4 (1200)	13.4	2272	71.2	8.3	1860	7.1
T6	with (matched)	7.6 (90)	7.3 (700)	7.6 (1800)	13.6	2279	69.2	8.6	1851	7.4

Again, the  $J_{SC}$  values were higher compared to the  $J_{QE}$  values measured from the  $QE$  measurements because an anti-reflection foil was used for the  $j$ - $V$  measurement.

The integration of the  $\mu\text{c-SiO}_x\text{:H}$  IR layer significantly enhanced  $J_{\text{SC}}$  from  $7.8 \text{ mA/cm}^2$  (cell T4) to  $8.3 \text{ mA/cm}^2$  (cell T5), mainly due to the increase of the middle cell photocurrent density from  $6.8 \text{ mA/cm}^2$  to  $7.1 \text{ mA/cm}^2$ . The current-matched cell T6 provided the highest  $J_{\text{SC}}$  value of  $8.6 \text{ mA/cm}^2$  and  $2279 \text{ mV}$  in  $V_{\text{OC}}$ . This shows that the presented approach resulted in an increase of  $0.8 \text{ mA/cm}^2$  and  $10 \text{ mV}$  relative to cell T5. The good current matching for cell T6 also resulted in a slightly decreased fill factor, which is expected for current-matched sub cells [181]. The quantum efficiency measurement of cell T6 is shown in Fig. 5.14.

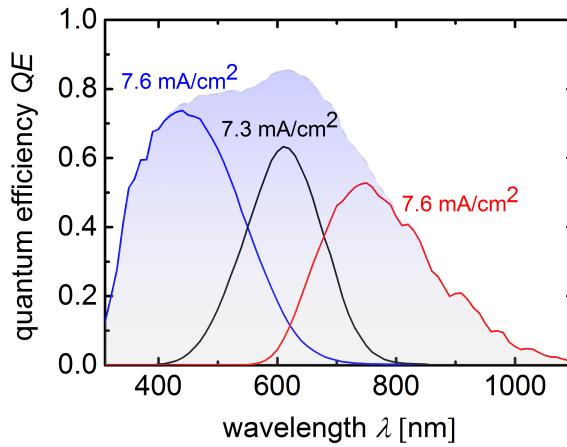


**Fig. 5.14** Quantum efficiency curves of a  $\text{a-Si:H/a-Si:H}/\mu\text{c-Si:H}$  triple junction device corresponding to cell T6 from Table 5.5. Sub cell photocurrent densities calculated from the  $QE$  curves are placed near the related measurements. The blue shaded area displays the total  $QE$  of the triple junction solar cell.

Overall, an efficiency of  $13.6 \%$  was obtained along with  $1851 \text{ mV}$  in  $V_{\text{MPP}}$  and with  $7.4 \text{ mA/cm}^2$  in  $J_{\text{MPP}}$ . Accordingly, in the PV-EC device configuration, the overpotential losses can be in the range of  $600 \text{ mV}$  ( $1.85 \text{ V} - 1.23 \text{ V}$ ) in order to operate the device near its maximum power point. In fact, these overpotential values lie close to the HER and OER overpotentials for state-of-the-art precious metal catalyst materials [21, 182]. The application of the multijunction solar cells in integrated water splitting device will be discussed in Chapter 6.

### 5.5.3 a-Si:H/a-Si:H/ $\mu$ C-Si:H/ $\mu$ C-Si:H

To increase the flexibility in choosing catalyst materials for water splitting, a large photovoltage ( $> 2.3$  V) is necessary. In particular, earth-abundant and non-precious metal catalysts, which usually are catalytically less active, require photovoltages over 800 mV, *i.e.* photovoltages of over 2.0 V at the MPP [182]. Open-circuit voltages of 2.8 V are feasible and were recently shown for quadruple junction solar cells [183–185]. In contrast to intrinsic a-SiO<sub>x</sub>:H used as top cell absorber layer [184] or a-SiGe:H used as middle cell absorber material [183], herein the aforementioned wide optical gap intrinsic a-Si:H material as top cell and the low optical gap a-Si:H material as middle cell absorber layers were applied. A  $\mu$ C-SiO<sub>x</sub>:H IR layer between the middle a-Si:H and the first  $\mu$ C-Si:H sub cell was integrated, as already presented in the previous Section 5.5.2. In order to match the sub cells in terms of the highest possible photocurrent density, the thicknesses of each cell were systematically adjusted.

Table 5.6 presents an overview of the absorber layer thicknesses for the three investigated quadruple solar cells, referred to as Q1-Q3. The intrinsic a-Si:H top cell absorber layer was the same as for the triple junction solar cells and had an optical gap energy of  $1.95 \text{ eV} \pm 25 \text{ meV}$ , while the a-Si:H middle cell 1 absorber layer had a lower optical gap energy ( $1.91 \text{ eV} \pm 25 \text{ meV}$ ). The  $\mu$ C-Si:H middle cell 2 and bottom cell were deposited at the same *SC* and only the thicknesses were varied, as indicated in Table 5.6. The respective initial photovoltaic parameters, as well as the sub cell photocurrent densities evaluated by means of *QE* measurements of the quadruple junction solar cells are also presented in Table 5.6. Note that for all photocurrent density values presented in Table 5.6, the  $J_{\text{SC}}$  values are slightly higher than the limiting sub cell photocurrent densities (evaluated by means of *QE* measurements) mainly because an anti-reflection foil was additionally used during *j-V* measurements.

The quadruple junction cell Q1 provided a high  $V_{\text{OC}}$  of 2775 mV. However, the current mismatch in the middle 1 and middle 2 sub cell (6.7 and 5.8 mA/cm<sup>2</sup>, respectively) was evident. The high fill factor value of 71.7 % may partly result from the non-optimised current matching in this cell [181]. The photocurrent density of the middle 2  $\mu$ C-Si:H sub cell limited the overall short-circuit current density ( $J_{\text{SC}}$ ) to 6.4 mA/cm<sup>2</sup>. The adjustment of the sub cell thicknesses in the solar cell Q2 led to a more even distribution of the total photocurrent between the sub cells, as can be concluded from the  $J_{\text{QE}}$  values in Table 5.6. The slight increase in the total  $J_{\text{SC}}$  and the reduction in the fill factor were in line with the *QE* evaluation. Nevertheless, the first  $\mu$ C-Si:H sub cell (middle 2) limited the overall photocurrent density for

**Table 5.6** Overview of the intrinsic sub cell absorber layer thicknesses of three investigated quadruple junction solar cells, referred to as Q1-Q3, based on a-Si:H and  $\mu\text{c-Si:H}$ . Additionally, the sub cell photocurrent densities (based on  $QE$  measurement without anti-reflection foil), and initial photovoltaic parameters of a-Si:H/a-Si:H/ $\mu\text{c-Si:H}$ / $\mu\text{c-Si:H}$  quadruple junction solar cells (based on illuminated  $j$ - $V$  measurements with anti-reflection foil) are presented.

	cell Q1	cell Q2	cell Q3
Top cell thickness [nm]	80	80	80
$J_{QE,top}$ [mA/cm <sup>2</sup> ]	6.3	6.3	6.6
Middle cell 1 thickness [nm]	700	550	400
$J_{QE,mid1}$ [mA/cm <sup>2</sup> ]	6.7	6.4	6.2
Middle cell 2 thickness [nm]	1800	2000	1600
$J_{QE,mid2}$ [mA/cm <sup>2</sup> ]	5.8	6.0	6.2
Bottom cell thickness [nm]	2700	2700	2300
$J_{QE,bot}$ [mA/cm <sup>2</sup> ]	6.4	6.3	6.3
$\eta_{PV}$ [%]	12.7	12.4	13.2
$V_{OC}$ [mV]	2775	2779	2802
$FF$ [%]	71.7	67.9	69.8
$J_{SC}$ [mA/cm <sup>2</sup> ]	6.4	6.5	6.9
$V_{MPP}$ [mV]	2253	2231	2278
$J_{MPP}$ [mA/cm <sup>2</sup> ]	5.6	5.5	5.8

Q1 and Q2. For the cell Q3, the thickness of the middle a-Si:H sub cell was reduced to provide more light in the wavelength range between 500 nm and 700 nm for the  $\mu\text{c-Si:H}$  middle cell. Additionally, a reduction in the absorber layer thickness of the bottom cell resulted in a current transfer from the bottom to the middle sub cells. Thereby, the photocurrent density of the middle 2  $\mu\text{c-Si:H}$  sub cell was increased. This enabled a good overall current matching, as also apparent in Fig. 5.15, showing the  $QE$  measurement of the cell Q3.

The quadruple cell provided a short-circuit current density  $J_{SC}$  of 6.9 mA/cm<sup>2</sup> with an efficiency of 13.2 %. Due to the reduced thickness of both  $\mu\text{c-Si:H}$  absorber layers,  $V_{OC}$  was also slightly increased by around 25 mV up to 2802 mV. In conclusion, the successful optimisation of the absorber layer thicknesses for the cell Q3 is all the more demonstrated, as  $J_{SC}$  was increased by decreasing the total cell thickness (compare with Table 5.6). Additionally, a reduced total thickness might lead to an



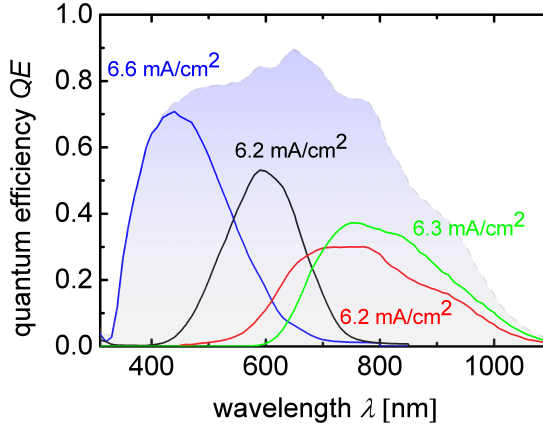


**Fig. 5.15** Quantum efficiency curves of the a-Si:H/a-Si:H/ $\mu$ c-Si:H/ $\mu$ c-Si:H quadruple junction solar cell Q3. Sub cell photocurrent densities calculated from the  $QE$  curves are placed near the related measurements and the total  $QE$  is displayed by the blue shaded area.

increased stability against light induced degradation, which is discussed in the next Section 5.6 for all multijunction solar cell types.

## 5.6 Light induced degradation

The multijunction solar cells presented in this work were investigated with respect to their stability against light induced degradation<sup>7</sup>. Fig. 5.16 displays the LID behavior on the conversion efficiency in absolute (a) and in normalised values (b), respectively, up to degradation times of 1000 hours for the tandem, triple, and quadruple junction solar cells presented in the previous sections. The respective cell description is included in Fig. 5.16(a).

Fig. 5.16(b) shows that the quadruple, the a-Si:H/ $\mu$ c-Si:H/ $\mu$ c-Si:H triple, and the a-Si:H/ $\mu$ c-Si:H tandem junction solar cells exhibited the highest stability against LID, as the relative degradation in efficiency was below 5 % for all cells after 1000

<sup>7</sup>Some of the results presented in this section were published in F. Urbain, *et al.*, Sol. Energy Mat. Sol. Cells **145** (2016), 142-147 [39].

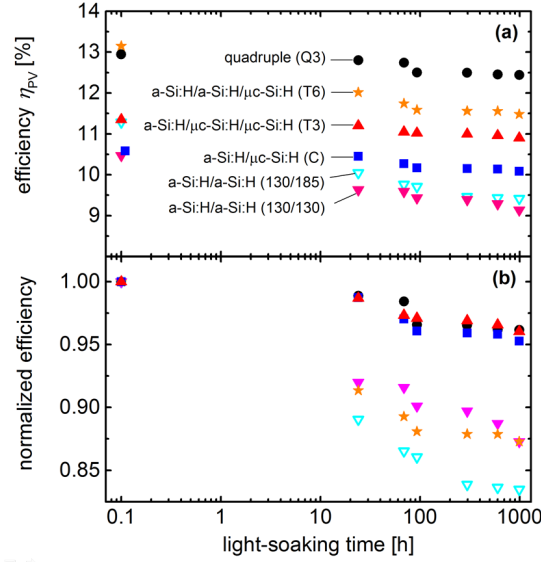


**Fig. 5.16** (a) Photovoltaic conversion efficiency  $\eta_{PV}$  plotted as a function of the light soaking time for tandem: a-Si:H/ $\mu$ c-Si:H (blue squares, cell C from Table 5.2), a-Si:H/a-Si:H (purple triangles: absorber layer  $T_s$  of 130/130 °C and open light blue triangles: absorber layer  $T_s$  of 130/180 °C from Table 5.3), triple (red triangles: cell T3 from Table 5.4 and orange stars: cell T6 from Table 5.5), and quadruple junction solar cells (black circles: cell Q3 from Table 5.6). (b) Conversion efficiency normalised to the initial value as a function of the light soaking time for the tandem, triple, and quadruple junction solar cells.

hours of illumination. From Fig. 5.16(a) it can be seen that the quadruple cell (Q3), which provided an initial efficiency of 12.9 %, showed the highest stabilised efficiency of 12.4 %. When an anti-reflection foil was attached to the glass side, an initial efficiency of 13.2 % and a stabilised efficiency of 12.6 % were measured for this cell, respectively.

As apparent from Fig. 5.16(b) the conversion efficiencies of the a-Si:H/a-Si:H (130/130) tandem and the a-Si:H/a-Si:H/ $\mu$ c-Si:H triple junction cell decreased considerably more by approx. 12 % after light soaking. Due to the thicker a-Si:H top cell (110 nm), the a-Si:H/a-Si:H (130/180) cell degraded even more by approx. 16 % after the LID test. The photovoltaic parameters of the investigated multijunction solar cells before (initial) and after light soaking (stabilised) are presented in Table 5.7.

**Table 5.7** Overview of the photovoltaic parameters of the a-Si:H/ $\mu$ c-Si:H and a-Si:H/a-Si:H tandem, the a-Si:H/ $\mu$ c-Si:H/ $\mu$ c-Si:H and a-Si:H/a-Si:H/ $\mu$ c-Si:H triple, and the a-Si:H/a-Si:H/ $\mu$ c-Si:H/ $\mu$ c-Si:H quadruple junction solar cells in initial and stabilised state (after 1000 hours of light soaking). The measurements were conducted without an anti-reflection foil.

	$\eta_{PV}$ [%]		$V_{OC}$ [mV]		$FF$ [%]		$J_{SC}$ [mA/cm <sup>2</sup> ]		$V_{MPP}$ [mV]		$J_{MPP}$ [mA/cm <sup>2</sup> ]	
	initial	stab.	initial	stab.	initial	stab.	initial	stab.	initial	stab.	initial	stab.
a-Si:H/ $\mu$ c-Si:H (C)	10.6	10.1	1504	1499	71.3	70.8	9.9	9.4	1245	1202	8.5	8.1
a-Si:H/a-Si:H (130/180)	11.2	9.4	1806	1780	73.1	63.2	8.3	8.2	1488	1363	7.5	6.9
a-Si:H/a-Si:H (130/130)	10.5	9.2	1913	1871	73.6	64.6	7.6	7.4	1580	1465	6.7	6.2
a-Si:H/ $\mu$ c-Si:H/ $\mu$ c-Si:H (T3)	11.2	10.9	1974	1982	68.1	68.6	8.4	8.0	1603	1620	7.1	6.8
a-Si:H/a-Si:H/ $\mu$ c-Si:H (T6)	13.2	11.5	2272	2250	70.2	62.3	8.3	8.2	1870	1750	7.0	6.4
a-Si:H/a-Si:H/ $\mu$ c-Si:H/ $\mu$ c-Si:H (Q3)	12.9	12.4	2798	2751	68.8	67.3	6.7	6.6	2280	2253	5.7	5.4

Note that the photovoltaic parameters underlying  $j$ - $V$  measurements, presented in Table 5.7 were conducted without an additional anti-reflection foil and therefore differ from the data in the above sections. For the stronger degrading (relative  $\eta_{PV}$ -degradation above 12 %) a-Si:H/a-Si:H (130/130 and 130/180) tandem and a-Si:H/a-Si:H/ $\mu$ c-Si:H triple junction solar cells,  $FF$  was the most affected photovoltaic parameter. An absolute decrease in  $FF$  of approx. 8%-10% was observed for the three cell types. Consequently,  $V_{MPP}$  and  $J_{MPP}$ , respectively, were also strongly influenced and decreased by approx. 100 mV and 0.6 mA/cm<sup>2</sup>, respectively. For the more stable cell types (relative  $\eta_{PV}$ -degradation less than 5 %), namely the a-Si:H/ $\mu$ c-Si:H tandem, the a-Si:H/ $\mu$ c-Si:H/ $\mu$ c-Si:H triple and the quadruple junction solar cells,  $FF$ , and therefore  $V_{MPP}$  and  $J_{MPP}$  decreased considerably less compared to the other investigated cell types after light soaking.

Overall, the quadruple junction solar cell showed the highest stability against LID (5 %) of all the multijunction solar cells. To evaluate its LID behavior in more detail, *i.e.* the separate LID behavior of the four sub cells, Fig. 5.17 plots the  $QE$  data of cell Q3 in the initial and stabilised state. It is evident that the photocurrent densities of the a-Si:H sub cells were stronger affected by LID (roughly

by around  $0.3 \text{ mA/cm}^2$ ) than the photocurrent densities of the  $\mu\text{c-Si:H}$  sub cells ( $0.1 \text{ mA/cm}^2$ ). Furthermore, the measurement shown in Fig. 5.17 revealed that  $J_{\text{QE}}$  of the 400 nm thick middle a-Si:H sub cell degraded even slightly less than  $J_{\text{QE}}$  of the 90 nm thick top a-Si:H cell. This might be explained by the fact that parts of the incoming UV-light were filtered by the top cell and thus, did not reach the a-Si:H middle cell [186]. Another explanation for the relatively small LID for the quadruple junction cell could be that the effect of LID is 'hidden' by a photocurrent mismatch of the individual sub cells. In single junction solar cells,  $FF$  is usually the most affected PV parameter upon LID [101]. In multijunction solar cells,  $FF$  is strongly influenced by the current matching and increases in general for an increased current mismatch [181]. Although the effect of LID remains the same in multijunction solar cells, a possible mismatch would therefore 'hide' or attenuate the deterioration of the fill factor upon LID, respectively.

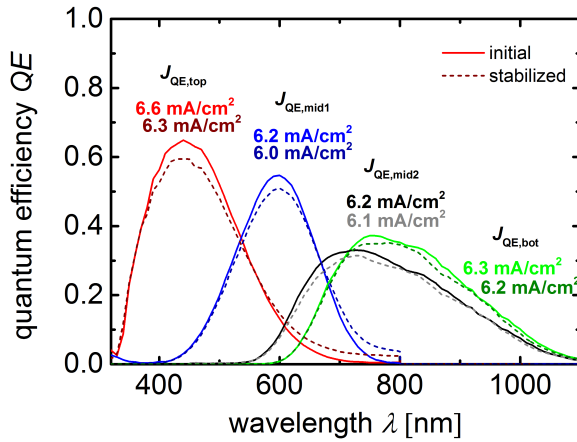


**Fig. 5.17** Quantum efficiency measurement of a-Si:H/a-Si:H/ $\mu\text{c-Si:H}$ / $\mu\text{c-Si:H}$  quadruple junction devices corresponding to cell Q3 from Table 5.6 in initial and stabilised state (after 1000 hours light soaking time). Initial sub cell photocurrent densities calculated from the  $QE$  curves are placed near the related measurements.

## 5.7 Temperature-dependent photovoltaic performance

In contrast to the standard test conditions, at a temperature of 25 °C, the operation temperature of a solar module (and a water splitting device) under practical conditions is typically in the range of 60 °C [187,188]. Therefore, it is important to evaluate the effect of an elevated temperature on the photovoltaic performance<sup>8</sup>, which was measured for the herein developed multijunction solar cells from 25 °C to 60 °C, exemplarily for a tandem (a-Si:H/a-Si:H 130/130, Table 5.3), a triple (a-Si:H/a-Si:H/ $\mu$ c-Si:H T6, Table 5.5), and a quadruple junction solar cell (Q3, Table 5.6). As example, Fig. 5.18 depicts the  $j$ - $V$  characteristics of the triple junction solar cell (a-Si:H/a-Si:H/ $\mu$ c-Si:H cell T6) as a function of the operating temperature  $T_{op}$  in 5 °C steps. The respective  $j$ - $V$  curves of the tandem and quadruple junction solar cell can be found in Fig. A1(a) and (b), respectively.

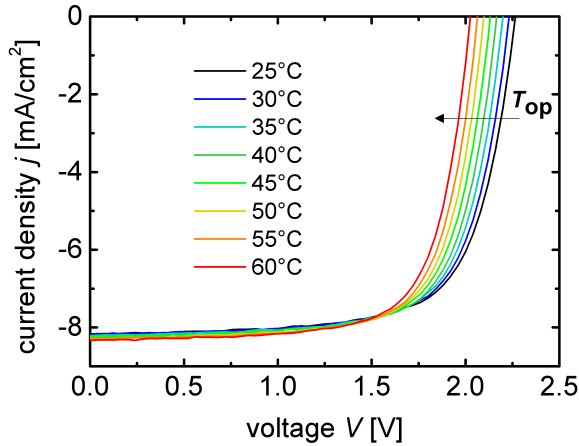


**Fig. 5.18** Current density-voltage  $j$ - $V$  curves of the a-Si:H/a-Si:H/ $\mu$ c-Si:H triple junction solar cell at various operating temperatures  $T_{op}$ . The temperature range between 25 °C and 60 °C was investigated in steps of 5 °C.

Like all semiconductor based devices, solar cells are sensitive to temperature

<sup>8</sup>Some of the results presented in this section were published in F. Urbain, *et al.*, Mater. Sci. Sem. Proc. **42** (2016), 142-146 [189].

variations [190]. In particular, the band gap energy of the absorber usually decreases with increasing temperature. Therefore, mainly  $V_{OC}$  and  $J_{SC}$  are affected. In general,  $V_{OC}$  decreases and  $J_{SC}$  increases (only slightly) upon a temperature increase. As long as the fill factor is not significantly affected, the photovoltaic efficiency of solar cells decreases in general with increasing temperature.

This behavior was also observed for the herein shown triple junction solar cell (see Fig. 5.18 and Table 5.8). A clear trend can be observed in this investigated temperature range:  $V_{OC}$  decreased with increasing  $T_{OP}$  by approx. 30 mV per 5 °C from 2279 mV to 2035 mV. On the contrary,  $J_{SC}$  slightly increased from 8.18 mA/cm<sup>2</sup> to 8.35 mA/cm<sup>2</sup> when the temperature of the solar cell was risen from 25 °C to 60 °C. Overall, however, the gain in  $J_{SC}$  cannot compensate the loss in  $V_{OC}$ . The fill factor values did not change significantly in the investigated temperature range. As a result,  $\eta_{PV}$  decreased from 13.1 % to 12.1 % with increasing temperature. All photovoltaic parameters of the three solar cell types (tandem, triple, and quadruple) can be found in Table 5.8 for  $T_{op}$  of 25 °C and 60 °C, respectively.

**Table 5.8** Overview of the photovoltaic parameters evaluated at room temperature and at 60 °C for a-Si:H/a-Si:H tandem, a-Si:H/a-Si:H/ $\mu$ c-Si:H triple, and a-Si:H/a-Si:H/ $\mu$ c-Si:H/ $\mu$ c-Si:H quadruple junction solar cells. The corresponding  $j$ - $V$  measurements were conducted without additional anti-reflection foils.

	a-Si:H/a-Si:H		a-Si:H/a-Si:H/ $\mu$ c-Si:H		a-Si:H/a-Si:H/ $\mu$ c-Si:H/ $\mu$ c-Si:H	
	25 °C	60 °C	25 °C	60 °C	25 °C	60 °C
$\eta_{PV}$ [%]	10.5	10.2	13.2	12.3	12.9	11.9
$V_{OC}$ [mV]	1913	1762	2272	2026	2798	2470
$FF$ [%]	73.6	74.5	70.2	71.2	68.8	69.2
$J_{SC}$ [mA/cm <sup>2</sup> ]	7.6	7.9	8.3	8.5	6.7	6.9
$V_{MPP}$ [mV]	1580	1488	1870	1685	2280	2012
$J_{MPP}$ [mA/cm <sup>2</sup> ]	6.7	7.0	7.0	7.2	5.7	6.0

A more pronounced increase of the photocurrent density for the three cell types was maybe hampered by current limitations of one of the sub cells. The photovoltaic efficiency decreased for all solar cell types in the investigated temperature range. From Table 5.8 it becomes apparent that the decrease in the open-circuit voltage  $\Delta V_{OC}$  increased from the tandem to the quadruple configuration ( $\Delta V_{OC,tandem} = -150$  mV,

$\Delta V_{\text{OC, triple}} = -250$  mV, and  $\Delta V_{\text{OC, quadruple}} = -320$  mV). This observation can be understood, as the number of absorber layers, *i.e.* the sensibility of the open-circuit voltage, increases from tandem to quadruple configuration. In summary,  $\eta_{\text{PV}}$  of the a-Si:H/a-Si:H solar cell slightly decreased by 0.3 %, while  $\eta_{\text{PV}}$  of the triple and quadruple junction solar cells decreased by approx. 0.9 % and 1.0 %, respectively. The findings of this section will be again considered in Section 6.3, where the performance of photoelectrochemical devices is investigated with respect to the operation temperature.

## 5.8 Summary and conclusions

Overall, the presented photovoltaic development deviates from prevalent routes, which aimed rather at record electrical conversion efficiencies. The optimisation routes presented in this chapter for the single and multijunction solar cells focused on high  $V_{\text{OC}}$  without impairing the conversion efficiency of the devices. Nevertheless, the conversion efficiencies of the multijunction junction solar cells developed in this work are very close to the highest efficiencies reported for solar cells made of thin film silicon [191]. In the following the main results will be summarised and discussed. Furthermore, the implication of the findings for the application in solar water splitting, especially for the multijunction solar cells, will be elaborated.

### $V_{\text{OC}}$ tunability in a-Si:H single junction solar cells

The optimisation of the a-Si:H single junction solar cells, presented in Section 5.2.2, focused on high  $V_{\text{OC}}$  and was conducted as a function of  $SC$  and  $T_s$ . In total, the open-circuit voltage in a-Si:H single junction solar cells could be systematically tuned in a range of approx. 150 mV by varying  $SC$  and  $T_s$  (see Fig. 5.3). Both parameters influence the hydrogen content in the intrinsic material, which in turn influences the optical gap  $E_{04}$  [98]. To elucidate the  $E_{04}$ - $V_{\text{OC}}$  relationship, Fig. 5.19 shows the  $V_{\text{OC}}$  data of the a-Si:H solar cells as a function of  $E_{04}$  of the respective a-Si:H absorber layers. As one would expect,  $V_{\text{OC}}$  increased with  $E_{04}$  of the absorber layer.

Nevertheless, the concomitant issues related to the usage of low-temperature fabricated a-Si:H material shall not be neglected. In general, a reduction in the deposition temperature (below 180 °C) may lead to a reduction in device performance

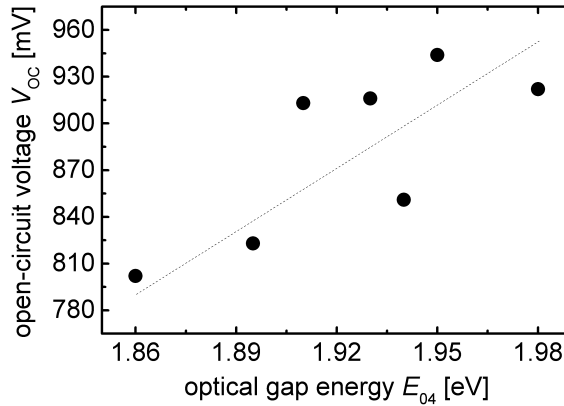


**Fig. 5.19** Open-circuit-voltage  $V_{OC}$  of a-Si:H single junction solar cells as a function of the optical gap energy  $E_{04}$  of the respective intrinsic a-Si:H absorber layers. The dotted line serves as a guide to the eye.

due to an increasing defect density of the a-Si:H material [165]. Here, the focus was, however, primarily set on the development of devices with high adjustable photovoltages, rather than on high conversion efficiencies. Yet, as shown in Fig. 5.3, the adjustment of the silane concentration together with  $T_s$ , allowed to fabricate solar cells with reasonable conversion efficiencies even at a very low deposition temperature of below 180 °C. Hence, the high voltage/high efficiency gap could be partly reduced.

Another generally observed problem associated with the application of low-temperature processed a-Si:H cells is the considerable LID of this material [43]. However, as presented in Section 5.6, the effect of LID can be attenuated when the low-temperature a-Si:H material is integrated in multijunction solar cells.

### **$V_{OC}$ tunability in $\mu$ c-Si:H single junction solar cells**

The aim of the development of the  $\mu$ c-Si:H single junction solar cells was specifically to relax the tradeoff between high open-circuit voltages and high photocurrents, also in advance to the usage in multijunction solar cells. The development routes of  $\mu$ c-Si:H single junction solar cells with high  $V_{OC}$  presented in 5.3 consisted in the



reduction of the intrinsic  $\mu\text{-Si:H}$  absorber layer thickness, in the  $SC$  profiling, and in the buffer layer incorporation. All the routes distinctly contributed to the closure of the high voltage/high current gap and considerably improved the open-circuit voltage in  $\mu\text{-Si:H}$  single junction solar cells. In total, the development of high voltage  $\mu\text{-Si:H}$  solar cells showed that  $V_{OC}$  can be varied over a 100 mV range from 480 to 580 mV. Within this voltage range, the photocurrent density was kept at a reasonable high level. For instance, a conversion efficiency of 8.1 % along with an open-circuit voltage  $V_{OC}$  of 570 mV was achieved for a 650 nm thick solar cell. Furthermore, it was shown that  $V_{OC}$  of the single junction solar cells can be increased in small steps of 10-20 mV, which is of importance when applied in multijunction solar cells to precisely adjust the photovoltage at high values (over 2.0 V).

### a-Si:H and $\mu\text{-Si:H}$ based multijunction solar cells

Subsequently the a-Si:H and  $\mu\text{-Si:H}$  absorber layers were implemented in multijunction solar cells. It was found that the open-circuit voltage of these solar cells can be tuned in both large (600 mV) and small (20-50 mV) steps from 1.5 V to 2.8 V in  $V_{OC}$  and from 1.3 V to 2.3 V in  $V_{MPP}$ . Fig. 5.20 displays the achieved  $V_{OC}$  as a function of  $J_{SC}$  of the developed single and multijunction solar cells.

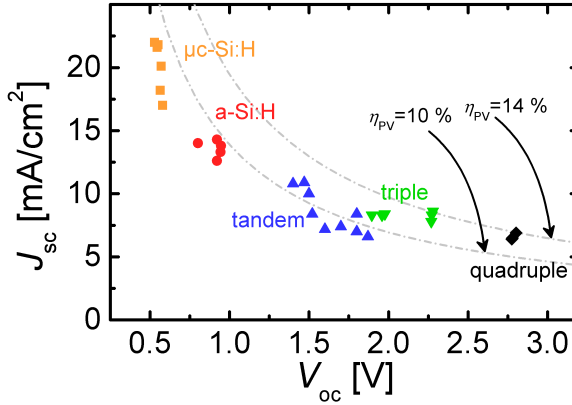


**Fig. 5.20** Open-circuit voltages  $V_{OC}$  as a function of the short-circuit photocurrent densities  $J_{SC}$  of the developed a-Si:H and  $\mu\text{-Si:H}$  based single and multijunction solar cells. The grey dotted lines indicate a photovoltaic efficiency  $\eta_{PV}$  of 10 % and 14 %, respectively, assuming a FF of 72 %.

Fig. 5.20 nicely shows the  $V_{OC}$ - $J_{SC}$  tradeoff of thin film silicon solar cells mentioned earlier. The presented development routes allowed to tune the  $V_{OC}$  data of the photovoltaic cells over a wide range while keeping the device efficiency over 11 % for the multijunction solar cells. The highest efficiency in combination with a high  $V_{OC}$  of 2.3 V was achieved with the a-Si:H/a-Si:H/ $\mu$ c-Si:H triple junction solar cells, which exhibited a photovoltaic efficiency of 13.6 %. Overall, the ability to vary the photovoltaic parameters over a wider range, as presented in Fig. 5.20, is vital to fulfil the particular requirements of various PV-EC systems with different catalyst overpotential losses, *i.e.* when different voltage requirements are implied, as will be discussed in the next chapter.

To elucidate this further, Fig. 5.21 illustrates the effect of the overpotential losses on the solar-to-hydrogen efficiency of a PV-EC device based on the developed multijunction solar cells. The illuminated  $j$ - $V$  curves of the developed tandem, triple and quadruple junction solar cells are plotted and linked to the theoretical operation point of a PV-EC device. In an ideal system without overpotential losses, the PV-EC device would operate at a voltage of 1.23 V of the solar cell, indicated by a straight vertical dashed line in Fig. 5.21. In real systems overpotential losses cause that the operation point is shifted towards more positive bias, as indicated in Fig. 5.21. The photocurrent density  $j_{op}$  at this required voltage can be translated to a maximum STH efficiency  $\eta_{STH_{max}}$  (under the assumption of 100 % faradaic efficiency) of the PV-EC device using Eq. 4.4. Assuming that all the PV parameters of the solar cells remain unchanged when they are integrated in a PV-EC device, Fig. 5.21 then allows to illustratively predict the performance of PV-EC devices based on the developed solar cells. On the right ordinate, the STH efficiency, calculated according to Eq. 4.4, is plotted and can be read at the crossing point of the solar cell  $j$ - $V$  with the operation point line at the respective overpotential from the upper abscissa.

As can be deduced from Fig. 5.21, the a-Si:H/ $\mu$ c-Si:H tandem junctions could provide a maximum STH efficiency over 10 % when the PV-EC device would operate ideally, *i.e.* without any overpotential losses. When considering losses, triple and quadruple junction photocathodes seem to be more beneficial. Based on the presented photovoltaic results it is already possible to derive the practical performance limits of the state-of-the-art thin film silicon technology for water splitting applications. The measurements of the real PV-EC devices will be shown in the following chapter.

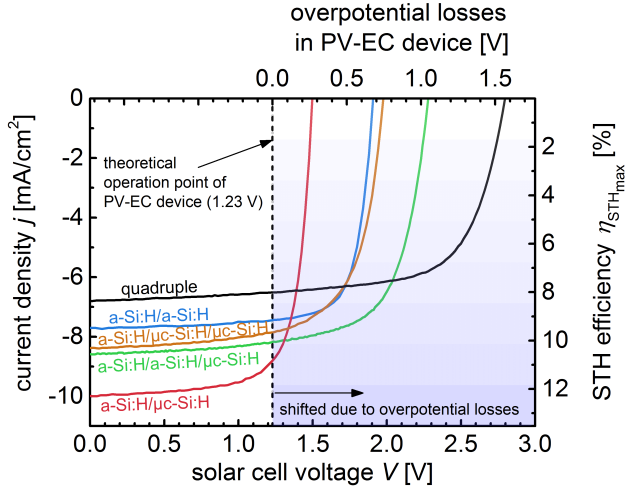


**Fig. 5.21** Illustration of the achievable solar-to-hydrogen efficiency  $\eta_{\text{STH}_{\text{max}}}$  in PV-EC devices for water splitting based on thin film silicon solar cells. The illuminated  $j$ - $V$  curves of the tandem, triple, and quadruple junction solar cells are linked with the theoretical operation point of a PV-EC device at 1.23 V (dashed vertical line, without overpotential losses). In real PV-EC devices this operation point is shifted due to overpotential losses, which are plotted on the upper abscissa. The right ordinate depicts the achievable STH efficiency as a function of the respective photocurrent density at a certain overpotential multiplied by the value of 1.23 (see Section 4.4).

### Stability against LID and temperature increase

The effects of light induced degradation and increased operating temperatures on the photovoltaic performance of the developed solar cells were also investigated. Light soaking experiments (1000 h light exposure) revealed an excellent stability against LID for the a-Si:H/ $\mu$ c-Si:H, the a-Si:H/ $\mu$ c-Si:H/ $\mu$ c-Si:H, and the quadruple junction solar cells, for which the conversion efficiency degraded less than 5 %. The highest stabilised conversion efficiency of 12.6 % was achieved with the quadruple junction solar cell. The a-Si:H/a-Si:H/ $\mu$ c-Si:H cell, which showed the highest initial efficiency, degraded around 13 %, and had a stabilised efficiency of 11.5 %.

By increasing the operation temperature from 25 °C to 60 °C, a clear trend of decreasing  $V_{\text{OC}}$  with increasing  $T_{\text{op}}$  was observed. Furthermore, it became apparent

---

that the decrease in the open-circuit voltage  $\Delta V_{OC}$  increased from the tandem to the quadruple junction configuration. On the contrary, the  $J_{SC}$  data slightly increased when  $T_{op}$  was increased. Overall, however, the gain in  $J_{SC}$  could not compensate the loss in  $V_{OC}$ , as the fill factor values did not change significantly in the investigated temperature range. As a result,  $\eta_{PV}$  decreased for all investigated cell types with increasing temperature. The impact of LID and temperature increase for the PV-EC device performance will be discussed in detail in the following chapter.



## 6 Thin film silicon based photovoltaic-electrochemical devices

*This chapter presents the results on the application of the developed high voltage multijunction solar cells as photocathodes in photovoltaic-electrochemical devices for water splitting. First, the solar cell/electrolyte interface is highlighted. This contact plays a major role in the PV-EC device, not only in terms of the optical and catalytic properties, but also regarding the electrochemical stability of the device. The three aspects are discussed in Section 6.1. In the following part of this chapter, the focus is set on the performance of the PV-EC devices for water splitting. In Section 6.2 the current density-voltage characteristics of the multijunction based PV-EC devices are evaluated as a function of the used HER catalysts and as a function of the used electrolyte solution. Furthermore, the influence of light induced degradation of the solar cell component on the PV-EC device performance is examined. The results on the modeling of the integrated PV-EC device system can be found in Section 6.3. It is shown that the model, which was introduced in Section 4.3, exhibits a very good agreement with the experimental results and allows for a detailed analysis of the relevant system losses. In this regard, it is demonstrated that the model can be further used to predict the efficiency limits for thin film silicon-based PV-EC devices and to investigate the effect of elevated operation temperatures and different catalyst materials for the HER and OER, respectively, on the solar-to-hydrogen efficiency. The chapter is finally concluded in Section 6.4.*

### 6.1 Photocathode/electrolyte contact

As already pointed out in Section 2.3.4, the photocathode/electrolyte contact has to fulfil several tasks. While the metal contact in a solar cell merely has to provide sufficient reflection of light and charge carrier collection, the photocathode contact is implemented for multiple purposes:

- like in the PV cell, it functions as a back reflector for transmitted photons and thereby increases the probability of photon absorption and charge carrier generation in the absorber layer(s), and thus enhances the photocurrent of the device,
- it provides a good electrical contact to the photoelectrode,
- it protects the silicon solar cell against corrosion, and
- it should enhance the catalytic activity and thus, lower the overpotential for the HER.

Additionally, it preferably consists of earth-abundant materials. Considering this broad range of demands, the metal contact design has to be chosen carefully<sup>1</sup>.

### 6.1.1 Catalytic and optical properties of single metal layer contacts

In this work, thin layers of gold (Au), titanium (Ti), platinum (Pt), nickel (Ni), aluminum (Al), copper (Cu), and silver (Ag) were deposited by electron beam evaporation at a thickness of 300 nm on glass substrates, to ensure a compact film. Subsequently, the layers were evaluated with regards to their catalytic activity, regarding the cathodic overpotential  $\eta_{\text{HER}}$  for the HER. Fig. 6.1(a) displays the  $\eta_{\text{HER}}$  values of the metals that were evaluated from the corresponding linear sweep voltammetry measurements (voltammograms) in 0.1 M KOH and 0.1 M H<sub>2</sub>SO<sub>4</sub>, shown in Fig. 6.1(b) and (c), respectively. The potentials of these voltammograms were corrected by the  $jR$ -drop in the electrolyte. The  $\eta_{\text{HER}}$  values were taken at a current density of  $-7 \text{ mA/cm}^2$ , which represents a reasonable operation photocurrent density of a PV-EC device [144]. Furthermore, the same metals were deposited as reflecting contacts (approx. 300 nm on the pure Si surface without ZnO:Al) on a-Si:H/a-Si:H tandem solar cells (cell 130/130 from Table 5.3 in Section 5.4) to evaluate their optical performance in terms of  $J_{\text{SC}}$ . The illuminated  $j$ - $V$  curves of the different tandem solar cells can be found in Fig. 6.1(d).

From Fig. 6.1(d) it is apparent that Ag and Al are the most efficient back reflectors and provided  $7.7 \text{ mA/cm}^2$  and  $7.3 \text{ mA/cm}^2$  as back contact in the a-Si:H/a-Si:H solar cell, respectively. The solar cells coated with the other investigated metals

---

<sup>1</sup>Some of the results presented in this section were published in F. Urbain, *et al.*, Chem. Phys. Lett. **638** (2015), 25-30 [179].

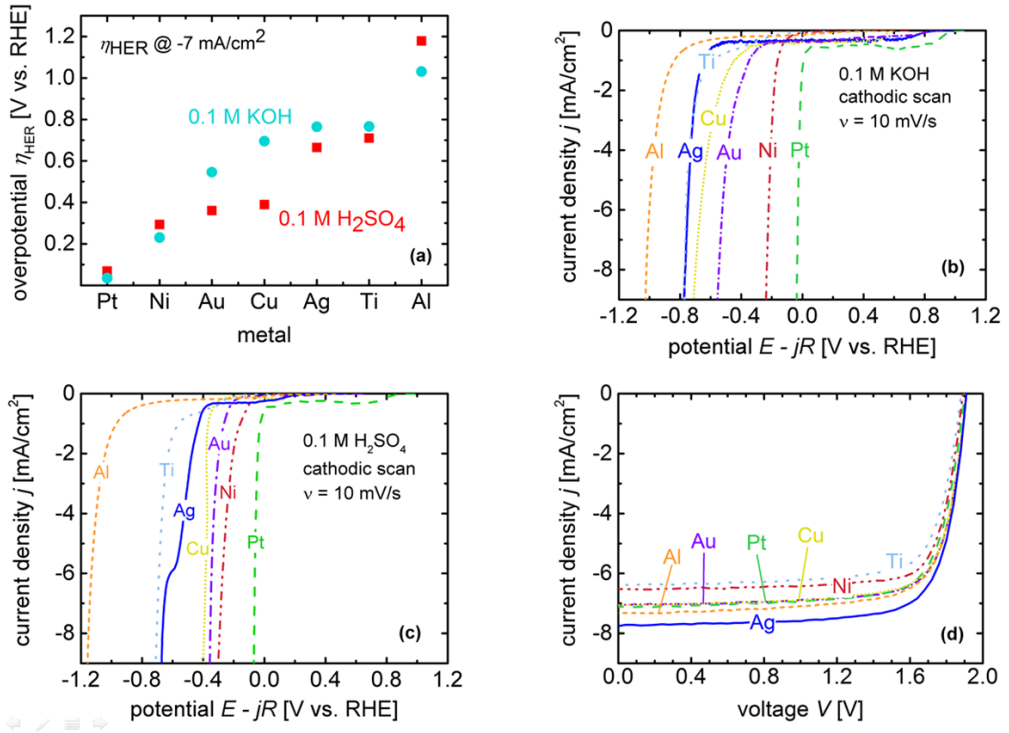


**Fig. 6.1** (a) Cathodic overpotentials (at  $-7 \text{ mA/cm}^2$ ) measured in 0.1 M KOH (light blue circles) and in 0.1 M  $\text{H}_2\text{SO}_4$  (red squares) for Au, Cu, Ti, Ni, Ag, Pt, and Al evaluated as single layers on ZnO:Al coated glass substrates. (b) Linear sweep voltammetry measurements, conducted in 0.1 M KOH, of single metal layers (approx. 150 nm of Al, Au, Ag, Cu, Ti, Ni, Pt) on glass substrates at a scan rate of 10 mV/s. (c) The same measurements conducted in 0.1 M  $\text{H}_2\text{SO}_4$ . The data in (b) and (c) were corrected by the electrolyte series resistance, which was measured by electrochemical impedance spectroscopy. The overpotentials presented in Fig. 6.1(a) are taken at a current density of  $-7 \text{ mA/cm}^2$  in (b) and (c). (d) Current density-voltage  $j - V$  measurements of the a-Si:H/a-Si:H solar cells (cell 130/130 from Table 5.3 in Section 5.4) with different metallic back reflecting layers as back contact (approx. 300 nm).

as reflecting contacts (Pt, Cu, Au, Ni, and Ti) provided lower  $J_{\text{SC}}$  values. However, the optical and catalytic properties of the investigated metals deviated significantly. For instance, Ag functions as the best reflecting metal, but is not efficient as HER



catalyst because its overpotential in both electrolyte solutions exceeded 600 mV at  $-7 \text{ mA/cm}^2$  (see Fig. 6.1(a)). Pt, on the other hand, provides a very low overpotential of around 70 mV in 0.1 M  $\text{H}_2\text{SO}_4$  and even only 30 mV in 0.1 M KOH (see Fig. 6.1(a)). Al, as a non-precious and earth-abundant material, is a more suitable back reflector (see Fig. 6.1(d)) than a HER catalyst, as its catalytic activity was the lowest of all tested metals with an overpotential of around 1000 mV in 0.1 M KOH and 0.1 M  $\text{H}_2\text{SO}_4$  (see Fig. 6.1(a)). Ni commended itself with the second best catalytic activity among the tested metals and exhibited 220 mV and 290 mV overpotential in KOH and  $\text{H}_2\text{SO}_4$ , respectively (see Fig. 6.1(a)). As can be deduced from Fig. 6.1(d), the optical properties, however, were rather poor ( $J_{\text{SC}} = 6.4 \text{ mA/cm}^2$ ). Cu, Au and Ti were less catalytically active than Pt and Ni. Overall, this result clearly showed that there is a tradeoff between the optical and the catalytic properties of the investigated single metal layers. Instead of single layers, the feasibility of metal layer stacks as photocathode contacts therefore would be beneficial and was subsequently investigated. In this way, the aforementioned advantages of the individual metals can be combined.

### 6.1.2 Metal stacks as photocathode contact

Based on the results depicted in Fig. 6.1(a) and (d), Pt and Ni were chosen as HER catalyst materials, whereas Ag and Al were selected as suitable back reflecting metals, respectively. The measurements were conducted in 0.1 M KOH. Furthermore, the cost effectiveness was considered by fabricating two metal stacks: (i) an expensive, precious metal stack of Ag and Pt and (ii) a low-cost and earth-abundant stack of Al and Ni. In both cases, the catalyst layers, namely Pt and Ni, entirely covered the reflecting Ag and Al metals, respectively, and by this also acted as protection layers. As an example, the costs for the deposition of 100 nm of various metals on  $1 \text{ cm}^2$  area were compared in Fig. A2. The linear sweep voltammetry measurements of the photocathodes with the accordingly adapted contact design are shown in Fig. 6.2. The underlying a-Si:H/a-Si:H tandem structure was the same as cell 130/130 from Table 5.3. From this measurements the onset potential for cathodic current  $E_{\text{onset}}$  (dark dashed line in Fig. 6.2) and the photocurrent density  $J_0$  at 0 V vs. RHE (see upper abscissa in Fig. 6.2), which correlate with the open-circuit voltage  $V_{\text{OC}}$  and the short-circuit current density  $J_{\text{SC}}$  of the solar cells [85], were determined for the photocathodes and are listed in Table 6.1.

From Fig. 6.2 and from Table 6.1 it can be deduced that the layer stack concept can be successfully applied on the a-Si:H/a-Si:H photocathodes because the optical

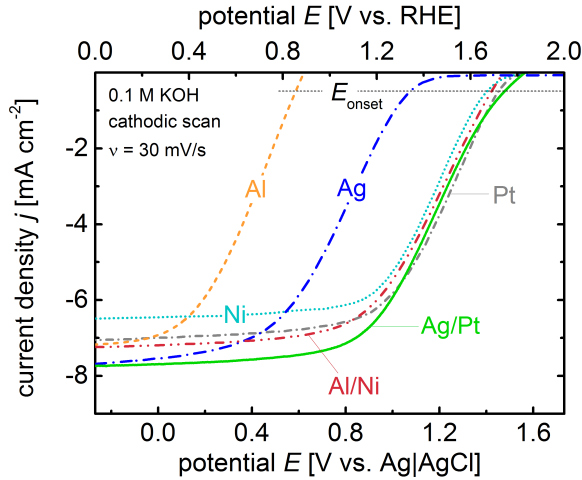


**Fig. 6.2** Linear sweep voltammetry measurements under AM 1.5 illumination ( $100 \text{ mW/cm}^2$ ) of the photocathodes with different metal contact designs (same a-Si:H/a-Si:H tandem structure as cell 130/130 from Table 5.3). The single metal layer back contacts are assigned as follows: orange dashed curve: Al; blue dotted curve: Ag; light blue dotted curve: Ni; grey dashed curve: Pt. The stacks of two metal layers combine the optical and the catalytic properties of each individual metal and are assigned as follows: red dashed curve: Al/Ni; green solid curve: Ag/Pt. The measurements were conducted in 0.1 M KOH at a scan rate  $\nu$  of 30 mV/s. The photoelectrochemical parameters are listed in Table 6.1. The potential of the photocathode is plotted versus the RHE and versus the Ag|AgCl reference electrode on the upper and on the lower abscissa, respectively.  $E_{\text{onset}}$  is taken at a photocurrent density value of  $-0.5 \text{ mA/cm}^2$ .

and catalytic properties of each metal were maintained.  $J_{\text{SC}}$  and  $J_0$  values stayed the same (differences within a few percent) upon usage of the same back reflecting metal (metal layer on top of the silicon device) for the solar cell and the photocathode, respectively. This can be understood because the light absorption and the mechanisms of the photogenerated charge carrier separation of the solar cell remained unaffected when used as photocathode in the photoelectrochemical arrangement. Furthermore, the  $J_0$  values of the photocathodes with single back reflecting layers of Al and Ag, respectively, were not changed when other metals were deposited on top of these photocathodes (compare  $J_0$  for Ag and Ag/Pt and for Al and Al/Ni in Fig. 6.2). This was additionally confirmed by reflectance measurements of single and stacked metal contacts, as exemplarily shown for Ag and Ag/Pt in Fig. 6.3.

**Table 6.1** Overview of the photovoltaic and the photoelectrochemical parameters of the photocathodes with different metal contacts. The respective metal layer thicknesses are indicated in the second column.  $J_0$  denotes the photocurrent density at 0 V vs. RHE. The onset potential for cathodic current  $E_{\text{onset}}$  was taken as the value at a photocurrent density of  $-0.5 \text{ mA/cm}^2$  from Fig. 6.2. The short-circuit current density  $J_{\text{SC}}$  for the corresponding solar cells were taken from Fig. 6.1(d).

Photocathode contact	Thicknesses [nm]	$J_0$ [mA/cm <sup>2</sup> ]	$E_{\text{onset}}$ [mV vs. RHE]	$J_{\text{SC}}$ [mA/cm <sup>2</sup> ]
Ag	300	7.7	1343	7.7
Pt	300	7.1	1745	7.1
Ag/Pt	300/150	7.7	1752	7.7
Al	300	7.2	855	7.2
Ni	300	6.5	1683	6.5
Al/Ni	300/150	7.2	1692	7.2

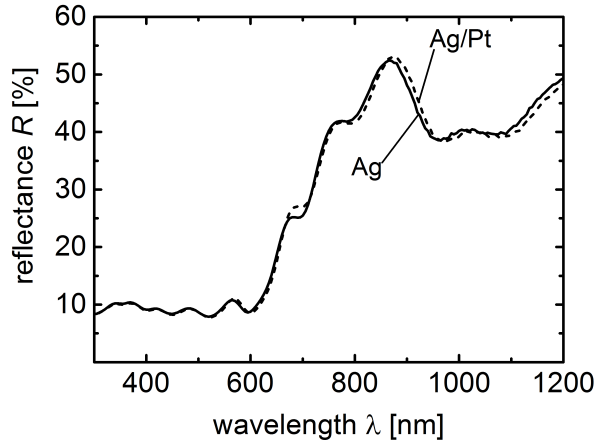


**Fig. 6.3** Reflectivity measurements of a-Si:H/a-Si:H solar cells with different back contacts consisting of ZnO:Al and a single metal Ag layer (solid) and a metal layer stack of Ag and Pt (dotted line).

The good catalytic activity of Pt and Ni, with respect to the  $E_{\text{onset}}$  values, was also maintained when they were deposited as catalyst layers on top of highly reflecting metals, such as Ag and Al, respectively (compare  $E_{\text{onset}}$  for Pt and Ag/Pt and for Ni and Al/Ni in Fig. 6.2). The  $E_{\text{onset}}$  values for the Ag/Pt and the Al/Ni contacted devices lie very close to the  $V_{\text{OC}}$  values (approx. 1.9 V) of the Ag and Al contacted solar cells, presented in Fig. 6.1(d). The  $V_{\text{OC}} - E_{\text{onset}}$  differences were in good agreement with the measured overpotentials of the single metal layers shown in Fig. 6.1(a).

By depositing Pt as HER catalyst on top of the a-Si:H/a-Si:H/ZnO:Al/Ag photocathode, the  $E_{\text{onset}}$  value was significantly shifted in positive bias direction providing an  $E_{\text{onset}}$  of 1752 mV vs. RHE (from 1343 to 1752 mV vs. RHE) with a photocurrent density at 0 V vs. RHE of 7.7 mA/cm<sup>2</sup>. At the maximum power point (MPP) the a-Si:H/a-Si:H/ZnO:Al/Ag/Pt photocathode provided 6.6 mA/cm<sup>2</sup> at 1195 mV vs. RHE. The anodic shift in  $E_{\text{onset}}$  from the Al to the Al/Ni layer stack contacted photocathode was over 800 mV from 855 to 1692 mV vs. RHE. In the MPP the a-Si:H/a-Si:H/ZnO:Al/Al/Ni photocathode exhibited 6.3 mA/cm<sup>2</sup> at 1160 mV vs. RHE. Although the photocurrent density and the onset potential for cathodic current were lower compared to the photocathode with the Ag/Pt designed contact, this photocathode is an all-earth-abundant and precious metal-free device, and thus very alluring for low-cost and efficient water splitting applications. From Fig. A2 it can be deduced that Al/Ni vs. Ag/Pt offers a significant cost reduction (more than 1000 times), with respect to the used thicknesses (300/150 nm) and area ( $1 \times 1 \text{ cm}^2$ ).

A good electrochemical stability against corrosion is an additional requirement for photocathode contacts. In this regard, the long-term stability of the a-Si:H/a-Si:H photocathode with Ag/Pt contact was monitored. Concerning the Al/Ni contact, primarily the delamination of the Al layer hindered longer operations (less than 20 minutes of operation, data not shown). This problem may be solved by integrating very thin adhesion layers, for example, Chromium or Titanium between the Si surface and the Al layer [192, 193]. The adhesion layer would have to be as thin as possible in order to ensure a good reflectivity from the subsequent Al layer.

Fig. 6.4 shows the potentiostatic measurement of the Ag/Pt contacted photocathode in 0.1 M KOH biased at 0 V vs. RHE. During the measurement periodical fluctuations in the photocurrent density were caused by repetitive accumulation and detachment of  $H_2$  bubbles at the photocathode surface. Nevertheless, a stable photocurrent density of around  $7.7 \text{ mA/cm}^2$  was measured over the course of four hours of operation.

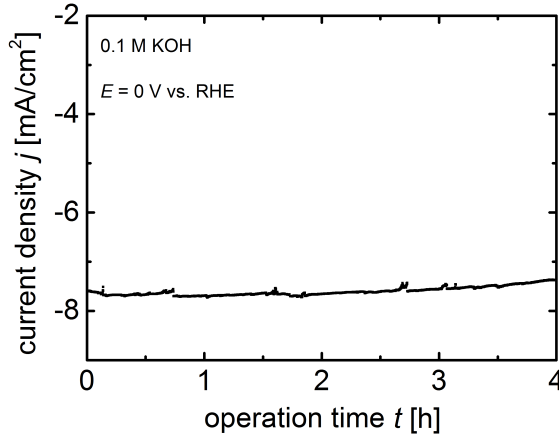


**Fig. 6.4** Potentiostatic measurement of the a-Si:H/a-Si:H photocathode with an Ag/Pt contact at 0 V vs. RHE under AM 1.5 illumination. The measurement was conducted in 0.1 M KOH over the course of four hours of operation.

In summary, the presented results demonstrate that the photocathode metal contact requires careful designing as it needs to fulfil several tasks at once. The usage of stacked metal layers as contact therefore becomes necessary and it was shown that this allows to combine advantages of each individual layer, with respect to light reflection, catalysis, low cost, and photostability.

## 6.2 Multijunction based PV-EC devices

So far, only the HER half-cell reaction at the photocathode was examined, while the OER reaction at the anode side was neglected in the three-electrode measurement. To investigate the complete PV-EC device characteristics, two-electrode measurements have to be conducted and are presented in this section<sup>2</sup>.

Fig. 6.5 depicts the voltammograms in the two-electrode configuration of the PV-EC devices based on the multijunction solar cells developed in Chapter 5 (see initial cells in Table 5.7). The measurements were conducted in 0.1 M KOH and Pt was used as HER catalyst layer (approx. 150 nm) on top of the solar cell Ag contacts (same Ag/Pt contact as shown in the preceding section). As already discussed in

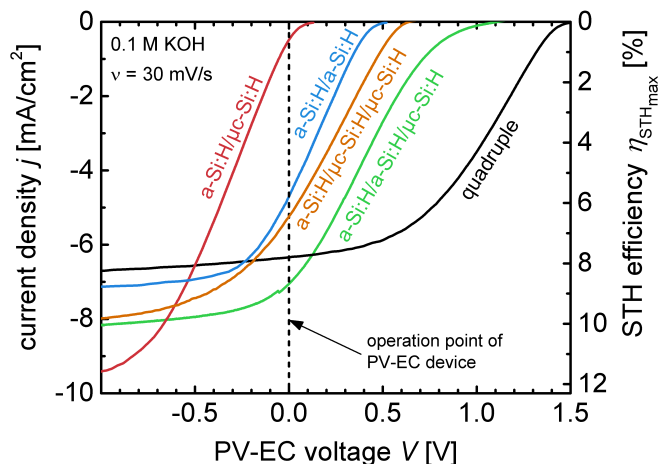


**Fig. 6.5** Linear sweep voltammetry measurements of the PV-EC devices based on thin film silicon multijunction solar cells (same initial cells as in Table 5.7) with a 150 nm thick Pt layer as HER catalyst on top of the Ag contact and a  $\text{RuO}_2$  counter electrode for the OER reaction. The measurements were conducted in 0.1 M KOH at a scan rate of 30 mV/s. The right ordinate depicts the achievable STH efficiency as a function of the photocurrent density at 0 V applied bias (according to Eq. 4.4).

<sup>2</sup>The results presented in this section were published in F. Urbain *et al.*, Energy Environ. Sci. **9** (2016), 145-154 [144].

Section 4.2.2 and 4.3, the shape of the curves differs from the pure solar cell  $j$ - $V$  presented in Fig. 5.21. In particular  $FF$  and  $V_{OC}$  were reduced, mainly because of the electrolyte resistance and the overpotential losses at the electrode surfaces (Pt and  $\text{RuO}_2$ ), respectively. The saturation photocurrent is slightly reduced compared with the  $j$ - $V$  measurement on the solar cells, because for the PV-EC measurements no anti-reflection foil was used.

As could be predicted from Fig. 5.21, the measurement shown in Fig. 6.5 confirmed that the photovoltage generated by the a-Si:H/ $\mu\text{c}$ -Si:H tandem photocathode was not sufficient to operate this water splitting device in its maximum power point (MPP) in real operating conditions. Even though the device provided the highest  $J_{SC}$  of all investigated solar cell types (see Fig. 5.21), it only operated at  $j_{op}$  of  $0.5 \text{ mA/cm}^2$  in the PV-EC device configuration. This result demonstrated that the open-circuit voltage  $V_{OC}$  of 1.5 V provided by the a-Si:H/ $\mu\text{c}$ -Si:H solar cell (see Table 5.2) is the minimum output voltage required to run this specific PV-EC device for water splitting (Pt and  $\text{RuO}_2$  as HER and OER catalyst, respectively, and 0.1 M KOH electrolyte solution) bias-free.

The a-Si:H/a-Si:H based device generated  $4.8 \text{ mA/cm}^2$  as  $j_{op}$ . Its operation point lied in the steep slope of the voltammogram, where small variations in the PV-EC voltage will result in large changes in  $j_{op}$ . Although the a-Si:H/ $\mu\text{c}$ -Si:H/ $\mu\text{c}$ -Si:H triple junction devices provided a higher  $V_{OC}$ , and consequently a higher  $E_{onset}$  (as apparent in Fig. 6.5),  $j_{op}$  was not increased compared to the a-Si:H/a-Si:H tandem devices. Here, further improvements in the fill factor of the a-Si:H/ $\mu\text{c}$ -Si:H/ $\mu\text{c}$ -Si:H solar cell have to be made in order to reach the MPP photocurrent in the short-circuit condition, and thus, achieve a higher STH efficiency. The highest operation photocurrent density  $j_{op}$  was provided by the a-Si:H/a-Si:H/ $\mu\text{c}$ -Si:H based PV-EC device. The device operated close to its MPP at  $7.1 \text{ mA/cm}^2$ , which corresponds to an estimated STH efficiency of 8.7 %. The operation point of the quadruple junction device lied in the current plateau region at  $6.3 \text{ mA/cm}^2$ . Albeit the corresponding 7.6 % STH efficiency was lower compared to the a-Si:H/a-Si:H/ $\mu\text{c}$ -Si:H device for the respective used catalysts,  $j_{op}$  of the device was located in a relatively flat region of the voltammogram (current plateau region). Hence, this device provided a certain 'excess' voltage, which offers a higher flexibility in choosing other non-precious catalyst materials, as will be discussed in the following section. Please note that the assumption of a faradaic efficiency of 100 % for the system under study was confirmed by a volumetric measurement of the evolved gases (see Section 4.4).

### 6.2.1 Influence of the catalyst

From Fig. 6.5, it can be deduced that for an approx. 200 mV increase in overpotential losses the quadruple based device would exhibit a higher  $j_{\text{op}}$  than its a-Si:H/a-Si:H/ $\mu\text{c-Si:H}$  triple junction counterpart. To validate this result, Ni, instead of Pt, was deposited on top of the Ag contact of the quadruple and triple junction solar cell. Ni is catalytically less active than Pt, but as a non-precious and earth-abundant catalyst material it is alluring due to its lower cost [194]. The comparison between the measured voltammograms of the triple and quadruple junction based PV-EC devices with Pt and Ni layers as HER catalysts, respectively, is shown in Fig. 6.6.

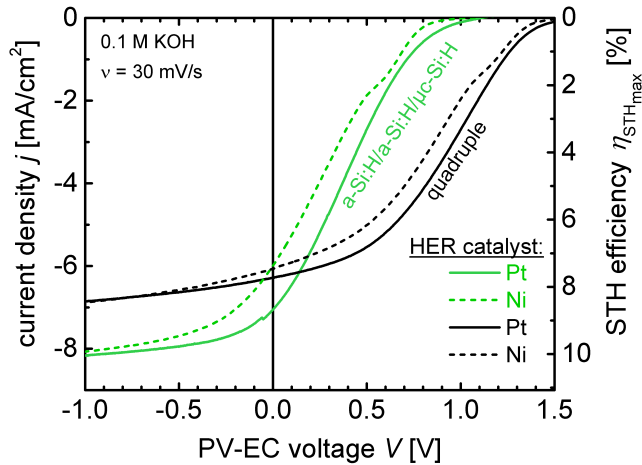


**Fig. 6.6** Linear sweep voltammetry measurements of PV-EC devices based on a-Si:H/a-Si:H/ $\mu\text{c-Si:H}$  triple and quadruple junction photocathodes with a  $\text{RuO}_2$  counter electrode for the OER reaction. For the HER reaction, 150 nm of Ni (dotted curves) and Pt (solid curves) were deposited on top of the Ag solar cell contacts, respectively. The measurements were conducted in 0.1 M KOH at 30 mV/s. The right ordinate depicts the achievable STH efficiency as a function of the photocurrent density at 0 V (see Eq. 4.4).

As expected, the operation photocurrent density  $j_{\text{op}}$  for the Ni-coated triple and quadruple devices was lower compared to the platinised devices. But, the a-Si:H/a-Si:H/ $\mu\text{c-Si:H}$  based device showed a significant decrease in  $j_{\text{op}}$  from 7.1 to 6.1  $\text{mA}/\text{cm}^2$ ,



while  $j_{\text{op}}$  for the quadruple based device only decreased by  $0.1 \text{ mA/cm}^2$  when Ni was used as a catalyst layer instead of Pt. Both Ni-coated devices operated at the same photocurrent density of  $6.1 \text{ mA/cm}^2$  (*i.e.* at the same estimated STH efficiency of 7.5 %) in 0.1 M KOH. However, the operation point of the triple junction based device lied in the steep slope of its current density-voltage characteristics, where a slight deterioration of the device parameters, due to photocorrosion during long-term operation for instance, could significantly deteriorate the STH efficiency. The operation point of the quadruple based device, on the other hand, lied in the plateau of its voltammogram, and thus, was less sensitive to potential changes in the photovoltage or to variations of the electrolyte series resistance, *i.e.* variations in the "fill factor" (see Section 4.2.2). Nevertheless, the devices shown in Fig. 6.6, exhibited a rather poor "fill factor" due to the series resistance imposed by the 0.1 M KOH electrolyte solution. Therefore, the influence of higher concentrated, *i.e.* high conductive electrolytes will be elucidated in the following.

## 6.2.2 Influence of the electrolyte

The effect of the KOH electrolyte concentration on the performance and stability of the triple (a-Si:H/a-Si:H/ $\mu\text{c-Si:H}$ ) and quadruple junction based PV-EC devices are shown in Fig. 6.7 and Fig. 6.8, respectively. In the case of the triple junction based device an increase of  $0.7 \text{ mA/cm}^2$  in the operation photocurrent density  $j_{\text{op}}$  to  $7.7 \text{ mA/cm}^2$  was observed when 1 M KOH was used as electrolyte solution instead of 0.1 M KOH. From Fig. 6.7 it becomes apparent that this increase was caused by an improvement of the "fill factor" in the voltammograms of the triple junction based PV-EC devices, as already mentioned in the foregoing section. In fact, as discussed in Section 4.3, an increase in the electrolyte concentration reduces the series resistance of the complete PV-EC device, which leads to an improved "fill factor" [154]. According to Eq. 4.4, an STH efficiency of 9.5 % was estimated from the  $j_{\text{op}}$  value of  $7.7 \text{ mA/cm}^2$  for the triple based PV-EC device with Pt as HER and  $\text{RuO}_2$  as OER catalyst.

Referring to a recently published overview of demonstrated STH conversion efficiencies [32], this is the highest reported STH efficiency for an integrated thin film silicon based photoelectrochemical device. A comparison of the reported solar-to-hydrogen efficiencies of thin film silicon based solar water splitting systems is given in Section 6.4 in Fig. 6.17. STH efficiencies over 10 % would become feasible by using anti-reflection foils to enhance the saturation photocurrent densities of

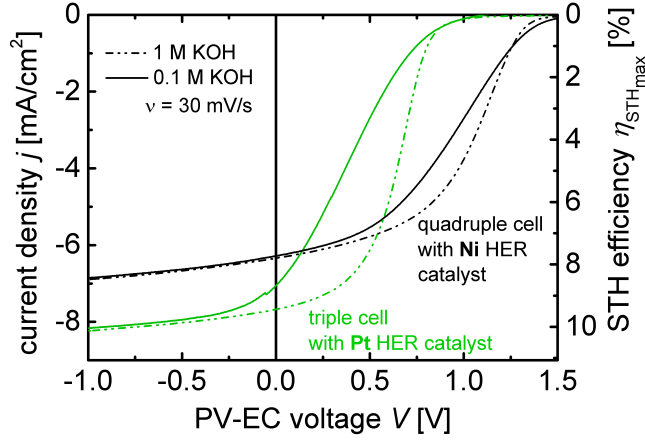


**Fig. 6.7** Linear sweep voltammetry measurements of the a-Si:H/a-Si:H/ $\mu$ c-Si:H and the quadruple junction based PV-EC devices with Pt and Ni catalyst layers, respectively, in 0.1 M (solid curves) and 1 M KOH (dotted curves).  $\text{RuO}_2$  was used as a counter electrode for the OER reaction and the measurements were conducted in 0.1 M KOH at a scan rate of 30 mV/s. The right ordinate depicts the achievable STH efficiency as a function of the photocurrent density at 0 V applied bias.

the a-Si:H/a-Si:H/ $\mu$ c-Si:H solar cell in the PV-EC device configuration by around  $0.4 \text{ mA/cm}^2$  from  $8.2$  to  $8.6 \text{ mA/cm}^2$  (see Fig. 5.21).

However, the issue of photocorrosion, particularly present for electrolyte concentrations of or above 1 M, need to be solved at the same time. Fig. 6.8 displays the photocurrent density at 0 V applied bias monitored over a prolonged period of time for the quadruple junction based device with a Ni HER catalyst and for the a-Si:H/a-Si:H/ $\mu$ c-Si:H based device with a Pt HER catalyst in 0.1 M and 1 M KOH, respectively. In 0.1 M KOH a stable photocurrent of approx.  $6.1 \text{ mA/cm}^2$  and  $7.0 \text{ mA/cm}^2$ , respectively, was measured for both PV-EC devices over the course of 4 hours (approx. 15000 s). The periodical fluctuations in the photocurrent densities were caused by repetitive accumulation and detachment of  $\text{H}_2$  bubbles at the photocathode surface. The measurements in 1 M KOH revealed that both devices did not operate longer than approx. 30 and 60 minutes with the Ni and the Pt HER catalyst, respectively. This result confirms that a change in the pH value from approx. 13 (0.1 M KOH) to approx. 14 (1 M KOH) can cause significant effects on the stability

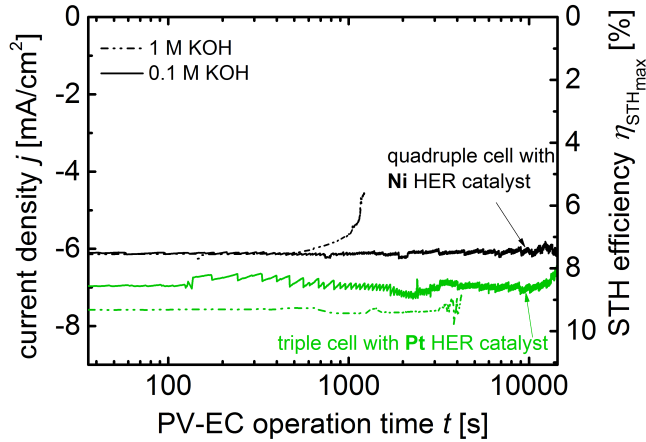


**Fig. 6.8** Chronoamperometric stability measurement monitoring the long-term stability of the a-Si:H/a-Si:H/ $\mu$ c-Si:H and the quadruple junction based PV-EC devices with Pt and Ni catalyst layers (on top of Ag contacts), respectively, at 0 V applied bias. The measurements were conducted in 0.1 M (solid curves) and in 1 M KOH (dotted curves) under AM 1.5 illumination (100 mW/cm<sup>2</sup>). RuO<sub>2</sub> was used as a counter electrode for the OER reaction. The right ordinate depicts the achievable STH efficiency as a function of the photocurrent density at 0 V applied bias. The abscissa indicates the PV-EC operation time on a logarithmic scale.

of the PV-EC devices. In particular, pitting corrosion and subsequent delamination of the metal contact stack at the solar cell/electrolyte interface prevented longer operation times.

In this regard, the high photovoltage provided by the quadruple junction based device offers an additional advantage. As apparent from Fig. 6.7 and from Fig. 6.8 (black curves), the increase in electrolyte concentration did not affect the operation photocurrent density of the quadruple based PV-EC device, which exhibited 6.1 mA/cm<sup>2</sup> as  $j_{\text{op}}$  for the measurements conducted in 0.1 M and 1 M KOH, respectively. This result can be understood, because the device operated in the current plateau region, where an improved "fill factor" did not improve the current density (see Fig. 6.7). This overall shows that quadruple junction solar cells not only promote the usage of cheaper catalyst materials, but also allow for the operation in low-concentrated electrolytes without impairing the device efficiency, and thus, for an

increased long-term stability of the device and the catalysts.

Concerning the aspect of stability, also the stability against LID affects the PV-EC device performance. In this regard, the high stability against LID of the quadruple junction solar cell, presented in Section 5.6, might offer an additional advantage and will be discussed in the following section.

### 6.2.3 Influence of light induced degradation

In Section 5.6 the effects of light induced degradation of the silicon layers with respect to the photovoltaic parameters of the developed multijunction solar cells were examined. Here, the focus is set on the impact of LID on the solar-to-hydrogen efficiency for silicon based PV-EC devices<sup>3</sup>. To evaluate the effect of LID on the PV-EC device performance, the stabilised solar cells (after 1000 h of light soaking, see Table 5.7) were used as photocathodes in PV-EC devices and compared to the performance of the initial solar cell based PV-EC devices from Fig. 6.5. In Fig. 6.9 the initial and stabilised PV-EC device types are plotted together.

The voltammograms in Fig. 6.9 revealed that the solar cell related parameters, such as the photocurrent densities, the photovoltages and the fill factors, showed similar trends in the PV and in the PV-EC configuration upon LID. For instance, as already apparent from Table 5.7, the "fill factor" of the a-Si:H/a-Si:H based PV-EC device was stronger affected than the "fill factor" of the a-Si:H/a-Si:H/ $\mu$ c-Si:H based device. Nevertheless,  $j_{\text{op}}$ , *i.e.*  $\eta_{\text{STH}_{\text{max}}}$ , was affected differently compared to the photovoltaic efficiency  $\eta_{\text{PV}}$ . To elucidate this, Table 6.2 lists the estimated initial and stabilised solar-to-hydrogen efficiencies of the PV-EC devices ( $\eta_{\text{STH}_{\text{max}}}$  and  $\eta_{\text{STH}_{\text{max,stab}}}$ ) along with the relative degradation in the PV-EC and in the PV configuration ( $\eta_{\text{STH}_{\text{max}}}/\eta_{\text{STH}_{\text{max,stab}}}$  and  $\eta_{\text{PV}}/\eta_{\text{PV,stab}}$ ), which are presented in the last columns of Table 6.2.

For all cell types the relative efficiency degradation was less pronounced in the PV-EC configuration than in the PV configuration, except for the a-Si:H/a-Si:H based device. As apparent from Fig. 6.9, the strong decrease in "fill factor" shifted the operation point of the a-Si:H/a-Si:H device to significant lower values, which is why  $\eta_{\text{STH}_{\text{max}}}/\eta_{\text{STH}_{\text{max,stab}}}$  was decreased compared to  $\eta_{\text{PV}}/\eta_{\text{PV,stab}}$ .

<sup>3</sup>Some of the results presented in this section were published in F. Urbain, *et al.*, Sol. Energy Mater. Sol. Cells **145** (2016), 142-147. [39]

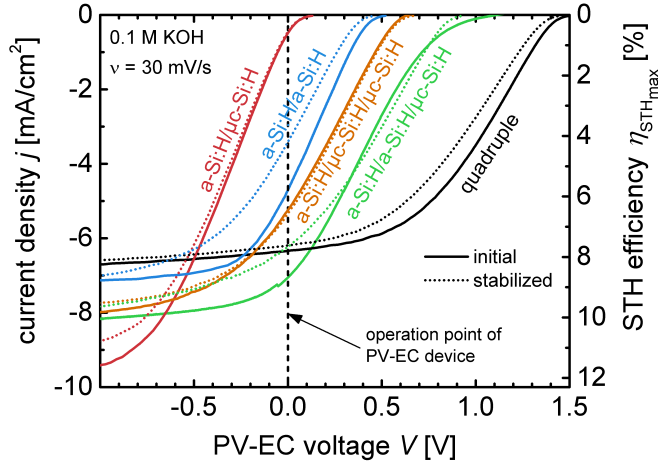


**Fig. 6.9** Comparison of the current density-voltage characteristics of PV-EC devices based on the initial (solid lines, same curves as in Fig. 6.5) and the light soaked ("stabilised", dotted lines) multijunction solar cells. A 150 nm thick Pt layer was used as the HER catalyst and a RuO<sub>2</sub> counter electrode for the OER reaction. The measurements were conducted in 0.1 M KOH at a scan rate of 30 mV/s. The right ordinate depicts the achievable STH efficiency as a function of the photocurrent density at 0 V applied bias.

The highest  $\eta_{\text{STH,max,stab}}$  of 7.6 % was provided by the quadruple junction and by the a-Si:H/a-Si:H/ $\mu$ c-Si:H based PV-EC devices. Whereas the estimated solar-to-hydrogen efficiency of the triple based device degraded by around 12 % upon prolonged light exposure, the quadruple based device showed a high stability against LID and degraded only by less than 2 %. The corresponding voltammogram in Fig. 6.9 showed a slight shift in the onset potential for cathodic photocurrent density (taken as the value at  $-0.5 \text{ mA/cm}^2$ ) of approx. 50 mV (from 1360 mV to 1310 mV). This corresponds to the reduction in  $V_{\text{OC}}$  from the initial to the stabilised state for the quadruple junction solar cell (see cell Q3 in Table 5.7). The decrease of  $FF$  after light soaking was apparent in both, the PV-EC and the photovoltaic arrangement. However, in the PV-EC configuration, the reduction in  $FF$  did not affect the operation point of the PV-EC device significantly, which after light soaking of the solar cell still lied in the photocurrent plateau region (see Fig. 6.9).

**Table 6.2** Overview of the estimated initial and stabilised (after 1000 h of light soaking) solar-to-hydrogen efficiencies of multijunction based PV-EC devices. The  $\eta_{\text{STH}_{\text{max}}}$  and  $\eta_{\text{STH}_{\text{max,stab}}}$  values are evaluated from the  $j_{\text{op}}$  values in Fig. 6.9. The relative degradation of the solar-to-hydrogen efficiency is also listed and compared to the degradation of the photovoltaic efficiency  $\eta_{\text{PV}}$ , calculated from Table 5.7.

PV-EC Device type	$\eta_{\text{STH}_{\text{max}}}$ [%]	$\eta_{\text{STH}_{\text{max,stab}}}$ [%]	$\eta_{\text{STH}_{\text{max}}} / \eta_{\text{STH}_{\text{max,stab}}}$	$\eta_{\text{PV}} / \eta_{\text{PV,stab}}$
a-Si:H/ $\mu$ c-Si:H	0.61	0.60	0.98	0.95
a-Si:H/a-Si:H	5.8	4.2	0.72	0.88
a-Si:H/ $\mu$ c-Si:H/ $\mu$ c-Si:H	6.5	6.4	0.99	0.97
a-Si:H/a-Si:H/ $\mu$ c-Si:H	8.7	7.6	0.88	0.87
a-Si:H/a-Si:H/ $\mu$ c-Si:H/ $\mu$ c-Si:H	7.8	7.6	0.98	0.96

In total, it can be concluded that the degradation upon illumination (up to 1000 h) for the quadruple, the a-Si:H/ $\mu$ c-Si:H/ $\mu$ c-Si:H, and for the a-Si:H/ $\mu$ c-Si:H based PV-EC devices is nearly negligible compared to degradation due to corrosion of the electrodes, which leads to much more severe failure of the device. Please note that actually the LID and the electrochemical stability cannot be linked to each other that easily. Whereas the corrosion very abruptly degrades and destroys the photoelectrode, the LID imposes a continuous degradation on the photoelectrode. In the literature, typical electrochemical durabilites of silicon based photoelectrochemical devices are in the range of less than 100 h [154, 195, 196]. For the a-Si:H/a-Si:H and a-Si:H/a-Si:H/ $\mu$ c-Si:H based PV-EC devices the impact of LID needs to be taken into account, also in the PV-EC configuration.

## 6.3 Device analysis by modeling

So far, the fabricated PV-EC devices, composed of photovoltaic and electrochemical components, were evaluated only by means of photoelectrochemical measurements. This section highlights to what extend the PV-EC device characteristics can be modeled in terms of a series connection of a solar cell and an electrolysis cell. In the series circuit model, introduced in Section 4.3, the corresponding photovoltaic and electrochemical components are decoupled. This allows to closely link the PV

performance of the used solar cell with the PV-EC behavior of the integrated device, from which the relevant loss processes in the overall system will be identified. The model was further used to compare calculated and measured current density-voltage characteristics of the investigated PV-EC device<sup>4</sup>.

### 6.3.1 Modeling of the current-voltage characteristics

#### System loss analysis

The two-electrode measurements shown in the preceding section (*e.g.* Fig. 6.5, Fig. 6.6, or Fig. 6.7) display the overall behavior of the complete PV-EC device. However, this data does not allow to quantitatively evaluate the individual contributions of the PV-EC components separately. For this purpose, the PV-EC device must be treated as a series connection of its four main circuit components: (1) the solar cell with the ZnO:Al/Ag back reflector, (2) the HER catalyst layer, which was deposited on top of the ZnO:Al/Ag back reflector, (3) the electrolyte, and (4) the anode. As presented in Section 4.3, the current density-voltage characteristic  $V_{\text{PV-EC}}(j)$  of the whole PV-EC device can be calculated via Eq.4.1. For the implementation in the model,  $\eta_{\text{OER}}(j)$  and  $\eta_{\text{HER}}(j)$  can either be measured or modeled by using the Tafel relation in combination with literature data (see Section 2.2.3). Here,  $\eta_{\text{OER}}(j)$  and  $\eta_{\text{HER}}(j)$  were measured in a three-electrode arrangement. The resistance of the electrolyte  $R$  was determined by impedance spectroscopy and the  $j$ - $V$  characteristics of the solar cell  $V_{\text{PV}}(j)$  were measured under AM 1.5 illumination. The model underlying series connection of the PV-EC device components is also shown in Section 4.3 in Fig. 4.3.

In fact, as apparent from Eq. 4.1, the performance of the PV-EC cell is deteriorated by the relevant loss mechanisms in the system represented by  $\eta_{\text{OER}}(j)$ ,  $\eta_{\text{HER}}(j)$ , and  $R$ : The OER and HER overpotential at the anode and cathode surfaces, respectively, and the ohmic drop due to the resistance of the electrolyte given by the value of  $R$ . To graphically illustrate this, Fig. 6.10 shows the current density-voltage measurements of the four circuit components. As example, an a-Si:H/a-Si:H tandem junction cell was chosen as solar cell, the HER catalyst was a Pt layer, the OER catalyst was a RuO<sub>2</sub> coated electrode, and H<sub>2</sub>SO<sub>4</sub> was taken as electrolyte solution. The hereout calculated current density-voltage characteristic  $V_{\text{PV-EC}}(j)$  of the PV-EV device, based on Eq. 4.1, is also plotted in Fig. 6.10.

<sup>4</sup>Some of the results presented in this section were published in F. Urbain, *et al.*, Sol. Energy Mater. Sol. Cells **140** (2015), 275-280. [154]

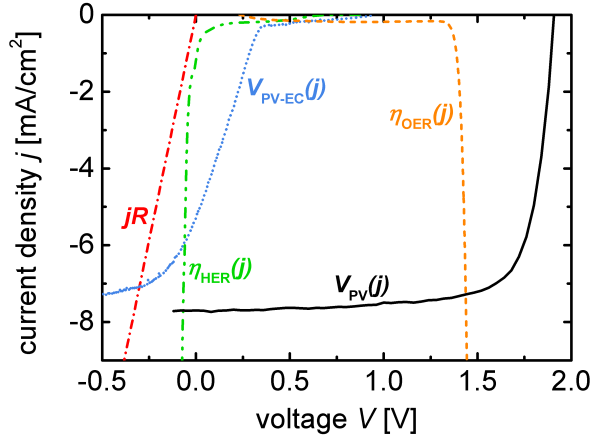


**Fig. 6.10** Current density-voltage characteristics of the main four circuit components of the PV-EC device:  $j$ - $V$  measurement of an a-Si:H/a-Si:H/ZnO:Al/Ag solar cell ( $V_{PV}(j)$ , black solid curve), voltammogram of the RuO<sub>2</sub> anode in a 0.1 M H<sub>2</sub>SO<sub>4</sub> solution at a scan rate of 5 mV/s (with the associated  $\eta_{OER}(j)$ , orange dashed curve), voltammogram of the Pt HER catalyst layer in a 0.1 M H<sub>2</sub>SO<sub>4</sub> solution at a scan rate of 5 mV/s (with the associated  $\eta_{HER}(j)$ , green dashed curve), and resistance of the 0.1 M H<sub>2</sub>SO<sub>4</sub> electrolyte ( $jR$ , red dotted line). The current density-voltage characteristic of the PV-EC device ( $V_{PV-EC}(j)$ , blue dashed curve) was calculated based on Eq. 4.1.

This graph allows for a decoupled evaluation of the photoelectrochemical and photovoltaic performance of the complete PV-EC device  $V_{PV-EC}(j)$  and of the integrated solar cell  $V_{PV}(j)$ , respectively, and highlights the main differences between both. The saturation photocurrent densities and the "fill factors" showed the same behavior as already discussed in Section 4.3 (see Fig. 4.4). The discrepancy in the open-circuit voltage values for the PV and the PV-EC devices arises from the Pt and the RuO<sub>2</sub> electrode overpotential losses, respectively.

### Validation of the model by using empirical data

In order to validate the model, it was applied to several PV-EC device configurations with different component assemblies (different solar cell types, different HER and OER catalysts, respectively, and different electrolytes). The  $j - V$  data of the



corresponding components were experimentally measured and implemented in the model. Fig. 6.11 presents the comparison between the measured and calculated current density-voltage characteristics of the exemplarily chosen PV-EC device from Fig. 6.10 and two other PV-EC device configurations with varying device components (solar cell type, HER/OER catalyst, and electrolyte).

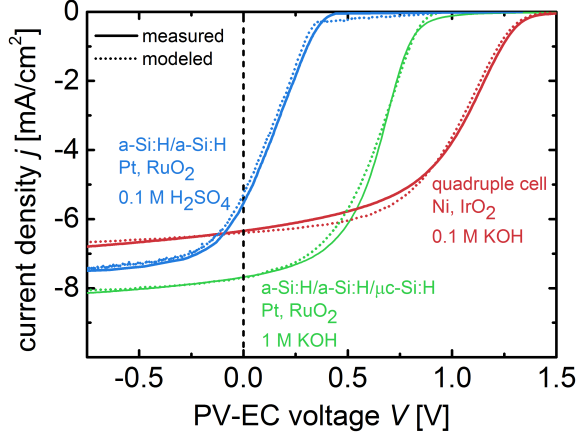


**Fig. 6.11** Comparison of measured (solid curves, scan rate 30 mV/s) and calculated (dashed curves) voltammograms of three PV-EC devices with different configurations. The blue curves represent the current density-voltage behavior of a PV-EC device composed of an a-Si:H/a-Si:H tandem junction solar cell with Pt and RuO<sub>2</sub> as HER and OER catalyst, respectively, measured in 0.1 M H<sub>2</sub>SO<sub>4</sub> (individual measurements can be found in Fig. 6.10). The green curves show the current density-voltage characteristics of an a-Si:H/a-Si:H/ $\mu$ c-Si:H triple junction based PV-EC device with Pt and RuO<sub>2</sub> as catalyst materials, measured in 1 M KOH. The red curves display the current density-voltage characteristics of a PV-EC device based on a quadruple junction solar cell with Ni and IrO<sub>2</sub> as HER and OER catalysts, respectively, measured in 0.1 M KOH.

It is apparent that the calculated voltammograms nearly perfectly match the experimental data and thus, mirror the overall behavior of the PV-EC device. This confirms that the presented series circuit model allows for both, the separate evaluation of the losses of the individual PV-EC components, as shown in Fig. 6.10, and the prediction of the overall PV-EC performance considering these losses. The

slight discrepancies may arise from fluctuations in the open-circuit potential region during the individual HER and OER catalyst measurements. Additional fluctuations may arise from interfacial charging effects at the catalyst/electrolyte double-layer interfaces, respectively [58].

In conclusion, the presented empirical series circuit model offers a useful and elegant tool to analyse and predict the performance of integrated PV-EC devices based on experimental data of each individual functional component. Therefore, as the model allows for the decoupled evaluation of all functional device components, one can estimate to what extent an improvement of an individual component (*e.g.*  $V_{OC}$  and  $J_{SC}$  of the solar cell or catalytic activity of the HER and OER catalyst material) or a reduction of a specific loss mechanism (*e.g.* electrolyte resistance or overpotential loss at one of the electrodes) would improve the overall PV-EC device performance and increase STH efficiency further.

### PV-EC device performance for different catalysts by using literature data

In Table 6.3 some of the state-of-the-art HER and OER catalyst materials are listed along with their experimentally determined Tafel slopes and exchange current densities, available from literature.

**Table 6.3** Tafel slopes and exchange current densities of benchmarking catalyst materials for the HER and OER. The corresponding literature references are given in the last column.

Catalyst	Tafel slope $b$ [mV/dec]	Exchange current density $j_0$ [mA/cm <sup>2</sup> ]	Reaction	Reference
Pt	30	1.0	HER	[197]
Ni	80	$6.0 \cdot 10^{-2}$	HER	[198]
Mo <sub>2</sub> C	78	$4.4 \cdot 10^{-3}$	HER	[199]
MoS <sub>2</sub>	50	$6.9 \cdot 10^{-4}$	HER	[200]
RuO <sub>2</sub>	42	$1.2 \cdot 10^{-4}$	OER	[201]
IrO <sub>2</sub>	33	$9.5 \cdot 10^{-5}$	OER	[201]
NiO <sub>x</sub>	63	$2.5 \cdot 10^{-4}$	OER	[202]
Co <sub>3</sub> O <sub>4</sub>	49	$2.0 \cdot 10^{-7}$	OER	[203]

Fig. 6.12 shows the current density-voltage characteristics for different HER and OER catalysts as obtained *via* Eq. 2.14 using the Tafel parameters provided in Table 6.3. Obviously, the overpotentials  $\eta_{\text{HER}}(j)$  and  $\eta_{\text{OER}}(j)$  at a given current density are lowest for the very active catalysts Pt and  $\text{RuO}_2$ , respectively.  $\text{Co}_3\text{O}_4$  exhibits the highest overpotential among the three OER catalysts and  $\text{MoS}_2$  shows the highest  $\eta_{\text{HER}}(j)$ . Thus, a better photoelectrochemical performance of the integrated device can be expected when  $\text{MoS}_2$  and  $\text{Co}_3\text{O}_4$  are replaced by  $\text{Mo}_2\text{C}$ , Ni, or Pt as for the HER and by  $\text{NiO}_x$ ,  $\text{IrO}_2$ , or  $\text{RuO}_2$  for the OER. These expectations are

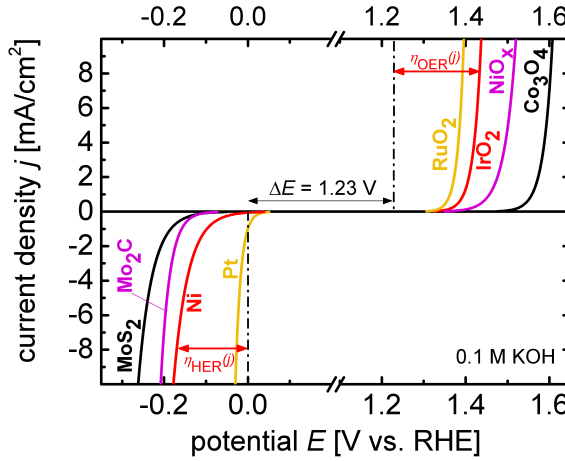


**Fig. 6.12** Modeled current density-voltage curves of the HER and OER catalysts considered in this section. The curves were computed *via* Eq. 2.14 using the Tafel parameters provided in Table 6.3. As example, the overpotentials for Ni ( $\eta_{\text{HER}}(j)$ ) and for  $\text{IrO}_2$  ( $\eta_{\text{OER}}(j)$ ) are indicated.

confirmed by Fig. 6.13 which plots the photoelectrochemical voltammograms of an a-Si:H/a-Si:H tandem, of an a-Si:H/a-Si:H/ $\mu\text{c-Si:H}$  triple, and of a quadruple junction based PV-EC device featuring different pairs of HER and OER catalysts. An electrolyte resistance of  $56\ \Omega$  was assumed (0.1 M KOH, see Table 6.4). This investigation underlies the assumption that the given values of  $b$  and  $j_0$  are applicable for 0.1 M KOH electrolyte solution. In fact, only slight deviations in  $b$  and  $j_0$  were observed in strong alkaline or acid solutions [204].

Fig. 6.13(a)-(c) graphically illustrate the impact of the catalyst choice for the PV-EC device performance. As expected, the usage of expensive and precious metal

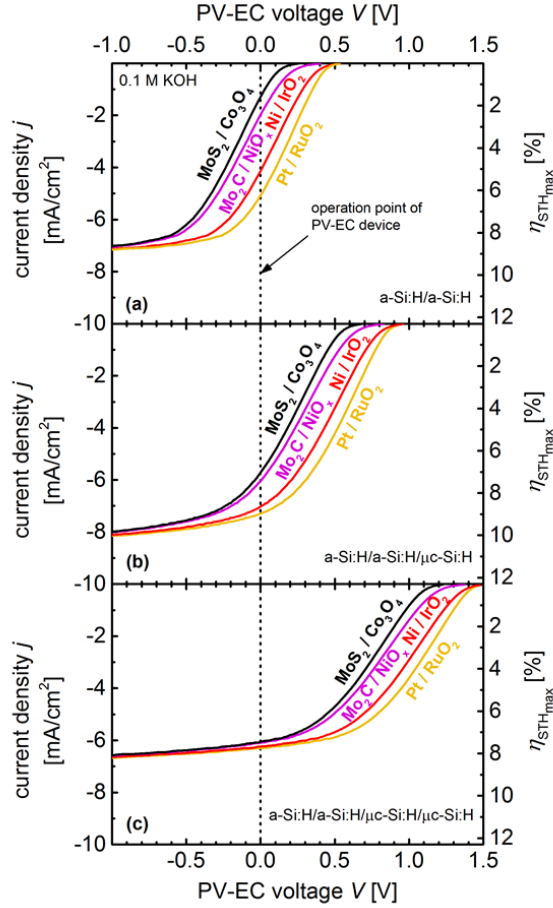


**Fig. 6.13** Calculated voltammograms of a-Si:H/a-Si:H (a), a-Si:H/a-Si:H/ $\mu$ c-Si:H (b), and quadruple junction (c) based PV-EC devices with varying HER and OER catalysts. The HER/OER catalyst combinations are: Pt/RuO<sub>2</sub> (yellow curves), Ni/IrO<sub>2</sub> (red curves), Mo<sub>2</sub>C/NiO<sub>x</sub> (purple curves), and MoS<sub>2</sub>/Co<sub>3</sub>O<sub>4</sub> (black curves). The respective values of  $b$  and  $j_0$  for the  $j$ - $V$  calculation are taken from Table 6.3. An electrolyte resistance of 56  $\Omega$  was assumed (0.1 M KOH, see Table 6.4). The respective solar cell type is indicated in the corresponding figure. The right ordinate depicts the achievable STH efficiency as a function of the photocurrent density at 0 V applied bias.

HER and OER catalysts, such as Pt and RuO<sub>2</sub>, respectively, led to the highest calculated photocurrent densities  $j_{op}$  at 0 V applied bias, and thus, to the highest STH values. When cost-effective and more earth-abundant material combinations are used to catalyse the HER and OER reactions, which suffer from lower reaction kinetics, *i.e.* higher overpotential losses, a clear shift of the onset potential for cathodic current in negative bias direction was observed. In the case of the a-Si:H/a-Si:H and a-Si:H/a-Si:H/ $\mu$ c-Si:H based devices, this significantly affected the  $j_{op}$  of the voltammograms. For the a-Si:H/a-Si:H devices the STH efficiency decreased from 6.2 % for a Pt/RuO<sub>2</sub> catalyst combination to 1.5 % for a MoS<sub>2</sub>/Co<sub>3</sub>O<sub>4</sub> combination (see Fig. 6.13(a)). Due to the higher photovoltages of the a-Si:H/a-Si:H/ $\mu$ c-Si:H cell, which led to higher onset potentials for cathodic current, the operation point of the corresponding PV-EC devices was shifted more to the MPP (see Fig. 6.13(b)). In this region of the voltammograms the decrease in STH efficiency (from 9.0 % to 7.0 %) was less pronounced compared to the a-Si:H/a-Si:H based devices. Finally, as shown in Fig. 6.13(c), the  $j_{op}$  values for the quadruple based PV-EC devices remained nearly unaffected by the variation of the HER and OER catalysts. In spite of the fact that the STH efficiency for the Pt/RuO<sub>2</sub> catalyst combination ( $\eta_{STH_{max}} = 7.8$  %) was lower compared to the a-Si:H/a-Si:H/ $\mu$ c-Si:H device ( $\eta_{STH_{max}} = 9.0$  %), the quadruple based device provided enough excess voltage to compensate the overpotential losses of the cost-effective and earth-abundant catalyst materials. For the MoS<sub>2</sub>/Co<sub>3</sub>O<sub>4</sub> HER/OER catalyst combination, the STH efficiency only slightly decreased to a minimum STH efficiency of 7.5 %.

Overall, this result elucidates the importance in PV-EC devices to adapt the photovoltaic to the electrochemical properties and *vice versa*. In this regard, the tunability of the photovoltaic parameters, especially of the  $V_{OC}$ , is a vital feature and offers a lot of freedom in the design of all kinds of photoelectrochemical devices.

### 6.3.2 Temperature-dependent photoelectrochemical performance

In this part, the effects of a temperature increase on the performance of PV-EC devices are addressed exemplarily for the a-Si:H/a-Si:H/ $\mu$ c-Si:H triple junction solar cell<sup>5</sup>. The investigation of temperature effects is a crucial aspect when the implementation on an industrial level is considered. Herein, the temperature-dependent current

---

<sup>5</sup>The results presented in this section were published in F. Urbain, *et al.*, Mater. Sci. Sem. Proc. **42** (2016), 142-146 [189].

density-voltage behavior of the individual PV-EC device components were measured, *i.e.* of the triple junction thin film silicon solar cell (see Section 5.7) and of both catalyst carrying electrodes: a thin Pt layer attached on top of the solar cell for the HER and a  $\text{RuO}_2$  counter electrode for the OER. Furthermore, KOH was used as an electrolyte and its resistance was measured as a function of the temperature for concentrations of 0.1 M and 1 M. The current density-voltage behavior of the whole device was finally obtained by merging the individual parts in terms of the empirical series circuit model, presented in the preceding section. The results provide important guidelines for the PV-EC operation parameters that account for various performance trade-offs of the PV-EC components at different operation temperatures  $T_{\text{op}}$ .

### Temperature dependence of the electrolyte resistance

Table 6.4 lists the resistance  $R$  of the electrolyte for the given set-up as a function of the operation temperature  $T_{\text{op}}$  for 0.1 M and 1 M KOH as determined by electrochemical impedance spectroscopy. The resistance linearly decreased with increasing temperature for both electrolyte concentrations. In the 0.1 M KOH solution the resistance decreased from  $56.0\ \Omega$  to  $35.3\ \Omega$  and in the 1 M KOH solution a decrease from  $5.8\ \Omega$  at  $25\ ^\circ\text{C}$  to  $4.0\ \Omega$  at  $60\ ^\circ\text{C}$  was measured.

The resistance of the electrolyte is strongly related to the mobility of the ions in solution. A temperature increase stimulates higher ion mobility and thus, a lower electrolyte resistance [205]. This trend was confirmed in the measurements for both 0.1 M and 1 M KOH, respectively.

### Temperature dependence of the HER and OER catalysts

Fig. 6.14(a) and (b) depict the current density-voltage measurements of the Pt and  $\text{RuO}_2$  electrodes measured at various temperatures  $T_{\text{op}}$  in a three-electrode configuration in 0.1 M and 1 M KOH solutions, respectively. For the Pt cathode, the slight shift of the onset potential for the cathodic current density  $E_{\text{onset}}$  in anodic direction as well as the steeper slope indicate that the HER catalysis was enhanced with increasing temperature. In the case of the  $\text{RuO}_2$  anode, a similar, however, more distinct trend was observed. In 0.1 M KOH the onset potential for the anodic current density  $E_{\text{onset}}$  (taken at a value of  $0.5\ \text{mA}/\text{cm}^2$ ) was shifted in cathodic direction by around 65 mV. Note that during the measurement, fluctuations in the current density were caused by repetitive accumulation and detachment of  $\text{H}_2$  bubbles covering parts of the electrode surface. In 1 M KOH, anodic  $E_{\text{onset}}$  shifted

**Table 6.4** The resistances  $R$  of the electrolyte for the used set-up with KOH concentrations of 0.1 M and 1 M, respectively. The resistances were determined by means of electrochemical impedance spectroscopy at different temperatures of the electrolyte.

Temperature $T_{\text{op}}$ [°C]	Electrolyte resistance $R$ [Ω]	
	0.1 M KOH	1 M KOH
25	56.0	5.8
30	53.7	5.4
35	48.6	5.2
40	47.4	4.9
45	43.3	4.9
50	40.1	4.7
55	37.8	4.3
60	35.3	4.0

to more cathodic potentials by approx. 45 mV in the investigated temperature range. Hence, the catalysis of the OER on the  $\text{RuO}_2$  anode was also enhanced by elevated operation temperatures in both 0.1 M and 1 M KOH solutions. The enhanced catalytic performance with temperature can be related to a kinetically enhanced charge carrier transfer from the catalyst material into the electrolyte at elevated operation temperatures [206].

### Temperature dependence of the PV-EC device

As it was previously shown, the PV-EC device can be separated into a series connection of its components. Thus, for a given operation temperature the current density-voltage characteristic  $V_{\text{PV-EC}}(j, T)$  of the whole PV-EC device can be calculated by merging (similar to Eq. 4.1) the current density-voltage characteristics of all its components at the respective temperature  $T$  via

$$V_{\text{PV-EC}}(j, T) = V_{\text{PV}}(j, T) - \Delta E - \eta_{\text{OER}}(-j, T) + \eta_{\text{HER}}(j, T) + jR(T) \quad . \quad (6.1)$$

Here  $V_{\text{PV}}(j, T)$  denotes the temperature-dependent current density-voltage measurement of the a-Si:H/a-Si:H/ $\mu\text{c-Si:H}$ /ZnO:Al/Ag solar cell (see Fig. 5.18 in Section 5.7).

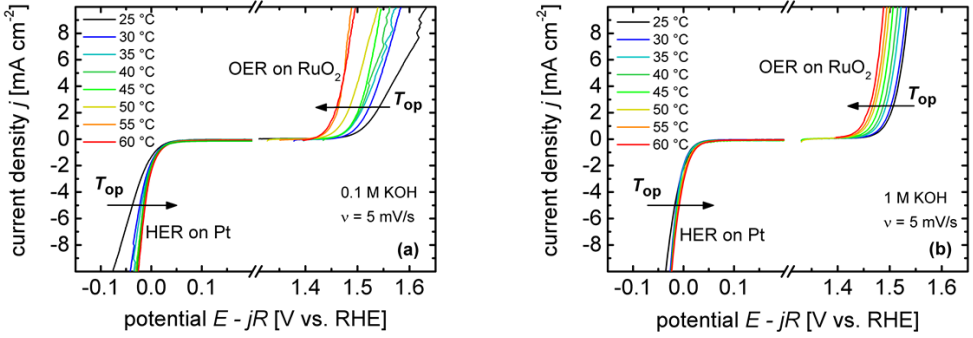


**Fig. 6.14** (a) Linear sweep voltammetry measurements showing the cathodic and anodic current density-voltage dependence of the Pt and RuO<sub>2</sub> electrodes, respectively, in 0.1 M KOH. (b) Linear sweep voltammetry measurements showing the cathodic and anodic current density-voltage dependence of the Pt and RuO<sub>2</sub> electrodes, respectively, in 1 M KOH. The measurements were conducted at a scan rate of 5 mV/s at different operation temperatures  $T_{op}$ . The potentials were corrected by the  $jR$ -drop in the electrolyte.

$\eta_{OER}(-j, T)$  is the temperature-dependent current density-potential measurement of the RuO<sub>2</sub> anode including the electrode potential for the OER and  $\eta_{HER}(j, T)$  is the temperature-dependent current density-potential measurement of the Pt cathode. The resistance of the electrolyte as a function of temperature is denoted by  $R(T)$ . In order to take the different sign of the anodic current for the RuO<sub>2</sub> anode into account, the corresponding three-electrode measurement has to be mirrored at the abscissa, *i.e.* subtracted in Eq. 6.1. The temperature dependence of  $\Delta E$  is expressed by the Nernst equation (see Eq. 2.5 in Section 2.2.2) [207].

When the model is fed with the experimentally measured temperature-dependent data, the current density-voltage behavior of the PV-EC device can be calculated. In Fig. 6.15 the calculated  $V_{PV-EC}(j, T)$  curves for 0.1 M and 1 M KOH, respectively, are displayed for all investigated operation temperatures. The cathodic shift in the onset potentials of the calculated  $V_{PV-EC}(j, T)$  curves, in 0.1 M and 1 M KOH, correlates with the decrease in  $V_{OC}$  of the underlying triple junction solar cell, shown in Fig. 5.18. Furthermore, the saturation photocurrent density increased slightly with increasing temperature. Again, this reflects the temperature-dependence of the solar cell (see the  $J_{SC}$  values in Fig. 5.18).



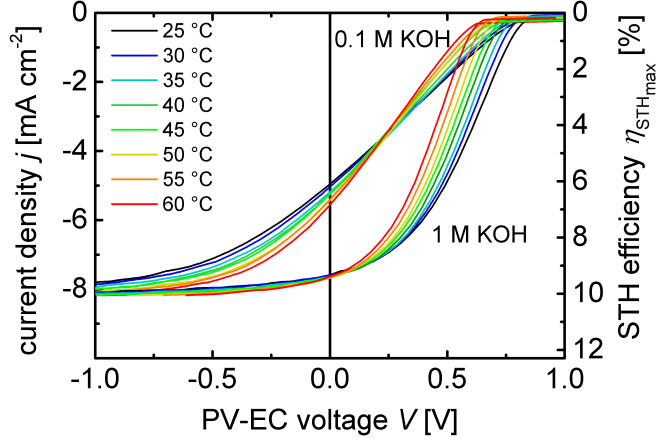


**Fig. 6.15** Calculated current density-voltage curves of the a-Si:H/a-Si:H/ $\mu$ c-Si:H based PV-EC device at different operation temperatures in 0.1 M and 1 M KOH, respectively. The data for the calculation of the  $V_{\text{PV-EC}}(j, T)$  (based on Eq. 6.1) curves was taken from Table 6.4 ( $T$ -dependent electrolyte resistances  $R(T)$ ), from Fig. 6.14(a) and (b), respectively ( $T$ -dependent HER and OER performance,  $\eta_{\text{HER}}(j, T)$  and  $\eta_{\text{OER}}(j, T)$ , respectively). The current density at 0 V applied bias defines the operation point of the PV-EC device.

Additionally, Fig. 6.15 illustrates the impact of the electrolyte concentration on the operating current density (at 0 V)  $j_{\text{op}}$ , which is crucial for the PV-EC device. In the 1 M solution a significantly higher  $j_{\text{op}}$  was found than in the 0.1 M solution. This discrepancy is mainly due to the distinct change in "fill factor" of the  $V_{\text{PV-EC}}(j, T)$  curves. The poor "fill factor" of the curves in 0.1 M KOH reflects the high electrolyte resistance presented in Table 6.4, which caused the operation point (at 0 V applied bias) of the PV-EC device to be located in the steep slope of the  $V_{\text{PV-EC}}(j, T)$  curves. Nevertheless, the current density at 0 V increased from 25 °C to 60 °C from 4.96 mA/cm<sup>2</sup> to 5.58 mA/cm<sup>2</sup>. In the 1 M KOH solution, the electrolyte resistance was significantly lower, which led to an improved "fill factor". As a consequence, the operation point of the PV-EC devices lied in the current plateau of the  $V_{\text{PV-EC}}(j, T)$  curves, which resulted in higher current densities  $j_{\text{op}}$  of approx. 7.6 mA/cm<sup>2</sup> for all investigated temperatures.

In Fig. 6.16, the calculated solar-to-hydrogen efficiencies are plotted versus the operation temperature. In the 0.1 M KOH solution the  $\eta_{\text{STH}_{\text{max}}}$  followed the

trend of  $j_{\text{op}}$  and increased with increasing temperature from 6.1 % at 25 °C up to a value of 6.9 % at 60 °C. In the 1 M KOH solution the  $\eta_{\text{STH}_{\text{max}}}$  was less sensitive to temperature variations, which is beneficial for outdoor operation under varying conditions. At 25 °C a  $j_{\text{op}}$  of 7.6 mA/cm<sup>2</sup> was found, which can be translated into a solar-to-hydrogen efficiency of 9.4 %, while a maximum solar-to-hydrogen efficiency (9.6 %) was shown at 50 °C. The  $V_{\text{PV-EC}}(j, T)$  characteristics of tandem and quadruple junction based PV-EC devices can be found in Fig. A3(a) and (b), respectively. In both cases the  $\eta_{\text{STH}_{\text{max}}}$  was not deteriorated upon temperature increase, and thus, confirms the findings presented in this section.

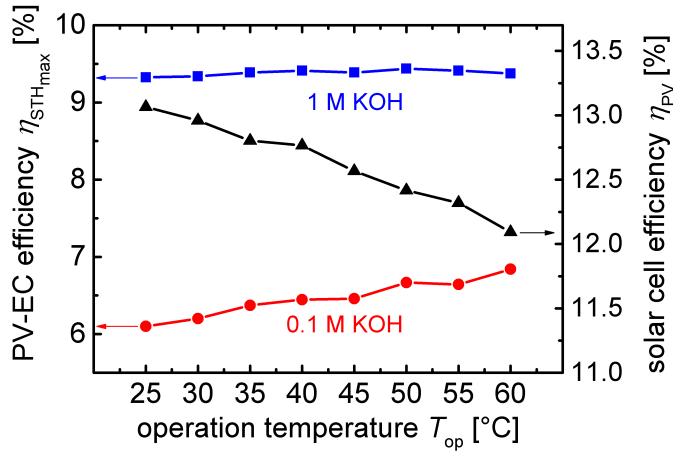


**Fig. 6.16** On the left ordinate, the estimated solar-to-hydrogen efficiency  $\eta_{\text{STH}_{\text{max}}}$  of the triple junction based PV-EC device in 0.1 M (red circles) and 1 M KOH (blue squares), respectively, is plotted as a function of the operation temperature. The  $\eta_{\text{STH}_{\text{max}}}$  was calculated based on Eq. 4.4 using the  $j_{\text{op}}$  values from Fig. 6.15. On the right ordinate, the photovoltaic efficiency of the triple junction solar cell as a function of the operation temperature is shown (black triangles).

In total, this investigation revealed that the reduction in solar cell performance with increasing temperature can be compensated by an enhanced performance of the electrochemical components (electrolyte, HER and OER electrodes). This result is an important aspect for practical outdoor applications with typical operation temperatures above 50 °C and contributes to the progress in practical solar-assisted water splitting.

## 6.4 Summary and conclusions

In the present chapter numerous aspects of thin film silicon based PV-EC devices are presented and discussed. Here, an overview of all relevant aspects shall be given by summarising the most important results from the preceding sections.

### Photocathode/electrolyte contact

First, the contact at the photocathode/electrolyte interface was examined. It was shown that the photocathode contact undertakes a crucial role in the PV-EC device and has to fulfil a broad range of demands. Thin metal layer stacks turned out to be suitable candidates to meet the important requirements, because they allow to combine the advantages of each individual layer, such as good reflectivity for the incident light, high catalytic activity, reasonable electrochemical stability, and low cost fabrication. This was examined by measuring only the HER reaction at the photocathode surface in a three-electrode configuration, neglecting the reactions at the counter electrode. The most efficient photocathode contact, in terms of onset potential for cathodic current and photocurrent density was made of an Ag/Pt layer stack. This photocathode exhibited a photocurrent density of  $6.6 \text{ mA/cm}^2$  at large positive bias of 1.2 V vs. RHE and provided a stable photocurrent density of around  $7.7 \text{ mA/cm}^2$  at 0 V vs. RHE over the course of 4 hours. A significant cost reduction can be achieved by an Al/Ni layer stack contacted device. This all earth-abundant and precious metal-free photocathode exhibited a photocurrent density of  $6.3 \text{ mA/cm}^2$  at a positive bias of 1.2 V vs. RHE. Although the performance is slightly reduced compared to the Ag/Pt contacted photocathode, it is still among the highest photocurrent densities at such positive bias with respect to RHE for all reported silicon based photocathodes. However, this contact suffered stability problems, which were mainly caused by the delamination of the Al layer from the silicon surface. Possible solutions may be the integration of very thin adhesion layers between the silicon and the Al layer. Despite the stability issues, this low-cost photocathode presents a promising device for efficient and cost-effective solar hydrogen production.

### Multijunction based PV-EC devices

Secondly, complete PV-EC devices for stand-alone water splitting were fabricated based on the developed multijunction solar cells and measured in a two-electrode

configuration. Several performance influencing factors were examined, namely the influence of the HER catalyst, the influence of the electrolyte concentration, and the impact of light induced degradation. The best performance was provided by the a-Si:H/a-Si:H/ $\mu$ c-Si:H based PV-EC device with a Ag/Pt photocathode contact and RuO<sub>2</sub> as oxygen evolution catalyst. This device exhibited the highest photocurrent density of 7.1 mA/cm<sup>2</sup> and 7.7 mA/cm<sup>2</sup> at 0 V applied bias, in 0.1 M and 1 M KOH, respectively. Assuming a 100 % faradaic efficiency (confirmed for the system under study in Section 4.4), this corresponds to solar-to-hydrogen efficiencies of 8.7 % and 9.5 %, respectively. The increase in the STH efficiency from 0.1 to 1 M KOH, mainly resulted from the decreased electrolyte resistance leading to an increased "fill factor" in the current density-voltage characteristics.

To bring the achieved STH efficiencies in this work into line with the state-of-the-art devices reported in literature, Fig. 6.17 compares the reported STH efficiencies of thin film silicon based solar water splitting devices. Besides purely thin film silicon based systems (buried junctions, see 2.3.4), also the data of devices are included, which combine buried thin film silicon junctions with semiconductor liquid junctions (SLJ) such as BiVO<sub>4</sub>, WO<sub>3</sub> or a-SiC:H (see Fig. 6.17). Please note that module based devices are not considered here. For the majority of the devices in Fig. 6.17, Eq. 4.4 was employed to estimate the STH efficiency from a measured current density at zero bias. Please note that none of the references included in Fig. 6.17 incorporated a membrane for gas separation into the device set-up. Thus, hydrogen and oxygen co-evolve. In a commercial device the half cells would have to be physically separated by porous separators or membranes to avoid explosive gas mixtures and further purification steps [208–210].

Theoretical performance limits of STH efficiencies of above 20 % were proposed for tandem devices based on crystalline semiconductors for solar water splitting in several studies [21, 188, 223]. This work, however, suggests that in the particular case of thin film silicon based devices, the maximum STH efficiency under practical conditions is certainly well below 20 %. The theoretical studies do not take into account the free energy losses in thin film silicon, which are relatively high compared to crystalline semiconductors and thus, limit the photovoltage to a value considerably lower than the band gap. Nevertheless, this study clearly shows that STH efficiencies above 10 % are well within range for thin film silicon devices.

In addition to that, the quadruple junction (a-Si:H/a-Si:H/ $\mu$ c-Si:H/ $\mu$ c-Si:H) based PV-EC device exhibited enough 'excess' photovoltage to substitute Pt as precious metal HER catalyst by a more abundant material, such as Ni, and to work

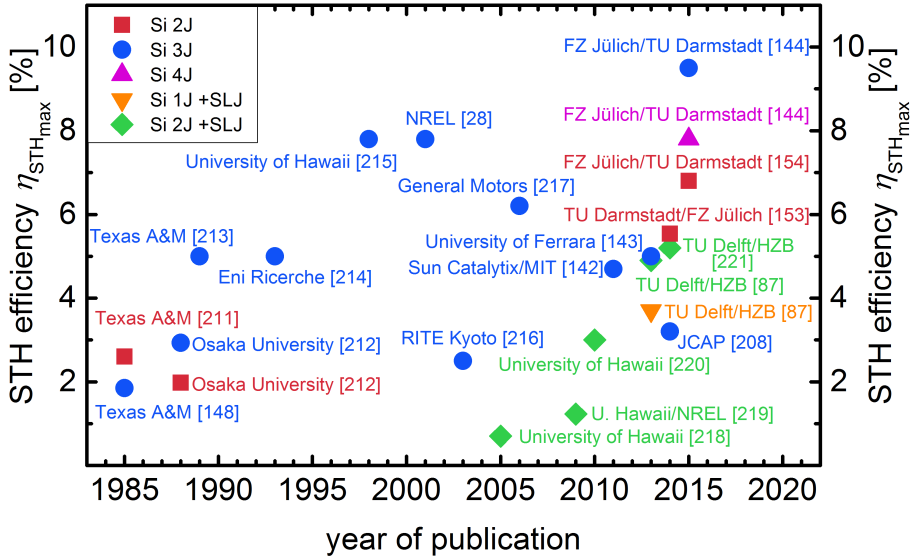


**Fig. 6.17** Reported experimental solar-to-hydrogen efficiencies of thin film silicon based devices that are able to spontaneously split water in the presence of solar radiation. Silicon tandem (2J) [153, 154, 211, 212], triple (3J) [28, 142–144, 148, 208, 212–217], and quadruple (4J) [144] junction devices are plotted in different colours. Furthermore, hybrid devices are considered which combine single [87] or tandem thin film silicon junctions [87, 218–221] with a semiconductor liquid junction (SLJ). The figure is adapted from Ref. [222]

in low-concentrated electrolyte solutions without impairing the solar-to-hydrogen efficiency. With Ni as HER catalyst, this device provided  $6.1 \text{ mA/cm}^2$  at 0 V applied bias over the course of 4 hours and may be an alluring alternative to the precious metal Pt catalyst, in terms of cost reduction.

The impact of LID was measured by using the stabilised solar cells (presented in Section 5.6) as photocathodes in the PV-EC devices. It was found that the STH efficiency is less affected by LID than the photovoltaic efficiency. Furthermore, it was concluded that the degradation upon illumination is negligible compared to degradation due to corrosion of the electrodes for the quadruple, the a-Si:H/ $\mu\text{c-Si:H}/\mu\text{c-Si:H}$ , and for the a-Si:H/ $\mu\text{c-Si:H}$  based PV-EC devices. For the a-Si:H/a-Si:H

and a-Si:H/a-Si:H/ $\mu$ c-Si:H based PV-EC devices, however, the impact of LID needs to be considered also in the PV-EC configuration. The highest stabilised STH efficiency of 7.6 % was achieved by the a-Si:H/a-Si:H/ $\mu$ c-Si:H triple and by the quadruple junction based PV-EC devices. The latter showed a high stability against LID and its STH efficiency degraded only by 2 % (relative) to 7.6 %.

### PV-EC device modeling

The presented empirical serial circuit model allowed for the decoupled evaluation of all the functional PV-EC device components: the solar cell, the HER and OER catalysts, and the electrolyte. By merging the  $j$ - $V$  characteristics of these components, in terms of a simple series connection, the PV-EC device performance could be accurately predicted. After having validated the model for various PV-EC device configurations, where excellent agreement with experimental data was achieved, the model was used to predict the influence of various photocathode-catalyst combinations on the PV-EC performance. For this purpose, literature data of various state-of-the-art catalyst materials for the HER and the OER, respectively, were used to implement in the model and merged with the experimentally measured  $j$  -  $V$  curves of tandem, triple, and quadruple junction solar cells. By doing so, the  $j$  -  $V$  characteristics and thus, the STH efficiency of various photocathode-catalyst combinations could be predicted. This allowed to designate the adequate OER and HER catalysts for a specific solar cell type. In fact, the corresponding results elucidated all the more the importance to adapt the photovoltaic to the electrochemical properties and *vice versa*.

In addition to this investigation, the model was also used to evaluate the effect of elevated operation temperatures on the PV-EC device performance. To do so, the temperature-dependent characteristics of the PV-EC components were measured and implemented into the model. As a result, the important effects of temperature variations for PV-EC devices were identified and it was shown that the performance of the PV-EC device, in contrast to the solar cell performance, was not deteriorated and even slightly increased by an increased operation temperature of the device. A maximum solar-to-hydrogen efficiency of 9.5 % was found at 50 °C operation temperature in 1 M KOH for an a-Si:H/a-Si:H/ $\mu$ c-Si:H based PV-EC device.

In total, the presented results provide evidence that the series circuit model is a very elegant and powerful tool to predict the performance of PV-EC devices based on the individual component characteristics. It therefore allows to adopt the photovoltaic development routes with respect to the specific overpotential requirements of the

electrochemical components in a targeted way. *Vice versa*, the model can also be used to designate the adequate OER and HER catalysts for a specific solar cell type.

## 7 Conclusion and future prospects

The primary aim of this work was the development of efficient and high voltage multijunction solar cells made of amorphous and microcrystalline silicon for the application as photocathodes in integrated photovoltaic-electrochemical devices for light induced water splitting. Concomitant with this, special attention was devoted to the solar cell/electrolyte interface, with respect to stability issues and high catalytic activity for the HER and the OER, respectively. Moreover, modeling of the PV-EC device was employed, which contributed to the identification and understanding of the relevant loss processes in the overall system.

This work was embedded in the conjoint research project between the Institute for Photovoltaics (IEK-5) of the Forschungszentrum Jülich and the Technical University of Darmstadt and was supported by the Deutsche Forschungsgemeinschaft (DFG) within the Priority Programme 1613 and by the German Bundesministerium für Bildung und Forschung (BMBF). The presented photovoltaic development could draw upon a high level of scientific expertise on single junction and multijunction solar cell technology in the IEK-5. The (photo)electrochemical know-how, however, required a largely new development including the design of a suitable PV-EC measurement assembly, the fabrication of efficient photoelectrodes (based on the developed solar cells), and the identification of the relevant loss mechanisms, leading to an improvement in the overall PV-EC device performance. Thanks to the fruitful collaboration with the project partners, in particular with the Technical University of Darmstadt, it became after all possible to merge the photovoltaic and the electrochemical know-how and to establish a profound electrochemical expertise at the IEK-5.

Nevertheless, also the photovoltaic development route needed to be specifically adapted and deviates from the prevalent routes. In this work, the focus for the solar cells was set more on high tunable output voltages rather than on the improvement of the electrical conversion efficiencies. However, one objective herein was to avoid impairing the electrical conversion efficiency while increasing the photovoltage in the solar cells. As contrasted with related pioneering studies on light induced water splitting, where mainly off-the-shelf photovoltaic devices have been used and where the adjustment of the photovoltaic parameters was not in the focus of research [215,224,225], the development presented in this work intended to specifically tune both, the electrochemical (catalytic) and the photovoltaic parameters of the photoelectrodes. Therefore, it is vital to extend beyond former studies on thin film



silicon multijunction solar cells and photoelectrodes, also to increase the variety of feasible applications in photoelectrochemical systems.

The results presented in Chapter 5 provide evidence that the photovoltage of the multijunction solar cells can be adjusted from 1.5 V to 2.8 V without impairing the device efficiency. In fact, the developed solar cells provided electrical conversion efficiencies up to 13.6 %, which is very close to the record efficiency reported for solar cells made of thin film silicon. In terms of solar-to-hydrogen efficiency, high performance solar cells are crucial, because water splitting devices not only require high photovoltages, but also high photocurrent densities and good fill factors from the solar cells. Additionally, the ability to vary the photovoltaic parameters within a wide range represents a vital feature of the developed solar cells in order to fulfil the particular overpotential requirements of various water splitting systems. In Chapter 6, this was demonstrated by the high excess voltage of quadruple junction solar cells that is mandatory for the usage of inexpensive and earth-abundant catalysts with higher overpotential requirements. Exemplarily, this was shown by replacing Pt with Ni as HER catalyst without impairing the PV-EC device efficiency.

A major role in the operation of integrated water splitting devices is undertaken by the solar cell/electrolyte contact. It is implemented for several reasons, namely for efficient light reflection into the solar cell, high catalytic activity for the HER (photocathode contact in this work), and robust protection from the electrolyte. Considering this broad range of demands, the presented concept of a metal layer stack as photocathode contact emerged as the best solution. In Chapter 6, a Ag/Pt contact stack was compared with an Al/Ni stack, as cheap and earth-abundant alternative. Although the Al/Ni contacted photocathode nearly provided the same efficiency as the Ag/Pt contacted device, stability issues, in particular delamination problems prevented further usage of Al/Ni as contacts in this work. This issue could be solved by integrating thin adhesion layers between the Si surface and the Al layer, which however must be sufficiently transparent for the reflected light from the Al layer. The photocathode with the Ag/Pt contact operated stable for over four hours.

The influence of light induced degradation and the operating temperature on the performance of the PV-EC devices are important aspects for the implementation of stand-alone water splitting devices on an industrial level. In the literature, however, relatively little attention has been payed to these aspects. In this work, it was demonstrated that for both aspects the PV-EC devices are less affected compared to the PV devices. For increasing operation temperatures, it was demonstrated that the STH efficiency even increased, in contrary to the efficiency of PV cells, which

decreased upon temperature increase. Upon illumination (up to 1000 hours) the quadruple junction solar cells and the quadruple junction based PV-EC devices showed a very low degradation of less than 5 % and 3 % (relative), respectively. This corresponds to a minor reduction in the conversion efficiency from 13.2 to 12.6 % for the PV and from 7.8 to 7.6 % for the PV-EC configuration, respectively. For other configurations, such as a-Si:H/a-Si:H and a-Si:H/a-Si:H/ $\mu$ c-Si:H based PV-EC devices, however, the impact of LID was more significant in the photovoltaic and in the PV-EC configuration.

For improvements in the PV-EC device efficiency it becomes vital to determine the relevant loss mechanisms in the system under investigation. The empirical serial circuit model, presented in Section 6.3, offers a useful and elegant tool to analyse and predict the performance of integrated PV-EC devices based on experimental data of each individual functional component (solar cell, HER and OER catalysts, and electrolyte). As compared with the photovoltaic cells, it was shown that primarily the overpotentials at the HER and OER catalyst surfaces, respectively, and the electrolyte resistance impose additional constraints on the current-voltage characteristics of the PV-EC system. Moreover, the decoupled evaluation of all functional device components in the model allowed to estimate to what extent an improvement of an individual component or a reduction of a specific loss mechanism would improve the overall PV-EC device performance and increase the STH efficiency. In fact, this work provides evidence that the model can be employed to derive the practical performance limits of a certain solar cell type for water splitting applications.

In this work, a very high maximum STH efficiency of 9.5 % was achieved with a monolithic triple junction a-Si:H/a-Si:H/ $\mu$ c-Si:H based photocathode containing a ZnO:Al/Ag/Pt contact and a RuO<sub>2</sub> counter electrode, measured in 1 M KOH. This is the highest reported STH efficiency for an integrated thin film silicon based photo-electrochemical device, according to the overview of demonstrated STH conversion efficiencies published by Ager *et al.* [32] in 2015. This result demonstrates that the target of 10 % STH efficiency, declared by the U.S. Department of Energy (DOE), clearly is within the reach of the described thin film silicon based integrated PV-EC device pathway [226].

Besides the achievements in the frame of this work, it is also important to touch on the technical and economic constraints concomitant with the development of water splitting devices. In this context, the preliminary results on the stability presented in this work suggest that the durability remains one of the most critical issues with respect to the development of water splitting assemblies. Therefore,

further substantial investigations with respect to robust devices, extending beyond the herein illustrated stability issues should be in the scope of future works. A review on the use of protective thin films to improve the electrochemical stability of otherwise unstable semiconductor photoelectrodes is given by Hu *et al.* [227]. Another critical aspect, which was not explicitly covered in the framework of this work, is the upscaling of the (photo)electrode surfaces in integrated water splitting devices. Upscaling is potentially within range for the thin film silicon technology, but it is still very rarely employed, neither in industry nor in research.

Nevertheless, the presented PV-EC device concept in combination with the presented modeling approach and the broad range of tunable photovoltaic parameters, in particular the photovoltages, offers an efficient and versatile toolbox for the investigation of related research challenges under practical water splitting conditions. This may include (i) the design of integrated device architectures with robust surface coatings and new catalyst materials, or (ii) the investigation of electrochemical reactions to produce solar fuels, others than the water splitting reaction.

With regard to new device architectures (i), hybrid device concepts, comprising silicon thin films or c-Si and organic semiconductor structures, may emerge as suitable solutions to reach STH efficiencies well above 10 %. PV efficiencies above 18 % were recently reported for c-Si/perovskite tandem devices by Albrecht *et al.* [228]. This monolithic device provided a  $V_{OC}$  of 1.78 V, which is appropriate for bias-free water splitting, as demonstrated by this work. However, the current matching of the individual PV sub cells remains challenging in monolithic hybrid multijunction structures. An alternative hybrid device concept would be to combine a photocathode and a photoanode. Similar to the device configuration presented in this work, the photocathode could be made of a herein developed thin film silicon solar cell, whereas the metal oxide coated anode would be replaced by another photovoltaic cell, made of any semiconductor material [229]. Thanks to the wide range of achievable photovoltages of the photocathode, the photoanode could be chosen in a more flexible way, with respect to the required output voltage. Therefore, this PV-EC configuration would offer to test a large variety of semiconductor structures as photoanodes for water splitting, such as perovskite or *nip* thin film silicon solar cells, for instance.

Among the photoelectrochemical reactions for solar fuel production (ii), the direct solar reduction of  $CO_2$  to liquid organic substances, such as carbon monoxide (CO), methane ( $CH_4$ ), or formic acid ( $CH_2O_2$ ) has recently attracted considerable attention due to the higher energy density and accessible storage advantages compared with hydrogen energy [230]. Several device assemblies based on various catalysts and

light absorbers for CO<sub>2</sub> reduction with varying levels of integration have been demonstrated experimentally [231–234]. In this process, however, particularly the cathodic half reaction suffers significant kinetic overpotentials, which have been considered much more difficult than the hydrogen generation reaction in the water splitting process. The overpotentials depend largely on the nature of the used catalysts and on the additional constraint that electrochemical CO<sub>2</sub> reduction must be performed at near-neutral pH [231]. Hence, a voltage of at least 2.0 V is demanded to drive an efficient fuel production *via* CO<sub>2</sub> reduction. Additionally, the product selectivity at the electrodes is highly potential-dependent, *i.e.* a number of different products can be generated by reduction processes depending on the applied potential. This must be accounted for when defining the required photoelectrode operating potential [232]. Considering all these aspects, it becomes apparent that the herein developed thin film silicon photocathodes with the precisely adjustable photovoltages up to 2.8 V represent ideal photoelectrodes for applications in photoelectrochemical CO<sub>2</sub> reduction.

These few examples show that the findings of this work considerably extend the variety of feasible applications and material combinations in photoelectrochemical systems. Ultimately, emphasis needs to be put on conjoint research activities between solar hydrogen production, hydrogen storage and fuel cell technologies. Bringing together the interdisciplinary knowledge may eventually help to bridge the gaps between the different hydrogen related disciplines more easily, in research but also in industry. This would offer the prospect of a sustainable future energy infrastructure based on sunlight, hydrogen, and electricity.



# Bibliography

- [1] C. Grimes, O. K. Varghese, and S. Ranjan, *Light, Water, Hydrogen: The Solar Generation of Hydrogen by Water Photoelectrolysis*, Springer, New York, USA, 2008.
- [2] P. Gerland, A. E. Raftery, H. Ševčíková, N. Li, D. Gu, T. Spoorenberg, L. Alkema, B. K. Fosdick, J. Chunn, N. Lalic, G. Bay, T. Buettner, G. K. Heilig, and J. Wilmoth, *World population stabilization unlikely this century*, *Science* **346** (2014), 234–237.
- [3] M. I. Hoffert, K. Caldeira, A. K. Jain, E. F. Haites, L. D. D. Harvey, S. D. Potter, M. E. Schlesinger, S. H. Schneider, R. G. Watts, T. M. L. Wigley, and D. J. Wuebbles, *Energy implications of future stabilization of atmospheric CO<sub>2</sub> content*, *Nature* **395** (1998), 881–884.
- [4] J. R. McKone, N. S. Lewis, and H. B. Gray, *Will Solar-Driven Water-Splitting Devices See the Light of Day?*, *Chem. Mater.* **26** (2014), 407–414.
- [5] N. S. Lewis and D. G. Nocera, *Powering the planet: Chemical challenges in solar energy utilization*, *Proc. Natl. Acad. Sci. USA* **103** (2006), 15729–15735.
- [6] *BP Statistical Review of World Energy 2014*, Tech. report, 2014.
- [7] R. van de Krol and M. Grätzel, *Photoelectrochemical Hydrogen Production*, Springer, New York, USA, 2012.
- [8] E. E. Barton, D. M. Rampulla, and A. B. Bocarsly, *Selective Solar-Driven Reduction of CO<sub>2</sub> to Methanol Using a Catalyzed p-GaP Based Photoelectrochemical Cell*, *J. Am. Chem. Soc.* **130** (2008), 6342–6344.
- [9] O. K. Varghese, M. Paulose, T. J. LaTempa, and C. A. Grimes, *High-Rate Solar Photocatalytic Conversion of CO<sub>2</sub> and Water Vapor to Hydrocarbon Fuels*, *Nano Lett.* **9** (2009), 731–737.
- [10] P. Jena, *Materials for Hydrogen Storage: Past, Present, and Future*, *J. Phys. Chem. Lett.* **2** (2011), 206–211.
- [11] G. W. Crabtree, M. S. Dresselhaus, and M. V. Buchanan, *The hydrogen economy*, *Physics Today* **57** (2004), 39–44.

- [12] Z. Li, W. Luo, M. Zhang, J. Feng, and Z. Zou, *Photoelectrochemical cells for solar hydrogen production: current state of promising photoelectrodes, methods to improve their properties, and outlook*, Energy Environ. Sci. **6** (2013), 347–370.
- [13] A. J. Nozik and J. Miller, *Introduction to Solar Photon Conversion*, Chem. Rev. **110** (2010), 6443–6445.
- [14] A. Fujishima and K. Honda, *Electrochemical Photolysis of Water at a Semiconductor Electrode*, Nature **238** (1972), 37–38.
- [15] H.-J. Lewerenz and L. Peter (eds.), *Photoelectrochemical Water Splitting*, RSC Energy and Environment Series, The Royal Society of Chemistry, 2014.
- [16] Z. Chen, H. Dinh, and E. Miller, *Photoelectrochemical Water Splitting*, Springer, New York, USA, 2014.
- [17] W. Shockley and H. J. Queisser, *Detailed Balance Limit of Efficiency of p-n Junction Solar Cells*, J. Appl. Phys. **32** (1961), 510–519.
- [18] R. T. Ross and T.-L. Hsiao, *Limits on the yield of photochemical solar energy conversion*, J. Appl. Phys. **48** (1977), 4783–4785.
- [19] M. C. Hanna and A. J. Nozik, *Solar conversion efficiency of photovoltaic and photoelectrolysis cells with carrier multiplication absorbers*, J. Appl. Phys. **100** (2006), 0745101–8.
- [20] B. A. Pinaud, J. D. Benck, L. C. Seitz, A. J. Forman, Z. Chen, T. G. Deutsch, B. D. James, K. N. Baum, G. N. Baum, S. Ardo, H. Wang, E. Miller, and T. F. Jaramillo, *Technical and economic feasibility of centralized facilities for solar hydrogen production via photocatalysis and photoelectrochemistry*, Energy Environ. Sci. **6** (2013), 1983–2002.
- [21] L. C. Seitz, Z. Chen, A. J. Forman, B. A. Pinaud, J. D. Benck, and T. F. Jaramillo, *Modeling Practical Performance Limits of Photoelectrochemical Water Splitting Based on the Current State of Materials Research*, ChemSusChem **7** (2014), 1372–1385.
- [22] K. Vetter, *Elektrochemische Kinetik*, Springer, Berlin / Heidelberg, Germany, 1961.
- [23] U. Rau, *Reciprocity relation between photovoltaic quantum efficiency and electroluminescent emission of solar cells*, Phys. Rev. B **76** (2007), 085303.

- [24] R. Memming, *Semiconductor electrochemistry*, Wiley-VCH, Weinheim, Germany, 2001.
- [25] J. R. Bolton, S. J. Strickler, and J. S. Connolly, *Limiting and realizable efficiencies of solar photolysis of water*, *Nature* **316** (1985), 495–500.
- [26] A. De Vos, *Detailed balance limit of the efficiency of tandem solar cells*, *J. Phys. D: Appl. Phys.* **13** (1980), 839–846.
- [27] S. Licht, B. Wang, S. Mukerji, T. Soga, M. Umeno, and H. Tributsch, *Over 18% solar energy conversion to generation of hydrogen fuel; theory and experiment for efficient solar water splitting*, *Int. J. Hydrogen Energy* **26** (2001), 653–659.
- [28] O. Khaselev, A. Bansal, and J. Turner, *High-efficiency integrated multijunction photovoltaic/electrolysis systems for hydrogen production*, *Int. J. Hydrogen Energy* **26** (2001), 127–132.
- [29] M. M. May, H.-J. Lewerenz, D. Lackner, F. Dimroth, and T. Hannappel, *Efficient direct solar-to-hydrogen conversion by in situ interface transformation of a tandem structure*, *Nat. Commun.* **6** (2015).
- [30] A. Shah (ed.), *Thin-Film Silicon Solar Cells*, EPFL Press, Lausanne, Switzerland, 2010.
- [31] K. Sun, S. Shen, Y. Liang, P. E. Burrows, S. S. Mao, and D. Wang, *Enabling Silicon for Solar-Fuel Production*, *Chem. Rev.* **114** (2014), 8662–8719.
- [32] J. W. Ager III, M. Shaner, K. Walczak, I. D. Sharp, and S. Ardo, *Experimental Demonstrations of Spontaneous, Solar-Driven Photoelectrochemical Water Splitting*, *Energy Environ. Sci.* **8** (2015), 2811–2824.
- [33] P. Würfel, *Physics of Solar Cells: From Basic Principles to Advanced Concepts*, 2<sup>nd</sup> ed., Wiley VCH, Weinheim, Germany, 2009.
- [34] R. A. Smith, *Semiconductors*, 2<sup>nd</sup> ed., Vol. 4, Cambridge University Press, New York, USA, 1979.
- [35] C. Kittel, *Introduction to solid state physics*, 8<sup>th</sup> ed., Wiley, New York, USA, 2005.
- [36] R. E. I. Schropp and M. Zeman, *Amorphous and microcrystalline Silicon Solar Cells: Modeling Materials and Device Technology*, Vol. 5, Springer, New York, USA, 1998.



- [37] S. M. Sze, *Physics of semiconductor devices*, 3<sup>rd</sup> ed., Wiley, New York, 2007.
- [38] S. Schicho, D. Hrunski, R. van Aabel, and A. Gordijn, *High potential of thin ( $< 1\mu\text{m}$ )  $a\text{-Si:H}/\mu\text{c-Si:H}$  tandem solar cells*, Prog. Photovolt: Res. Appl. **18** (2010), 83–89.
- [39] F. Urbain, V. Smirnov, J.-P. Becker, A. Lambertz, U. Rau, and F. Finger, *Light-induced degradation of adapted quadruple junction thin film silicon solar cells for photoelectrochemical water splitting*, Sol. Energy Mater. Sol. Cells **145** (2016), 142–147, Selected papers of the EMRS 2015 Spring meeting "Symposium C on Advanced Inorganic Materials and Structures for Photovoltaics".
- [40] F. Urbain, V. Smirnov, J.-P. Becker, U. Rau, F. Finger, J. Ziegler, B. Kaiser, and W. Jaegermann,  *$a\text{-Si:H}/\mu\text{c-Si:H}$  tandem junction based photocathodes with high open-circuit voltage for efficient hydrogen production*, J. Mater. Res. **29** (2014), 2605–2614, Invited Feature Paper (MRS 2014 Spring Meeting).
- [41] S. Hänni, S. nni, M. Boccard, G. Bugnon, M. Despeisse, J.-W. Schütttauf, F.-J. Haug, F. Meillaud, and C. Ballif, *Microcrystalline silicon solar cells with passivated interfaces for high open-circuit voltage*, Phys. Stat. Sol. A **212** (2015), 840–845.
- [42] W. Böttler, *Light scattering and trapping in thin film silicon solar cells with an  $n\text{-i-p}$  configuration*, Ph.D. thesis, Rheinisch Westfälische Technische Hochschule Aachen, Germany, 2015.
- [43] R. A. Street, *Hydrogenated amorphous silicon*, Cambridge University Press, New York, USA, 1991.
- [44] M. A. Green, *Third Generation Photovoltaics - Advanced Solar Energy Conversion*, Springer Berlin / Heidelberg, Germany, 2006.
- [45] O. Isabella, A. H. M. Smets, and M. Zeman, *Thin-film silicon-based quadruple junction solar cells approaching 20% conversion efficiency*, Sol. Energy Mater. Sol. Cells **129** (2014), 82–89.
- [46] S. Schicho, *Amorphous and microcrystalline silicon applied in very thin tandem solar cells*, Ph.D. thesis, Rheinisch Westfälische Technische Hochschule Aachen, Germany, 2011.
- [47] B. Bills, X. Liao, D. Galipeau, and Q. Fan, *Effect of Tunnel Recombination Junction on Crossover Between the Dark and Illuminated Current–Voltage*

- Curves of Tandem Solar Cells*, IEEE Transactions on Electron Devices **59** (2012), 2327–2330.
- [48] J. Kwak, S. W. Kwon, and K. S. Lim, *Fabrication of a n-p-p tunnel junction for a protocrystalline silicon multilayer/amorphous silicon tandem solar cell*, J. Non-Cryst. Solids **352** (2004), 1847–1850.
- [49] L. Gui-Jun, H. Guo-Fu, H. Xiao-Yan, Y. Yu-Jie, W. Chang-Chun, S. Jian, Z. Yin, and G. Xin-Hua, *The study of a new n/p tunnel recombination junction and its application in a-Si:H/ $\mu$ c-Si:H tandem solar cells*, Chin. Phys. B **18** (2009), 1674.
- [50] C. Ulbrich, C. Zahren, A. Gerber, B. Blank, T. Merdzhanova, A. Gordijn, and U. Rau, *Matching of Silicon Thin-Film Tandem Solar Cells for Maximum Power Output*, Int. J. Photoenergy **2013** (2013), 314097.
- [51] K. Rajeshwar, *Fundamentals of Semiconductor Electrochemistry and Photoelectrochemistry*, Wiley Online Library, 2007.
- [52] A. J. Bard, R. Parsons, and J. Jordan (eds.), *Standard Potentials in Aqueous Solutions*, Vol. 6, CRC press, New York, USA, 1985.
- [53] D. J. G. Ives and G. J. Janz (eds.), *Reference electrodes: theory and practice*, Academic Press, New York, USA, 1961.
- [54] C. A. Koval and J. N. Howard, *Electron transfer at semiconductor electrode-liquid electrolyte interfaces*, Chem. Rev. **92** (1992), 411–433.
- [55] A. D. McNaught and A. Wilkinson, *IUPAC Compendium of Chemical Terminology*, 2<sup>nd</sup> ed., Blackwell Scientific Publications, Oxford, UK, 1997.
- [56] W. M. Haynes, *CRC Handbook of Chemistry and Physics*, 93<sup>rd</sup> ed., Taylor and Francis, Boca Raton, USA, 2012.
- [57] W. Schmickler and E. Santos, *Interfacial electrochemistry*, 2<sup>nd</sup> ed., Springer, Heidelberg, Germany, 2010.
- [58] A. J. Bard and L. R. Faulkner, *Electrochemical methods: fundamentals and applications*, Wiley, New York, USA, 2001.
- [59] Y. Cai and A. B. Anderson, *The Reversible Hydrogen Electrode: Potential-Dependent Activation Energies over Platinum from Quantum Theory*, J. Phys. Chem. B **108** (2004), 9829–9833.

- [60] A. C. Covington, R. G. Bates, and R. A. Durst, *Definition of pH scales, standard reference values, measurement of pH and related terminology*, Pure Appl. Chem. **57** (1985), 531–542.
- [61] I. Valov and R. Waser, *Elektrochemische Prozesse und Wasserstoff-Technologie*, Lecture from the Institut für Werkstoffe der Elektrotechnik II, RWTH Aachen, Germany, 2012.
- [62] G. Kear and F. C. Walsh, *The characteristics of a true Tafel slope*, Corr. Mater. **30** (2005), 51–55.
- [63] M. Pagliaro and A. G. Konstandopoulos, *Solar Hydrogen*, The Royal Society of Chemistry, 2012.
- [64] A. Hernández-Ramírez and I. Medina-Ramirez (eds.), *Photocatalytic Semiconductors*, Springer, International Publishing Switzerland, 2015.
- [65] H. Gerischer, *Über den Ablauf von Redoxreaktionen an Metallen und an Halbleitern*, Z. Phys. Chem. **27** (1961), 48–79.
- [66] W. Plieth, *Structure and Bonding*, Electrochemistry for Materials Science, Elsevier, Amsterdam, Netherlands, 2008, pp. 27 – 69.
- [67] M. Malizia, B. Seger, I. Chorkendorff, and P. C. K. Vesborg, *Formation of a p-n heterojunction on GaP photocathodes for H<sub>2</sub> production providing an open-circuit voltage of 710 mV*, J. Mater. Chem. A **2** (2014), 6847–6853.
- [68] B. Kaiser, D. Fertig, J. Ziegler, J. Klett, S. Hoch, and W. Jaegermann, *Solar Hydrogen Generation with Wide-Band-Gap Semiconductors: GaP(100) Photoelectrodes and Surface Modification*, ChemPhysChem **13** (2012), 3053–3060.
- [69] O. Khaselev and J. A. Turner, *A Monolithic Photovoltaic-Photoelectrochemical Device for Hydrogen Production via Water Splitting*, Science **280** (1998), 425–427.
- [70] B. Seger, A. B. Laursen, P. C. K. Vesborg, T. Pedersen, O. Hansen, S. Dahl, and I. Chorkendorff, *Hydrogen Production Using a Molybdenum Sulfide Catalyst on a Titanium-Protected n<sup>+</sup>p-Silicon Photocathode*, Angew. Chem. Int. Ed. **51** (2012), 9128–9131.
- [71] R. N. Dominey, N. S. Lewis, J. A. Bruce, D. C. Bookbinder, and M. S. Wrighton, *Improvement of photoelectrochemical hydrogen generation by surface*

- modification of p-type silicon semiconductor photocathodes*, J. Am. Chem. Soc. **104** (1982), 467–482.
- [72] H. Tributsch, *Layer-Type Transition Metal Dichalcogenides - a New Class of Electrodes for Electrochemical Solar Cells*, Berichte der Bunsengesellschaft für physikalische Chemie **81** (1977), 361–369.
- [73] H. Tributsch, *Hole Reactions from d-Energy Bands of Layer Type Group VI Transition Metal Dichalcogenides: New Perspectives for Electrochemical Solar Energy Conversion*, J. Electrochem. Soc. **125** (1978), 1086–1093.
- [74] G. Kline, K. K. Kam, R. Ziegler, and B. Parkinson, *Further studies of the photoelectrochemical properties of the group VI transition metal dichalcogenides*, Sol. Energy Mater. **6** (1982), 337–350.
- [75] J. R. McKone, A. P. Pieterick, H. B. Gray, and N. S. Lewis, *Hydrogen Evolution from Pt/Ru-Coated p-Type WSe<sub>2</sub> Photocathodes*, J. Am. Chem. Soc. **135** (2013), 223–231.
- [76] M. Moriya, T. Minegishi, H. Kumagai, M. Katayama, J. Kubota, and K. Domen, *Stable Hydrogen Evolution from CdS-Modified CuGaSe<sub>2</sub> Photoelectrode under Visible-Light Irradiation*, J. Am. Chem. Soc. **135** (2013), 3733–3735.
- [77] Y. Pihosh, I. Turkevych, K. Mawatari, J. Uemura, Y. Kazoe, S. Kosar, K. Makita, T. Sugaya, T. Matsui, D. Fujita, M. Tosa, M. Kondo, and T. Kitamori, *Photocatalytic generation of hydrogen by core-shell WO<sub>3</sub>/BiVO<sub>4</sub> nanorods with ultimate water splitting efficiency*, Scientific reports **5** (2015), 11141.
- [78] K. Sivula, F. Le Formal, and M. Grätzel, *Solar Water Splitting: Progress Using Hematite ( $\alpha$ -Fe<sub>2</sub>O<sub>3</sub>) Photoelectrodes*, ChemSusChem **4** (2011), 432–449.
- [79] R. M. N. Yerga, M. C. Álvarez Galván, F. del Valle, J. A. V. de la Mano, and J. L. G. Fierro, *Water Splitting on Semiconductor Catalysts under Visible-Light Irradiation*, ChemSusChem **2** (2009), 471–485.
- [80] R. T. Ross, *Thermodynamic Limitations on the Conversion of Radiant Energy into Work*, J. Chem. Phys. **45** (1966), 1–7.
- [81] M. F. Weber and M. J. Dignam, *Efficiency of Splitting Water with Semiconducting Photoelectrodes*, J. Electrochem. Soc. **131** (1984), 1258–1265.
- [82] R. Williams, *Becquerel Photovoltaic Effect in Binary Compounds*, J. Chem. Phys. **32** (1960), 1505–1514.

- [83] A. B. Ellis, S. W. Kaiser, J. M. Bolts, and M. S. Wrighton, *Study of n-type semiconducting cadmium chalcogenide-based photoelectrochemical cells employing polychalcogenide electrolytes*, J. Am. Chem. Soc. **99** (1977), 2839–2848.
- [84] M. G. Walter, E. L. Warren, J. R. McKone, S. W. Boettcher, Q. Mi, E. A. Santori, and N. S. Lewis, *Solar Water Splitting Cells*, Chem. Rev. **110** (2010), 6446–6473.
- [85] F. Urbain, K. Wilken, V. Smirnov, O. Astakhov, A. Lambertz, J.-P. Becker, U. Rau, J. Ziegler, W. Kaiser, B. and Jaegermann, and F. Finger, *Development of Thin Film Amorphous Silicon Tandem Junction Based Photocathodes Providing High Open-Circuit Voltages for Hydrogen Production*, Int. J. Photoenergy **2014** (2014), 249317.
- [86] A. C. Nielander, M. R. Shaner, K. M. Papadantonakis, S. A. Francis, and N. S. Lewis, *A taxonomy for solar fuels generators*, Energy Environ. Sci. **8** (2015), 16–25.
- [87] F. F. Abdi, L. Han, A. H. M. Smets, M. Zeman, B. Dam, and R. van de Krol, *Efficient solar water splitting by enhanced charge separation in a bismuth vanadate-silicon tandem photoelectrode*, Nat. Commun. **4** (2013).
- [88] M. A. Green, A. W. Blakers, and C. R. Osterwald, *Characterization of high-efficiency silicon solar cells*, J. Appl. Phys. **58** (1985), 4402–4408.
- [89] K. Tanaka, E. Maruyama, T. Shimada, and H. Okamoto, *Amorphous Silicon*, Wiley, New York, USA, 1999.
- [90] V. Smirnov, O. Astakhov, R. Carius, Y. Petrusenko, V. Borysenko, and F. Finger, *Variation in Absorber Layer Defect Density in Amorphous and Microcrystalline Silicon Thin Film Solar Cells with 2 MeV Electron Bombardment*, Jap. J. Appl. Phys. **51** (2012), 022301.
- [91] R. A. Street, *Technology and Applications of Amorphous Silicon*, Springer Series in Materials Science, Berlin / Heidelberg, Germany, 1999.
- [92] L. Ley, *The Physics of Hydrogenated Amorphous Silicon II: Topics in Applied Physics - Photoemission and optical properties*, Vol. 56, Springer Berlin / Heidelberg, Germany, 1984.

- [93] B. Rech, *Solarzellen aus amorphem Silizium mit hohem stabilem Wirkungsgrad : zum Einfluß des p/i-Grenzflächenbereichs un der intrinsischen Absorberschicht*, Ph.D. thesis, Rheinisch Westfälische Technische Hochschule Aachen, Germany, 1997.
- [94] A. Rocket (ed.), *The Materials Science of Semiconductors*, Springer, New York, USA, 2008.
- [95] J. Robertson, *Growth mechanism of hydrogenated amorphous silicon*, J. Non-Cryst. Solids **266-269, Part 1** (2000), 79–83.
- [96] A. Matsuda, *Growth mechanism of microcrystalline silicon obtained from reactive plasmas*, Thin Solid Films **337** (1999), 1–6.
- [97] T. Soga, *Nanostructured Materials for Solar Energy Conversion*, Elsevier Science, Oxford, UK, 2007.
- [98] K. Wilken, *Tandem Cells providing High Open Circuit Voltages for photoelectrochemical Water Splitting*, Master’s thesis, Technische Universität Darmstadt, Germany, 2013.
- [99] R. Carius, *Optical gap and photoluminescence properties of amorphous silicon alloys*, Phil. Mag. B **80** (2000), 741–753.
- [100] D. L. Staebler and C. R. Wronski, *Reversible conductivity changes in discharge-produced amorphous Si*, Appl. Phys. Lett. **31** (1977), 292–294.
- [101] A. Lambertz, F. Finger, R. E. I. Schropp, U. Rau, and V. Smirnov, *Preparation and measurement of highly efficient a-Si:H single junction solar cells and the advantages of  $\mu\text{c-SiO}_x\text{:H}$  n-layers*, Prog. Photovolt: Res. Appl. **23** (2015), 939–948.
- [102] L. Houben, *Plasmaabscheidung von mikrokristallinem Silizium: Merkmale und Mikrostruktur und deren Bedeutung im Sinne von Wachstumsvorgängen*, Ph.D. thesis, Universität Düsseldorf, Germany, 1999.
- [103] O. Vetterl, F. Finger, R. Carius, P. Hapke, L. Houben, O. Kluth, A. Lambertz, A. Mück, B. Rech, and H. Wagner, *Intrinsic microcrystalline silicon: A new material for photovoltaics*, Sol. Energy Mater. Sol. Cells **62** (2000), 97–108.
- [104] A. Matsuda, *Formation kinetics and control of microcrystals in  $\mu\text{c-Si:H}$  from glow discharge plasma*, J. Non-Cryst. Solids **59** (1983), 767–774.

- [105] L. Houben, M. Luysberg, P. Hapke, R. Carius, F. Finger, and H. Wagner, *Structural properties of microcrystalline silicon in the transition from highly crystalline to amorphous growth*, Phil. Mag. A **77** (1998), 1447–1460.
- [106] M. Luysberg, P. Hapke, R. Carius, and F. Finger, *Structure and growth of hydrogenated microcrystalline silicon: Investigation by transmission electron microscopy and Raman spectroscopy of films grown at different plasma excitation frequencies*, Phil. Mag. A **75** (1997), 31–47.
- [107] F. Finger, R. Carius, T. Dylla, S. Klein, S. Okur, and M. Gunes, *Stability of microcrystalline silicon for thin film solar cell applications*, Circuits, Devices and Systems, IEE Proceedings **150** (2003), 300–308.
- [108] M. Kondo and A. Matsuda, *Preparation and Properties of Nanocrystalline Silicon*, Springer, Berlin / Heidelberg, Germany, 2004.
- [109] W. B. Jackson and N. M. Amer, *Direct measurement of gap-state absorption in hydrogenated amorphous silicon by photothermal deflection spectroscopy*, Phys. Rev. B **25** (1982), 5559–5562.
- [110] S. Klein, F. Finger, R. Carius, T. Dylla, and J. Klomfass, *Relationship between the optical absorption and the density of deep gap states in microcrystalline silicon*, J. Appl. Phys. **102** (2007), 103501.
- [111] M. A. Green and M. J. Keevers, *Optical properties of intrinsic silicon at 300 K*, Prog. Photovolt: Res. Appl. **3** (1995), 189–192.
- [112] J. K. Rath, *Low temperature polycrystalline silicon: a review on deposition, physical properties and solar cell applications*, Sol. Energy Mater. Sol. Cells **76** (2003), 431–487.
- [113] H. Keppner, J. Meier, P. Torres, D. Fischer, and A. Shah, *Microcrystalline silicon and micromorph tandem solar cells*, Appl. Phys. A **69** (1999), 169–177.
- [114] J. Meier, R. Flückiger, H. Keppner, and A. Shah, *Complete microcrystalline p-i-n solar cell - Crystalline or amorphous cell behavior?*, Appl. Phys. Lett. **65** (1994), 860–862.
- [115] T. Roschek, T. Repmann, J. Müller, B. Rech, and H. Wagner, *Comprehensive study of microcrystalline silicon solar cells deposited at high rate using 13.56 MHz plasma-enhanced chemical vapor deposition*, J. Vac. Sci. Technol. A **20** (2002), 492–498.

- [116] O. Vetterl, *On the physics of microcrystalline silicon thin film solar cells - From the material to devices with high conversion efficiencies*, Ph.D. thesis, Heinrich-Heine-Universität Düsseldorf, 2001.
- [117] S. Klein, F. Finger, R. Carius, T. Dylla, B. Rech, M. Grimm, L. Houben, and M. Stutzmann, *Intrinsic microcrystalline silicon prepared by hot-wire chemical vapour deposition for thin film solar cells*, *Thin Solid Films* **430** (2003), 202–207.
- [118] Y. Wang, X. Geng, H. Stiebig, and F. Finger, *Stability of microcrystalline silicon solar cells with HWCVD buffer layer*, *Thin Solid Films* **516** (2008), 733–735.
- [119] K. Deng and E. A. Schiff, *Amorphous Silicon-based Solar Cells*, John Wiley & Sons Ltd, Chichester, UK, 2003.
- [120] B. Chapman, *Glow Discharge Processes: Sputtering and Plasma Etching*, John Wiley & Sons, New York, USA, 1980.
- [121] W. Luft and Y. S. Tsu, *Hydrogenated Amorphous Silicon Alloy Deposition Processes*, Taylor & Francis, New York, USA, 1993.
- [122] A. Lambertz, *Development of Doped Microcrystalline Silicon Oxide and its Application to Thin-Film Silicon Solar Cells*, Ph.D. thesis, University Utrecht, Netherlands, 2015.
- [123] T. Grundler, *Silicon Oxide as an Intermediate Reflector in Silicon Thin Film Solar Cells*, Ph.D. thesis, Rheinisch Westfälische Technische Hochschule Aachen, Germany, 2009.
- [124] V. Smirnov, A. Lambertz, S. Tillmanns, and F. Finger, *p- and n-type microcrystalline silicon oxide ( $\mu\text{c-SiO}_x\text{:H}$ ) for applications in thin film silicon tandem solar cells*, *Can. J. Phys.* **92** (2014), 932–935.
- [125] A. Lambertz, V. Smirnov, T. Merdzhanova, K. Ding, S. Haas, G. Jost, R. Schropp, F. Finger, and U. Rau, *Microcrystalline silicon-oxygen alloys for application in silicon solar cells and modules*, *Sol. Energy Mater. Sol. Cells* **119** (2013), 134–143.
- [126] J. Müller, O. Kluth, S. Wieder, H. Siekmann, G. Schöpe, W. Reetz, O. Vetterl, D. Lundszen, A. Lambertz, F. Finger, B. Rech, and H. Wagner, *Development of highly efficient thin film silicon solar cells on texture-etched zinc oxide-coated glass substrates*, *Sol. Energy Mater. Sol. Cells* **66** (2001), 275–281.



- [127] R. Rech, J. Müller, T. Repmann, O. Kluth, T. Roschek, J. Hüpkas, H. Stiebig, and W. Apenzeller, *Amorphous and Microcrystalline Silicon Based Solar Cells and Modules on Textured Zinc Oxide Coated Glass Substrates*, Mater. Res. Soc. Symp. Proc. **762** (2003), 285–292.
- [128] W. Böttler, V. Smirnov, J. Hüpkas, and F. Finger, *Texture-etched ZnO as a versatile base for optical back reflectors with well-designed surface morphologies for application in thin film solar cells*, Phys. Stat. Sol. A **209** (2012), 1144–1149.
- [129] C. Ulbrich, A. Gerber, K. Hermans, A. Lambertz, and U. Rau, *Analysis of short circuit current gains by an anti-reflective textured cover on silicon thin film solar cells*, Prog. Photovolt: Res. Appl. **21** (2012), 1672–1681.
- [130] S. Haas, A. Gordijn, and H. Stiebig, *High speed laser processing for monolithical series connection of silicon thin-film modules*, Prog. Photovolt: Res. Appl. **16** (2008), 195–203.
- [131] D. Long, *Raman Spectroscopy*, Mcraw-Hill International Book Company, New York, USA, 1977.
- [132] F. Köhler, *Zur Mikrostruktur siliziumbasierter Dünnschichten für die Photovoltaik*, Ph.D. thesis, Rheinisch-Westphälische Technische Hochschule, Germany, 2012.
- [133] F. Köhler, S. Schicho, B. Wolfrum, A. Gordijn, S. E. Pust, and R. Carius, *Gradient etching of silicon-based thin films for depth-resolved measurements: The example of Raman crystallinity*, Thin Solid Films **520** (2012), 2605–2608.
- [134] V. Smirnov, C. Das, T. Melle, A. Lambertz, M. Hülsbeck, R. Carius, and F. Finger, *Improved homogeneity of microcrystalline absorber layer in thin-film silicon tandem solar cells*, Mater. Sci. Eng. B **159-160** (2009), 44–47.
- [135] F. Einsele, *Amorphe Siliziumoxidschichten zur Oberflächenpassivierung und Kontaktierung von Heterostruktur-Solarzellen aus amorphem und kristallinem Silizium*, Ph.D. thesis, Rheinisch Westfälische Technische Hochschule Aachen, Germany, 2010.
- [136] W. B. Jackson, N. M. Amer, A. C. Boccara, and D. Fournier, *Photothermal deflection spectroscopy and detection*, Appl. Opt. **20** (1981), 1333–1344.
- [137] N. M. Amer and W. B. Jackson, *Optical Properties of Defect States in  $\alpha$ -Si:H*, Semiconductors and Semimetals (J. J. Pankove, ed.), Academic Press, New York, USA, 1984.

- [138] M. Berginski, *Lichtstreuende Oberflächen, Schichten und Schichtsysteme zur Verbesserung der Lichteinkopplung in Silizium-Dünnschichtsolarzellen*, Ph.D. thesis, Rheinisch Westfälische Technische Hochschule Aachen, Germany, 2007.
- [139] F. Lindholm, J. Fossum, and E. Burgess, *Application of the superposition principle to solar-cell analysis*, IEEE Transactions on Electron Devices **26** (1979), 165–171.
- [140] W. Reetz, H. Stiebig, T. Brammer, B. Rech, and J. Fölsch, *Spectral response of stacked solar cells based on a-Si:H*, Proceedings of the 2nd ISEC-Europe Solar Congress, Eurosun98 (1999), V.1.5–1.
- [141] A. J. Nozik and R. Memming, *Physical Chemistry of Semiconductor-Liquid Interfaces*, J. Phys. Chem. **100** (1996), 13061–13078.
- [142] S. Y. Reece, J. A. Hamel, K. Sung, T. D. Jarvi, A. J. Esswein, J. J. H. Pijpers, and D. G. Nocera, *Wireless Solar Water Splitting Using Silicon-Based Semiconductors and Earth-Abundant Catalysts*, Science **334** (2011), 645–648.
- [143] V. Cristino, S. Berardi, S. Caramori, R. Argazzi, S. Carli, L. Meda, A. Tacca, and C. A. Bignozzi, *Efficient solar water oxidation using photovoltaic devices functionalized with earth-abundant oxygen evolving catalysts*, Phys. Chem. Chem. Phys. **15** (2013), 13083–13092.
- [144] F. Urbain, V. Smirnov, J.-P. Becker, A. Lambertz, F. Yang, J. Ziegler, B. Kaiser, W. Jaegermann, U. Rau, and F. Finger, *Multijunction Si photocathodes with tunable photovoltages from 2.0 V to 2.8 V for light induced water splitting*, Energy Environ. Sci. **9** (2016), 145–154.
- [145] T. J. Jacobsson, V. Fjallstrom, M. Sahlberg, M. Edoff, and T. Edvinsson, *A monolithic device for solar water splitting based on series interconnected thin film absorbers reaching over 10 % solar-to-hydrogen efficiency*, Energy Environ. Sci. **6** (2013), 3676–3683.
- [146] C. R. Cox, J. Z. Lee, D. G. Nocera, and T. Buonassisi, *Ten-percent solar-to-fuel conversion with nonprecious materials*, Proc. Nat. Acad. Sci. USA **111** (2014), 14057–14061.
- [147] J. Luo, J.-H. Im, M. T. Mayer, M. Schreier, M. K. Nazeeruddin, N.-G. Park, S. D. Tilley, H. J. Fan, and M. Grätzel, *Water photolysis at 12.3 % efficiency via perovskite photovoltaics and Earth-abundant catalysts*, Science **345** (2014), 1593–1596.

- [148] A. Delahoy, S. Gau, O. Murphy, M. Kapur, and J. Bockris, *A one-unit photo-voltaic electrolysis system based on a triple stack of amorphous silicon (pin) cells*, Int. J. Hydrogen Energy **10** (1985), 113–116.
- [149] G. Hodes, *Photoelectrochemical Cell Measurements: Getting the Basics Right*, J. Phys. Chem. Lett. **3** (2012), 1208–1213.
- [150] Z. Huang, J. R. McKone, C. Xiang, R. L. Grimm, E. L. Warren, J. M. Spurgeon, H.-J. Lewerenz, B. S. Brunschwig, and N. S. Lewis, *Comparison between the measured and modeled hydrogen-evolution activity of Ni- or Pt-coated silicon photocathodes*, Int. J. Hydrogen Energy **39** (2014), 16220–16226.
- [151] T. J. Mills, F. Lin, and S. W. Boettcher, *Theory and Simulations of Electrocatalyst-Coated Semiconductor Electrodes for Solar Water Splitting*, Phys. Rev. Lett. **112** (2014), 148304.
- [152] M. T. Winkler, C. R. Cox, D. G. Nocera, and T. Buonassisi, *Modeling integrated photovoltaic–electrochemical devices using steady-state equivalent circuits*, Proc. Nat. Acad. Sci. USA **110** (2013), E1076–E1082.
- [153] J. Ziegler, B. Kaiser, W. Jaegermann, F. Urbain, J.-P. Becker, V. Smirnov, and F. Finger, *Photoelectrochemical and Photovoltaic Characteristics of Amorphous-Silicon-Based Tandem Cells as Photocathodes for Water Splitting*, ChemPhysChem **15** (2014), 4026–4031.
- [154] F. Urbain, V. Smirnov, J.-P. Becker, U. Rau, J. Ziegler, B. Kaiser, W. Jaegermann, and F. Finger, *Application and modeling of an integrated amorphous silicon tandem based device for solar water splitting*, Sol. Energy Mater. Sol. Cells **140** (2015), 275–280.
- [155] R. H. Coridan, A. C. Nielander, S. A. Francis, M. T. McDowell, V. Dix, S. M. Chatman, and N. Lewis, *Methods for Comparing the Performance of Energy-Conversion Systems for Use in Solar Fuels and Solar Electricity Generation*, Energy Environ. Sci. **8** (2015), 2886–2901.
- [156] H. Döschner, J. L. Young, J. F. Geisz, J. A. Turner, and T. G. Deutsch, *Solar-to-hydrogen efficiency: shining light on photoelectrochemical device performance*, Energy Environ. Sci. (2016).
- [157] Z. Chen, T. F. Jaramillo, T. G. Deutsch, A. Kleiman-Shwarscstein, A. J. Forman, N. Gaillard, R. Garland, K. Takanabe, C. Heske, M. Sunkara, E. W. McFarland, K. Domen, E. L. Miller, J. A. Turner, and H. N. Dinh, *Accelerating*

- materials development for photoelectrochemical hydrogen production: Standards for methods, definitions, and reporting protocols*, J. Mater. Res. **25** (2010), 3–16.
- [158] C. Levy-Clement, A. Heller, W. A. Bonner, and B. A. Parkinson, *Spontaneous Photoelectrolysis of HBr and HI*, J. Electrochem. Soc. **129** (1982), 1701–1705.
- [159] M. A. Schoonen, Y. Xu, and D. R. Strongin, *An introduction to geocatalysis*, J. Geochem. Explor. **62** (1998), 201–215.
- [160] L. M. Peter, *Photoelectrochemical Water Splitting. A Status Assessment*, Electroanalysis **27** (2015), 864–871.
- [161] L. Han, F. F. Abdi, P. Perez Rodriguez, B. Dam, R. van de Krol, M. Zeman, and A. H. M. Smets, *Optimization of amorphous silicon double junction solar cells for an efficient photoelectrochemical water splitting device based on a bismuth vanadate photoanode*, Phys. Chem. Chem. Phys. **16** (2014), 4220–4229.
- [162] P. Borno, F. F. Abdi, S. D. Tilley, B. Dam, R. van de Krol, M. Graetzel, and K. Sivula, *A Bismuth Vanadate-Cuprous Oxide Tandem Cell for Overall Solar Water Splitting*, J. Phys. Chem. C **118** (2014), 16959–16966.
- [163] J. Meier, J. Spitznagel, U. Kroll, C. Bucher, S. Faj, T. Moriarty, and A. Shah, *Potential of amorphous and microcrystalline silicon solar cells*, Thin Solid Films **451-452** (2004), 518–524.
- [164] B. Vet and M. Zeman, *Relation between the open-circuit voltage and the band gap of absorber and buffer layers in a-Si:H solar cells*, Thin Solid Films **516** (2008), 6873–6876.
- [165] G. Ganguly and A. Matsuda, *Importance of surface processes in defect formation in a-Si:H*, J. Non-Cryst. Sol. **164-166, Part 1** (1993), 31–36.
- [166] A. H. M. Smets, W. M. M. Kessels, and M. C. M. van de Sanden, *Vacancies and voids in hydrogenated amorphous silicon*, Appl. Phys. Lett. **82** (2003), 1547–1549.
- [167] A. H. M. Smets and M. C. M. van de Sanden, *Relation of the Si-H stretching frequency to the nanostructural Si-H bulk environment*, Phys. Rev. B **76** (2007), 073202–1/4.

- [168] V. Smirnov, O. Astakhov, R. Carius, B. E. Pieters, Y. Petrusenko, V. Borysenko, and F. Finger, *Performance of p- and n-side illuminated microcrystalline silicon solar cells following 2 MeV electron bombardment*, Appl. Phys. Lett. **101** (2012), 143903.
- [169] C. Droz, E. Vallat-Sauvain, J. Bailat, L. Feitknecht, J. Meier, and A. Shah, *Relationship between Raman crystallinity and open-circuit voltage in microcrystalline silicon solar cells*, Sol. Energy Mater. Sol. Cells **81** (2004), 61–71.
- [170] S. Reynolds, R. Carius, F. Finger, and V. Smirnov, *Correlation of structural and optoelectronic properties of thin film silicon prepared at the transition from microcrystalline to amorphous growth*, Thin Solid Films **517** (2009), 6392–6395.
- [171] O. Vetterl, A. Lambertz, A. Dasgupta, F. Finger, B. Rech, O. Kluth, and H. Wagner, *Thickness dependence of microcrystalline silicon solar cell properties*, Sol. Energy Mater. Sol. Cells **66** (2001), 345–351.
- [172] B. E. Pieters, H. Stiebig, M. Zeman, and R. A. C. M. M. van Swaaij, *Determination of the mobility gap of intrinsic  $\mu\text{c-Si:H}$  in p-i-n solar cells*, J. Appl. Phys. **105** (2009), 044502.
- [173] T. Brammer and H. Stiebig, *Applying analytical and numerical methods for the analysis of microcrystalline silicon solar cells*, Sol. Energy Mater. Sol. Cells **90** (2006), 3021–3030.
- [174] Y. Mai, S. Klein, R. Carius, H. Stiebig, X. Geng, and F. Finger, *Open circuit voltage improvement of high-deposition-rate microcrystalline silicon solar cells by hot wire interface layers*, Appl. Phys. Lett. **87** (2005), 073503.
- [175] M. N. van den Donker, S. Klein, B. Rech, F. Finger, W. M. M. Kessels, and M. C. M. van de Sanden, *Microcrystalline silicon solar cells with an open-circuit voltage above 600mV*, Appl. Phys. Lett. **90** (2007), 183504.
- [176] G. Bugnon, G. Parascandolo, S. Hänni, M. Stuckelberger, M. Charrère, M. Despeisse, F. Meillaud, and C. Ballif, *Silicon oxide buffer layer at the p-i interface in amorphous and microcrystalline silicon solar cells*, Sol. Energy Mater. Sol. Cells **120, Part A** (2014), 143–150.
- [177] S. Olibet, E. Vallat-Sauvain, and C. Ballif, *Model for a-Si:H/c-Si interface recombination based on the amphoteric nature of silicon dangling bonds*, Phys. Rev. B **76** (2007), 035326.

- [178] S. De Wolf, S. Olibet, and C. Ballif, *Stretched-exponential a-Si:H/c-Si interface recombination decay*, Appl. Phys. Lett. **93** (2008), 32101.
- [179] F. Urbain, V. Smirnov, J.-P. Becker, U. Rau, J. Ziegler, F. Yang, B. Kaiser, W. Jaegermann, S. Hoch, M. Blug, and F. Finger, *Solar water splitting with earth-abundant materials using amorphous silicon photocathodes and Al/Ni contacts as hydrogen evolution catalyst*, Chem. Phys. Lett. **638** (2015), 25–30.
- [180] S. Kirner, S. Calnan, O. Gabriel, S. Neubert, M. Zelt, B. Stannowski, B. Rech, and R. Schlatmann, *An improved silicon-oxide-based intermediate-reflector for micromorph solar cells*, Phys. Stat. Sol. C **9** (2012), 2145–2148.
- [181] W. E. McMahon, K. E. Emery, D. J. Friedman, L. Ottoson, M. S. Young, J. S. Ward, C. M. Kramer, A. Duda, and S. Kurtz, *Fill factor as a probe of current-matching for GaInP<sub>2</sub>/GaAs tandem cells in a concentrator system during outdoor operation*, Prog. Photovolt: Res. Appl. **16** (2008), 213–224.
- [182] C. C. L. McCrory, S. Jung, J. C. Peters, and T. F. Jaramillo, *Benchmarking Heterogeneous Electrocatalysts for the Oxygen Evolution Reaction*, J. Am. Chem. Soc. **135** (2013), 16977–16987.
- [183] J.-W. Schüttauf, B. Niesen, L. Löfgren, M. Bonnet-Eymard, M. Stuckelberger, S. Hänni, M. Boccard, G. B. Bugnon, M. Despeisse, F.-J. Haug, F. Meillaud, and C. Ballif, *Amorphous silicon-germanium for triple and quadruple junction thin-film silicon based solar cells*, Sol. Energy Mater. Sol. Cells **133** (2015), 163–169.
- [184] S. Fai Tong, D. Y. Kim, R. Santbergen, H. Tan, R. A. C. M. M. van Swaaij, A. H. M. Smets, O. Isabella, and M. Zeman, *Quadruple-junction thin-film silicon-based solar cells with high open-circuit voltage*, Appl. Phys. Lett. **105** (2014), 063902.
- [185] S. Kirner, S. Neubert, C. Schultz, O. Gabriel, B. Stannowski, B. Rech, and R. Schlatmann, *Quadruple-junction solar cells and modules based on amorphous and microcrystalline silicon with high stable efficiencies*, Jap. J. Appl. Phys. **54** (2015), 08KB03.
- [186] A. S. Ferlauto, G. M. Ferreira, J. M. Pearce, C. R. Wronski, R. W. Collins, X. Deng, and G. Ganguly, *Analytical model for the optical functions of amorphous semiconductors from the near-infrared to ultraviolet: Applications in thin film photovoltaics*, J. Appl. Phys. **92** (2002), 2424–2436.

- [187] M. Koehl, M. Heck, S. Wiesmeier, and J. Wirth, *Modeling of the nominal operating cell temperature based on outdoor weathering*, Sol. Energy Mater. Sol. Cells **95** (2011), 1638–1646.
- [188] S. Haussener, S. Hu, C. Xiang, A. Z. Weber, and N. S. Lewis, *Simulations of the irradiation and temperature dependence of the efficiency of tandem photoelectrochemical water-splitting systems*, Energy Environ. Sci. **6** (2013), 3605–3618.
- [189] F. Urbain, J.-P. Becker, V. Smirnov, J. Ziegler, F. Florent Yang, B. Kaiser, W. Jaegermann, S. Hoch, A. Maljusch, U. Rau, and F. r. Finger, *Influence of the operating temperature on the performance of silicon based photoelectrochemical devices for water splitting*, Mater. Sci. Sem. Proc. **42** (2016), 142–146.
- [190] N. D. Arora and J. R. Hauser, *Temperature dependence of silicon solar cell characteristics*, Sol. Energy Mater. **6** (1982), 151–158.
- [191] M. A. Green, K. Emery, Y. Hishikawa, W. Warta, and E. D. Dunlop, *Solar cell efficiency tables (Version 45)*, Prog. Photovolt: Res. Appl. **23** (2015), 1–9.
- [192] O. Heavens, *Some factors influencing the adhesion of films produced by vacuum evaporation*, J. Phys. Radium **11** (1950), 355–360.
- [193] S. Russell, S. Rafalski, R. Spreitzer, J. Li, M. Moinpour, F. Moghadam, and T. Alford, *Enhanced adhesion of copper to dielectrics via titanium and chromium additions and sacrificial reactions*, Thin Solid Films **262** (1995), 154–167.
- [194] J. R. McKone, E. L. Warren, M. J. Bierman, S. W. Boettcher, B. S. Brunschwig, N. S. Lewis, and H. B. Gray, *Evaluation of Pt, Ni, and Ni-Mo electrocatalysts for hydrogen evolution on crystalline Si electrodes*, Energy Environ. Sci. **4** (2011), 3573–3583.
- [195] B. Mei, B. Seger, T. Pedersen, M. Malizia, O. Hansen, I. Chorkendorff, and P. C. K. Vesborg, *Protection of  $p^+$ - $n$ -Si Photoanodes by Sputter-Deposited Ir/IrO<sub>x</sub> Thin Films*, J. Phys. Chem. Lett. **5** (2014), 1948–1952.
- [196] S. Hu, M. R. Shaner, J. A. Beardslee, M. Lichterman, B. S. Brunschwig, and N. S. Lewis, *Amorphous TiO<sub>2</sub> coatings stabilize Si, GaAs, and GaP photoanodes for efficient water oxidation*, Science **344** (2014), 1005–1009.
- [197] S. Trasatti, *Work function, electronegativity, and electrochemical behaviour of metals: III. Electrolytic hydrogen evolution in acid solutions*, J. Electroanal. Chem. **39** (1972), 163–184.

- [198] M. Kibria, M. Mridha, and A. Khan, *Electrochemical studies of a nickel electrode for the hydrogen evolution reaction*, Int. J. Hydrogen Energy **20** (1995), 435–440.
- [199] C. G. Morales-Guio, K. Thorwarth, B. Niesen, L. Liardet, J. Patscheider, C. Ballif, and X. Hu, *Solar Hydrogen Production by Amorphous Silicon Photocathodes Coated with a Magnetron Sputter Deposited  $\text{Mo}_2\text{C}$  Catalyst*, J. Am. Chem. Soc. **137** (2015), 7035–7038.
- [200] J. Kibsgaard, Z. Chen, B. N. Reinecke, and T. F. Jaramillo, *Engineering the surface structure of  $\text{MoS}_2$  to preferentially expose active edge sites for electrocatalysis*, Nature Materials **11** (2012), 963–969.
- [201] P. Rasiyah and A. C. C. Tseung, *The role of the lower metal oxide/higher metal oxide couple in oxygen evolution reactions*, J. Electrochem. Soc. **131** (1984), 803–808.
- [202] M. H. Miles, Y. H. Huang, and S. Srinivasan, *The oxygen electrode reaction in alkaline solutions on oxide electrodes prepared by the thermal decomposition method*, J. Electrochem. Soc. **125** (1978), 1931–1934.
- [203] J. A. Koza, Z. He, A. S. Miller, and J. A. Switzer, *Electrodeposition of Crystalline  $\text{Co}_3\text{O}_4$  - A Catalyst for the Oxygen Evolution Reaction*, Chem. Mater. **24** (2012), 3567–3573.
- [204] C. C. L. McCrory, S. Jung, I. M. Ferrer, S. M. Chatman, J. C. Peters, and T. F. Jaramillo, *Benchmarking Hydrogen Evolving Reaction and Oxygen Evolving Reaction Electrocatalysts for Solar Water Splitting Devices*, J. Am. Chem. Soc. **137** (2015), 4347–4357.
- [205] R. Gilliam, J. Graydon, D. Kirk, and S. Thorpe, *A review of specific conductivities of potassium hydroxide solutions for various concentrations and temperatures*, Int. J. Hydrogen Energy **32** (2007), 359–364.
- [206] W. Sheng, H. A. Gasteiger, and Y. Shao-Horn, *Hydrogen oxidation and evolution reaction kinetics on platinum: acid vs alkaline electrolytes*, J. Electrochem. Soc. **157** (2010), B1529–B1536.
- [207] S. G. Bratsch, *Standard Electrode Potentials and Temperature Coefficients in Water at 298.15 K*, J. Phys. Chem. Ref. Data **18** (1989), 1–21.
- [208] J. Jin, K. Walczak, M. R. Singh, C. Karp, N. S. Lewis, and C. Xiang, *An experimental and modeling/simulation-based evaluation of the efficiency and operational performance characteristics of an integrated, membrane-free, neutral*



- pH solar-driven water-splitting system*, Energy Environ. Sci. **7** (2014), 3371–3380.
- [209] A. Berger, R. A. Segalman, and J. Newman, *Material requirements for membrane separators in a water-splitting photoelectrochemical cell*, Energy Environ. Sci. **7** (2014), 1468–1476.
- [210] E. Verlage, S. Hu, R. Liu, R. J. R. Jones, K. Sun, C. Xiang, N. S. Lewis, and H. A. Atwater, *A monolithically integrated, intrinsically safe, 10% efficient, solar-driven water-splitting system based on active, stable earth-abundant electrocatalysts in conjunction with tandem III-V light absorbers protected by amorphous TiO<sub>2</sub> films*, Energy Environ. Sci. **8** (2015), 3166–3172.
- [211] A. Appleby, A. Delahoy, S. Gau, O. Murphy, M. Kapur, and J. Bockris, *An amorphous silicon-based one-unit photovoltaic electrolyzer*, Energy **10** (1985), 871–876.
- [212] Y. Sakai, S. Sugahara, M. Matsumura, Y. Nakato, and H. Tsubomura, *Photo-electrochemical water splitting by tandem type and heterojunction amorphous silicon electrodes*, Can. J. Chem. **66** (1988), 1853–1856.
- [213] G. H. Lin, M. Kapur, R. C. Kainthla, and J. O. Bockris, *One step method to produce hydrogen by a triple stack amorphous silicon solar cell*, Appl. Phys. Lett. **55** (1989), 386–387.
- [214] C. Gramaccioni, A. Selvaggi, and F. Galluzzi, *Thin film multi-junction solar cell for water photoelectrolysis*, Electrochim. Acta **38** (1993), 111–113.
- [215] R. E. Rocheleau, E. L. Miller, , and A. Misra, *High-Efficiency Photoelectrochemical Hydrogen Production Using Multijunction Amorphous Silicon Photoelectrodes*, Energy Fuels **12** (1998), 3–10.
- [216] Y. Yamada, N. Matsuki, T. Ohmori, H. Mametsuka, M. Kondo, A. Matsuda, and E. Suzuki, *One chip photovoltaic water electrolysis device*, Int. J. Hydrogen Energy **28** (2003), 1167–1169.
- [217] N. A. Kelly and T. L. Gibson, *Design and characterization of a robust photo-electrochemical device to generate hydrogen using solar water splitting*, Int. J. Hydrogen Energy **31** (2006), 1658–1673.
- [218] E. L. Miller, D. Paluselli, B. Marsen, and R. E. Rocheleau, *Development of reactively sputtered metal oxide films for hydrogen-producing hybrid multijunction photoelectrodes*, Sol. Energy Mater. Sol. Cells **88** (2005), 131–144.

- [219] F. Zhu, J. Hu, I. Matulionis, T. Deutsch, N. Gaillard, A. Kunrath, E. Miller, and A. Madan, *Amorphous silicon carbide photoelectrode for hydrogen production directly from water using sunlight*, *Phil. Mag.* **89** (2009), 2723–2739.
- [220] N. Gaillard, Y. Chang, J. Kaneshiro, A. Deangelis, and E. L. Miller, *Status of research on tungsten oxide-based photoelectrochemical devices at the University of Hawaii*, *Proc. SPIE* **7770** (2010), 1–14.
- [221] L. Han, F. F. Abdi, R. van de Krol, R. Liu, Z. Huang, H.-J. Lewerenz, B. Dam, M. Zeman, and A. H. M. Smets, *Efficient Water-Splitting Device Based on a Bismuth Vanadate Photoanode and Thin-Film Silicon Solar Cells*, *ChemSusChem* **7** (2014), 2832–2838.
- [222] J.-P. Becker, F. Urbain, V. Smirnov, U. Rau, J. Ziegler, B. Kaiser, W. Jaegermann, and F. Finger, *Modeling and practical realization of thin film silicon-based integrated solar water splitting devices*, *Phys. Stat. Sol. A* (2016).
- [223] S. Hu, C. Xiang, S. Haussener, A. D. Berger, and N. S. Lewis, *An analysis of the optimal band gaps of light absorbers in integrated tandem photoelectrochemical water-splitting systems*, *Energy Environ. Sci.* **6** (2013), 2984–2993.
- [224] E. Miller, R. Rocheleau, and X. Deng, *Design considerations for a hybrid amorphous silicon/photoelectrochemical multijunction cell for hydrogen production*, *Int. J. Hydrogen Energy* **28** (2003), 615–623.
- [225] M. Matsumura, Y. Sakai, S. Sugahara, Y. Nakato, and H. Tsubomura, *Photoelectrochemical hydrogen evolution using amorphous silicon electrodes having p-i-n or p-i-n-p-i-n junctions*, *Sol. Energy. Mater.* **13** (1986), 57–64.
- [226] B. D. James, G. N. Baum, J. Perez, and K. N. Baum, *Technoeconomic Analysis of Photoelectrochemical (PEC) Hydrogen Production*, DOE Report (2009).
- [227] S. Hu, N. S. Lewis, J. W. Ager, J. Yang, J. R. McKone, and N. C. Strandwitz, *Thin-Film Materials for the Protection of Semiconducting Photoelectrodes in Solar-Fuel Generators*, *J. Phys. Chem. C* **119** (2015), 24201–24228.
- [228] S. Albrecht, M. Saliba, J. P. Correa Baena, F. Lang, L. Kegelman, M. Mews, L. Steier, A. Abate, J. Rappich, L. Korte, R. Schlattmann, M. K. Nazeeruddin, A. Hagfeldt, M. Grätzel, and B. Rech, *Monolithic perovskite/silicon-heterojunction tandem solar cells processed at low temperature*, *Energy Environ. Sci.* (2015).

- [229] B. Seger, I. E. Castelli, P. C. K. Vesborg, K. W. Jacobsen, O. Hansen, and I. Chorkendorff, *2-Photon tandem device for water splitting: comparing photocathode first versus photoanode first designs*, *Energy Environ. Sci.* **7** (2014), 2397–2413.
- [230] S. N. Habisreutinger, L. Schmidt-Mende, and J. K. Stolarczyk, *Photocatalytic Reduction of  $\text{CO}_2$  on  $\text{TiO}_2$  and Other Semiconductors*, *Angew. Chem. Int. Ed.* **52** (2013), 7372–7408.
- [231] M. Schreier, L. Curvat, F. Giordano, L. Steier, A. Abate, S. M. Zakeeruddin, J. Luo, M. T. Mayer, and M. Grätzel, *Efficient photosynthesis of carbon monoxide from  $\text{CO}_2$  using perovskite photovoltaics*, *Nat. Commun.* **6** (2015).
- [232] M. R. Singh and A. T. Bell, *Design of an artificial photosynthetic system for production of alcohols in high concentration from  $\text{CO}_2$* , *Energy Environ. Sci.* (2015).
- [233] Y. Sugano, A. Ono, R. Kitagawa, J. Tamura, M. Yamagiwa, Y. Kudo, E. Tsutsumi, and S. Mikoshiba, *Crucial role of sustainable liquid junction potential for solar-to-carbon monoxide conversion by a photovoltaic photoelectrochemical system*, *RSC Adv.* **5** (2015), 54246–54252.
- [234] T. Arai, S. Sato, and T. Morikawa, *A monolithic device for  $\text{CO}_2$  photoreduction to generate liquid organic substances in a single-compartment reactor*, *Energy Environ. Sci.* **8** (2015), 1998–2002.
- [235] P. J. Mohr, B. N. Taylor, and D. B. Newell, *CODATA recommended values of the fundamental physical constants: 2010*, *Rev. Mod. Phys.* **84** (2012), 1527–1605.

# Appendix

## Appendix-Chapter 5

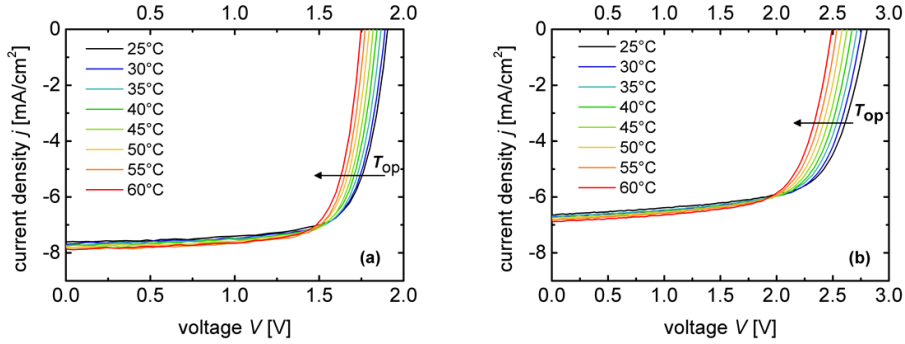


**Fig. A1** (a) Current density-voltage  $j$ - $V$  curves of the a-Si:H/a-Si:H tandem junction solar cell (cell 130/130, Table 5.3) at various operating temperatures  $T_{op}$ . (b) Current density-voltage  $j$ - $V$  curves of the a-Si:H/a-Si:H/ $\mu$ c-Si:H/ $\mu$ c-Si:H quadruple junction solar cell (see Table 5.3) at various operating temperatures  $T_{op}$ . In both measurements, the temperature range between 25 °C and 60 °C was investigated in steps of 5 °C.

## Appendix-Chapter 6

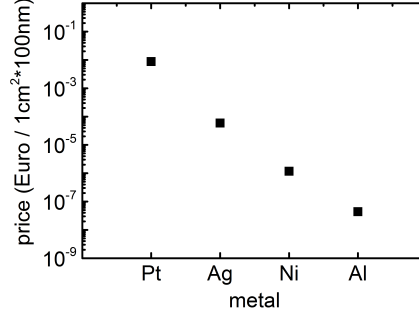


**Fig. A2** Established prices (in Euro/1 cm² \* 100 nm) for Pt, Ag, Ni, and Al. Source: London Metal Exchange, 10 February 2015.

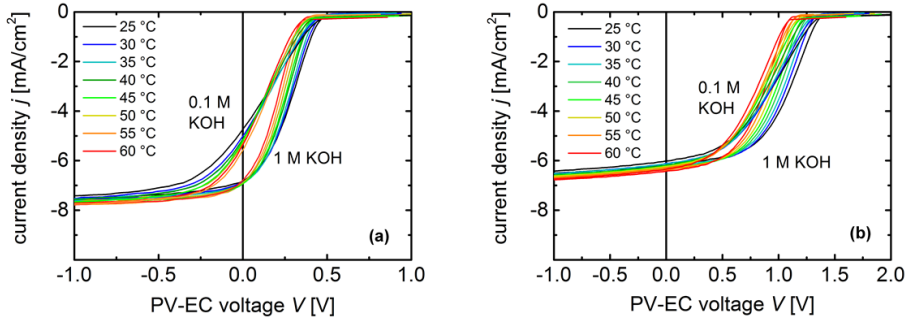


**Fig. A3** (a) Calculated current density-voltage curves of the a-Si:H/a-Si:H tandem junction PV-EC device at different operation temperatures in both 0.1 M and 1 M KOH, respectively. (b) Calculated current density-voltage curves of the a-Si:H/a-Si:H/ $\mu$ c-Si:H/ $\mu$ c-Si:H quadruple junction PV-EC device at different operation temperatures in both 0.1 M and 1 M KOH, respectively. The data for the calculation of the  $V_{PV-EC}(j, T)$  (based on Eq. 6.1) curves was taken from Table 6.4 ( $T$ -dependent electrolyte resistances  $R(T)$ ) and from Fig. 6.14(a) and (b), respectively ( $T$ -dependent HER and OER performance,  $\eta_{HER}(j, T)$  and  $\eta_{OER}(j, T)$ , respectively). The current density at 0 V applied bias defines the operation point of the PV-EC device.

## Appendix-Sample list

**Table A1** Deposition and photovoltaic parameters for the **a-Si:H single junction solar cells** discussed in Section 5.2.2. The deposition parameters refer to the intrinsic absorber layers of the a-Si:H solar cells and are abbreviated as follows: silane concentration  $SC$  and substrate temperature  $T_s$ . The photovoltaic parameters describe the conversion efficiency  $\eta_{PV}$ , the open-circuit voltage  $V_{OC}$ , the fill factor  $FF$ , and the short-circuit current density  $J_{SC}$ . The solar cells were deposited on Asahi type "VU" glass substrates with an Ag back contact and the intrinsic absorber layers had a thickness of 400 nm. More details on the solar cell fabrication process and deposition parameters can be found in Section 3.2.2 and in Table 3.1, respectively.

sample name	$SC$ [%]	$T_s$ [°C]	$\eta_{PV}$ [%]	$V_{OC}$ [mV]	$FF$ [%]	$J_{SC}$ [mA/cm <sup>2</sup> ]
13B-026	4	70	7.7	922	66.4	12.6
13B-014	4	110	9.1	944	72.5	13.3
13B-044	4	130	9.6	946	73.4	13.8
13B-011	4	180	9.7	921	74.2	14.3
13B-020	4	250	7.9	802	70.2	14.0
13B-025	10	70	5.1	851	51.9	11.6
13B-015	10	110	8.8	916	68.3	14.1
13B-006	10	180	10.3	913	73.8	15.2
13B-021	10	250	7.5	823	69.0	13.2

**Table A2** Deposition and photovoltaic parameters for the  $\mu\text{c-Si:H}$  single junction solar cell series shown in Fig. 5.9. The deposition parameters refer to the intrinsic absorber layers of the  $\mu\text{c-Si:H}$  solar cells and are abbreviated as follows: silane concentration  $SC$ ,  $i$ -layer thickness. The layer preparation parameters, such as  $SC$  profiling and  $ni$  buffer layer thickness are also listed. The photovoltaic parameters of the different  $\mu\text{c-Si:H}$  solar cell series describe the conversion efficiency  $\eta_{\text{PV}}$ , the open-circuit voltage  $V_{\text{OC}}$ , the fill factor  $FF$ , and the short-circuit current density  $J_{\text{SC}}$ . The solar cells were deposited on textured ZnO:Al coated glass substrates. More details on the solar cell fabrication process and deposition parameters can be found in Section 3.2.2 and in Table 3.1, respectively.

sample name	Series	$SC$ [%]	$i$ -layer thickness [nm]	$SC$ profiling [%]	$n-i$ buffer layer [nm]	$\eta_{\text{PV}}$ [%]	$V_{\text{OC}}$ [mV]	$FF$ [%]	$J_{\text{SC}}$ [mA/cm <sup>2</sup> ]
13B-204	1300 nm	4.4	1300	-	-	7.3	499	68.1	21.5
13B-208	1300 nm	4.7	1300	-	-	7.3	507	69.3	20.7
13B-183	1300 nm	5.0	1300	-	-	8.0	528	71.3	22.0
13B-193	1300 nm	5.3	1300	-	-	7.4	520	68.2	20.9
13B-189	1300 nm	5.6	1300	-	-	6.3	510	70.2	17.6
13B-192	1300 nm	5.8	1300	-	-	5.5	507	67.8	16.1
13B-196	1300 nm	6.0	1300	-	-	3.4	548	58.3	10.6
13B-220	650 nm	4.7	650	-	-	6.5	53.4	71.4	16.9
13B-219	650 nm	5.0	650	-	-	6.8	543	72.2	17.3
13B-288	650 nm	5.3	650	-	-	8.6	545	72.6	21.6
13B-275	650 nm	5.6	650	-	-	7.5	559	69.8	19.1
13B-289	650 nm	5.8	650	-	-	6.7	550	66.2	18.3
13B-294	650 nm	6.0	650	-	-	3.6	575	53.2	11.8
13B-313	450 nm	5.0	450	-	-	6.7	548	72.2	17.0
13B-324	450 nm	5.3	450	-	-	7.5	565	72.8	18.2
13B-314	450 nm	5.6	450	-	-	5.6	575	66.4	14.6
13B-295	450 nm	6.0	450	-	-	4.8	564	54.9	15.6
14B-089	1300 nm + $SC$ profiling + buffer layer	5.0	1300	5.0-5.6	50	8.2	551	70.7	21.8
14B-031	650 nm + buffer layer	5.3	650	-	20	8.1	570	70.6	20.1
14B-005	450 nm + buffer layer	5.3	450	-	5	6.7	580	67.7	17.0

**Table A3** Deposition and photovoltaic parameters for the **a-Si:H/ $\mu$ c-Si:H tandem junction solar cells** discussed in Section 5.4.1. The deposition parameters of the individual sub cells can be found in Table 5.2. The photovoltaic parameters describe the conversion efficiency  $\eta_{PV}$ , the open-circuit voltage  $V_{OC}$ , the fill factor  $FF$ , and the short-circuit current density  $J_{SC}$ . The solar cells were deposited on textured ZnO:Al coated glass substrates. More details on the solar cell fabrication process and deposition parameters can be found in Section 3.2.2 and in Table 3.1, respectively.

sample name	Tandem cell	$\eta_{PV}$ [%]	$V_{OC}$ [mV]	$FF$ [%]	$J_{SC}$ [mA/cm <sup>2</sup> ]
13B-049	A	10.9	1390	72.3	10.8
14B-089	B	10.5	1474	65.6	10.9
14B-079	C	11.0	1504	73.0	10.0
14B-093	D	9.7	1515	76.2	8.4

**Table A4** Deposition and photovoltaic parameters for the **a-Si:H/a-Si:H tandem junction solar cells** discussed in Section 5.4.2. The deposition parameters of the individual sub cells can be found in Table 5.3. The photovoltaic parameters describe the conversion efficiency  $\eta_{PV}$ , the open-circuit voltage  $V_{OC}$ , the fill factor  $FF$ , and the short-circuit current density  $J_{SC}$ . The solar cells were deposited on Asahi type "VU" glass substrates. More details on the solar cell fabrication process and deposition parameters can be found in Section 3.2.2 and in Table 3.1, respectively.

sample name	Tandem cell	$\eta_{PV}$ [%]	$V_{OC}$ [mV]	$FF$ [%]	$J_{SC}$ [mA/cm <sup>2</sup> ]
14B-221	250/250	8.3	1602	71.8	7.2
14B-123	180/250	8.7	1700	68.5	7.4
13B-052	110/110	9.5	1870	77.5	6.6
13B-048	180/180	9.8	1796	78.8	7.0
14B-206	130/180	11.3	1806	74.2	8.4
14B-205	130/130	10.9	1913	74.0	7.7



**Table A5** Deposition and photovoltaic parameters for the **triple junction solar cells** discussed in Section 5.5 and presented in Table 5.4 and Table 5.5, respectively. The photovoltaic parameters describe the conversion efficiency  $\eta_{PV}$ , the open-circuit voltage  $V_{OC}$ , the fill factor  $FF$ , and the short-circuit current density  $J_{SC}$ . The a-Si:H/ $\mu$ c-Si:H/ $\mu$ c-Si:H solar cells (referred to as T1-T3) were deposited on textured ZnO:Al coated glass substrates and the a-Si:H/a-Si:H/ $\mu$ c-Si:H (referred to as T4-T6) were deposited on Asahi type "VU" glass substrates. More details on the solar cell fabrication process and deposition parameters can be found in Section 3.2.2 and in Table 3.1, respectively.

sample name	Triple cell	Cell type	$\eta_{PV}$ [%]	$V_{OC}$ [mV]	$FF$ [%]	$J_{SC}$ [mA/cm <sup>2</sup> ]
14B-149	T1	a-Si:H/ $\mu$ c-Si:H/ $\mu$ c-Si:H	11.1	1895	70.8	8.3
14B-162	T2	a-Si:H/ $\mu$ c-Si:H/ $\mu$ c-Si:H	11.1	1958	68.1	8.3
14B-167	T3	a-Si:H/ $\mu$ c-Si:H/ $\mu$ c-Si:H	11.2	1976	67.6	8.4
14B-163	T4	a-Si:H/a-Si:H/ $\mu$ c-Si:H	12.8	2269	72.3	7.8
14B-176	T5	a-Si:H/a-Si:H/ $\mu$ c-Si:H	13.4	2272	71.2	8.3
14B-210	T6	a-Si:H/a-Si:H/ $\mu$ c-Si:H	13.6	2279	69.2	8.6

**Table A6** Deposition and photovoltaic parameters for the **quadruple junction solar cells** discussed in Section 5.5 and presented in Table 5.6. The photovoltaic parameters describe the conversion efficiency  $\eta_{PV}$ , the open-circuit voltage  $V_{OC}$ , the fill factor  $FF$ , and the short-circuit current density  $J_{SC}$ . The a-Si:H/a-Si:H/ $\mu$ c-Si:H/ $\mu$ c-Si:H solar cells were deposited on textured ZnO:Al coated glass substrates. More details on the solar cell fabrication process and deposition parameters can be found in Section 3.2.2 and in Table 3.1, respectively.

sample name	Quadruple cell	$\eta_{PV}$ [%]	$V_{OC}$ [mV]	$FF$ [%]	$J_{SC}$ [mA/cm <sup>2</sup> ]
14B-225	Q1	12.7	2775	71.7	6.4
14B-235	Q2	12.4	2779	67.9	6.5
14B-217	Q3	13.2	2802	69.8	6.9

# Glossary

## Common Abbreviations

Acronym	Meaning
AC	alternating current
AM	air mass
CE	counter electrode
CVD	chemical vapor deposition
DC	direct current
DSR	differential spectral response
FTIR	Fourier transform infrared spectroscopy
HER	hydrogen evolution reaction
IEK-5	Institut für Energie- und Klimaforschung 5
IHL	inner Helmholtz layer
IR	infrared
LID	light induced degradation
MPP	maximum power point
OER	oxygen evolution reaction
OHL	outer Helmholtz layer
PDS	photothermal deflection spectroscopy
PEC	photoelectrochemical cell
PECVD	plasma enhanced chemical vapor deposition
PLD	pulsed laser deposition
PV-EC	photovoltaic-electrochemical
RE	reference electrode
RF	radio frequency (13.56 MHz)
RHE	reversible hydrogen electrode
RT	room temperature
sccm	standard cubic centimeter per minute (cm <sup>3</sup> /(60 s) at 101325 Pa and 273.15 K)
SHE	standard hydrogen electrode
SLJ	semiconductor liquid junctions
SQ	Shockley-Queisser
STH	solar-to-hydrogen
TCO	transparent conductive oxide

UHV	ultra-high vacuum
UV	ultraviolet
VHF	very high frequency
WE	working electrode

### Formula Abbreviations

Symbol	Description	Unit
$b$	Tafel slope	mV/dec
$C$	ion concentration	mol/cm <sup>3</sup>
$C$	capacitance	F
$d$	thickness	nm
$E$	potential	mV
$E^0$	standard electrode potential	mV
$E_{04}$	optical gap energy	eV
$E_C$	conduction band edge energy	eV
$E_F$	Fermi energy	eV
$E_{Fn}$	quasi-Fermi energy for electrons	eV
$E_{Fp}$	quasi-Fermi energy for holes	eV
$E_g$	band gap energy	eV
$E_{\text{onset}}$	onset potential	mV
$E_{\text{ph}}$	energy of incident light	eV
$E_V$	valence band edge energy	eV
$f$	frequency	Hz
$FF$	fill factor	%
$G$	Gibbs energy	J
$J$	current	mA
$I_C^{\text{RS}}$	crystalline volume fraction	%
$j$	current density	mA/cm <sup>2</sup>
$j_0$	exchange current density	mA/cm <sup>2</sup>
$J_0$	saturation current density	mA/cm <sup>2</sup>
$J_{0,\text{SQ}}$	saturation current density in the SQ-limit	mA/cm <sup>2</sup>
$J_{\text{SC}}$	short-circuit current density	mA/cm <sup>2</sup>
$J_{\text{SC},\text{SQ}}$	short-circuit current density in the SQ-limit	mA/cm <sup>2</sup>
$j_{\text{op}}$	PV-EC operation photocurrent density	mA/cm <sup>2</sup>
$M$	molar mass	g/mol
$n$	number of charge carriers	

---

$N_C$	density of states at conduction band edge	$\text{eV}^{-1} \text{ cm}^{-3}$
$N_i$	number of particles of species $i$	
$p$	pressure	mbar
$P$	power	W
$q$	charge density	$\text{mC}/\text{cm}^2$
$Q$	charge	C
$R$	resistance	$\Omega$
$R$	reflectance	%
$R_p$	parallel resistance	$\Omega/\text{cm}^2$
$R_s$	series resistance	$\Omega/\text{cm}^2$
$R_{\text{sh}}$	shunt resistance	$\Omega$
$SC$	silane concentration	%
$t$	time	s
$T$	temperature	K or $^{\circ}\text{C}$
$T_s$	substrate temperature	K or $^{\circ}\text{C}$
$T_{\text{op}}$	PV-EC operation temperature	K or $^{\circ}\text{C}$
$V_{\text{OC}}$	open-circuit voltage	mV
$z$	charge number	
$z_i$	charge number of species $i$	

### Greek symbols

Symbol	Description	Unit
$\alpha$	transfer coefficient	
$\alpha_{\text{abs}}$	absorption coefficient	$\text{cm}^{-1}$
$\eta_{\text{PV}}$	photovoltaic efficiency	%
$\eta_{\text{STHmax}}$	photovoltaic-electrochemical efficiency	%
$\lambda$	wavelength	nm
$\mu_i$	chemical potential of species $i$	J/mol
$\tilde{\mu}_i$	electrochemical potential of species $i$	J/mol
$\mu$	mobility	$\text{cm}^2/\text{Vs}$
$\nu$	scan rate	mV/s
$\eta$	overpotential	mV vs. RHE
$\phi$	inner potential	V
$\varphi_{\text{sc}}$	potential drop across the space charge region	V
$\sigma$	electric conductivity	S/cm

**Chemical symbols**

a-Si:H	hydrogenated amorphous silicon
$\mu$ c-Si:H	hydrogenated microcrystalline silicon
AgCl	silver chloride
BiVO <sub>4</sub>	bismuth vanadate
CdS	cadmium sulfide
CdSe	cadmium selenide
CuGaSe <sub>2</sub>	copper gallium selenide
Co <sub>3</sub> O <sub>4</sub>	cobalt(II,III) oxide
CO <sub>2</sub>	carbon dioxide
Fe <sub>2</sub> O <sub>3</sub>	iron(III) oxide (hematite)
GaInP <sub>2</sub>	gallium indium phosphide
GaP	gallium phosphide
H <sub>2</sub> O	water
H <sub>2</sub> SO <sub>4</sub>	sulfuric acid
HCl	hydrochloric acid
HI	hydriodic acid
HBr	hydrobromic acid
IrO <sub>2</sub>	iridium dioxide
KCl	potassium chloride
KOH	potassium hydroxide
KTaO <sub>3</sub>	potassium Tantalate
Mo <sub>2</sub> C	molybdenum carbide
MoS <sub>2</sub>	molybdenum disulfide
NiO <sub>x</sub>	nickel oxide
PTFE	polytetrafluoroethylene
RuO <sub>2</sub>	ruthenium dioxide
SiH <sub>4</sub>	mono silane
SiC	silicon carbide
SnO:F	fluoride doped tin oxide
SrTiO <sub>3</sub>	strontium titanate
TiO <sub>2</sub>	titanium dioxide
WO <sub>3</sub>	tungsten trioxide
ZnO	zinc oxide
ZnO:Al	aluminum-doped zinc oxide
ZnS	zinc sulfide
ZrO <sub>2</sub>	zirconium dioxide

**Constants**

Boltzmann constant	$k$	$= 1.380\,648\,8(13) \times 10^{-23} \text{ J K}^{-1}$ $= 8.617\,332\,4(78) \times 10^{-5} \text{ eV K}^{-1}$
Molar gas constant	$R$	$= 8.314\,462\,1(75) \text{ J mol}^{-1} \text{ K}^{-1}$
Planck constant	$h$	$= 6.626\,069\,57(29) \times 10^{-34} \text{ J s}$ $= 4.135\,667\,516(91) \times 10^{-15} \text{ eV s}$
Elementary charge	$e$	$= 1.602\,176\,565(35) \times 10^{-19} \text{ C}$
Faraday constant	$F$	$= 96\,485.3365(21) \text{ C mol}^{-1}$
Temperature at absolute zero	$T_0$	$= 0 \text{ K} = -273.15 \text{ }^\circ\text{C}$

Values were taken from Ref. [235].



# List of Publications

## Journal Publications

### Publications as first author

1. F. Urbain, K. Wilken, V. Smirnov, O. Astakhov, A. Lambertz, J.-P. Becker, U. Rau, J. Ziegler, B. Kaiser, W. Jaegermann, and F. Finger, *Development of thin film amorphous silicon tandem junction based photocathodes providing high open-circuit voltages for hydrogen production*, Int. J. Photoenergy **2014** (2014), 249317.
2. F. Urbain, V. Smirnov, J.-P. Becker, U. Rau, J. Ziegler, B. Kaiser, W. Jaegermann, F. Finger, *a-Si:H/ $\mu$ c-Si:H tandem junction based photocathodes with high open-circuit voltage for efficient hydrogen production*, J. Mater. Res. **29** (2014), 2605-2614 (Invited Feature Paper).
3. F. Urbain, V. Smirnov, J.-P. Becker, U. Rau, J. Ziegler, B. Kaiser, W. Jaegermann, and F. Finger, *Application and modeling of an integrated amorphous silicon tandem based device for solar water splitting*, Sol. Energy Mater. Sol. Cells **140** (2015), 275-280.
4. F. Urbain, V. Smirnov, J.-P. Becker, U. Rau, J. Ziegler, F. Yang, B. Kaiser, W. Jaegermann, S. Hoch, M. Blug, and F. Finger, *Solar water splitting with earth-abundant materials using amorphous silicon photocathodes and Al/Ni contacts as hydrogen evolution catalyst*, Chem. Phys. Lett. **638** (2015), 25-30.
5. F. Urbain, V. Smirnov, J.-P. Becker, A. Lambertz, U. Rau, and F. Finger, *Light-induced degradation of adapted quadruple junction thin film silicon solar cells for photoelectrochemical water splitting*, Sol. Energy Mater. Sol. Cells **145** (2016), 142-147 (Selected papers of the EMRS 2015 Spring meeting – Symposium C on Advanced Inorganic Materials and Structures for Photovoltaics).
6. F. Urbain, J.-P. Becker, V. Smirnov, J. Ziegler, F. Yang, B. Kaiser, W. Jaegermann, S. Hoch, A. Maljusch, U. Rau, and F. Finger, *Influence of the operating temperature on the performance of silicon based photoelectrochemical devices for water splitting*, Mater. Sci. Sem. Proc. **42** (2016), 142-146.



7. F. Urbain, V. Smirnov, J.-P. Becker, A. Lambertz, F. Yang, J. Ziegler, B. Kaiser, W. Jaegermann, U. Rau, and F. Finger, *Multijunction Si photocathodes with tunable photovoltages from 2.0 V to 2.8 V for light induced water splitting*, Energy. Environ. Sci. **9** (2016), 145-154 (Front cover story).

## Publications as co-author

1. J. Ziegler, B. Kaiser, W. Jaegermann, F. Urbain, J.-P. Becker, V. Smirnov, and F. Finger, *Photoelectrochemical and Photovoltaic Characteristics of Amorphous-Silicon-Based Tandem Cells as Photocathodes for Water Splitting*, ChemPhysChem **15** (2014), 4026-4031.
2. M. Llusà, F. Urbain, V. Smirnov, A. Antony, J. Andreu, and J. Bertomeu, *Aluminium induced texturing of glass substrates with improved light management for thin film solar cells*, Sol. Energy Mater. Sol. Cells **147** (2016), 276-280.
3. J. Klett, J. Ziegler, B. Kaiser, A. Radetinac, W. Jaegermann, R. Schäfer, F. Urbain, J.-P. Becker, V. Smirnov, and F. Finger, *Band engineering for efficient catalyst-substrate coupling for photoelectrochemical water splitting*, Phys. Chem. Chem. Phys. **18** (2016), 10751-10757.
4. J.-P. Becker, F. Urbain, V. Smirnov, U. Rau, and F. Finger, *Modelling thin film silicon based integrated water splitting devices*, Phys. Stat. Sol. A (2016), in press.
5. W. Jaegermann, B. Kaiser, J. Ziegler, F. Urbain, J.-P. Becker, V. Smirnov, F. Finger, J. Klett, and R. Schäfer, *Optimisation and characterisation of thin-film multijunction photovoltaic cells based on silicon for buried junction photovoltaic-electrochemical water splitting devices*, submitted to J. Mater. Chem. A (2015).

## Conference Presentations

### Oral Presentations

1. F. Urbain, K. Wilken, V. Smirnov, J.-P. Becker, and F. Finger, *Thin film silicon tandem junction solar cells for photoelectrochemical water splitting*, MRS Spring Meeting, San Francisco, USA, 21-25 April 2014.
2. F. Urbain, K. Wilken, O. Astakhov, V. Smirnov, J.-P. Becker, F. Finger, and U. Rau, *Photoelectrochemical water splitting using adapted thin film silicon tandem junction solar cells*, MRS Spring Meeting, San Francisco, USA, 21 - 25 April 2014.
3. F. Urbain, V. Smirnov, J.-P. Becker, U. Rau, and F. Finger, *All-Silicon Thin Film Solar Cell Based Photoelectrodes for Efficient Hydrogen Production: Cell Structure Development and Photovoltaic-Photoelectrochemical System Comparison*, 20<sup>th</sup> International Conference on Conversion and Storage of Solar Energy (IPS-20), Berlin, Germany, 27 July - 1 August 2014.
4. J.-P. Becker, F. Urbain, V. Smirnov, U. Rau, and F. Finger, *All-Silicon Thin Film Solar Cell Based Photoelectrodes for Efficient Hydrogen Production: Interface design and corrosion stability*, 20<sup>th</sup> International Conference on Conversion and Storage of Solar Energy (IPS-20), Berlin, Germany, 27 July - 1 August 2014.
5. F. Urbain, V. Smirnov, J.-P. Becker, F. Yang, J. Ziegler, B. Kaiser, W. Jaegermann, U. Rau, and F. Finger, *Multijunction thin film silicon photocathodes with photovoltages up to 2.8 V for the application in integrated PEC devices*, International Conference on Light Driven Water Splitting Using Semiconductor Based Devices (SolarFuel15), Mallorca, Spain, 10 - 13 March 2015.
6. F. Urbain, V. Smirnov, J.-P. Becker, A. Lambertz, U. Rau, and F. Finger, *Efficient multijunction thin film silicon solar cells with output voltages up to 2.8 V for the application in photoelectrochemical energy storage devices*, EMRS Spring Meeting, Lille, France, 11 - 15 May 2015.
7. W. Jaegermann, F. Urbain, V. Smirnov, J.-P. Becker, F. Yang, J. Ziegler, B. Kaiser, W. Jaegermann, U. Rau, and F. Finger, *Efficient multijunction thin film silicon based photocathodes for hydrogen production*, EMRS Spring Meeting, Lille, France, 11 - 15 May 2015.

8. F. Urbain, V. Smirnov, J.-P. Becker, F. Yang, J. Ziegler, B. Kaiser, W. Jaegermann, U. Rau, and F. Finger, *Efficient multijunction thin film silicon based photocathodes for hydrogen production*, EMRS Spring Meeting, Lille, France, 11 - 15 May 2015.
9. J.-P. Becker, F. Urbain, V. Smirnov, F. Yang, J. Ziegler, B. Kaiser, W. Jaegermann, U. Rau, and F. Finger, *Modeling silicon photovoltaic based integrated water-splitting devices*, 26<sup>th</sup> International Conference on Amorphous and Nanocrystalline Semiconductors (ICANS 26), Aachen, Germany, 13 - 18 September 2015.
10. S. Reynolds, F. Urbain, and V. Smirnov, *Spectral matching in high-voltage multi-junction thin-film silicon solar cells*, 26<sup>th</sup> International Conference on Amorphous and Nanocrystalline Semiconductors (ICANS 26), Aachen, Germany, 13 - 18 September 2015.
11. F. Urbain, *Hydrogen from Sunlight: Solar Fuel Production using Thin Film Silicon Solar Cells*, 4<sup>th</sup> Symposium of the HiTEC Graduate School for energy and climate, Jülich, Germany, 25 April 2016.  
**Award:** HiTEC Communicator Award - 1<sup>st</sup> price
12. F. Urbain, V. Smirnov, J.-P. Becker, F. Yang, J. Ziegler, B. Kaiser, W. Jaegermann, U. Rau, and F. Finger, *High Performance Water Splitting Devices Based on Multijunction Thin Film Silicon Solar Cells*, Photovoltaic Technical Conference, Marseille, France, 9 - 11 May 2016.

## Poster Presentations

1. F. Urbain, K. Wilken, V. Smirnov, A. Lambertz, O. Astakhov, F. Finger, and U. Rau, *Thin film silicon tandem junction solar cells for photoelectrochemical water splitting*, International Conference on New Advances in Materials Research for Solar Fuels Production (SolarFuel13), Granada, Spain, 12 - 14 June 2013.
2. J.-P. Becker, F. Urbain, V. Smirnov, J. Ziegler, B. Kaiser, S. Hoch, M. Blug, and F. Finger, *Solar hydrogen production using a silicon-based integrated photovoltaic-electrochemical water-splitting system*, MRS Spring Meeting, San Francisco, USA, 6 - 10 April 2015.

3. V. Smirnov, F. Urbain, A. Lambertz, and F. Finger, *High stabilized efficiency single and multi-junction thin film silicon solar cells*, 26<sup>th</sup> International Conference on Amorphous and Nanocrystalline Semiconductors (ICANS 26), Aachen, Germany, 13 - 18 September 2015.
4. F. Urbain, V. Smirnov, J.-P. Becker, F. Yang, J. Ziegler, B. Kaiser, W. Jaegermann, U. Rau, and F. Finger, *High performance photoelectrochemical devices based on multijunction thin film silicon solar cells*, 26<sup>th</sup> International Conference on Amorphous and Nanocrystalline Semiconductors (ICANS 26), Aachen, Germany, 13 - 18 September 2015.  
**Award:** physica status solidi Young Researcher Award

## Patent Applications

Alkalische photoelektrochemische Zelle, AKZ: 10 2015 003 003.5



# Curriculum vitae

Félix Urbain

born November 27th, 1986 in Luxembourg

---

## **Education**

1999-2006	Secondary school education at Lycée des Garçons in Luxembourg
2006	Degree: Diplôme de fin d'études secondaires (Section B)
2006-2010	Undergraduate studies in Materials Science at RWTH Aachen University, Germany
2010	Degree: Bachelor of Science (B.Sc. RWTH)
2010-2012	Graduate studies in Materials Science at RWTH Aachen University, Germany
2012	Degree: Master of Science (M.Sc. RWTH)
2011-2013	Postgraduate studies in Management, Business, Economics at RWTH Aachen University, Germany
2013	Degree: Master of Science (M.Sc. MBE RWTH)
2012-2015	Ph.D. studies at the Photovoltaics Department (IEK-5) of Forschungszentrum Jülich

## **Professional Experience**

2009-2011	Research assistant at the teaching and research group GaN Device Technology at RWTH Aachen University
2011	Research assistant at the Chair of Inorganic Chemistry and Electrochemistry at RWTH Aachen University
2011-2012	Research assistant at the teaching and research group GaN Device Technology at RWTH Aachen University
2012-2013	Researcher at the Innovation and Entrepreneurship Group at RWTH Aachen University
2015-present	Scientist at the Photovoltaics Department (IEK-5) of Forschungszentrum Jülich

**Awards and Achievements**

January 2012	Germany Scholarship - Deutschlandstipendium
September 2015	physica status solidi Young Researcher Award
April 2016	Communicator Award from the HiTEC Graduate School for energy and climate (1 <sup>st</sup> price)

# Acknowledgments

It is with great pleasure that I thank the many people who helped make this thesis possible, whether directly or indirectly.

I would like to express the deepest appreciation to Prof. Dr. Uwe Rau for giving me the possibility to pursue my research at a world renowned institute and for taking such a great interest and supporting me in my research. Prof. Dr. Uwe Rau always made time for me and helped me to clarify my goals and the steps that needed to be taken to reach them.

I also kindly thank Prof. Dr. Wolfram Jaegermann for his willingness to review this thesis. As coordinator of the thesis project from the Deutsche Forschungsgemeinschaft (DFG), Prof. Dr. Wolfram Jaegermann was strongly involved in my work and supported me with valuable and intense discussions.

I am deeply grateful to Dr. Friedhelm Finger for his guidance, his criticism, and for his confidence in me. His constructive comments and encouragements helped me to improve my personal skills, my publications, and allowed me to grow as a scientist. I highly value the leadership of Dr. Friedhelm Finger. As a mentor, he struck the perfect balance between encouraging me to take initiative and guiding me whenever I needed advice, which has been invaluable on both an academic and a personal level.

I would like to express my deep gratitude to Dr. Vladimir Smirnov, for being the best possible supervisor. His constant support, encouragement, and invaluable advice enabled me to become acquainted with the field of thin film semiconductors quickly and gave me the necessary tools to monitor and handle every situation. I admire his dedication towards research and his structured and logical thinking. Dr. Vladimir Smirnov always made time for me and helped me when I was unable to figure things out on my own. He gently encouraged me towards independence while at the same time giving me the security that he was always there if I needed him. On top of that, I appreciate our friendship, which made my life at work very enjoyable.

I thank Dr. Jan-Philipp Becker for being such a great colleague and advisor for me. His good advice, support, and friendship has been invaluable and helped me to considerably improve my work effectiveness and the present work.



I admire Andreas Lambertz's energy, passion, and creativity with respect to research on thin-film silicon. He was always open to share his experience he gained over more than ten years and helped me to move forward.

I thank my colleagues from the Technical University of Darmstadt for their support and many discussions during regularly organised meetings: Dr. Jürgen Ziegler, Dr. Florent Yang, and Dr. Bernhard Kaiser.

I would particularly like to thank Prof. Dr. Joan Ramón Morante for intense discussions and for his hospitality during my visits at the Catalonia Institute for Energy Research (IREC) in Barcelona. These journeys were clearly highlights during my time as a Ph.D. researcher.

I specially thank all those who helped me with sample preparation: Sandra Moll, Hildegard Siekmann, Ulrike Gerhards, Lars Petter, Andreas Schmalen, Johannes Wolff, Jürgen Radde, and Alain Doumit. The many who assisted with sample characterisation: Brigitte Zwaygardt, Christoph Zahren, Wilfried Reetz, Lars Nießen, Thomas Birrenbach, and Markus Hülsbeck. And last but not least, Andrea Mülheims, Astrid Nogga, and Petra Lorbach, who helped me with many administrative tasks.

A special thanks also to my direct colleagues and friends for making life at work so much fun and also for all the helpful discussions and comments during group meetings and otherwise. Thank you Karen Wilken, Andrew Paolo Cadiz Bedini, Beatrix Blank, Michael Smeets, Thomas Fink, Dr. Shuo Wang, Jan Flohre, Guillermo Olivera Pimentel, Nicolas Sommer, and Dr. Stefan Muthmann.

I would also like to acknowledge the financial support of the Deutsche Forschungsgemeinschaft (DFG), Priority Programme 1613 (Regeneratively produced fuels by light-driven water splitting: Investigation of involved elementary processes and perspectives of technologic implementation), for which I am grateful.

This thesis would not exist without the indispensable and committed support from my close friends. I thank them for bringing so much joy and color to my life and for helping me regenerate after stressful weeks. Thank you Imogen Moody, Michel Schiltz, Steve Laux, Tom Rihm, Hendrik Janssen, and many others.

Finally, I thank my parents, Alice Urbain-Liber and Arsène Urbain, who gave me a solid base from which to grow, shared happy and sad moments with me, supported me in every possible way, and always believed in me without a doubt. It is because of their unconditional love and utmost dedication that I have always felt free to follow my dreams.

*Et gin net genuch Wieder fier auszedrecken waat fier eng grouss Hellef Dier fier mech  
sid an wifill ech Iech ze verdanken hun. Daat heiten hun mier zesummen gepackt.  
Merci.*



# List of Figures

1.1	Solar-to-hydrogen efficiency $\eta_{\text{STH}}$ as a function of the open-circuit voltage $V_{\text{OC}}$ of a single absorber photovoltaic (PV) cell for varying performance of the PV cell and electrochemical catalyst. The yellow solid curve shows the Shockley-Queisser (SQ) limit for a single band gap PV cell efficiency $\eta_{\text{PV}}$ . The thermodynamically required voltage for the operation of a photoelectrochemical device for water splitting is 1.23 V. The black arrow indicates an improved electrochemical catalytic activity and the green arrow indicates an improved PV cell performance. For the black, blue, and red curves the transfer coefficient $\alpha$ was varied from 0.15 to 0.25 to 1 and the exchange current density $j_0$ was varied from $10^{-8}$ to $10^{-6}$ to $0.1 \times 10^3$ mA/cm <sup>2</sup> . For the dotted, dashed, and solid curves, $J_{\text{SC}}$ was varied from 0.9 to 0.95 to $1 \times J_{\text{SC,SQ}}$ and $J_0$ was varied from 100 to 20 to $1 \times J_{0,\text{SQ}}$ . A theoretical maximum efficiency of 30.5 % can be found at the crossing point of the red solid curve with the SQ-limit. For this ideal case of zero losses, the theoretical operation point of the PV-EC device (1.23 V) coincides with the maximum power point of the ideal PV cell in the SQ-limit. . . . .	4
2.1	Schematic illustration of optical transitions in a semiconductor (at 300 K) upon light excitation. Electrons are excited from the valence band into the conduction band by the absorption of a photon with the energy $h\nu$ , while leaving a vacancy or a hole in the valence band. The energy $E_g$ defines the width of the band gap of a semiconductor (details can be found in the text). . . . .	8
2.2	Relative position of the Fermi level $E_F$ for an intrinsic semiconductor <b>(a)</b> , for a <i>p</i> -type semiconductor <b>(b)</b> , and for an <i>n</i> -type semiconductor <b>(c)</b> . The splitting of the quasi-Fermi levels $E_{\text{Fn}}$ for electrons and $E_{\text{Fp}}$ for holes upon excitation by light, for instance, is shown in the illustration <b>(d)</b> . . . . .	10
2.3	Energy band diagrams of a homo- <i>pn</i> junction <b>(a)</b> , of a hetero- <i>pn</i> junction <b>(b)</b> , and of a <i>pin</i> junction <b>(c)</b> in equilibrium condition (details can be found in the text). . . . .	12

- 2.4 **(a)** Structure of a *pin* a-Si:H solar cell in superstrate configuration. The incident light enters the solar cell through a transparent conductive oxide (TCO) coated glass substrate. The rear side of the solar cell is composed of a ZnO:Al/Ag back contact. **(b)** Band diagram of a *pin* solar cell under illuminated conditions. The *p*- and *n*-layer produce an electric field that leads to the separation and the transportation of photogenerated charge carriers to the electrodes. Electrons move to the *n*-side and holes are transported to the *p*-side of the solar cell. The splitting of the quasi-Fermi levels  $E_{Fn}$  and  $E_{Fp}$  defines the photovoltage of the solar cell. . . . . 13
- 2.5 Schematic drawing of the a-Si:H/a-Si:H and a-Si:H/ $\mu$ c-Si:H tandem, the a-Si:H/a-Si:H/ $\mu$ c-Si:H and a-Si:H/ $\mu$ c-Si:H/ $\mu$ c-Si:H triple and the a-Si:H/a-Si:H/ $\mu$ c-Si:H/ $\mu$ c-Si:H quadruple junction solar cell structures in *pin* configuration investigated in this work. . . . . 15
- 2.6 **(a)** Illustration of the spectral distribution in a multijunction solar cell structure, for the example of a triple junction cell. **(b)** Band diagram of a *pin* multijunction solar cell under illuminated conditions (as an example a triple junction solar cell is shown). Holes and electrons from the a-Si:H top and middle cell, and the  $\mu$ c-Si:H bottom cell, respectively, have to recombine at the *n*/*p*-interfaces to ensure a continuous current. The interfaces are called recombination junctions. The sum of the splitting of the quasi-Fermi levels  $E_{Fn}$  and  $E_{Fp}$  of the top, middle and bottom cell defines the photovoltage of the multijunction cell. . . 16
- 2.7 Comparison of the Fermi energy scale using the vacuum level as a reference and the electrochemical scale using the standard hydrogen electrode (SHE) potential as a reference. The electrochemical potential of the oxygen evolution reaction ( $O_2/H_2O$ ) was calculated for *pH* 0. The standard electrode potentials of various redox couples under standard conditions ( $T = 298.15$  K;  $p = 1$  bar;  $c_{Ox} = c_{Red} = 1$ ) have been compiled in tables in literature (*e.g.* [56]). . . . . 19
- 2.8 Free-energy versus reaction coordinate diagram for a redox system under equilibrium (blue curve) and under polarisation (red curve) for  $c_{Ox} > c_{Red}$ .  $\Delta G_{eq-}^*$  and  $\Delta G_{eq+}^*$  denote the activation energies for the cathodic and anodic reactions, respectively under equilibrium.  $\Delta G_-^*$  and  $\Delta G_+^*$  denote the activation energies for the cathodic and anodic reactions, respectively, for applied bias conditions.  $\alpha$  is the transfer coefficient and  $\eta_{ct}$  is the overpotential. The figure is adapted from Ref. [61]. . . . . 21

- 2.9 Schematic illustration of the metal/electrolyte interface according to the Helmholtz model. The model consists of a double layer (inner and outer Helmholtz layer, IHL and OHL, respectively) and of a diffusion layer (adjacent to the double layer) and the electrolyte solution (adjacent to the diffusion layer, not shown here), which contains solvated cations and anions, respectively, and water dipoles. The potential drop across the metal/electrolyte interface is shown below the illustration. The figure is adapted from Ref. [61]. . . . . 24
- 2.10 **(a)** Schematic illustration of the energy levels in a semiconductor (left-hand side) and in a redox electrolyte (right hand side) shown on a common vacuum reference scale. **(b)** The semiconductor/electrolyte interface before and after equilibration (*i.e.* contact of the two phases) shown for an *n*-type semiconductor. **(c)** Same as in (b), but for a *p*-type semiconductor. . . . . 26
- 2.11 Schematic illustration of the potential drop at the semiconductor/electrolyte interface. A simplified equivalent circuit for the interface at equilibrium, including the three capacitors  $C_{SC}$ ,  $C_H$ , and  $C_D$ , is shown in the lower part of the figure. The figure is adapted from Ref. [51]. . . . . 27
- 2.12 Schematic illustration of the band structures of various photocatalyst materials, including the band gap energies and the positions of the band edges relative to the water reduction and oxidation potentials (V vs. SHE, *pH* 0) [79]. Cathodic (negative) and anodic (positive) potential directions are indicated on the right side of the illustration. . . . . 28
- 2.13 Band diagram illustration and schematic structure of a buried junction device, with its components: the multijunction photocathode (as example a-Si:H/a-Si:H/ $\mu$ c-Si:H) under non-biased illumination condition, a hydrogen evolution reaction (HER) catalyst layer at the photocathode/electrolyte interface, the electrolyte, and the anode with the oxygen evolution reaction (OER) catalyst. The energy levels for the HER and OER and the respective reactions are indicated in the illustration. Hydrogen evolution occurs at the rear side of the photocathode and oxygen occurs at the anode side.  $\Delta E = 1.23$  V is the thermodynamic potential required for water electrolysis at 25 °C.  $\eta_{HER}$  and  $\eta_{OER}$  indicate the overpotentials for the HER and OER, respectively. The different colors of the silicon absorber layers indicate different band gaps. . . . . 30

3.1	Electronic structure of hydrogenated amorphous silicon (a-Si:H) described by a density of states $N(E)$ , taken from Ref. [91]. Three types of states can be identified: extended band-like states (valence and conduction band), localised band-like states (band tails), and localised defect states in the energy gap. . . . .	34
3.2	Schematic drawing of the growth mechanism of amorphous silicon. $\text{SiH}_3$ molecule fragments diffuse over a hydrogen terminated surface and can abstract a hydrogen atom from a Si-atom, leaving a dangling bond. $\text{SiH}_4$ is formed which does not contribute to the film growth. A second $\text{SiH}_3$ may diffuse to the left dangling bond and attach to the substrate [96]. . . . .	35
3.3	A schematic model which illustrates the microstructure of hydrogenated microcrystalline silicon ( $\mu\text{c-Si:H}$ ) deposited by plasma enhanced chemical vapor deposition on a glass substrate. From the left side to the right hand side the film structure changes from highly microcrystalline silicon to almost amorphous silicon, <i>i.e.</i> the crystalline volume fraction decreases. This illustration is taken from Ref. [102]. .	37
3.4	Absorption coefficient $\alpha_{\text{abs}}$ as a function of the photon energy $E_{\text{ph}}$ of a-Si:H (blue solid curve), $\mu\text{c-Si:H}$ (red dashed curve), and c-Si (orange dotted curve). . . . .	38
3.5	Photograph of the PECVD system used to process the thin film silicon layers and solar cells. The system consists of six chambers used for different doped and undoped deposition processes. . . . .	40
3.6	Schematic outline of the six-Chamber PECVD deposition system used in this work for the deposition of the silicon thin films and shown in Fig. 3.5. Each chamber is only used for a certain type of process. The respective <i>p</i> -, <i>i</i> -, and <i>n</i> -layer processes are indicated. The chambers are connected <i>via</i> evacuated transfer locks and load locks to transfer the substrate, using the transport system. This system allows to move the substrate between the process chambers without breaking the vacuum. The transfer valves separate the chambers from each other. The chamber designated for electron spin resonance (ESR) sample preparation was not used in this work. . . . .	41
3.7	Principle design of the process chambers in the 6-chamber system for the preparation of silicon thin films. Except from the electrode distance, all the process chambers have the same construction. Capacitive plasma excitation between the powered and grounded electrode is provided by an RF-field. The picture is not drawn to scale. . . . .	42

- 3.8 Illuminated current density-voltage ( $j$ - $V$ ) characteristic of a solar cell (black curve), indicating the maximum power point (MPP),  $J_{SC}$ ,  $V_{OC}$ ,  $V_{MPP}$ ,  $J_{MPP}$ , and the derivation of  $FF$ . . . . . 48
- 4.1 Photograph of the PV-EC cell used in this work to characterise the PV-EC devices. The setup consists of a Teflon cell body and three electrodes: a working electrode (multijunction photocathode), a counter electrode and a Ag|AgCl reference electrode in 3 M potassium chloride (CH instruments, Inc., Austin, TX, USA). The photocathode is fixed in between the cell body and a metal plate, to which it is electrically contacted. The metal plate is connected with the potentiostat and has an  $0.5\text{ cm}^2$  optical aperture for illumination of the photocathode. 56
- 4.2 Schematic drawing of a tandem junction based photocathode in a three-electrode **(a)** and in a two-electrode setup **(b)**, respectively. In the three-electrode setup the reference electrode (RE) is positioned close to the working electrode (WE, photocathode). In the two-electrode setup only the WE and the CE are employed as electrodes. The corresponding voltammograms for the three-electrode setup **(c)** and for the two-electrode setup **(d)** are placed below the corresponding schematic drawing. In the three-electrode measurement the WE potential is measured with respect to the Ag|AgCl RE or with respect to the RHE (see Section 2.2.2). In the two-electrode setup the PV-EC device voltage is measured with respect to the CE (*e.g.* RuO<sub>2</sub>). The right ordinate in (d) depicts the achievable STH efficiency as a function of the photocurrent density at 0 V applied bias (operation point of PV-EC device). The onset potential for cathodic current  $E_{onset}$ , the scan rate, and the used electrolyte solution are indicated in **(c)** and **(d)**, respectively. . . . . 59
- 4.3 Schematic drawing of a tandem junction based PV-EC device with its photovoltaic and electrochemical components. Below, the equivalent circuit used to model the PV-EC device is depicted. The photovoltaic cell is connected in series with the electrolysis cell, which represents the electrochemical load of this device, including the current-dependent overpotentials for the HER and OER,  $\eta_{HER}(j)$  and  $\eta_{OER}(j)$  respectively, and the electrolyte ohmic drop  $jR$ . The photocurrent density  $j_{photo}$  is generated by the photovoltaic cell. The parallel and the shunt resistances of the photovoltaic cell are denoted by  $R_p$  and by  $R_s$ , respectively. . . . . 61



- 4.4 Current density-voltage characteristics of the main four circuit components of the PV-EC device:  $j$ - $V$  measurement of the solar cell ( $V_{PV}(j)$ , orange curve), modeled voltammogram of the  $\text{RuO}_2$  anode in a 0.1 M  $\text{H}_2\text{SO}_4$  solution with the associated  $\eta_{\text{OER}}(-j)$  (red curve), modeled voltammogram of the Ni HER catalyst layer in a 0.1 M KOH solution with the associated  $\eta_{\text{OER}}(j)$  (light blue curve), and the resistance of the 0.1 M KOH electrolyte ( $jR$ , dark blue line). The voltammogram of the PV-EC device ( $V_{\text{PV-EC}}(j)$ , green curve) was computed *via* on Eq. 4.1. . . . . 63
- 4.5 **(a)** Modeled current density-voltage curves of the PV-EC device for increasing electrolyte resistances  $R$ . The PV-EC device is composed of an a-Si:H/a-Si:H solar cell, a Pt HER and a  $\text{RuO}_2$  OER catalyst. The respective  $b$  and  $j_0$  values are kept constant and can be found in Table 6.3. The electrolyte resistance is increased from 0  $\Omega$  to 200  $\Omega$ . The  $j$ - $V$  curves were computed *via* on Eq. 4.1. **(b)** The solar-to-hydrogen efficiency calculated from the operation photocurrent density  $j_{\text{op}}$  of the PV-EC device from (a) as a function of the KOH electrolyte concentration  $C$ . **(c)** Corresponding measured resistances  $R$  of KOH electrolyte solutions for different concentrations  $C$ . The dotted lines in (b) and (c) serve as a guide to the eye. . . . . 64
- 4.6 Modeled current density-voltage curves of the HER catalyst **(a)** and of the PV-EC device **(b)** for a decreasing exchange current density  $j_0$  *via* Eq. 4.1. The respective  $b$  value was kept constant at 30 mV/dec. The PV-EC device is composed of an a-Si:H/a-Si:H solar cell and a  $\text{RuO}_2$  OER catalyst. An electrolyte resistance of 50  $\Omega$  was assumed. . . . . 66
- 4.7 Modeled current density-voltage curves of the HER catalyst **(a)** and of the PV-EC device **(b)** for a decreasing Tafel slope  $b$  *via* Eq. 4.1. The respective  $j_0$  value was kept constant at 1 mA/cm<sup>2</sup>. The PV-EC device is composed of an a-Si:H/a-Si:H solar cell and a  $\text{RuO}_2$  OER catalyst. An electrolyte resistance of 50  $\Omega$  was assumed. . . . . 66
- 4.8 **(a)** Generated volume of gas produced by an a-Si:H/a-Si:H/ $\mu\text{c-Si:H}$  triple junction based photocathode under AM 1.5 solar illumination for two hours of operation at 7 mA/cm<sup>2</sup> in 0.1 M KOH. The black line shows the theoretical gas volume for 100 % faradaic efficiency and the red stars are the measured data. The measurement error was estimated to be  $\Delta V_{\text{theo}} = \pm 0.2$  ml. **(b)** Evaluated faradaic efficiency over time calculated from the measured gas volume. . . . . 70

5.1	Hydrogen content $c_H$ as a function of the substrate temperature $T_s$ during the deposition of intrinsic a-Si:H layers, with different silane concentrations $SC$ . The thickness of the layers was 400 nm. The data is taken from Refs. [85,98] (By courtesy of K. Wilken, Forschungszentrum Jülich). . . . .	74
5.2	Optical gap energy $E_{04}$ as a function of the silane concentration $SC$ for intrinsic a-Si:H layers deposited at different substrate temperatures $T_s$ . The dotted lines are to guide the eye. The data is taken from Refs. [85,98] (By courtesy of K. Wilken, Forschungszentrum Jülich). .	75
5.3	Photovoltaic parameters of single junction solar cells (efficiency $\eta_{PV}$ <b>(a)</b> , open-circuit voltage $V_{OC}$ <b>(b)</b> , fill factor $FF$ <b>(c)</b> , short-circuit current density $J_{SC}$ <b>(d)</b> ) as a function of the substrate temperature $T_s$ of the intrinsic a-Si:H layer, with 10 % (blue squares) and 4 % (red triangles) silane concentration $SC$ , respectively. The intrinsic a-Si:H layers had a thickness of approx. 400 nm. The lines are to guide the eye. The data is taken from Refs. [85,98] (By courtesy of K. Wilken, Forschungszentrum Jülich). . . . .	76
5.4	Crystallinity $I_C^{RS}$ as a function of the silane concentration $SC$ of the intrinsic $\mu c$ -Si:H absorber layer. All investigated layers had a thickness of 800 nm. . . . .	78
5.5	Open-circuit voltage $V_{OC}$ of $\mu c$ -Si:H single junction solar cells as a function of the crystallinity $I_C^{RS}$ of the intrinsic $\mu c$ -Si:H absorber layers (arrow on the upper abscissa illustrates the corresponding trend for the silane concentration $SC$ ). Absorber layer thicknesses of 1300 nm (black triangles), 650 nm (red triangles), and 450 nm (green diamonds) were investigated. The dashed lines serve as a guide to the eye. . . .	79

- 5.6 **(a)** Raman crystallinity depth profile of the  $\mu\text{c-Si:H}$  *pin* solar cell structure without profiling of the silane concentration  $SC$  (standard, black dots) and with profiling of the silane concentration  $SC$  ( $SC$  profiling, red squares) during the deposition of the 1300 nm thick intrinsic absorber layer, respectively. *n*- and *p*-type layers and the intrinsic 1300 nm thick absorber layer are indicated by the blue dashed lines. **(b)** Silane concentration  $SC$  profile of a standard (dotted black line) and adapted (red line) deposition process of an intrinsic  $\mu\text{c-Si:H}$  absorber layer. **(c)** Current density-voltage  $j$ - $V$  measurements of  $\mu\text{c-Si:H}$  solar cells (1300 nm thick absorber layers) deposited with a standard deposition process (dotted black curve) and a  $\mu\text{c-Si:H}$  solar cell deposited with a stepwise adapted  $SC$  profile of the intrinsic absorber layer (red curve). Both solar cells have a Ag back reflecting contact. . . . . 81
- 5.7 **(a)** Schematic drawing of the  $\mu\text{c-Si:H}$  solar cell with the incorporated *n-i* buffer layer. **(b)** Open-circuit voltage  $V_{\text{OC}}$  of  $\mu\text{c-Si:H}$  solar cells as a function of *n-i* buffer layer thickness (5, 10, 20, 30, 50, 80 nm) for different intrinsic  $\mu\text{c-Si:H}$  absorber layer thicknesses (blue circles: 1300 nm, black squares: 650 nm, red triangles: 450 nm). All absorber layers were deposited at  $SC = 5\%$ . The maximum error in the  $V_{\text{OC}}$  determination is below 5 mV. . . . . 82
- 5.8 Photovoltaic parameters of  $\mu\text{c-Si:H}$  solar cells (conversion efficiency  $\eta_{\text{PV}}$  **(a)**, open-circuit voltage  $V_{\text{OC}}$  **(b)**, fill factor  $FF$  **(c)**, short-circuit current density  $J_{\text{SC}}$  **(d)**) as a function of the buffer layer thickness for different  $\mu\text{c-Si:H}$  absorber layer thicknesses: 1300 nm (blue circles), 650 nm (black squares), and 450 nm (red triangles). Dotted circles indicate the optimal buffer layer thickness for the corresponding *i*- $\mu\text{c-Si:H}$  layer thickness, in terms of  $V_{\text{OC}}$  and conversion efficiency  $\eta_{\text{PV}}$ . . . 83

- 5.9 Solar cell parameters: **(a)** conversion efficiency  $\eta_{PV}$ , **(b)** short-circuit current density  $J_{SC}$ , and **(c)** fill factor  $FF$  vs. the open-circuit voltage  $V_{OC}$  in a 1300 nm (■), a 650 nm (▲), and a 450 nm thick  $\mu c$ -Si:H absorber layer series (★), in a 1300 nm thickness combined with the *SC* profiling and incorporated buffer layer (50 nm) series (□), in a 650 nm thickness combined with incorporated buffer layer (20 nm) series (△), and in a 450 nm thickness combined with incorporated buffer layer (5 nm) series (☆). The trends of the six series around the best-cell  $V_{OC}$  are indicated by solid lines as a guide to the eye. Table 5.1 summarises the best-cell parameters for the solar cells indicated by arrows in (a). . . . . 85
- 5.10 Current density-voltage  $j$ - $V$  measurements of a-Si:H/ $\mu c$ -Si:H tandem solar cells with different  $\mu c$ -Si:H bottom cells: "1300 nm" reference series (cell A, green curve), "1300 nm + *SC* profiling + buffer layer (50 nm) series" (cell B, blue curve), "650 nm + buffer layer (20 nm)" series (cell C, red curve), and "450 nm + buffer layer (5 nm)" series (cell D, black curve). . . . . 89
- 5.11 Quantum efficiency measurements of the four a-Si:H/ $\mu c$ -Si:H tandem junction solar cells from Table 5.2. Letter A denotes the "1300 nm" reference series (green curves), B the "1300 nm + *SC* profiling + buffer layer (50 nm) series" (blue curves), C the "650 nm + buffer layer (20 nm)" series (red curves), and D the "450 nm + buffer layer (5 nm)" series (black curves). The photocurrent densities of the top and bottom cell,  $J_{QE,top}$  and  $J_{QE,bot}$  are depicted in the figure. Arrow indicates the trend of increasing bottom cell *QE* in the wavelength range between 400 and 600 nm with decreasing  $\mu c$ -Si:H absorber layer thickness. Top and bottom cell photocurrent densities calculated from the *QE* curves are placed near the related measurements. . . . . 90
- 5.12 Quantum efficiency measurements of the 130/180 and of the 130/130 a-Si:H/a-Si:H tandem junction solar cells from Table 5.3, respectively. The photocurrent densities of the top and bottom cell,  $J_{QE,top}$  and  $J_{QE,bot}$  are calculated from the *QE* curves and placed near the related measurements. . . . . 93
- 5.13 Quantum efficiency curves of a a-Si:H/ $\mu c$ -Si:H/ $\mu c$ -Si:H triple junction device corresponding to cell T3 from Table 5.4. Sub cell photocurrent densities calculated from the *QE* curves are placed near the related measurements and the total *QE* is displayed by the blue shaded area. 95

5.14	Quantum efficiency curves of a a-Si:H/a-Si:H/ $\mu$ c-Si:H triple junction device corresponding to cell T6 from Table 5.5. Sub cell photocurrent densities calculated from the $QE$ curves are placed near the related measurements. The blue shaded area displays the total $QE$ of the triple junction solar cell. . . . .	97
5.15	Quantum efficiency curves of the a-Si:H/a-Si:H/ $\mu$ c-Si:H/ $\mu$ c-Si:H quadruple junction solar cell Q3. Sub cell photocurrent densities calculated from the $QE$ curves are placed near the related measurements and the total $QE$ is displayed by the blue shaded area. . . . .	100
5.16	<b>(a)</b> Photovoltaic conversion efficiency $\eta_{PV}$ plotted as a function of the light soaking time for tandem: a-Si:H/ $\mu$ c-Si:H (blue squares, cell C from Table 5.2), a-Si:H/a-Si:H (purple triangles: absorber layer $T_s$ of 130/130 °C and open light blue triangles: absorber layer $T_s$ of 130/180 °C from Table 5.3), triple (red triangles: cell T3 from Table 5.4 and orange stars: cell T6 from Table 5.5), and quadruple junction solar cells (black circles: cell Q3 from Table 5.6). <b>(b)</b> Conversion efficiency normalised to the initial value as a function of the light soaking time for the tandem, triple, and quadruple junction solar cells. . . . .	101
5.17	Quantum efficiency measurement of a-Si:H/a-Si:H/ $\mu$ c-Si:H/ $\mu$ c-Si:H quadruple junction devices corresponding to cell Q3 from Table 5.6 in initial and stabilised state (after 1000 hours light soaking time). Initial sub cell photocurrent densities calculated from the $QE$ curves are placed near the related measurements. . . . .	103
5.18	Current density-voltage $j$ - $V$ curves of the a-Si:H/a-Si:H/ $\mu$ c-Si:H triple junction solar cell at various operating temperatures $T_{op}$ . The temperature range between 25 °C and 60 °C was investigated in steps of 5 °C. . . . .	104
5.19	Open-circuit-voltage $V_{OC}$ of a-Si:H single junction solar cells as a function of the optical gap energy $E_{04}$ of the respective intrinsic a-Si:H absorber layers. The dotted line serves as a guide to the eye. . . . .	107
5.20	Open-circuit voltages $V_{OC}$ as a function of the short-circuit photocurrent densities $J_{SC}$ of the developed a-Si:H and $\mu$ c-Si:H based single and multijunction solar cells. The grey dotted lines indicates a photovoltaic efficiency $\eta_{PV}$ of 10 % and 14 %, respectively, assuming a FF of 72 %. . . . .	108

5.21 Illustration of the achievable solar-to-hydrogen efficiency  $\eta_{\text{STH}_{\text{max}}}$  in PV-EC devices for water splitting based on thin film silicon solar cells. The illuminated  $j$ - $V$  curves of the tandem, triple, and quadruple junction solar cells are linked with the theoretical operation point of a PV-EC device at 1.23 V (dashed vertical line, without overpotential losses). In real PV-EC devices this operation point is shifted due to overpotential losses, which are plotted on the upper abscissa. The right ordinate depicts the achievable STH efficiency as a function of the respective photocurrent density at a certain overpotential multiplied by the value of 1.23 (see Section 4.4). . . . . 110

6.1 **(a)** Cathodic overpotentials (at  $-7 \text{ mA/cm}^2$ ) measured in 0.1 M KOH (light blue circles) and in 0.1 M  $\text{H}_2\text{SO}_4$  (red squares) for Au, Cu, Ti, Ni, Ag, Pt, and Al evaluated as single layers on ZnO:Al coated glass substrates. **(b)** Linear sweep voltammetry measurements, conducted in 0.1 M KOH, of single metal layers (approx. 150 nm of Al, Au, Ag, Cu, Ti, Ni, Pt) on glass substrates at a scan rate of 10 mV/s. **(c)** The same measurements conducted in 0.1 M  $\text{H}_2\text{SO}_4$ . The data in (b) and (c) were corrected by the electrolyte series resistance, which was measured by electrochemical impedance spectroscopy. The overpotentials presented in Fig. 6.1(a) are taken at a current density of  $-7 \text{ mA/cm}^2$  in (b) and (c). **(d)** Current density-voltage  $j - V$  measurements of the a-Si:H/a-Si:H solar cells (cell 130/130 from Table 5.3 in Section 5.4) with different metallic back reflecting layers as back contact (approx. 300 nm). . . . . 115

6.2	Linear sweep voltammetry measurements under AM 1.5 illumination (100 mW/cm <sup>2</sup> ) of the photocathodes with different metal contact designs (same a-Si:H/a-Si:H tandem structure as cell 130/130 from Table 5.3). The single metal layer back contacts are assigned as follows: orange dashed curve: Al; blue dotted curve: Ag; light blue dotted curve: Ni; grey dashed curve: Pt. The stacks of two metal layers combine the optical and the catalytic properties of each individual metal and are assigned as follows: red dashed curve: Al/Ni; green solid curve: Ag/Pt. The measurements were conducted in 0.1 M KOH at a scan rate $\nu$ of 30 mV/s. The photoelectrochemical parameters are listed in Table 6.1. The potential of the photocathode is plotted versus the RHE and versus the Ag AgCl reference electrode on the upper and on the lower abscissa, respectively. $E_{\text{onset}}$ is taken at a photocurrent density value of -0.5 mA/cm <sup>2</sup> . . . . .	117
6.3	Reflectivity measurements of a-Si:H/a-Si:H solar cells with different back contacts consisting of ZnO:Al and a single metal Ag layer (solid) and a metal layer stack of Ag and Pt (dotted line). . . . .	118
6.4	Potentiostatic measurement of the a-Si:H/a-Si:H photocathode with an Ag/Pt contact at 0 V vs. RHE under AM 1.5 illumination. The measurement was conducted in 0.1 M KOH over the course of four hours of operation. . . . .	120
6.5	Linear sweep voltammetry measurements of the PV-EC devices based on thin film silicon multijunction solar cells (same initial cells as in Table 5.7) with a 150 nm thick Pt layer as HER catalyst on top of the Ag contact and a RuO <sub>2</sub> counter electrode for the OER reaction. The measurements were conducted in 0.1 M KOH at a scan rate of 30 mV/s. The right ordinate depicts the achievable STH efficiency as a function of the photocurrent density at 0 V applied bias (according to Eq. 4.4). . . . .	121
6.6	Linear sweep voltammetry measurements of PV-EC devices based on a-Si:H/a-Si:H/ $\mu$ c-Si:H triple and quadruple junction photocathodes with a RuO <sub>2</sub> counter electrode for the OER reaction. For the HER reaction, 150 nm of Ni (dotted curves) and Pt (solid curves) were deposited on top of the Ag solar cell contacts, respectively. The measurements were conducted in 0.1 M KOH at 30 mV/s. The right ordinate depicts the achievable STH efficiency as a function of the photocurrent density at 0 V (see Eq. 4.4). . . . .	123

- 6.7 Linear sweep voltammetry measurements of the a-Si:H/a-Si:H/ $\mu$ c-Si:H and the quadruple junction based PV-EC devices with Pt and Ni catalyst layers, respectively, in 0.1 M (solid curves) and 1 M KOH (dotted curves). RuO<sub>2</sub> was used as a counter electrode for the OER reaction and the measurements were conducted in 0.1 M KOH at a scan rate of 30 mV/s. The right ordinate depicts the achievable STH efficiency as a function of the photocurrent density at 0 V applied bias. 125
- 6.8 Chronoamperometric stability measurement monitoring the long-term stability of the a-Si:H/a-Si:H/ $\mu$ c-Si:H and the quadruple junction based PV-EC devices with Pt and Ni catalyst layers (on top of Ag contacts), respectively, at 0 V applied bias. The measurements were conducted in 0.1 M (solid curves) and in 1 M KOH (dotted curves) under AM 1.5 illumination (100 mW/cm<sup>2</sup>). RuO<sub>2</sub> was used as a counter electrode for the OER reaction. The right ordinate depicts the achievable STH efficiency as a function of the photocurrent density at 0 V applied bias. The abscissa indicates the PV-EC operation time on a logarithmic scale. . . . . 126
- 6.9 Comparison of the current density-voltage characteristics of PV-EC devices based on the initial (solid lines, same curves as in Fig. 6.5) and the light soaked ("stabilised", dotted lines) multijunction solar cells. A 150 nm thick Pt layer was used as the HER catalyst and a RuO<sub>2</sub> counter electrode for the OER reaction. The measurements were conducted in 0.1 M KOH at a scan rate of 30 mV/s. The right ordinate depicts the achievable STH efficiency as a function of the photocurrent density at 0 V applied bias. . . . . 128
- 6.10 Current density-voltage characteristics of the main four circuit components of the PV-EC device:  $j$ - $V$  measurement of an a-Si:H/a-Si:H/ZnO:Al/Ag solar cell ( $V_{PV}(j)$ , black solid curve), voltammogram of the RuO<sub>2</sub> anode in a 0.1 M H<sub>2</sub>SO<sub>4</sub> solution at a scan rate of 5 mV/s (with the associated  $\eta_{OER}(j)$ , orange dashed curve), voltammogram of the Pt HER catalyst layer in a 0.1 M H<sub>2</sub>SO<sub>4</sub> solution at a scan rate of 5 mV/s (with the associated  $\eta_{HER}(j)$ , green dashed curve), and resistance of the 0.1 M H<sub>2</sub>SO<sub>4</sub> electrolyte ( $jR$ , red dotted line). The current density-voltage characteristic of the PV-EC device ( $V_{PV-EC}(j)$ , blue dashed curve) was calculated based on Eq. 4.1. . . . . 131



- 6.11 Comparison of measured (solid curves, scan rate 30 mV/s) and calculated (dashed curves) voltammograms of three PV-EC devices with different configurations. The blue curves represent the current density-voltage behavior of a PV-EC device composed of an a-Si:H/a-Si:H tandem junction solar cell with Pt and RuO<sub>2</sub> as HER and OER catalyst, respectively, measured in 0.1 M H<sub>2</sub>SO<sub>4</sub> (individual measurements can be found in Fig. 6.10). The green curves show the current density-voltage characteristics of an a-Si:H/a-Si:H/ $\mu$ c-Si:H triple junction based PV-EC device with Pt and RuO<sub>2</sub> as catalyst materials, measured in 1 M KOH. The red curves display the current density-voltage characteristics of a PV-EC device based on a quadruple junction solar cell with Ni and IrO<sub>2</sub> as HER and OER catalysts, respectively, measured in 0.1 M KOH. . . . . 132
- 6.12 Modeled current density-voltage curves of the HER and OER catalysts considered in this section. The curves were computed *via* Eq. 2.14 using the Tafel parameters provided in Table 6.3. As example, the overpotentials for Ni ( $\eta_{\text{HER}}(j)$ ) and for IrO<sub>2</sub> ( $\eta_{\text{OER}}(j)$ ) are indicated. . 134
- 6.13 Calculated voltammograms of a-Si:H/a-Si:H **(a)**, a-Si:H/a-Si:H/ $\mu$ c-Si:H **(b)**, and quadruple junction **(c)** based PV-EC devices with varying HER and OER catalysts. The HER/OER catalyst combinations are: Pt/RuO<sub>2</sub> (yellow curves), Ni/IrO<sub>2</sub> (red curves), Mo<sub>2</sub>/NiO<sub>x</sub> (purple curves), and MoS<sub>2</sub>/Co<sub>3</sub>O<sub>4</sub> (black curves). The respective values of  $b$  and  $j_0$  for the  $j$ - $V$  calculation are taken from Table 6.3. An electrolyte resistance of 56  $\Omega$  was assumed (0.1 M KOH, see Table 6.4). The respective solar cell type is indicated in the corresponding figure. The right ordinate depicts the achievable STH efficiency as a function of the photocurrent density at 0 V applied bias. . . . . 135
- 6.14 **(a)** Linear sweep voltammetry measurements showing the cathodic and anodic current density-voltage dependence of the Pt and RuO<sub>2</sub> electrodes, respectively, in 0.1 M KOH. **(b)** Linear sweep voltammetry measurements showing the cathodic and anodic current density-voltage dependence of the Pt and RuO<sub>2</sub> electrodes, respectively, in 1 M KOH. The measurements were conducted at a scan rate of 5 mV/s at different operation temperatures  $T_{\text{op}}$ . The potentials were corrected by the  $jR$ -drop in the electrolyte. . . . . 139

6.15 Calculated current density-voltage curves of the a-Si:H/a-Si:H/ $\mu$ c-Si:H based PV-EC device at different operation temperatures in 0.1 M and 1 M KOH, respectively. The data for the calculation of the  $V_{\text{PV-EC}}(j, T)$  (based on Eq. 6.1) curves was taken from Table 6.4 ( $T$ -dependent electrolyte resistances  $R(T)$ ), from Fig. 6.14(a) and (b), respectively ( $T$ -dependent HER and OER performance,  $\eta_{\text{HER}}(j, T)$  and  $\eta_{\text{OER}}(j, T)$ , respectively). The current density at 0 V applied bias defines the operation point of the PV-EC device. . . . . 140

6.16 On the left ordinate, the estimated solar-to-hydrogen efficiency  $\eta_{\text{STH}_{\text{max}}}$  of the triple junction based PV-EC device in 0.1 M (red circles) and 1 M KOH (blue squares), respectively, is plotted as a function of the operation temperature. The  $\eta_{\text{STH}_{\text{max}}}$  was calculated based on Eq. 4.4 using the  $j_{\text{op}}$  values from Fig. 6.15. On the right ordinate, the photovoltaic efficiency of the triple junction solar cell as a function of the operation temperature is shown (black triangles). . . . . 141

6.17 Reported experimental solar-to-hydrogen efficiencies of thin film silicon based devices that are able to spontaneously split water in the presence of solar radiation. Silicon tandem (2J) [153, 154, 211, 212], triple (3J) [28, 142–144, 148, 208, 212–217], and quadruple (4J) [144] junction devices are plotted in different colours. Furthermore, hybrid devices are considered which combine single [87] or tandem thin film silicon junctions [87, 218–221] with a semiconductor liquid junction (SLJ). The figure is adapted from Ref. [222] . . . . . 144

A1 **(a)** Current density-voltage  $j$ - $V$  curves of the a-Si:H/a-Si:H tandem junction solar cell (cell 130/130, Table 5.3) at various operating temperatures  $T_{\text{op}}$ . **(b)** Current density-voltage  $j$ - $V$  curves of the a-Si:H/a-Si:H/ $\mu$ c-Si:H/ $\mu$ c-Si:H quadruple junction solar cell (see Table 5.3) at various operating temperatures  $T_{\text{op}}$ . In both measurements, the temperature range between 25 °C and 60 °C was investigated in steps of 5 °C. . . . . I

A2 Established prices (in Euro/1 cm<sup>2</sup> \* 100 nm) for Pt, Ag, Ni, and Al. Source: London Metal Exchange, 10 February 2015. . . . . II

- A3 **(a)** Calculated current density-voltage curves of the a-Si:H/a-Si:H tandem junction PV-EC device at different operation temperatures in both 0.1 M and 1 M KOH, respectively. **(b)** Calculated current density-voltage curves of the a-Si:H/a-Si:H/ $\mu$ c-Si:H/ $\mu$ c-Si:H quadruple junction PV-EC device at different operation temperatures in both 0.1 M and 1 M KOH, respectively. The data for the calculation of the  $V_{\text{PV-EC}}(j, T)$  (based on Eq. 6.1) curves was taken from Table 6.4 ( $T$ -dependent electrolyte resistances  $R(T)$ ) and from Fig. 6.14(a) and (b), respectively ( $T$ -dependent HER and OER performance,  $\eta_{\text{HER}}(j, T)$  and  $\eta_{\text{OER}}(j, T)$ , respectively). The current density at 0 V applied bias defines the operation point of the PV-EC device. . . . . II

# List of Tables

3.1	Deposition parameters of the individual thin film silicon layers used in the present work unless otherwise stated. . . . .	43
3.2	Overview of the used light wavelengths for the saturation of the individual sub cells in tandem, triple and quadruple junction solar cells for the $QE$ evaluation. . . . .	50
5.1	Photovoltaic parameters of the best-cell $\mu\text{c-Si:H}$ devices from Fig. 5.9. The deposition parameters of teh fabricated solar cells regarding the thicknesses of the absorber layer, the application of a $SC$ profiling, and the incorporation of buffer layers at various thicknesses are listed.	87
5.2	Photovoltaic parameters of a-Si:H/ $\mu\text{c-Si:H}$ tandem junction solar cells fabricated with different series of $\mu\text{c-Si:H}$ bottom cells and a-Si:H top cells for different silane concentrations $SC$ and thicknesses. The corresponding current density-voltage measurements are depicted in Fig. 5.10. . . . .	88
5.3	Photovoltaic parameters of a-Si:H/a-Si:H tandem junction solar cells fabricated with varying $SC$ and $T_s$ of top and bottom cell based on the results from Fig. 5.3. . . . .	91
5.4	Overview of all relevant layer preparation and PV parameters ( $V_{OC}$ , $J_{SC}$ , $FF$ , and efficiency $\eta_{PV}$ ) of a-Si:H/ $\mu\text{c-Si:H}$ / $\mu\text{c-Si:H}$ devices. . . . .	94
5.5	Overview of all relevant layer preparation and PV parameters ( $V_{OC}$ , $J_{SC}$ , $FF$ , and efficiency $\eta_{PV}$ ) of a-Si:H/a-Si:H/ $\mu\text{c-Si:H}$ devices. . . . .	96
5.6	Overview of the intrinsic sub cell absorber layer thicknesses of three investigated quadruple junction solar cells, referred to as Q1-Q3, based on a-Si:H and $\mu\text{c-Si:H}$ . Additionally, the sub cell photocurrent densities (based on $QE$ measurement without anti-reflection foil), and initial photovoltaic parameters of a-Si:H/a-Si:H/ $\mu\text{c-Si:H}$ / $\mu\text{c-Si:H}$ quadruple junction solar cells (based on illuminated $j-V$ measurements with anti-reflection foil) are presented. . . . .	99
5.7	Overview of the photovoltaic parameters of the a-Si:H/ $\mu\text{c-Si:H}$ and a-Si:H/a-Si:H tandem, the a-Si:H/ $\mu\text{c-Si:H}$ / $\mu\text{c-Si:H}$ and a-Si:H/a-Si:H/ $\mu\text{c-Si:H}$ triple, and the a-Si:H/a-Si:H/ $\mu\text{c-Si:H}$ / $\mu\text{c-Si:H}$ quadruple junction solar cells in initial and stabilised state (after 1000 hours of light soaking). The measurements were conducted without an anti-reflection foil. . . . .	102

5.8	Overview of the photovoltaic parameters evaluated at room temperature and at 60 °C for a-Si:H/a-Si:H tandem, a-Si:H/a-Si:H/ $\mu$ c-Si:H triple, and a-Si:H/a-Si:H/ $\mu$ c-Si:H/ $\mu$ c-Si:H quadruple junction solar cells. The corresponding $j$ - $V$ measurements were conducted without additional anti-reflection foils. . . . .	105
6.1	Overview of the photovoltaic and the photoelectrochemical parameters of the photocathodes with different metal contacts. The respective metal layer thicknesses are indicated in the second column. $J_0$ denotes the photocurrent density at 0 V vs. RHE. The onset potential for cathodic current $E_{\text{onset}}$ was taken as the value at a photocurrent density of $-0.5 \text{ mA/cm}^2$ from Fig. 6.2. The short-circuit current density $J_{\text{SC}}$ for the corresponding solar cells were taken from Fig. 6.1(d).	118
6.2	Overview of the estimated initial and stabilised (after 1000 h of light soaking) solar-to-hydrogen efficiencies of multijunction based PV-EC devices. The $\eta_{\text{STH}_{\text{max}}}$ and $\eta_{\text{STH}_{\text{max,stab}}}$ values are evaluated from the $j_{\text{op}}$ values in Fig. 6.9. The relative degradation of the solar-to-hydrogen efficiency is also listed and compared to the degradation of the photovoltaic efficiency $\eta_{\text{PV}}$ , calculated from Table 5.7. . . . .	129
6.3	Tafel slopes and exchange current densities of benchmarking catalyst materials for the HER and OER. The corresponding literature references are given in the last column. . . . .	133
6.4	The resistances $R$ of the electrolyte for the used set-up with KOH concentrations of 0.1 M and 1 M, respectively. The resistances were determined by means of electrochemical impedance spectroscopy at different temperatures of the electrolyte. . . . .	138
A1	Deposition and photovoltaic parameters for the <b>a-Si:H single junction solar cells</b> discussed in Section 5.2.2. The deposition parameters refer to the intrinsic absorber layers of the a-Si:H solar cells and are abbreviated as follows: silane concentration $SC$ and substrate temperature $T_s$ . The photovoltaic parameters describe the conversion efficiency $\eta_{\text{PV}}$ , the open-circuit voltage $V_{\text{OC}}$ , the fill factor $FF$ , and the short-circuit current density $J_{\text{SC}}$ . The solar cells were deposited on Asahi type "VU" glass substrates with an Ag back contact and the intrinsic absorber layers had a thickness of 400 nm. More details on the solar cell fabrication process and deposition parameters can be found in Section 3.2.2 and in Table 3.1, respectively. . . . .	III

A2 Deposition and photovoltaic parameters for the  **$\mu\text{c-Si:H}$  single junction solar cell series** shown in Fig. 5.9. The deposition parameters refer to the intrinsic absorber layers of the  $\mu\text{c-Si:H}$  solar cells and are abbreviated as follows: silane concentration  $SC$ ,  $i$ -layer thickness. The layer preparation parameters, such as  $SC$  profiling and  $ni$  buffer layer thickness are also listed. The photovoltaic parameters of the different  $\mu\text{c-Si:H}$  solar cell series describe the conversion efficiency  $\eta_{PV}$ , the open-circuit voltage  $V_{OC}$ , the fill factor  $FF$ , and the short-circuit current density  $J_{SC}$ . The solar cells were deposited on textured ZnO:Al coated glass substrates. More details on the solar cell fabrication process and deposition parameters can be found in Section 3.2.2 and in Table 3.1, respectively. . . . . IV

A3 Deposition and photovoltaic parameters for the  **$\text{a-Si:H}/\mu\text{c-Si:H}$  tandem junction solar cells** discussed in Section 5.4.1. The deposition parameters of the individual sub cells can be found in Table 5.2. The photovoltaic parameters describe the conversion efficiency  $\eta_{PV}$ , the open-circuit voltage  $V_{OC}$ , the fill factor  $FF$ , and the short-circuit current density  $J_{SC}$ . The solar cells were deposited on textured ZnO:Al coated glass substrates. More details on the solar cell fabrication process and deposition parameters can be found in Section 3.2.2 and in Table 3.1, respectively. . . . . V

A4 Deposition and photovoltaic parameters for the  **$\text{a-Si:H}/\text{a-Si:H}$  tandem junction solar cells** discussed in Section 5.4.2. The deposition parameters of the individual sub cells can be found in Table 5.3. The photovoltaic parameters describe the conversion efficiency  $\eta_{PV}$ , the open-circuit voltage  $V_{OC}$ , the fill factor  $FF$ , and the short-circuit current density  $J_{SC}$ . The solar cells were deposited on Asahi type "VU" glass substrates. More details on the solar cell fabrication process and deposition parameters can be found in Section 3.2.2 and in Table 3.1, respectively. . . . . V

- A5 Deposition and photovoltaic parameters for the **triple junction solar cells** discussed in Section 5.5 and presented in Table 5.4 and Table 5.5, respectively. The photovoltaic parameters describe the conversion efficiency  $\eta_{PV}$ , the open-circuit voltage  $V_{OC}$ , the fill factor  $FF$ , and the short-circuit current density  $J_{SC}$ . The a-Si:H/ $\mu$ c-Si:H/ $\mu$ c-Si:H solar cells (referred to as T1-T3) were deposited on textured ZnO:Al coated glass substrates and the a-Si:H/a-Si:H/ $\mu$ c-Si:H (referred to as T4-T6) were deposited on Asahi type "VU" glass substrates. More details on the solar cell fabrication process and deposition parameters can be found in Section 3.2.2 and in Table 3.1, respectively. . . . . VI
- A6 Deposition and photovoltaic parameters for the **quadruple junction solar cells** discussed in Section 5.5 and presented in Table 5.6. The photovoltaic parameters describe the conversion efficiency  $\eta_{PV}$ , the open-circuit voltage  $V_{OC}$ , the fill factor  $FF$ , and the short-circuit current density  $J_{SC}$ . The a-Si:H/a-Si:H/ $\mu$ c-Si:H/ $\mu$ c-Si:H solar cells were deposited on textured ZnO:Al coated glass substrates. More details on the solar cell fabrication process and deposition parameters can be found in Section 3.2.2 and in Table 3.1, respectively. . . . . VI

Band / Volume 310

**Influence of H<sub>2</sub>O, HCl and H<sub>2</sub>S on the Release and Condensation of Trace Metals in Gasification**

M. Benito Abascal (2016), XIX, 172 pp

ISBN: 978-3-95806-125-5

Band / Volume 311

**Mechanical and Thermochemical Properties of Nano-structured Membranes for Gas Separation in Fossil-fired Power Plants**

J. Zhang (2016), II, 134 pp

ISBN: 978-3-95806-126-2

Band / Volume 312

**Development of Embedded Thermocouple Sensors for Thermal Barrier Coatings (TBCs) by a Laser Cladding Process**

Y. Zhang (2016), II, 108 pp

ISBN: 978-3-95806-129-3

Band / Volume 313

**Streamwater transit time distributions at the catchment scale: constraining uncertainties through identification of spatio-temporal controls**

M. Stockinger (2016), XIX, 161 pp

ISBN: 978-3-95806-131-6

Band / Volume 314

**Entwicklung eines metallbasierten Substratkonzepts für energieeffiziente Gastrennmembranen**

J. A. Kot (2016), xi, 201 pp

ISBN: 978-3-95806-134-7

Band / Volume 315

**Langzeitbeobachtung der Dosisbelastung der Bevölkerung in radioaktiv kontaminierten Gebieten Weißrusslands – Korma-Studie II (1998 – 2015)**

P. Zoriy, H. Dederichs, J. Pillath, B. Heuel-Fabianek, P. Hill, R. Lennartz (2016), ca 104 pp

ISBN: 978-3-95806-137-8

Band / Volume 316

**Oxidation Mechanisms of Metallic Carrier Materials for Gas Separation Membranes**

M. Schiek (2016), 148 pp

ISBN: 978-3-95806-138-5



Band / Volume 317

**Thermoschockverhalten und temperaturabhängige Eigenschaften  
kohlenstoffarmer und -freier Feuerfestwerkstoffe**

A. Böhm (2016), VI, 153 pp

ISBN: 978-3-95806-139-2

Band / Volume 318

**Theoretical and experimental studies of runaway electrons  
in the TEXTOR tokamak**

S.S. Abdullaev, K.H. Finken, K. Wongrach, O. Willi (2016), X, 109 pp

ISBN: 978-3-95806-140-8

Band / Volume 319

**Modelling Thermodynamic Properties of Intercalation Compounds  
for Lithium Ion Batteries**

S. O. Dang (2016), x, 133 pp

ISBN: 978-3-95806-141-5

Band / Volume 320

**Atmospheric Mixing in a Lagrangian Framework**

M. Tao (2016), 146 pp

ISBN: 978-3-95806-142-2

Band / Volume 321

**Statistical analysis and combination of active and passive  
microwave remote sensing methods for soil moisture retrieval**

K. Rötzer (2016), XIV, 112 pp

ISBN: 978-3-95806-143-9

Band / Volume 322

**Langzeitstabilität der Polymerelektrolyt-Wasserelektrolyse  
bei reduziertem Iridiumgehalt**

C. G. Rakousky (2016), VII, 199 pp

ISBN: 978-3-95806-147-7

Band / Volume 323

**Light induced water splitting using multijunction thin film  
silicon solar cells**

F. Urbain (2016), ix, 174, XLVI pp

ISBN: 978-3-95806-148-4

Weitere **Schriften des Verlags im Forschungszentrum Jülich** unter  
<http://wwwzb1.fz-juelich.de/verlagextern1/index.asp>



**Energie & Umwelt /  
Energy & Environment  
Band / Volume 323  
ISBN 978-3-95806-148-4**

